Design of a Compton camera for medical imaging and characterization ofits components

Dissertation der Fakultät für Physik
der
Ludwig-Maximilians-Universität München

München 2015

Design of a Compton camera for medical imaging and characterization of its components

Dissertation der Fakultät für Physik
der
Ludwig-Maximilians-Universität München

vorgelegt von
Christian Lang
geboren in Würzburg

München, den 05.05.2015

Erstgutachter: PD Dr. Peter Thirolf
Zweitgutachter: Prof. Dr. Otmar Biebel
Tag der mündlichen Prüfung: 11.08.2015

Contents

Zusammenfassung

Die Hadronentherapie hat sich wegen des steilen Dosisabfalls im Bragg-Peak des auf das Tumorvolumen einwirkenden Teilchenstrahls, als eine effektive Art zur Behandlung von Tumoren, speziell in der Nähe von kritschen Organen, erwiesen. Um jedoch voll von den Vorteilen der örtlich scharf begrenzten Dosis-Deposition der Ionen im Tumorvolumen profitieren zu können, wird ein verlässlicher Reichweitennachweis benötigt. Eine vielversprechende neue Methode ist die Detektion von prompt emittierten Photonen aus angeregten Kernen, die aus der Wechselwirkung des Teilchenstrahls mit dem menschlichen Gewebe stammen. Auf der Suche nach einer Methode zur Detektion dieser prompt emittierten γ Strahlung, hat das Konzept einer Compton-Kamera in jüngster Zeit verstärkt Aufmerksamkeit erhalten. Dieses stützt sich auf die Messung von Orte und Energien der Compton-Streukinematik, um daraus eine Photonenquellverteilung zu rekonstruieren. Für die Designspezifikation einer Compton-Kamera mit Elektronenspurverfolgung wurden Monte-Carlo-Simulationen durchgeführt. Die sich daraus ergebende optimierte Geometrie der Kamera besteht aus einem $LaBr_3$:(Ce) Szintillator (50 x 50 x 30 mm^3), oder alternativ aus einem 2D segmentierten hochreinen planaren Germaniumdetektor (64 x 64 x 15 mm^3), der als Absorptionsdetektor fungiert, in Kombination mit einer gestabelten Anordung aus 6 doppelseitigen Silizium-Streifenzählern (50 x 50 x 0.5 mm^3), die als Streudetektoren arbeiten. Die Wahl des Szintillatormaterials $LaBr_3$:(Ce) gründet auf seiner hervorragenden Energie- und Zeitauflösung, da die Kamera im Umfeld von laserbeschleunigten Teilchenstrahlen betrieben werden soll, wo der Laser ein konkurrenzlos scharfes sub-ps Triggersignal bereitstellt. Die Wahl auf doppelseitige Silizium-Streifenzähler fiel aufgrund der hohen 2D Granularität, sowie wegen der zusätzlichen Möglichkeit der Elektronenspurverfolgung. Die optimierte Compton-Kamera-Geometrie zeigt im wichtigen Energiebereich der prompt emittierten γ-Strahlen von 4 - 6 MeV eine räumliche Auflösung von 1.5° - 2.5° (entsprechend 1.5 - 2 mm bei 50 mm Quellenabstand), mit einer Effizienz von ca. $1.5 \cdot 10^{-4}$. Zusätzlich wird eine nuklearmedizinische Abbildungstechnik präsentiert, beruhend auf den Schnittpunkten von Dreifach-Photonen-Trajektorien von $\beta^+\gamma$ Koinzidenzen, die geeignetn ist, um Submillimeter-Auflösung in 3D mit weniger zu rekonstruierenden Schnittpunkten per Voxel als bei konventioneller PET-Rekonstruktions-Analyse zu erreichen. Diese "γ-PET"-Technik zielt auf spezielle β^+-zerfallende Isotope, die simultan zum β^+ -Zerfall ein zusätzliches promptes Photon emittieren. In Simulationen konnte eine räumliche Auflösung von ca. 0.4 mm (Halbwertsbreite) in allen Richtungen für die Abbildung einer ^{22}Na Punktquelle erreicht werden. Für eine verlässliche Submillimeter-Bildrekonstruktion einer Punktquelle, die in einem Streuvolumen aus Wasser mit einem Voxel-Volumens von ca. 1 mm^3 eingebettet ist, sind nur 40 Schnittpunkte ausreichend ("Hochauflösungs-Modus"). Darüber hinaus kann im Falle eines grösseren Voxel-Volumens von 2 x 2 x 3 mm^3 ("Hochempfindlichkeits-Modus"), mit der gleichen benötigten geringen Menge von ca. 40 Schnittpunkten rekonstruierter Ereignisse bei einer injizierten Aktivität von 400 MBq von ^{76}Br, die Aufnahmezeit für die Bildrekonstruktion (hier ca. 140 s) signifikant verringert werden, und so möglicherweise ein Weg zur Quasi-Echtzeitbildgebung geebnet werden. Anschliessend wurden die Zeit-, Orts- und Energieauflösung der Dektorkomponenten im Labor, sowie an zwei Synchrotron-Lichtquellen, charakterisiert und anschliessend zur Compton-Kamera zusammengefügt. Schliesslich wird ein Kernresonanz-Fluoreszenz-Experiment präsentiert, bei dem zum ersten Mal der medizinsch relevante 478 keV Kernübergang von ^{7}Li mit Synchrotronlicht angeregt wurde und mit dem zuvor beschriebenen $LaBr_3$ Szintillationsdetektor vermessen wurde.

Summary

Hadron therapy has been shown to provide an effective tumor treatment modality, especially in the vicinity of critical organs at risk, due to fact of the sharp distal dose falloff delivered by the particle beam to the human body. However, a reliable beam range verification is required, in order to fully benefit from the properties of the well-localized dose deposition of the ions in the tumor volume. A promising novel detection option is the registration of promptly emitted photons from excited nuclei, originating from the interaction of the particle beam with human tissue. The Compton camera concept has recently gained attention in the search for a technique to detect these prompt γ rays, based on measuring the spatial and energetic information of the Compton-scattering kinematics to reconstruct the photon source distribution. For the design specifications of a Compton camera with electron tracking capability, Monte-Carlo simulations and image reconstructions have been performed. The optimized geometry of the camera presented here consists of a $LaBr_3$:(Ce) scintillator (50 x 50 x 30 mm^3), or alternatively of a high-purity planar germanium detector (64 x 64 x 15 mm^3) acting as absorber component, in combination with a stack of 6 double-sided silicon strip detectors (50 x 50 x 0.5 mm^3) acting as scatterer. The choice of the scintillation material $LaBr_3$:(Ce) is based on its favorable energy resolution and fast timing, designed for the installation in the enviroment of laser-accelerated particle beams, where the laser is uniquely providing a sub-ps trigger signal, while for the DSSSD the high scatter probability, high 2D granularity and the option for electron tracking motivated this choice. In the interesting prompt γ energy range of 4-6 MeV, the spatial resolution of the optimized camera geometry is expected to be 1.5° - 2.5° (1.5 - 2 mm at 50 mm source distance), and a reconstruction efficiency of about $1.5 \cdot 10^{-4}$ is estimated. Additionally presented is a nuclear medical imaging technique, employing triple-γ trajectory intersections from $\beta^+\gamma$ coincidences, able to reach sub-millimeter spatial resolution in 3 dimensions with a reduced requirement of reconstructed intersections per voxel, compared to a conventional PET reconstruction analysis. This "γ-PET" technique draws on specific β^+-decaying isotopes, simultaneously emitting an additional photon. In simulations, the achievable spatial resolution has been found to reach ca. 0.4 mm (FWHM) in each direction for the visualization of a ^{22}Na point source. Only 40 intersections are sufficient for a reliable sub-millimeter image reconstruction of a point source embedded in a scattering volume of water with a voxel volume of about 1 mm^3 (high-resolution mode). Moreover, starting with an injected activity of 400 MBq for ^{76}Br, the same number of only about 40 reconstructed intersections are needed in case of a larger voxel volume of 2 x 2 x 3 mm^3 (high-sensitivity mode). Requiring such a low number of reconstructed events significantly reduces the required acquisition time for image reconstruction (in the above case to about 140 s) and thus may open up the perspective for a quasi real-time imaging. Subsequently, the detector components have been characterized in the laboratory, as well as at two synchrotron light sources in term of their timing, spatial- and energy resolution. Additionally, their combination forming a Compton camera has been accomplished. Finally, an experiment is presented, where nuclear resonance fluorescence of the 478 keV nuclear transition of ^{7}Li, for the first time excited via synchrotron radiation, was studied using the above described scintillation detector. A first estimate of the order of magnitude of the cross section of the nuclear transition of ^{7}Li has been derived.

Chapter 1

Introduction and Motivation

Cancer is a leading cause of disease worldwide. An estimated 14.1 million new cancer cases occurred worldwide in 2012 [1]. If recent trends in major cancers are globally projected into the future, the incidence rate of cancer will increase to 23.6 million new cases each year by 2030. Motivated by these alarming numbers of individual as well as socio-economic burden, the potential and prospects of tumor treatment by accelerated particle beams (called hadron therapy) will be presented. This will be followed by an introduction to one of the present key challenges in this field, which is the particle beam range verification. A short overview of current monitoring techniques will be presented at the end of this chapter.

1.1 Hadron therapy

Nowadays, cancer is the second highest cause of death in developed countries. An innovative cancer therapy for the treatment of early and advanced tumors, as an alternative to the widespread clinical use of photon-based radiotherapy, is hadron therapy, which is based on accelerated charged particles [2].
The first suggestion of using hadrons (protons or heavier ions) as an effective tumor treatment method was made 1946 by Robert R. Wilson [3], while 1990 the first hospital-based proton treatment center was founded in Loma Linda, California. Up to now, about 100,000 patients have been treated with protons worldwide, heavier ions (mostly carbon) so far are used more rarely ($\approx$ 10,000). The outstanding clinical interest in hadron therapy (see Fig. 1.1 for the number of worldwide installed proton therapy centers between 1950 and 2015) arises from the characteristic interaction of charged particles in matter [2]. While photons deposit their energy mainly exponentially decreasing as a function of depth in matter, charged particles deliver their energy mainly in the characteristic Bragg peak at the end of the stopping range.
In Fig. 1.2, the relative dose deposition of 21 MeV photons, 148 MeV protons and 270 MeV/u ^{12}C in water is shown, respectively [4]. Photons deposit their energy exponentially decreasing over a wider range, reaching a maximum energy deposit closely after their entrance into matter. In contrast, ions form a sharp dose falloff after a locally well-defined Bragg peak, thus enabling to target even deep-lying tumors in the body of

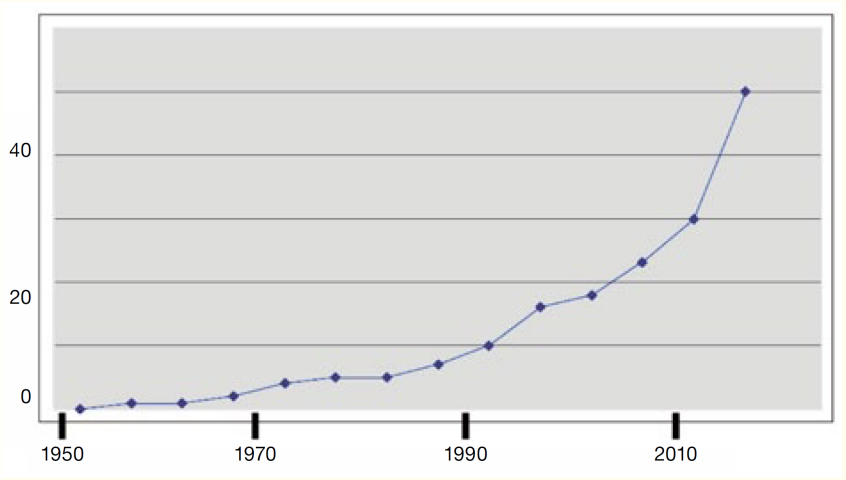

Figure 1.1: Number of worldwide installed proton therapy centers between 1950 and 2015 [2].

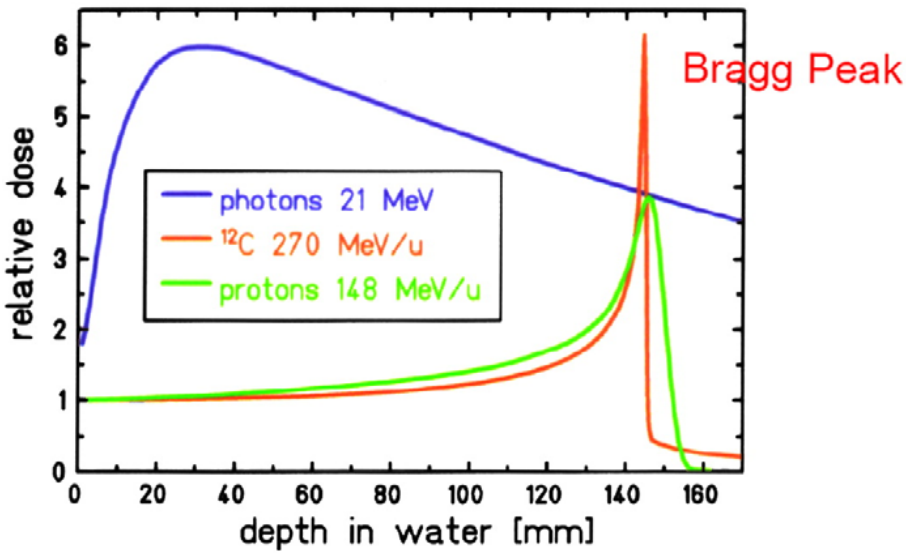

Figure 1.2: Depth-dose distribution for photons and monoenergetic Bragg curves for carbon ions and protons [4].

a patient, with highly-conformal dose application resulting in a reduced damage to the surrounding healthy tissue and organs at risk, leading to a lower integral dose delivered to the whole body and thus to lower morbidity [2]. Additionally, the linear energy transfer (LET) increases at the end of the particle range, resulting in a significantly increased relative biological effectiveness (RBE), caused by a high ionization density, which results in a higher density of double strand breaks of the DNA [4].

However, in order to allow to fully exploit the beneficial properties of this attractive treatment modality, still crucial challenges have to be mastered. Here, uncertainties of the dose delivery to the target volume are the key issues of hadron therapy. These uncertainties are, e.g., induced by variations of the particle beam range, which, under unfavorable conditions, can be large as about 1 - 2 cm [5]. Fig. 1.3 shows the impact of a locally increased density on the dose profile, originating, e.g., from an anatomical variation during the fractionated treatment [6]. For the treatment of tumor volumes, a so-called Spread-out Bragg peak (SOBP) (blue curve) is created by a variation of the beam energy, allowing to cover the full range of the tumor with the prescribed dose. It is obvious that the density-induced beam range variation leads to a significant under-dosage at the distal edge of the SOBP, while an excess of dose is deposited in healthy tissue in front of the tumor.

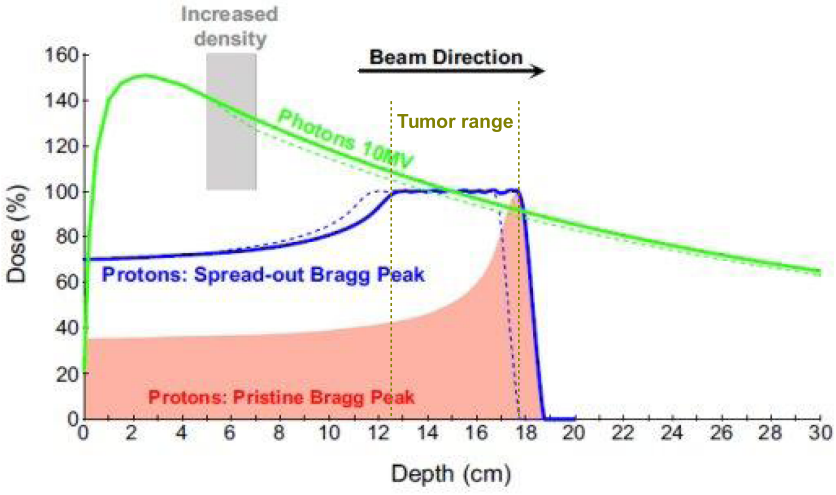

Figure 1.3: Depth-dose distribution for 10 MeV photons (green curve) and proton (blue curve) irradiation. Shown is the impact of an increased density, originating from an anatomical variation (grey area), on the dose profile (dashed line) [6].

Therefore, a particle beam range verification is mandatory to fully benefit from the advantages of the hadron therapy, requiring a precision of 1 -2 mm [5] for irradiating the tumor. Therefore, in the following a short overview of current beam range verification techniques will be given.

1.2 Particle beam range verification

Different in-vivo particle beam range verification methods have been developed so far. Most of these methods take advantage of secondary particles, produced by the particle beam interaction with the patient's body's main constituents: oxygen (> 95 %), hydrogen, carbon and nitrogen. Originating from nuclear reactions induced by the proton irradiation, positron emitters (such as ^{11}C, ^{15}O and ^{13}N) and excited nuclei emerge, which decay promptly via the emission of γ rays, typically in the energy range of below about 8 MeV [7]. This section provides a short overview of current techniques used for particle beam range verification. In particular, positron emission tomography (PET), prompt γ imaging and the "γ-PET" technique will be introduced. A detailed discussion about hadron therapy and ion beam range monitoring will later be given in Sect. 3, while detailed information about photon detection techniques for medical imaging can be found in Sect. 4.

1.2.1 Positron emission tomography (PET)

During the interaction of the hadron beam with the tissue elements, positron emitting isotopes are created by inelastic scattering. Positron emission tomography (PET) can be utilized to detect the annihilation photons, whose activity distribution correlates with the deposited dose.

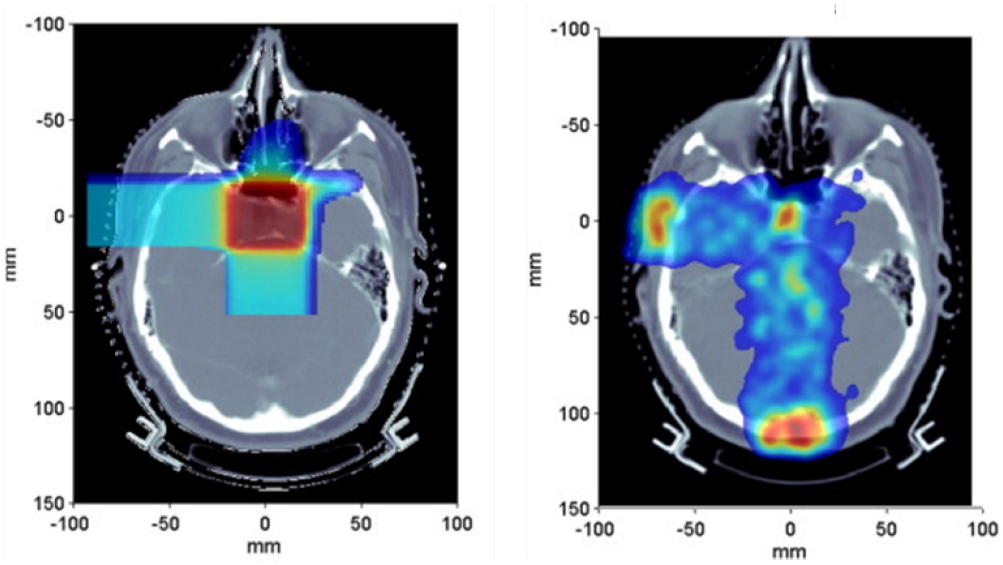

Figure 1.4: Comparison of the planned dose deposition from proton irradiation of a pituitary adenoma patient and the measured PET image after patient irradiation. According to the treatment plan (left panel), the patient received irradiation from the left and from the back side of the patient's head, resulting in two orthogonal proton fields. The measured PET image after the irradiation (right panel) shows a correlation of the delivered dose and the resulting positron activity and could be used as a measure for proton beam range verification [8].

In Fig. 1.4, a comparison of the planned dose deposition from proton irradiation of a pituitary adenoma patient and the PET image that was measured after the treatment is shown. According to the treatment plan (left panel), the patient received irradiation from the left and from the back side of the patient's head, resulting in two orthogonal proton fields. The measured PET image after the irradiation right panel) shows a correlation of the delivered dose and the resulting positron activity and could be used as a measure for proton beam range verification [8].
In Tab. 1.1, an overview of the main reaction channels from proton irradiation of an organic target leading to the production of β^+ emitters is given [9].

Reaction	Threshold energy [MeV]	Half-life [min]	Max. positron energy [MeV]
^{12}C(p,pn)^{11}C	20.61	20.39	0.96
^{16}O(p,pn)^{15}O	16.79	2.04	1.72
^{16}O(p,αpn)^{11}C	27.50	20.39	0.96
^{16}O(p,α)^{13}N	5.66	9.97	1.19
^{14}N(p,pn)^{13}N	11.44	9.97	1.19
^{14}N(p,α)^{11}C	3.44	20.39	0.96
^{12}C(p,p2n)^{10}C	34.5	0.32	1.87
^{16}O(p,3p4n)^{10}C	39.1	0.32	1.87
^{14}N(p,n)^{14}O	6.6	1.18	1.81
^{16}O(p,p2n)^{14}O	30.7	1.18	1.81

Table 1.1: Main reaction channels for β^+ emitter production in a human body, irradiated by a proton beam [9]. The threshold energy is the minimum proton energy needed to start the specific reaction (Q value), the half-life represents the time in which the reaction product decays under emission of a positron and the maximum positron energy is the maximum kinetic energy that the positron acquires from the decay. 95 % of the total production of β^+ emitters in a typical proton irradiation are contributed by the top three reactions. Of special interest are the bottom four reactions, emitting a positron in coincidence with an additional prompt third γ ray, originating from the deexcitation of the β-decay daughter nucleus, which is a feature exploited by the "γ-PET" technique that is described in more detail in Sect. 4.4.

95 % of the total production of β^+ emitters in a typical proton irradiation are contributed by the top three reactions. Of special interest are the bottom four reactions, emitting a positron in coincidence with an additional prompt third γ ray, originating from the deexcitation of the β-decay daughter nucleus, which is a feature exploited by the "γ-PET" technique that is described in more detail in Sect. 4.4.
Two promising methods of range verification via PET are under study, an in-beam (online) [10] and an offline range monitoring applied after patient irradiation, where the patient is transported to a nearby PET scanner [8]. Currently, both methods have their limitations. While the online monitoring suffers from a small field of view and geometrical problems for the beam orientation, the main disadvantage of the offline monitoring

is the transportation time of the patient from the hadron treatment room to the PET/CT scanner. This results in a loss of signal strength due to the decay of the reaction products and additionally due to the biological washout. Also positioning changes might occur during the transportation to the scanner room. So far, in-beam PET diagnostics for the use in medical practice (including carbon beam and proton therapy) are installed or under development worldwide in several facilities [11], e.g., the Gesellschaft für Schwerionenforschung (GSI), Darmstadt, Germany [12, 13] or the Heavy Ion Medical Accelerator (HIMA) in Chiba, Japan [14]. At the moment, a position reconstruction resolution of 4-5 mm can be achieved by clinical PET scanners [17], while the time-of-flight (TOF) PET is measuring the small PET signal more accurately. Achievable with TOF PET, the current clinical state-of-the-art of the localization of the annihilation position along the line of response (LOR) is 7 cm [17, 18]. Under laboratory conditions, a 1.5 mm (clinical practice: 2 mm) TOF PET position resolution has been already achieved [19]. A detailed discussion of the PET technique can be found in Sect. 4.3.

1.2.2 Prompt gamma-ray imaging

Another promising particle range verification technique is the prompt γ imaging method. In addition to the produced β^+ emitters, promptly emitted photons from excited nuclei originate from the proton beam interaction with human tissue. A correlation of the emission peaks with the dose falloff region has been demonstrated [5], a comparison of the spatial correlation is displayed in Fig 1.5.

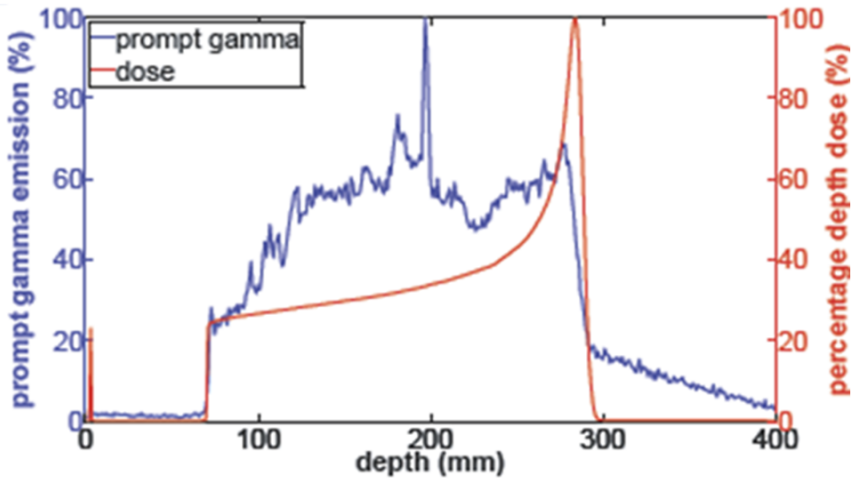

Figure 1.5: Comparison of the planned dose deposition (red Bragg curve) with the prompt γ emission profile (blue). A clear spatial correlation of the distal edge of both curves is visible [20].

Fig. 1.6 shows a Monte-Carlo simulation (utilizing the FLUKA code [21, 22]) of the prompt γ-ray energy spectrum emitted from a H_2O target (diameter 10 cm, length 50 cm), irradiated with 100 MeV protons.

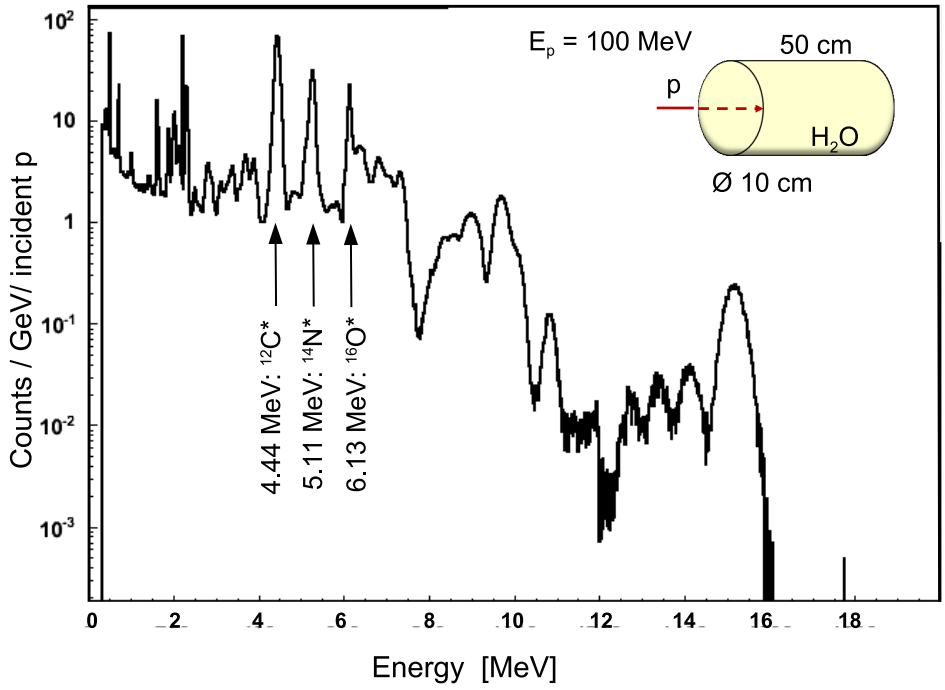

Figure 1.6: Monte-Carlo simulated photon emission energy spectrum (utilizing the FLUKA code [21, 22]) of a H_2O target (diameter 10 cm, length 50 cm), irradiated with 100 MeV protons. Dominant transition lines, suitable for prompt γ detection, are visible at 4.4 MeV from ^{12}C, 5.1 MeV from ^{14}N and 6.1 MeV from ^{16}O deexcitation.

Dominant transition lines, suitable for prompt γ detection, are visible at 4.4 MeV from ^{12}C, 5.1 MeV from ^{14}N and 6.1 MeV from ^{16}O deexcitation. The spectrum ranges up to photon energies of about 15 MeV, corresponding to the M1 transition from the excited 1^+ level in ^{12}C at 15.11 MeV. It should be mentioned that these peaks will be less pronounced in a measurement in the therapeutic practice, due to density inhomogeneities in the human body. Typically about 0.04 prompt γ rays are created per primary proton at this proton energy. An advantage of using prompt γ rays, compared to annihilation photons, is the higher production rate of the prompt photons (theoretically by up to a factor of 60 - 80 [23]). For detecting these prompt γ rays with the ability to reconstruct their spatial origin, the Compton camera technique has recently received increasing attention. A Compton camera typically consists of a scatter detector and an absorbing detector [24]. The first application of this photon source reconstruction technique occurred in the field of γ-ray astronomy [25, 26]. Current results indicate that for range verification in hadron therapy, the Compton camera could also provide a viable alternative method. Simulations and experimental set-ups with complementary Compton camera technologies have been studied by several groups worldwide [27, 28, 29, 30], however, no optimized design has yet been specified. More information on the Compton camera technique will be given in Sect. 4.2.

1.2.3 "γ-PET"

As already mentioned in Sect. 1.2.1, as a result of the hadron beam irradiation of human tissue, special isotopes (like ^{10}C or ^{14}O) are produced, emitting a positron in coincidence with an additional prompt third γ ray, originating from the deexcitation of the excited β-decay daughter nucleus. This feature will be exploited by the γ-PET technique. The γ-PET technique requires an arrangement of several (at least three) Compton cameras to enable a PET-like detection of the two 511 keV annihilation photons (leading to the determination of the line-of-response (LOR)) in coincidence with the (prompt) third photon, emitted from the excited β-decay daughter nucleus. The combination of the reconstruction of the source position of the prompt photon using the Compton-camera technique and the determination of the LOR allows for intersecting the different trajectories within an individual event. This γ-PET (or "triple-γ") technique enables a higher image reconstruction sensitivity than conventional PET diagnostics [31].
Even a hybrid photon detection system for online ion beam range verification could be installed, using again a setup of several (e.g. four) Compton cameras in a cubic arrangement. While the prompt photons could be used to reconstruct the source position during the irradiation, the delayed emission from produced positron emitters could be detected afterwards offline, either in PET- or γ-PET detection mode.
The γ-PET technique and their perspectives are the subject of Sect. 4.4 and Sect 5.3, respectively.

1.3 Particle acceleration

Besides of the purely medical aspects of the hadron therapy, the economic costs have a strong impact on the discussion of the potential future of this therapy modality. For producing ion energies in the range of up to 250 MeV for protons, or even up to 430 MeV/u for carbon ions, which are essential to reach tumors at all depths in the human body [30] (due to the energy dependence of the stopping range), an expensive infrastructure with cyclotron/synchrotron, beam transport systems and gantry is required. The high costs for particle therapy centers are the main reason for their limited availability. Therefore, a promising probably, more economical, way of accelerating ions could emerge from utilizing high-intensity, short-pulse lasers. This novel technique of laser-driven particle acceleration has recently received increasing attention for its potential in future biomedical applications (e.g. [32, 33]). More information can be found in Sect. 3.2.1.

1.4 Thesis context and objective

This thesis is embedded in the context of the ongoing efforts at the Chair for Medical Physics at the Ludwig-Maximilians-Universität München to develop a prototype of a Compton camera. The camera is primarily designed for an application in the online particle range verification of laser-accelerated proton beams, which is one of the objectives pursued by the Center for Advanced Laser Applications (CALA), currently under construction in Garching [34]. A typical scenario here would be a (sub-) ps pulse of protons

with an energy up to 100 MeV, designed for small animal irradiation. In this environment of laser-driven accelerated particles, with the opportunity of using the fast trigger of the laser, a fast timing imaging system like a Compton camera, based on a fast timing $LaBr_3$ scintillator acting as absorber, would be superior for the suppression of background radiation (mainly neutrons). Additionally, a Compton camera with the capability of tracking the Compton electron exhibits a better reconstruction efficiency compared to Compton cameras with conventional γ tracking. Moreover, the Compton camera could as well be applied in hadron therapy with conventional particle acceleration, and additionally in a combined installation to act in the above described γ-PET mode. In this investigation, a prompt γ-ray energy range of about 1 - 10 MeV is targeted, which is the expected energy range of emitted photons from a proton irradiation of a water phantom (see Fig. 1.6).
The objectives of the studies presented in this thesis are Monte-Carlo simulations for the design specifications and performance assessments of a Compton camera prototype, as well as the design specifications and performance estimates of a γ-PET detector setup. Furthermore, the characteristics of the scatter- and the absorber detector components of the Compton camera have been experimentally determined. In particular, the thesis describes the characterization of a monolithic $LaBr_3$ scintillation detector (read out by a 256-fold segmented multi-anode photo-multiplier) that will act as absorbing detector of the Compton camera. Time, energy and spatial resolution, as well as the photo detection efficiency, were determined for the scintillation crystal with an absorptive coating of the crystal side surfaces. Additionally, an alternative absorbing detector of the Compton camera has been explored for optimized detection of low-energy photons. Therefore, a 2D segmented high-purity planar germanium detector has been characterized in terms of its photo detection efficiency, energy and spatial resolution, while the polarization sensitivity of the germanium detector has been measured at the Deutsches Elektronen-Synchrotron (DESY). Finally, an experiment at the European Synchrotron Radiation Facility (ESRF) in Grenoble is presented, where nuclear resonance fluorescence of the 478 keV nuclear transition of ^{7}Li, for the first time excited via synchrotron radiation, was studied using the above described $LaBr_3$ scintillation detector.
The thesis is organized as follows: while the first chapter places this thesis in a wider context by giving a short introduction into hadron beam therapy and stresses the importance of (online) particle beam range verification, Chapter 2 presents the underlying physical principles of the study that are required for a thorough understanding of the experimental work. Subsequently, Chapter 3 contains a more detailed description of ion beam range monitoring, hadron therapy as well as laser-accelerated proton (or ion) beams. Photon detection techniques for medical imaging are the topic of Chapter 4, in particular, scintillation and semiconductor detectors. The Compton camera technique with the capability of γ-ray plus electron tracking, positron emission tomography (PET) and the γ-PET technique will be explained. Chapter 5 presents the results of Monte-Carlo simulations for the design specifications and performance characterization of a Compton camera system, as well as of a γ-PET detector system. Chapter 6 contains a comprehensive description of the experimental characterization studies of the different medical imaging detector components. Preceding the conclusions from the present work and an outlook to foreseeable further development steps outlined in Chapter 8, Chapter 7 contains the results from a nuclear resonance fluorescence experiment performed at the ESRF (Grenoble).

Chapter 2

Introduction to charged particle and photon interactions with matter

In this section, the basic physical processes of charged particle and photon interactions with matter are introduced to the extent relevant for the context of this thesis. It draws a line from photon interaction processes in matter, like the photo-electric effect and the Compton effect, to interaction processes of charged particles (electrons and protons / heavy ions) in matter.

2.1 Interaction Processes of Photons in Matter

The discovery, investigation and explanation of the nature of X rays and γ rays spanned several decades, starting from the seminal discoveries of the X rays by Konrad Wilhelm Röntgen in 1895 [35] and of the radiation from uranium by Henri Becquerel in 1896 [36]. The latter has been later on unveiled as α, β and γ radiation. In 1912, Max von Laue could first proof the photonic nature of X rays by using the crystal lattice as diffractive grid [37]. Moreover, in 1913 Rutherford and Andrade observed reflections of γ rays from radioactive decay processes from crystal surfaces, proving that also γ rays are photons [38]. Photons produced by processes involving the atomic electron shells are characterized as X rays, such as photons from bremsstrahlung or characteristic X rays. The term γ rays is used for nuclear production mechanisms, including electron-positron annihilation. The key difference of photon interaction in matter, compared to the behavior of charged particles passing through matter, is given by the fact that photons, in contrast to charged particles, do not change in energy, but rather their intensity is attenuated. The attenuation of photons in matter exponentially depends on the thickness of the absorber layer, its density and the photon interaction cross section of the absorber material, according to:

$$I = I_0 e^{-\sigma \rho x} \tag{2.1}$$

where I_0 is the initial intensity, σ is the total photon interaction cross section, ρ the density and x the thickness of the absorbing matter [39]. The total cross section is a sum of the relevant photon interaction processes, which are the photoelectric effect characterized by its cross section σ_{photo}, Compton scattering $\sigma_{Compton}$ and pair creation σ_{pair}

$$\sigma = \sigma_{photo} + \sigma_{Compton} + \sigma_{pair} \tag{2.2}$$

The product of σ and ρ is called linear attenuation coefficient μ (= $\sigma\rho$). Its inverse is the mean free path length λ (= μ^{-1}), typically ranging from a few mm to some tens of cm in solids for common photon energies between 1 keV and 100 MeV [39].

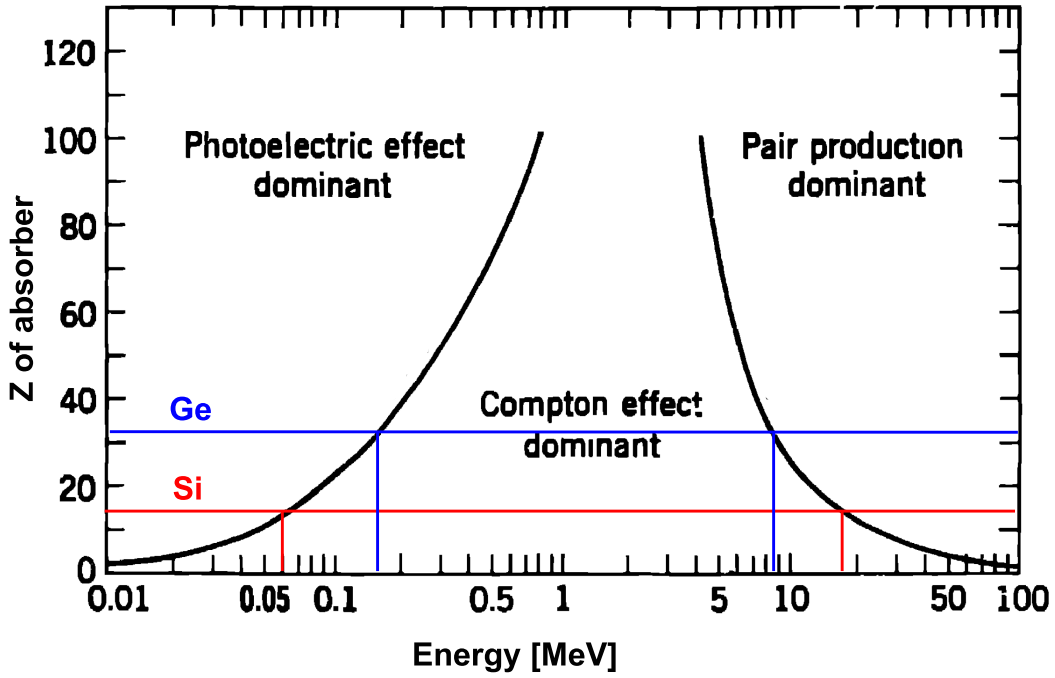

Figure 2.1: Domains of the three major photon-matter interaction processes (photoelectric effect, Compton scattering and pair production) for different incident photon energies and different atomic numbers Z of the absorber material. The black lines indicate equality between adjacent domains [39, 40]. The horizontal lines display the atomic numbers Z = 32 (Ge, blue) and Z = 14 (Si, red), showing the energies of the transitions of the interaction processes. The energy range of the Compton scattering process dominance is larger for Si (60 keV to 15 MeV) compared to Ge (150 keV to 9 MeV).

Figure 2.1 illustrates the domains of the three major processes, photoelectric effect, Compton scattering and pair production as a function of the incident photon energy and the atomic numbers Z of the absorber material. The black lines indicate equality between adjacent domains [39, 40]. The horizontal lines indicate the commonly used photon detector materials germanium (Ge) and silicon (Si). The vertical lines display the energies of the transitions of the interaction processes. The energy range where the Compton scattering process dominates is larger for Si (60 keV to 15 MeV) compared to Ge (150 keV to 9 MeV). The three different interaction processes will be now explained in detail.

2.1.1 Photoelectric Effect

The photoelectric effect, also known as the photo-absorption process, reflects the particle nature of photons. Here, a photon transfers its complete energy to a bound electron, when its energy is higher than the binding energy of the electron. The kinetic energy of this liberated photo electron is then given by the energy of the incoming photon minus the electron binding energy. For free electrons this process is not possible, because of the required momentum conservation. In case of bound electrons, the momentum is taken up by the nucleus. The probability of photo absorption drops exponentially with increasing energy of the photon. There exists no general analytic expression for the photo-electric absorption cross section, rather an approximation is given by Evans [40] as

$$\sigma_{photo} \simeq const \frac{Z^n}{{E_i}^{3.5}} \tag{2.3}$$

with E_i as the incident photon energy, Z as the atomic number of the absorbing matter and n ranging from 4 to 4.6 with increasing photon energy from 0.1 MeV to 3 MeV.

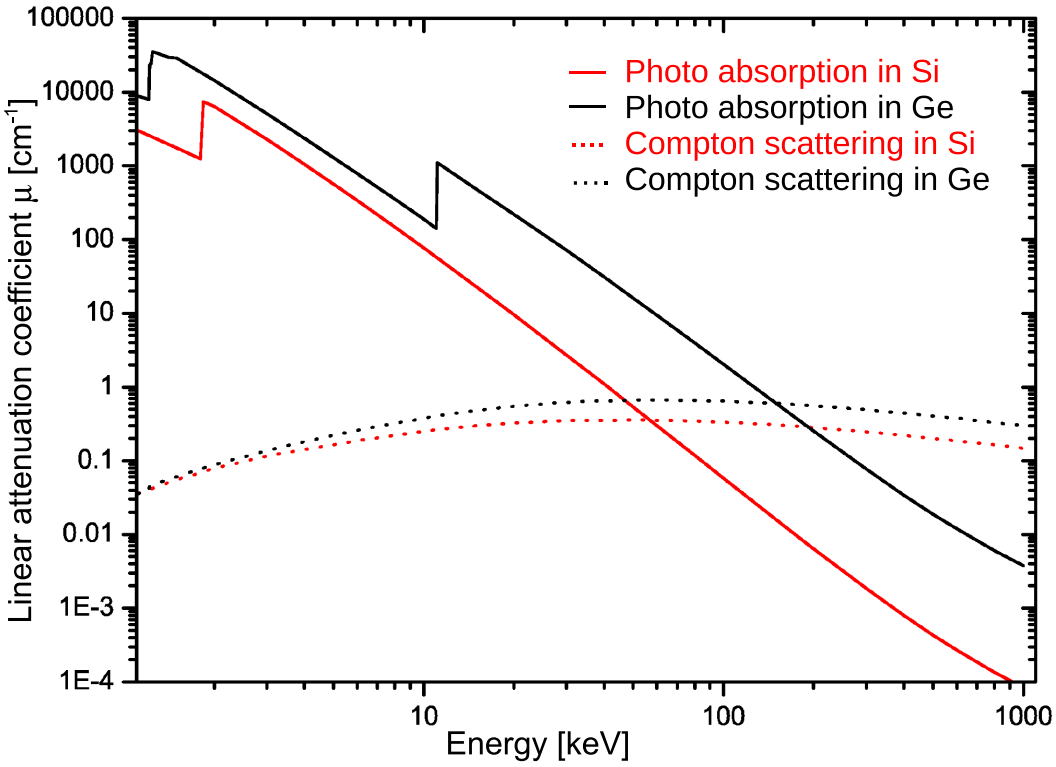

Figure 2.2: Shown is the linear attenuation coefficient μ for photo absorption (solid lines) and Compton scattering (dotted lines) in Si (red) and Ge (black), respectively. Characteristic absorption edges appear due to the strongly increased absorption probability, when the photon energy reaches the binding energy of the K shell, L shell, etc. [41].

Figure 2.2 shows the linear attenuation coefficient of the photo-absorption process (solid lines) in Si (red) and Ge (black). Characteristic absorption edges appear due to the

strongly increased absorption probability, when the photon energy reaches the binding energy of the K shell, L shell, etc.
Also included in Fig. 2.2 are the attenuation coefficients for the Compton scattering process (dotted lines), which dominates over the photo-absorption process for $E_i > 60$ keV and 150 keV for Si and Ge, respectively. As can be seen from Fig. 2.2, the attenuation coefficient for the photo-absorption process, as well as for the Compton scattering process, is larger for Ge compared to Si. However, in case of Si, already beyond ≈ 60 keV (intersection of the red lines), the attenuation coefficient for a Compton scatter event is larger compared to the one for a photo-absorption event. In case of Ge, the crossover occurs at a higher photon energy of ≈ 170 keV. This characteristic difference between the two semiconductor materials germanium and silicon can be illustrated even more pronounced by the ratio of the Compton scattering cross section $\sigma_{Compton}$ to the total photon interaction cross section σ_{total}, which is plotted in Fig. 2.3. The dotted horizontal line indicates equal contribution of cross sections from Compton scattering and photo-absorption [42]. It can be seen that Si is the better scatter material, while Ge is advantageous as absorbing material.

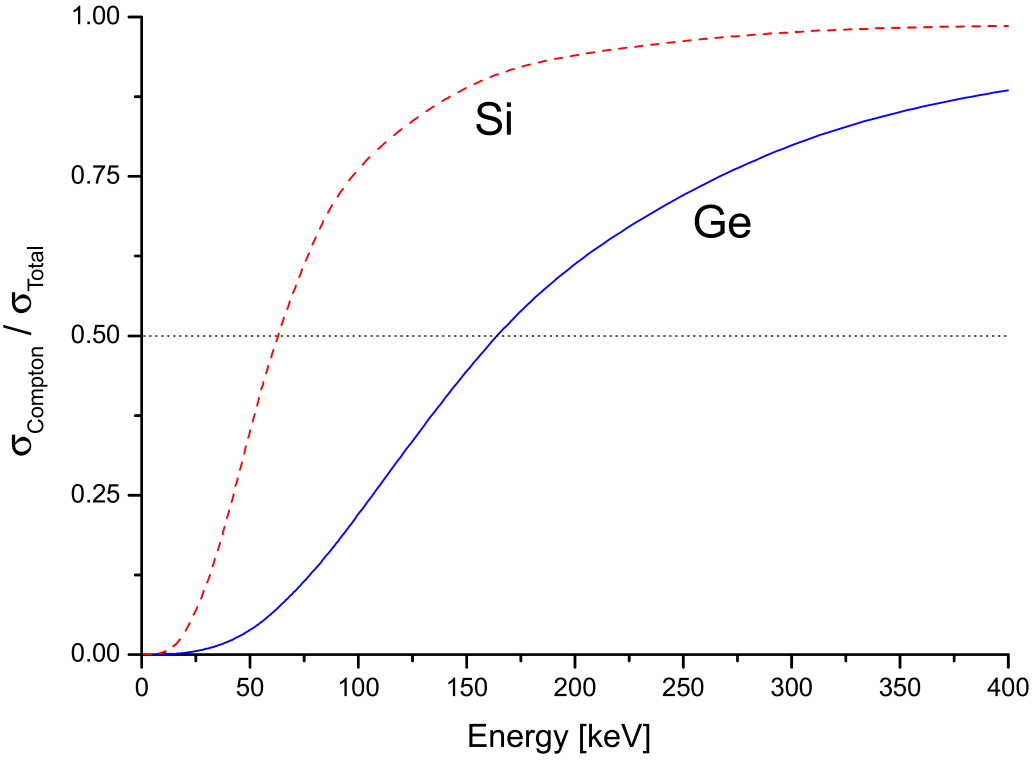

Figure 2.3: Ratio between the Compton scattering cross section and the total photon interaction cross section. The dotted line indicates equal contribution of Compton scattering and photo-absorption. It can be seen that Si is the better scatter material, while Ge is advantageous as absorbing material [42].

2.1.2 Compton Scattering

Like the photoelectric effect, the occurrence of Compton scattering reflects the particle nature of photons. It gets dominant over the photoelectric effect, when the initial photon energy is comparable to the rest mass of the electron of 511 keV/c^2. For materials like silicon (Si) or germanium (Ge) with atomic numbers of Z = 14 and Z = 32, respectively, the dominant energy region of the Compton effect is between 60 keV and 15 MeV for Si, and 150 keV and 9 MeV for Ge (see Fig 2.1). In this energy region, a sizable part of the initial photon energy gets transferred to the electron, while the photon gets scattered by an angle θ. Exemplary, the different cross sections for the main interaction processes (Rayleigh-scattering (coherent), Compton scattering (incoherent), photo-absorption and pair production) of energetic photons in germanium are shown in Fig. 2.4 together with the resulting total interaction cross section (black line).

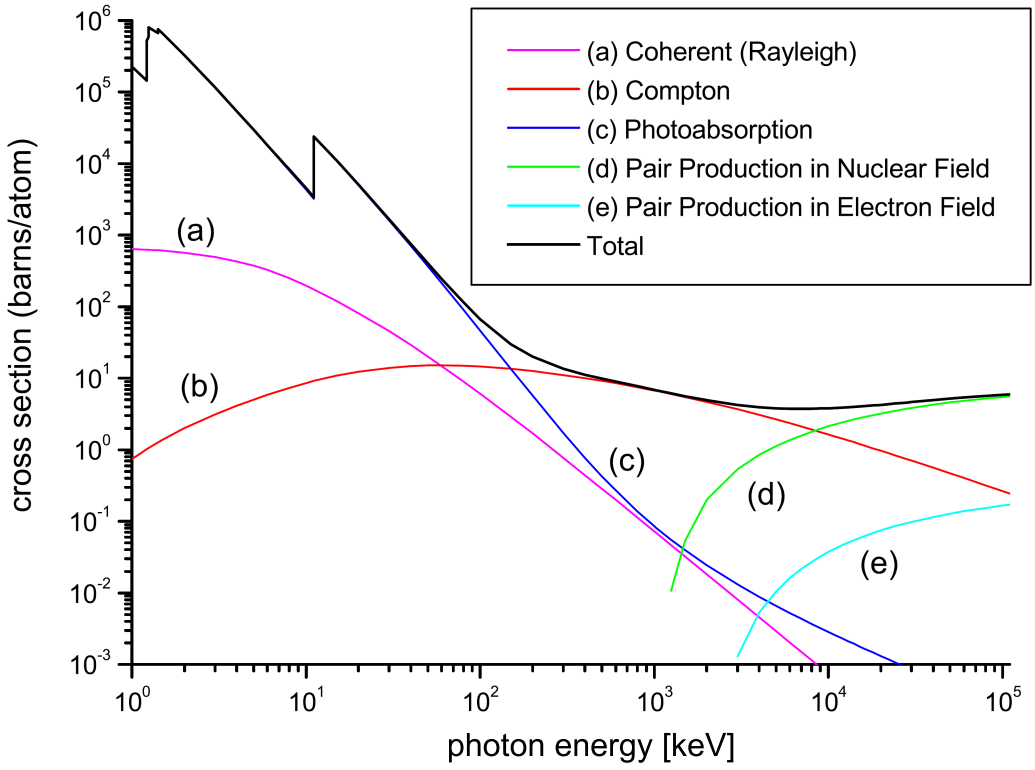

Figure 2.4: Different partial cross sections for Rayleigh-scattering (coherent), Compton scattering (incoherent), photo-absorption and pair production of energetic photons in germanium, together with the resulting total cross section (black line) [42].

In Fig. 2.5 the Compton scattering process kinematics is schematically shown. An initial photon with energy E_i and momentum p_i is hitting an electron at rest (rest mass of an electron m_e = 511 keV/c^2). The photon gets scattered under an angle θ, transferring energy ($E_e = E_i - E_s$) and momentum ($\vec{p_e} = \vec{p_i} - \vec{p_s}$) to the electron. The Compton electron is scattered under an angle ϵ with respect to the incident photon direction. This is

in contrast to Thomson or Rayleigh scattering, where a photon gets coherently scattered off an electron or atom/molecule, respectively, and no energy, wavelength nor phase is changed. Let us have a deeper look into the Compton scattering process, which is in the central interest of this thesis.
In 1923, Arthur Holly Compton discovered that X rays can be scattered from electrons [43, 44]. He found a relation between the scattering angle θ and the initial and scattered photon wavelengths λ_s and λ_i, respectively, according to

$$\lambda_s - \lambda_i = \Delta\lambda = \frac{h}{m_e c}(1 - \cos\theta) \tag{2.4}$$

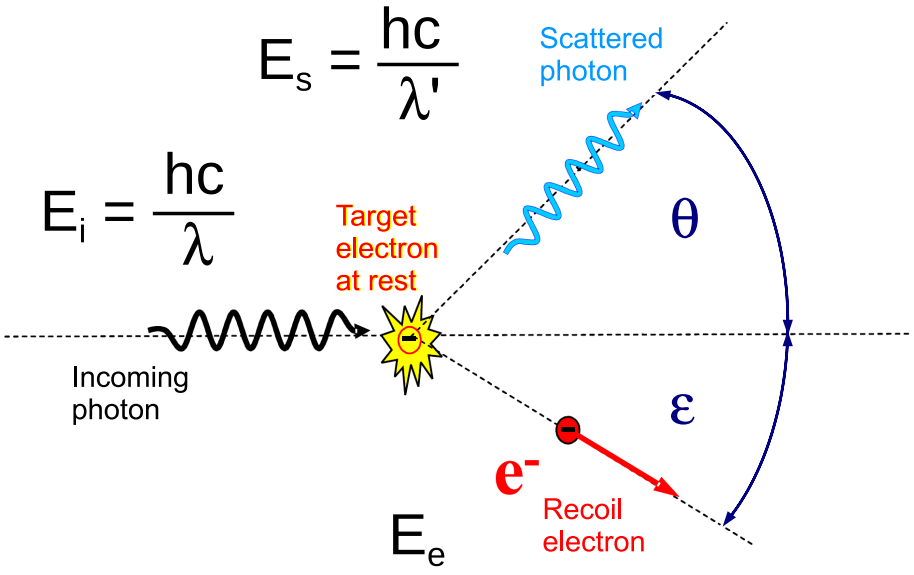

Figure 2.5: Kinematics of the Compton scattering process. An incoming photon with energy E_i and momentum p_i is hitting an electron at rest (rest mass of an electron m_e = 511 keV/c^2). The photon gets scattered under an angle θ with reduced energy E_s, transferring energy and momentum to the electron, which is scattered under an angle ϵ with respect to the direction of the photon incidence [42].

Equation (2.4) is the standard Compton formula, which can easily be derived from energy and momentum conservation. A rearrangement of the Compton formula leads to

$$\cos\theta = 1 - m_e c^2 \frac{E_s}{E_i(E_i - E_s)}. \tag{2.5}$$

with θ as the scattering angle, $E_i = h\nu$ as the initial photon energy and $E_s = h\nu'$ as the red-shifted energy of the scattered photon.

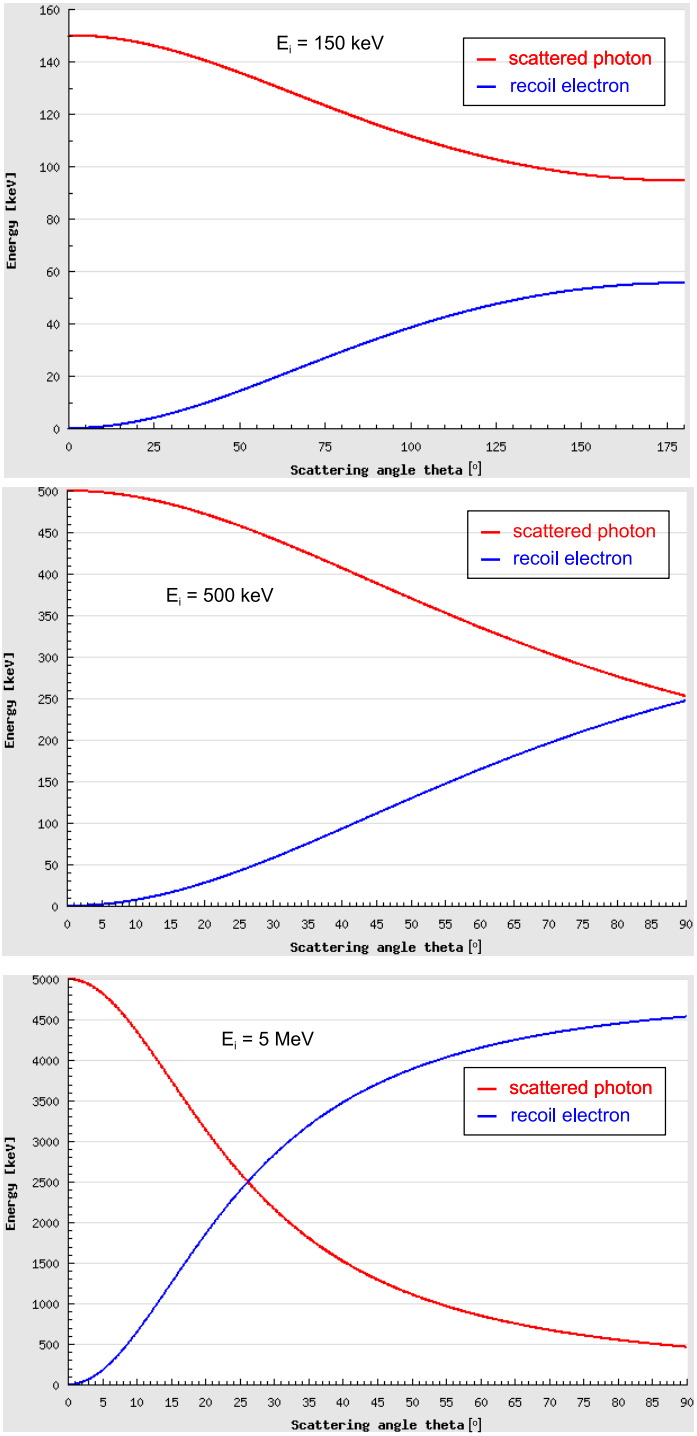

Figure 2.6: Calculated kinematic relations of the Compton scattering process. The panels show the dependence of the energy of the Compton scattered photon (red) and electron (blue) on the scattering angle θ for three incident photon energies of E_i = 150 keV (top), E_i = 500 keV (middle) and E_i = 5 MeV (bottom) [45].

Fig. 2.6 shows the calculated kinematic relations of Compton scattering for three incident photon energies of E_i = 150 keV, 500 keV and 5 MeV, respectively [45]. Plotted is the dependence of the energy of the Compton scattered photon E_s (red), and of the energy of the electron E_e (blue), on the scattering angle θ. It can be seen that the higher the incident photon energies, the lower the angle of the crossover of E_s and E_e. Another characteristic of the Compton scattering process is shown in Fig. 2.7. It shows the energy distribution of the Compton scattered recoil electrons for incident photon energies of 500 keV (black) and 1 MeV (blue), which induces a background to the measured photon spectrum, the so-called Compton continuum. The distributions show a strong increase and a sudden fall-off at 340 keV and 800 keV in the case of 500 keV and 1 MeV incident photon energies, respectively, assuming a 180° Compton scattering angle. This 'back scatter'-geometry allows the incident energetic photon to transfer maximum energy to the recoiled electron.

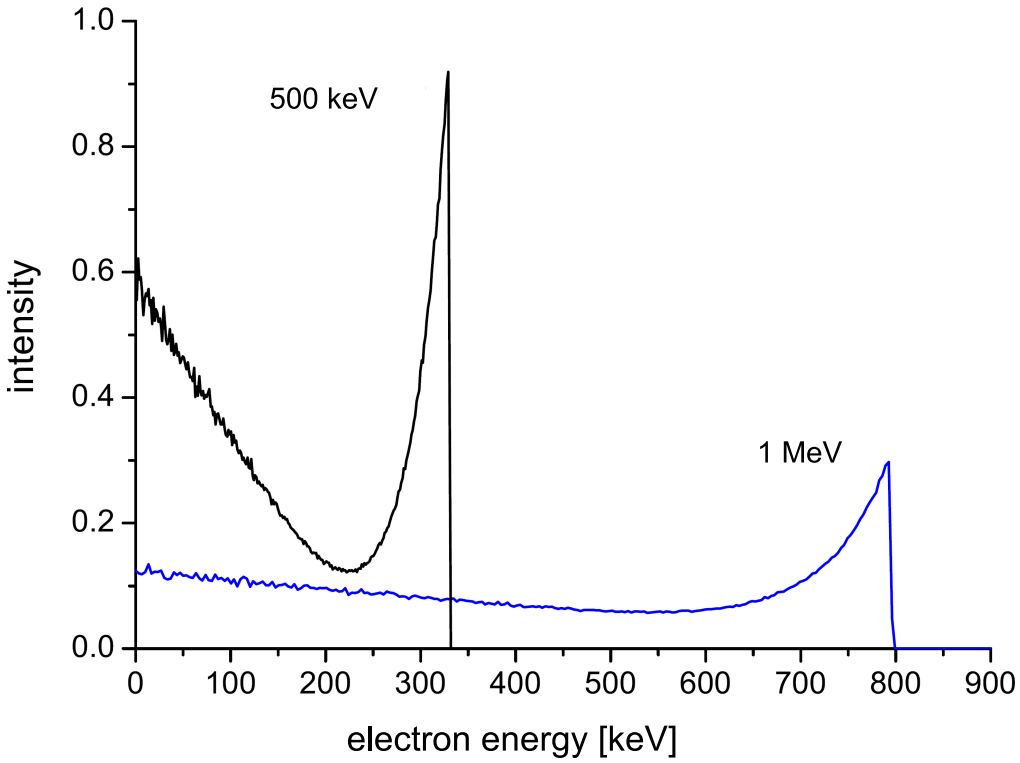

Figure 2.7: Energy distribution of Compton-scattered recoil electrons for incident photon energies of 500 keV (black) and 1 MeV (blue), inducing the so-called Compton continuum in photon measurements [42].

Equation (2.5) assumes the electron to be at rest ($p_e = 0$) before the interaction. However, a bound electron is not completely at rest, resulting in a Doppler broadening of the scattered photon energy, which will turn out to be the lower limit of the angular resolution achievable with a Compton camera [26], the imaging detector system to be introduced in Sect. 4.3 as the main experimental device studied in this thesis.

Compton scattering cross section

The differential cross section $d\sigma/d\Omega$ for Compton scattering of incident unpolarized photons is described by the Klein-Nishina formula (1929) [46]

$$\frac{d\sigma}{d\Omega} = \frac{r_e^2}{2}\left(\frac{E_s}{E_i}\right)^2\left(\frac{E_s}{E_i} + \frac{E_i}{E_s} - \sin^2\theta\right) \tag{2.6}$$

with $r_e = e^2/m_e c^2 = 2.818 \cdot 10^{-13} cm$ as the classical electron radius and θ as the Compton scattering angle (see Eq. (2.4)). Similar to the Compton formula (2.4), this equation is an approximation, as it only accounts for unbound, free electrons.

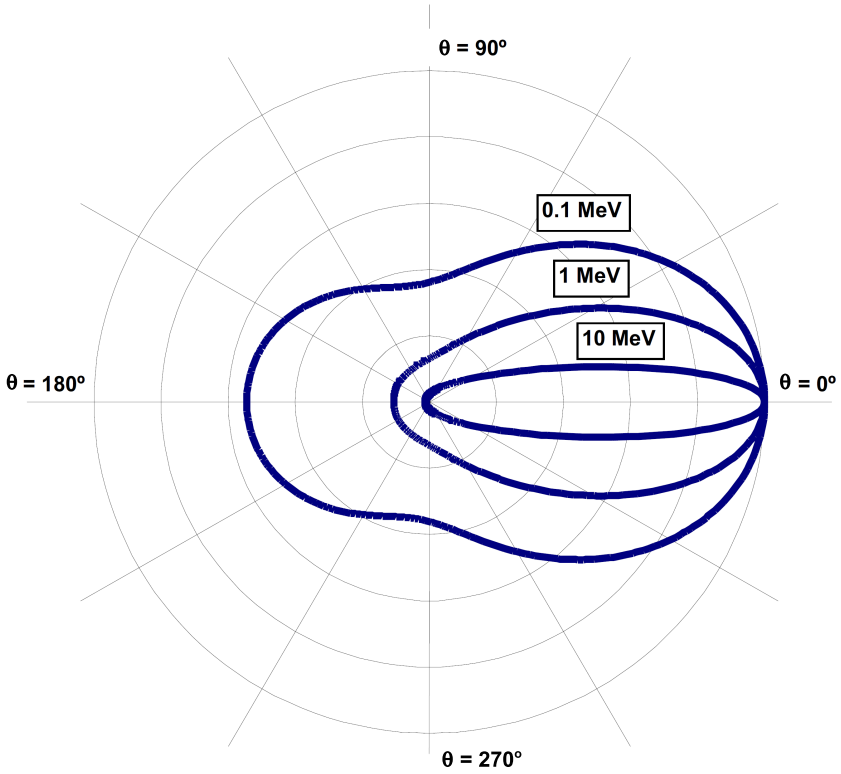

Figure 2.8: Compton scattering cross section as a function of the Compton scattering (polar) angle θ. Curves for three different incoming photon energies are drawn. The average Compton scattering angle θ is smaller for higher incident photon energies, resulting in a stronger forward scattering [26].

In Fig 2.8, the Compton scattering cross section is displayed as a function of the Compton scattering angle θ. Curves for three different incoming photon energies are drawn. The average Compton scattering angle θ is smaller for higher incident photon energies, resulting in a stronger forward scattering [26].

Photon polarization in Compton scattering

In case the incoming photon is linearly polarized, the Compton scattering process can also be used to determine the polarization direction of the incident photon, because the azimuthal scattering angle φ depends on the polarization vector $\vec{E}_i$. For polarized incoming photons, the Klein-Nishina formula for the differential scattering cross section $d\sigma/d\Omega$ expands to [46]

$$\frac{d\sigma}{d\Omega} = \frac{r_e^2}{2}\left(\frac{E_s}{E_i}\right)^2\left(\frac{E_s}{E_i} + \frac{E_i}{E_s} - 2\sin^2\theta\cos^2\varphi\right) \tag{2.7}$$

with φ as the azimuthal angle between the Compton scattering plane and the polarization vector $\vec{E}_i$. Figure 2.9 shows the geometry of the Compton scattering process for linearly polarized incoming photons. The azimuthal angle φ relates the polarization vector $\vec{E}_i$ of the incoming photon and the propagation direction of the scattered photon.

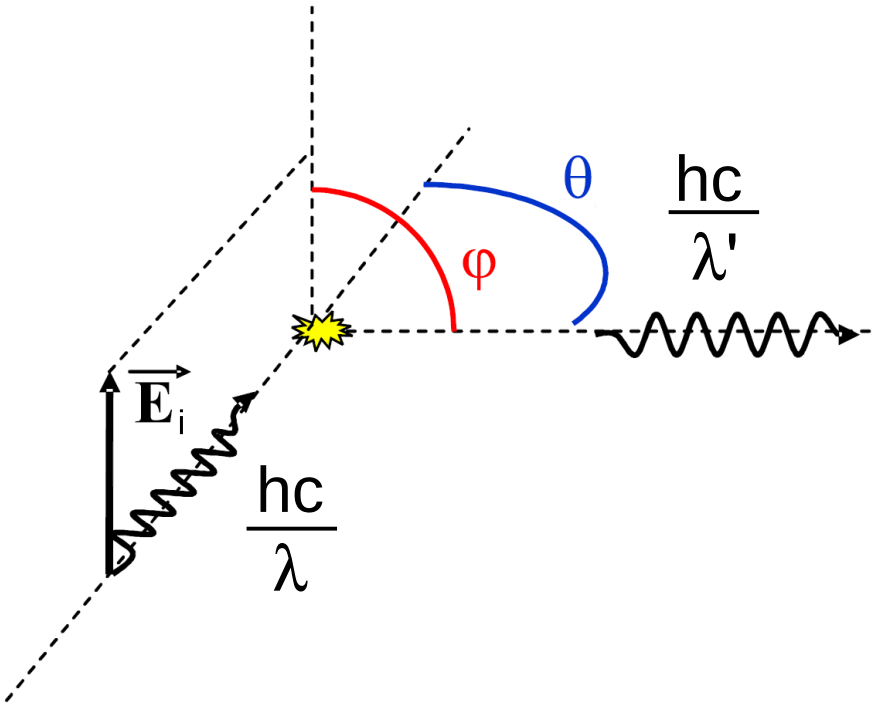

Figure 2.9: Geometry of the Compton-scattering process, showing the azimuthal angle φ between the polarization vector $\vec{E}_i$ of the incoming photon and the propagation direction of the scattered photon [42].

The probability distribution P(φ) of the azimuthal Compton scattering angle φ can be derived from Eq. (2.7)

$$P(\varphi) = P_0 + A\cos(2(\varphi - \varphi_0 + \pi/2)) \tag{2.8}$$

where A is the amplitude, P_0 is an offset and φ_0 is the direction of the original polarization vector. A plot of the differential cross section for the φ distribution for polarized incoming photons is shown in Fig. 2.10.

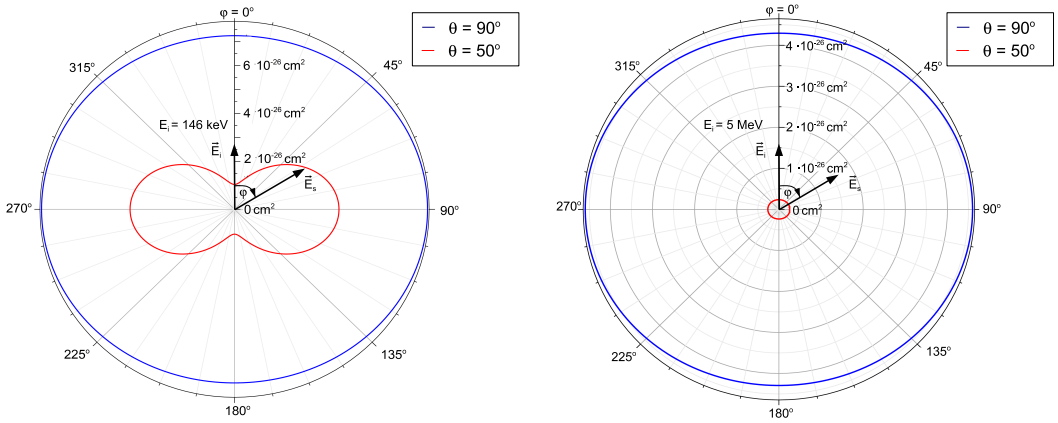

Figure 2.10: Calculated differential Compton-scattering cross section as a function of the azimuthal scattering angle φ for a vertically aligned photon polarization with energy $\vec{E_i}$ = 146 keV (left panel) and 5 MeV (right panel), for θ = 90° (red) and 50° (blue).

Paying attention to the $2\sin^2\theta\cos^2\varphi$ term in Eq. (2.7), some conclusions can be drawn. The scattered photons tend to scatter at right angles to the polarization vector $\vec{E_i}$. At higher incoming photon energies E_i, the Compton scattering angle θ decreases and therefore the $2\sin^2\theta\cos^2\varphi$ term also reduces, resulting in a reduced modulation of the differential cross section. The same occurs, if the Compton scattering angle θ is either small or large. The amount of the azimuthal modulation is described by the modulation fraction [26]

$$\begin{aligned} M(\varphi, \theta = \text{const}) &= \frac{P(max) - P(min)}{P(max) + P(min)} = \frac{A}{P_0} \\ &= \frac{N(\varphi + 90°) - N(\varphi)}{N(\varphi + 90°) + N(\varphi)} = \frac{\sigma_\perp - \sigma_\parallel}{\sigma_\perp + \sigma_\parallel} \end{aligned} \tag{2.9}$$

If φ is parallel to the polarization vector of the incident photon, then M(φ) reaches its maximum. In contrast, M(φ) reaches its minimum, when ϕ is perpendicular to the polarization vector of the incident photon. In Fig. 2.11 is shown, that, in addition, the maximum of the modulation fraction is shifting with increasing incoming photon energies to lower scattering angles θ.

For a better understanding of the detector response on linear polarized photons, the Compton cross section has to be considered. Fig. 2.12 shows the differential Compton cross section (blue lines) together with its product with the modulation factor (red lines). Compared to Fig. 2.11, the maximum intensity is now shifted to lower Compton angles θ, for the same incoming photon energy. For, e.g., an incoming photon energy of 100 keV, the maximum intensity is found of θ = 80°.

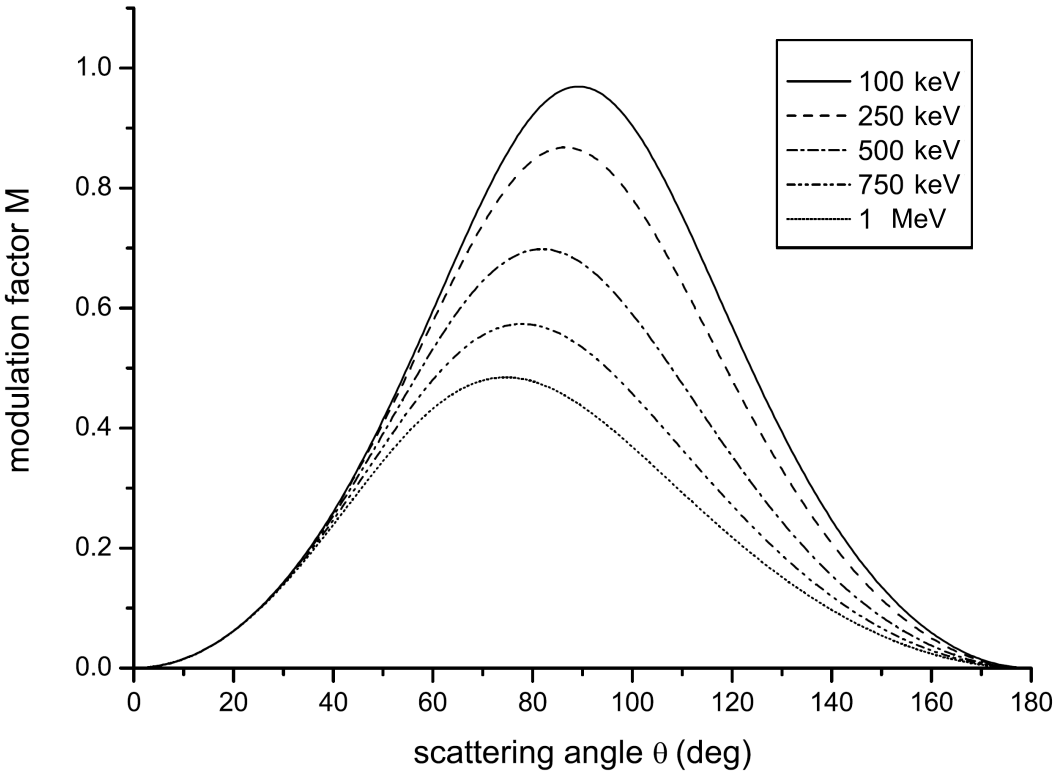

Figure 2.11: Dependency of the modulation factor $M(\varphi)$ (according to Eq.(2.9)) on the incoming photon energy and Compton scattering angle θ [42].

2.1.3 Pair production

In case the photon energy is higher than 1022 keV (i.e. two times the rest energy of the electron), it is possible that the photon gets converted into an electron-positron pair in the electromagnetic field of a nucleus. Energies exceeding 1022 keV will be converted into kinetic energies of the created electron-positron pair and into the recoil energy of the nucleus. The generated positron will annihilate, after slowing down, with another electron into two 511 keV photons. This signature is important for understanding the response of radiation detectors [39]. The cross section of pair production reaches considerable values of more than 10% of the total cross section above 2.5 MeV for Ge (Z = 32) and 4 MeV for Si (Z = 14), and will become the dominant process for higher photon energies beyond 8.5 MeV and 15 MeV for Ge and Si, respectively [47] (compare also Fig. 2.1). There is no simple expression for the pair production cross section, but its magnitude is approximately scaling with Z^2, leading to materials with high atomic numbers being good converters, also rising steeply with the energy (see Fig. 2.2) [39]. The kinematics of the pair production process is described by energy and momentum conservation, allowing to determine the origin of the incoming photon. Pair-tracking cameras exist, but for the purpose of medical imaging, as considered here, they are not suitable, due to the high photon energies needed (above $\sim$ 10 MeV), and also in view of the relatively large

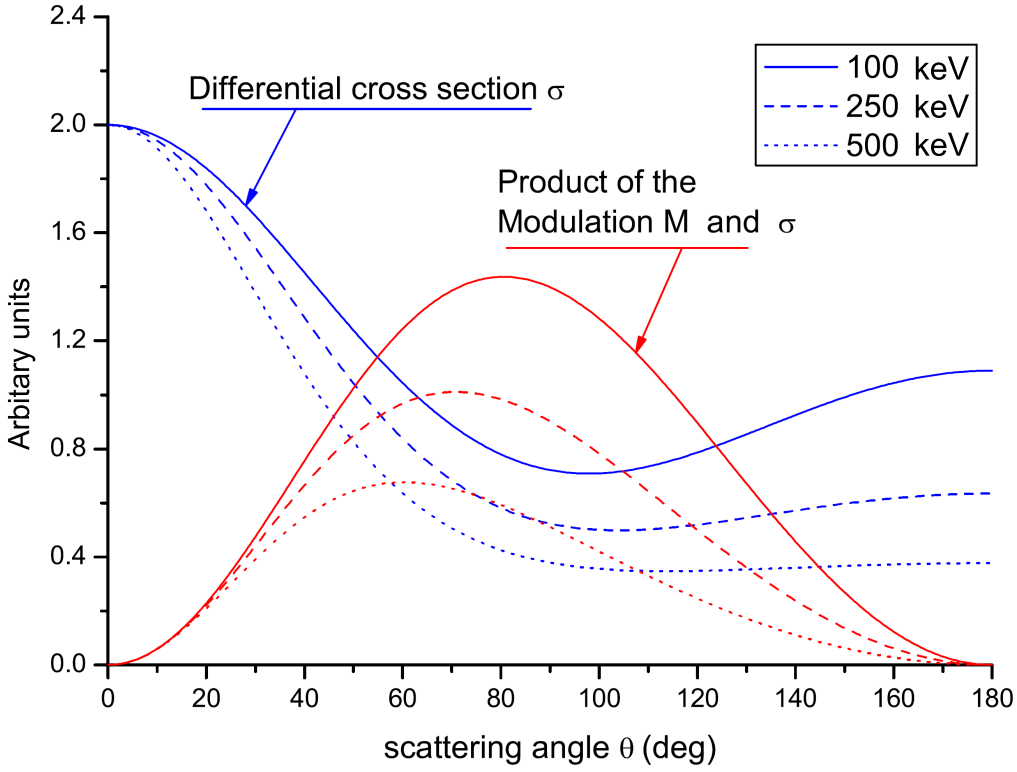

Figure 2.12: Dependency of the differential Compton cross section and its product with the modulation factor $M(\varphi)$ (according to Eq. (2.9) and (2.7)) on the incoming photon energy and Compton scattering angle θ [42].

angular resolution limit estimate of $\sim 9.5°$ at 10 MeV (in case of a 500 μm thick silicon tracker) [26].

2.2 Interaction processes of charged particles in matter

The most significant difference of charged particle interactions in matter compared to photons passing through matter is that their intensity during the transit will not be attenuated like for photons but that they rather will be slowed down by energy loss until finally being stopped in the Bragg peak. Charged particles lose energy in matter mainly due to Coulomb interactions (electronic stopping), with characteristic differences of the energy loss for light charged particles like electrons and heavy charged particles like ions. Starting with a basic explanation of interactions of electrons in matter, this section is then followed by an introduction of heavy ion interactions in matter.

2.2.1 Interaction of electrons in matter

When electrons pass through matter, they lose energy mostly via collisions with the atoms' Coulomb potential, which leads to excitation or even ionization. They also may lose energy by radiation due to deceleration in the electric field of the nuclei, producing bremsstrahlung. At electron energies of interest in this thesis ($E < 5\mathrm{MeV}$), the contribution of bremsstrahlung is negligible, because of the ratio of the specific energy loss being $\approx EZ/700$, where the electron energy E is given in units of MeV, and Z is the atomic number of the absorber material.
Bethe derived an equation similar to his famous energy loss formula for (heavy) charged particles in matter (Eq. (2.11)) for describing the energy loss of electrons in matter as [39]

$$-\frac{dE}{dx} = \frac{2\pi e^4 nZ}{m_e v^2}\left[ln\frac{m_e v^2 E}{2I^2(1-\beta^2)} - (ln2)(2\sqrt{1-\beta^2}-1+\beta^2) + (1-\beta^2) + \frac{1}{8}(1-\sqrt{1-\beta^2})^2\right] \quad (2.10)$$

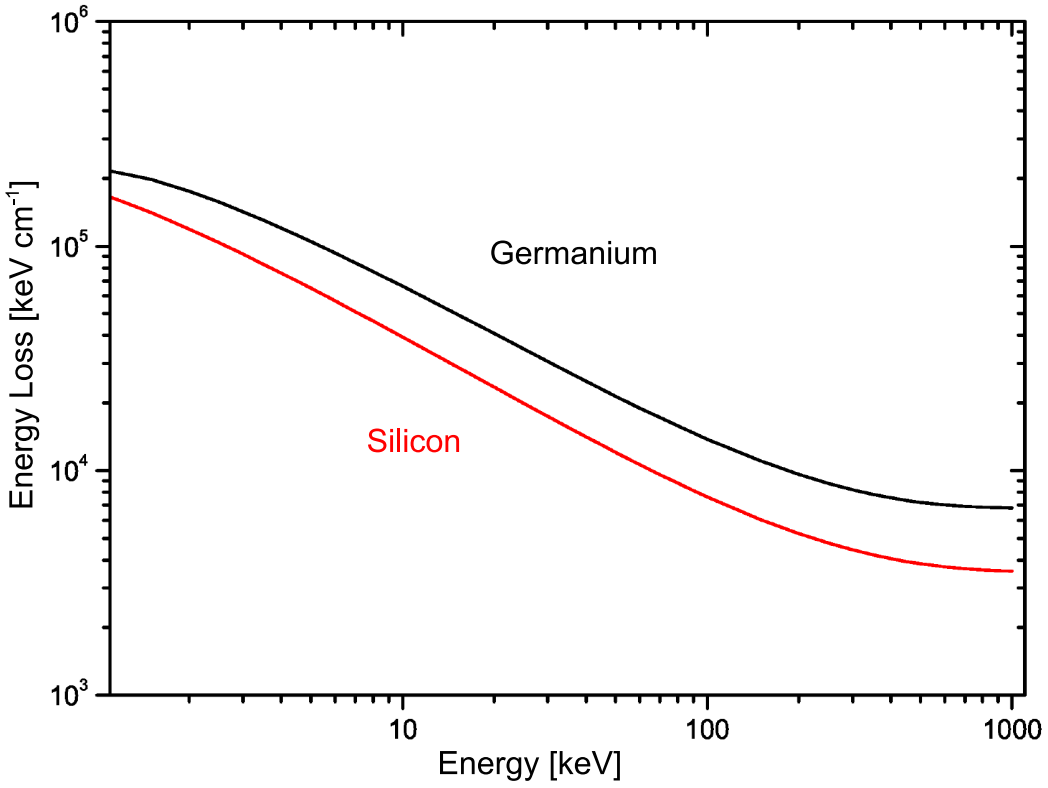

Figure 2.13: The energy loss of electrons in germanium and silicon is plotted as a function of the electron energy. Compared to germanium, the energy loss in silicon is about a factor two lower [41].

where v and e is the velocity and the charge of the electron, n and Z the number density and the atomic number of the absorber material, m_e the rest mass of the electron and $\beta =$

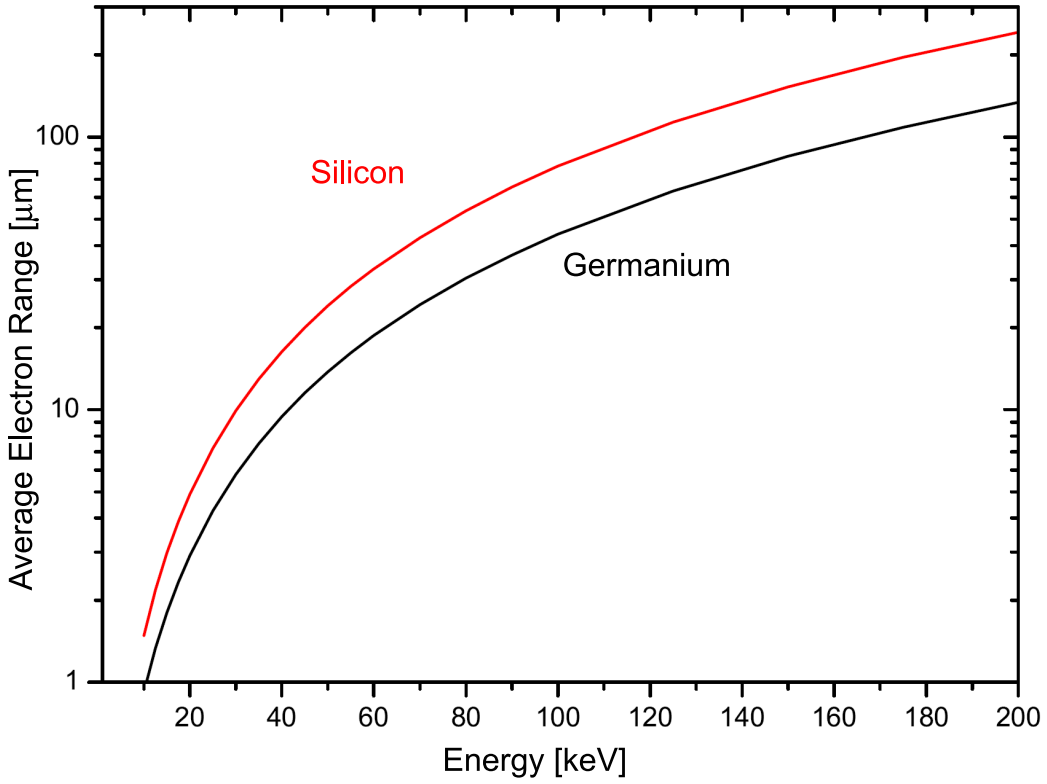

Figure 2.14: The average electron stopping range in germanium and silicon is plotted as a function of the electron energy. Silicon exhibits twice as large an electron stopping range compared to germanium [41].

v/c. The parameter I is experimentally determined and represents the average ionization potential of the absorber material. As an example for Eq. (2.10), Fig. 2.13 shows the specific energy loss of electrons in germanium (black curve) and silicon (red curve). In case of a 0.5 mm thick Si detector, a 200 keV electron would deposit an energy of only about 250 keV, while for a 1 MeV electron this value would be further reduced to about 170 keV. Such a small energy deposit requires highly resistive semiconductor detector materials with a low level of electronic noise to be able to register the passing electron. Alternatively, in Ge a twice as high energy of around 500 and 350 keV, respectively, could be deposited. However, in Ge the average electron stopping range for a 200 keV electron is ≈ 110 μm, which is half of the ≈ 210 μm in case of Si (see Fig. 2.14). This will prove to be particularly important when considering the choice of materials for a Compton camera detector system with the additional ability of electron tracking, where Compton-scattered electrons have to pass through at least one layer of the scatter detector component. The functionality of an electron-tracking Compton camera will be explained in Sect. 4.2.2.

Compared to heavy charged particles, electrons lose their energy more slowly and on a more tortuous path, because the mass of the passing electron is equal to the mass of the orbital electrons of the absorber matter. The interaction with the Coulomb potential leads

to many small-angle scatterings while passing through matter, this so-called Molière scattering is limiting the precision achievable for electron-tracking with a Compton camera (see Sect. 4.2.2 for details).

2.2.2 Interaction of ions in matter

The behavior of energetic ions traversing matter is the crucial feature that is exploited in medical hadron therapy. Ions will deposit their energy within the absorbing matter predominantly in a well localized volume, thus differing from photons, which show an exponentially decreasing energy profile as a function of the interaction depth.
In Fig. 2.15, the energy deposition of 15 MeV photons (red curve) and 140 MeV protons (blue curve) in polymethyl metacrylate (PMMA) is displayed. The red curve exhibits a broad maximum soon behind the photon entrance into the absorber, caused by the energy deposition of secondary electrons produced by the incoming photons and followed by an exponential decrease. The blue curve, also known as the Bragg curve, shows a slightly increasing energy deposition (roughly scaling with $1/E$), followed by a sharp peak, the so-called Bragg peak.
The behavior of the energy deposition of positively charged ions in matter can be explained by the fact that fast, energetic ions experience a short interaction time with the Coulomb forces of the atomic shell electrons in the absorbing matter, so little energy is transferred at high velocities. By increasing depth the particles are slowed down, the interaction time increases and increasingly more energy is transferred, finally ending in the Bragg peak. This behavior of the specific energy loss $-\frac{dE}{dx}$ is described by the Bethe-Bloch equation

$$-\frac{dE}{dx} = \frac{4\pi e z^2}{m_e v^2} nZ \left[ln\frac{2m_e v^2}{I} - ln(1-\beta^2) - \beta^2 \right] \tag{2.11}$$

where v and ze is the velocity and the charge of the incoming particle, n and Z the number density and the atomic number of the absorber material, m_e the rest mass of the electron, the parameter I is the average ionization potential of the absorber material and $\beta = v/c$. It should be mentioned that additional correction factors for the low energy part of the Bethe-Bloch equation are existing (shell correction: taking into account the momentum of shell electrons in the absorbing material; Barkas-Andersen correction: taking into account higher-order effects of Z). Those corrections are large at low energies and decrease with increasing electron energy. The above shown version of the Bethe-Bloch equations follows the description given in the book of Knoll [39].
Fig. 2.16 shows exemplarily a plot of the specific energy loss $-\frac{dE}{dx}$ (stopping power) for protons in silicon (Si). Data are from the PSTAR program (including the above mentioned correction factors), it calculates stopping power and range tables for protons up to 10^4 MeV [49]. The Bethe-Bloch formula reaches a minimum for particle energies of $\beta\gamma \approx$ 3-4 ($\gamma = 1/\sqrt{1-\beta^2}$). The energy loss in the minimum can be empirically parametrized for singly charged particles as

$$-\frac{dE}{dx} \approx 2\frac{\mathrm{MeV}}{\mathrm{g\ cm^{-2}}}\rho \tag{2.12}$$

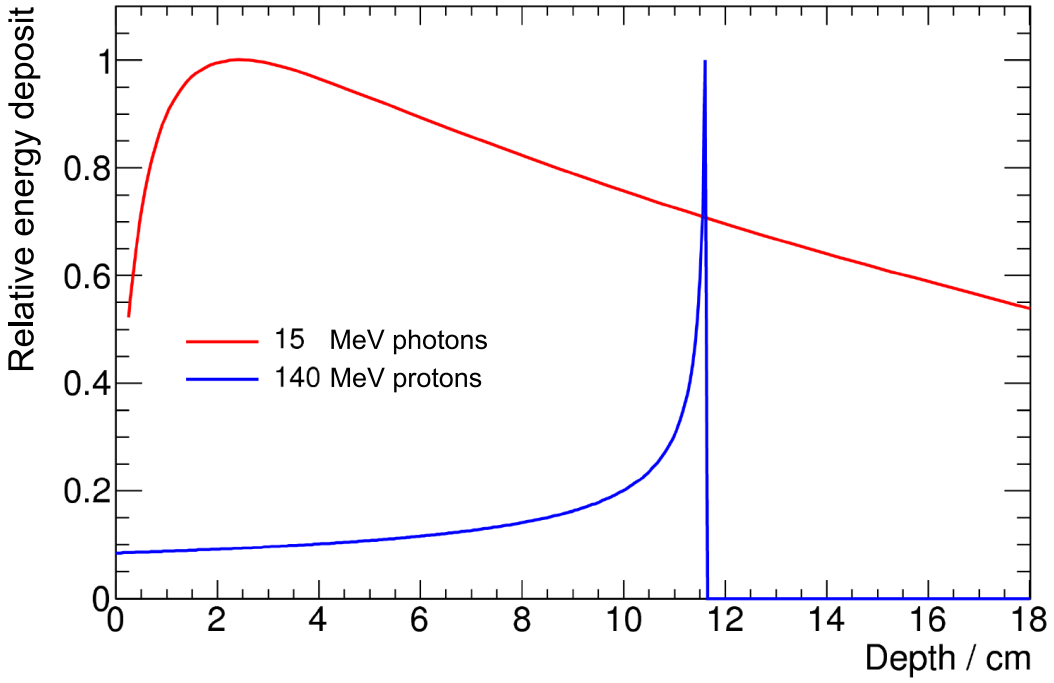

Figure 2.15: Energy deposition in polymethyl metacrylate (PMMA) of 15 MeV photons (red) and 140 MeV protons (blue) [48]. The energy deposition of photons peaks at a certain distance inside the absorber, due to the creation of secondary electrons, followed by an exponential decrease. The energy deposition of protons shows a slightly increasing behavior (roughly scaling with 1/E), followed by a sharp peak, the so-called Bragg peak.

and particles with energies within this minimum of the specific energy loss are called minimum ionizing particles (MIPs). At higher energies, the stopping power shows a logarithmic increase. For non-relativistic particles ($\beta \ll 1$), the terms $ln(1-\beta^2)$ and β^2 vanish. At these lower energies, the $1/v^2$ term mostly describes the interaction and explains why the particle slows down faster by losing energy, until the energy deposition reaches a sharp maximum at the and of the stopping range. The z^2 dependence indicates that ions with higher charge states will lose more energy and the term nZ represents the electron density in the absorber, advocating that for efficiently stopping incident ions the absorber material should have a high density and a high atomic number [39].

An important feature of ion interaction in matter is given by the fact that their specific energy loss occurs along a straight path, because the ions are not strongly deflected by the isotropic interactions with the much lighter shell electrons. However, elastic and inelastic nuclear processes are induced along the path, the latter resulting in a production of nuclear fragments and secondary particles like protons, neutrons, electrons, positrons and prompt γ rays. At proton energies from 60 - 250 MeV (i.e. at reasonable energies for

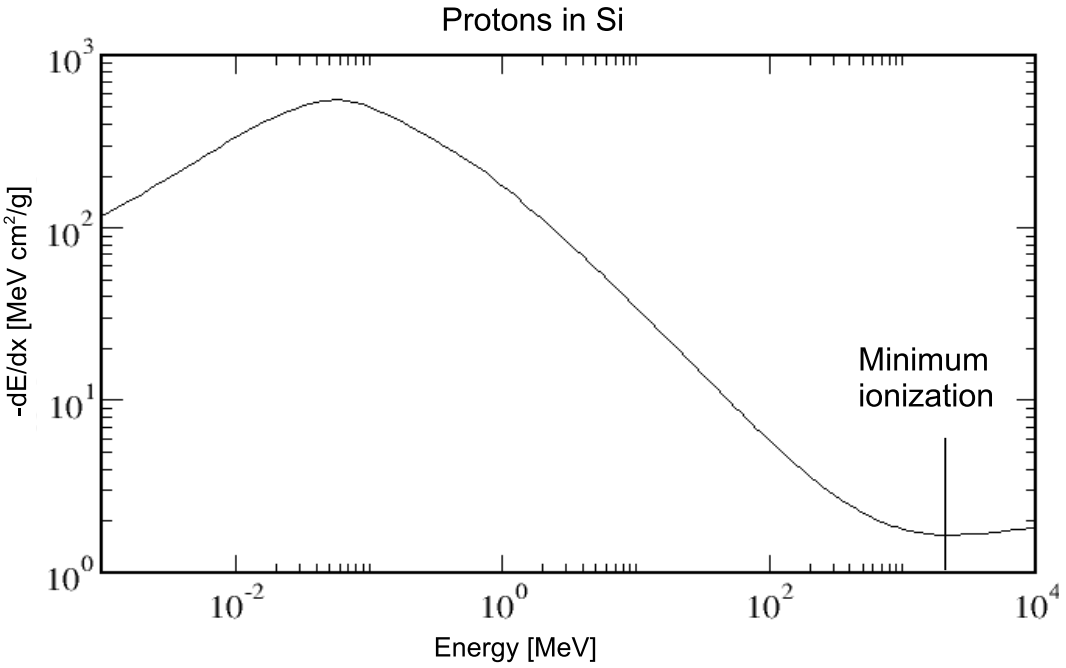

Figure 2.16: Specific energy loss $-\frac{dE}{dx}$ (stopping power) for protons in silicon (Si). Data are from the PSTAR program, it calculates stopping power and range tables for protons up to 10^4 MeV [49].

proton tumor treatment), fragmentation is the dominant interaction process. By collisions with the atomic nucleus within the absorbing matter, excited fragments are produced in $\approx 10^{-22}$ s, followed by nuclear evaporation and prompt γ-ray emission in $\approx 10^{-21}$ s - 10^{-16} s. Amongst the nuclear reaction products there may also be β-unstable species, resulting in the emission of an electron or positron (together with accompanying electron (anti-)neutrinos). In the case of β^+ decay, the positron will, after thermalization, annihilate into two almost diametrally emitted 511 keV photons. The produced nuclear fragments, together with the secondary particles, contribute to the energy deposition in the absorber material, the secondary particles usually stop close to the interaction point. Worthwhile to note is that the production of nuclear fragments leads to a small lateral spread of the energy deposition close to the Bragg peak [28]. Additionally, an ion beam undergoes angular and energy straggling inside matter, due to the statistical nature of energy loss. Therefore, a spread of the ion energy will occur while passing the absorbing matter, which will also result in a broadened Bragg peak.

Chapter 3

Hadron therapy and ion beam range monitoring

Hadron therapy is an efficient method for tumor treatment using heavy, high energetic particles like protons or carbon ions [74, 75]. Due to the well-localized energy deposition of those particles in matter according to the Bragg peak in Fig. 2.15, it is possible to kill target tumor cells inside a patient, while minimally harming the surrounding healthy tissue (in contrast to the X-ray treatment, which shows an exponentially decreasing depth-dose relation). Due to their light mass and shorter range, electrons are more suited for a close-to-surface treatment. As mentioned in Sect. 2.2.2, the depth of the Bragg peak depends on the initial energy of the projectiles and on the density of the target volume. Tuning the incident energy is the usual way for controlling the Bragg-peak depth and for the delivery of the energy to the specified target volume. Because of the heavy mass of the incident particles, only little lateral side scattering in the tissue occurs, thus no significant broadening of the hadron beam will occur. The interaction of energetic ionizing particles with organic tissue leads to double strand breaks of the desoxyribonucleic acid (DNA), a molecule with instructions for the development and functioning of cells. After the treatment, cells having absorbed a sufficiently high dose (i.e. deposited energy in a unit mass of the material), will decease. A precisely localized dose delivery to the tumor, not to the surrounding tissue, is demanded, because the target volume is often close to sensitive organs-at-risk (e.g spinal cord, healthy brain cells). Therefore a precise planning and monitoring of the dose delivery is mandatory.

3.1 Ion beam range monitoring

A hadron treatment is typically planned using X-ray Computed Tomography (CT) data to determine the density, position and structure of the target tumor and the surrounding tissue via the attenuation of the transmitted X-rays, sometimes assisted with data from Magnetic Resonance Imaging (MRI). For example, the treatment planning at the Gesellschaft für Schwerionenforschung in Darmstadt (GSI) for ^{12}C therapy is explained in [50]. Uncertainties like particle number, energy and spatial fluctuations of the hadron beam or moving of the patient (e.g. breathing) cannot be included in the treatment plan. These

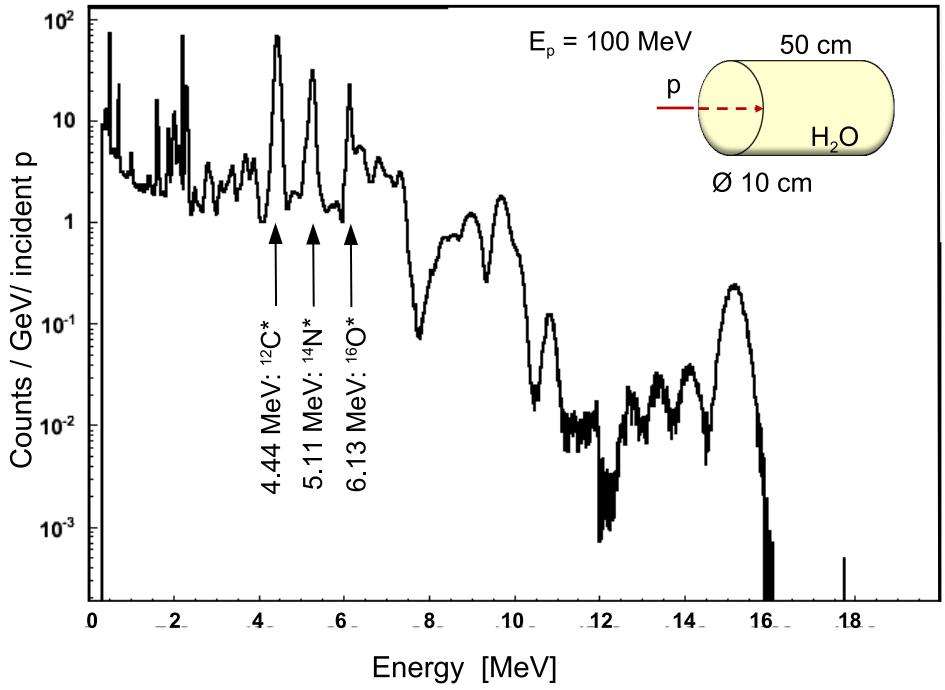

Figure 3.1: Monte-Carlo simulated photon emission spectrum (utilizing the FLUKA code [21, 22]) of a H_2O target (diameter 10 cm, thickness 50 cm), irradiated with 100 MeV protons. Dominant transition lines, suitable for prompt γ detection, are visible at 4.4 MeV from ^{12}C, 5.1 MeV from ^{14}N and 6.1 MeV ^{16}O from deexcitation.

uncertainties have to be monitored online, aiming for exploiting the signature of the produced secondary particles like annihilating positrons or prompt γ rays. A measurement of these secondary particles, produced by fragmentation reactions, would allow to monitor the produced activity of the hadron treatment within the target volume.

Conventionally, a post irradiation PET measurement is applied for ion beam monitoring, in contrast to the in-beam (online) monitoring, which is at present actively under research and which is in the focus of this thesis.

Two approaches for monitoring and online ion beam range verification can be pursued: a measurement of the delayed emission of 511 keV photons originating from β^+ decay and the registration of prompt γ-ray emission from nuclear transitions, both originating from nuclear fragmentation reactions inside the target (see Sect. 2.2.2).

The first approach of in-beam monitoring of the ion range is using positron emission tomography (PET) via β^+ decaying isotopes (typically ^{11}C and ^{15}O), produced during proton or carbon ion irradiation [10, 13, 8]. By exploiting the coincident 511 keV annihilation photons from the β^+ decay, it is possible to localize the produced activity. For calculating the dose distribution, it is necessary to utilize Monte-Carlo simulations (MC). Despite of the short halflives of the two isotopes ^{10}C and ^{14}O (19.3 s and 70.6 s, respectively), produced during hadron irradiation using a carbon or proton beam, it is possible to qualify them as candidates for online ion-beam range monitoring during therapy treat-

ment [51, 52]. Moreover, proposals have been presented to directly use positron emitter beams, such as ^{11}C [53, 54, 55], ^{10}C [56] or ^{15}O [57] as therapeutic beams, allowing for fast online ion-beam range verification.
An alternative approach is the measurement of the produced prompt γ ray emission from nuclear transitions induced by the hadron irradiation. Inside organic tissue (or a tissue-equivalent water phantom), nuclear reactions on hydrogen, oxygen or carbon nuclei can lead to characteristic γ ray emission from nuclear transitions. Prominent examples are γ lines like the 2.2 MeV transition from ^{1}H(n,γ)^{2}H, 6.1 MeV photons from ^{16}O deexcitation, 5.1 MeV from ^{14}N and 4.4 MeV γ rays originating from the first excited state in ^{12}C. A Monte-Carlo simulated (utilizing the FLUKA software [21, 22]) photon emission spectrum of a H_2O target (diameter 10 cm, length 50 cm), irradiated with 100 MeV protons, shows these transition lines in Fig. 3.1. The lifetime of the excited states in ^{16}O and ^{12}C is 20 ps and 64 fs, respectively, and thus significantly faster compared to the typical thermalization and annihilation times of a few picoseconds of positrons from β^+ decay [39, 28]. Aiming for in-beam measurements and online range monitoring, neutron background arising from nuclear reactions has to be considered as well. A suppression of this neutron background component is utilizing the prompt γ-ray emission method and can be achieved with a time-of-flight technique, necessarily requiring for providing a detector system with excellent timing capabilities.

3.2 Hadron therapy facilities

Ion beams for hadron therapy can be produced by linear accelerators (linac), cyclotrons, synchrotrons or combined facilities, like the synchro-cyclotron at the Rinecker Proton Therapy Center (RPTC) [60], or like the planned linac-cyclotron at the CArbon BOoster for Therapy in Oncology (CABOTO), which will be capable to accelerate C^{6+} ions and H_2 molecules to energies of 150 - 410 MeV/u in $\approx$ 24 m [61]. As an example, a layout of the Heidelberg Ion-Beam Therapy Center (HIT) is shown in Fig. 3.2. The facility consists of an ion source (1), a linear accelerator (2), a synchrotron (3), beam tubes heading to the treatment rooms (4), treatment rooms (5), a digital X-ray-system based position control (6), a gantry, which is a rotating beam delivery system (for realizing the optimum angle of the therapy beam to the patient) (7) and a treatment room in the gantry (8).
Those large conventional accelerator facilities require massive investments in the order of 100 - 200 Million Euro (for multiple treatment room facilities). Thus it is intriguing to explore the perspectives of alternative acceleration techniques like laser-driven particle acceleration, holding promise to provide a compact and cost-effective scheme to generate medically relevant particle beams. Particles, which are accelerated by the strong field of high-power, short-pulse lasers, additionally offer the advantage of providing a fast (< 1 ps) trigger signal from the laser, well suited to facilitate suppressing neutron background (produced during hadron irradiation) via a time-of-flight technique. Recent studies show that laser-driven ion delivery systems can be used for radiobiological studies during in-vitro cell irradiations [62]. Also, living cell irradiation experiments, with a dose application of up to 7 Gy, have been performed, using nanosecond quasi-monoenergetic proton bunches generated from a table-top laser system [63]. Also, besides of conven-

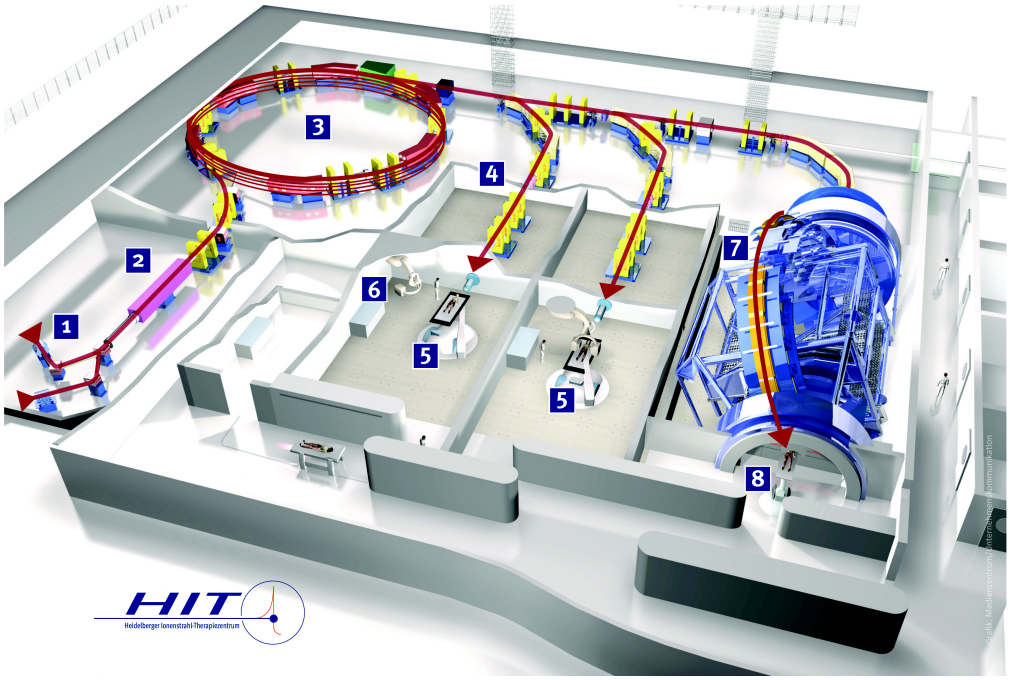

Figure 3.2: The Heidelberg Ion-Beam Therapy Center (HIT) consists of an ion source (1), a linear accelerator (2), a synchrotron (3), beam tubes heading to the treatment rooms (4), treatment rooms (5), a digital X-ray-system based position control (6), a gantry, which is a rotating beam delivery system (for realizing the optimum angle of the therapy beam to the patient) (7) and a treatment room in the gantry (8) [59].

tional ion acceleration, the OncoRay facility in Dresden is planning to treat tumors with laser-accelerated proton beams in the future [64].

3.2.1 Laser-accelerated therapeutic ion beams

High-power, short-pulse lasers are capable to accelerate ions in a range of few μm to energies in the MeV range. This acceleration is possible due to the strong electric laser field, when the laser beam is focused to high intensities, resulting in ultra-short ion beam bunches. Depending on laser and target parameters, different ion acceleration mechanisms can be addressed. A petawatt laser focused (in vacuum) to high intensities of $I_L \approx 10^{23}$ W/cm^2 on a thin diamond-like carbon (DLC) foil, will reach the acceleration regime of Radiation Pressure Acceleration (RPA) [65, 66]. RPA is a more efficient ion acceleration mechanism compared to Target Normal Sheet Acceleration (TNSA) [67, 68, 69], the maximum ion energy is scaling linearly with the laser intensity I_L, $E^{ion}_{max} \propto I_L$, instead of $E^{ion}_{max} \propto \sqrt{I_L}$ in case of TNSA. In addition, in case of RPA, the energy spectra of the accelerated ions promise to be mono-energetic, compared to TNSA, where an exponentially decreasing spectrum is obtained.

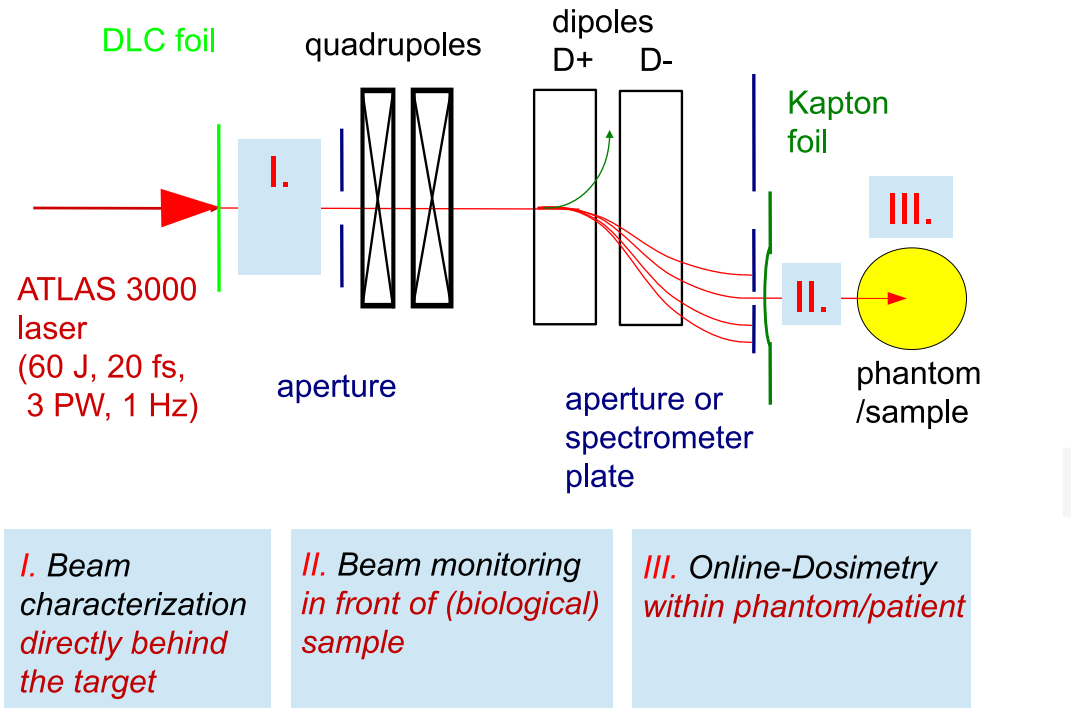

Figure 3.3: Sketch of a biomedical irradiation setup based on laser-driven proton acceleration. After the production of $\lesssim 100$ MeV protons in the electric field of a multi-petawatt laser system, the particles are characterized in a first stage directly after the target (DLC foil). A sequence of focusing quadrupoles and energy dispersive dipole magnets, together with apertures, purify the beam and assure the biomedically targeted quality .

In Fig. 3.3 a sketch of a possible layout of a laser-driven proton acceleration setup for biomedical irradiation is shown. Such a system is envisaged for the new CALA facility in Garching (Centre for Advanced Laser Application), which is presently under construction [34]. The ATLAS 3000 is a 3 petawatt Ti:Sapphire laser system with a repetition rate of 1 Hz, capable to deliver a peak pulse energy of 60 J at a wavelength of 795 nm within a 20 fs pulse (FWHM). Focused on a ≈ 5 nm thick DLC foil up to intensities of $I_L \approx 10^{22}$ W/cm^2, a beam of $\lesssim 100$ MeV protons in the electric field of the laser will be produced. However, the beam will exhibit a broad proton energy spectrum and contain also an electron component, therefore it will be characterized in a first step directly after the target. This can be performed by scintillators or by measuring the (residual-) gas ionization, allowing to reach an accuracy of $\approx$ 10-20 %. Afterwards, a sequence of beam focusing quadrupoles and energy dispersive dipoles and apertures will purify the beam and select the biomedical targeted quality. The second ion beam characterization will be made directly in front of the (biological) sample, after the beam left the evacuated beam tube. Pixel detectors (e.g. CMOS detectors like RadEye [70] or Medipix [71, 72]) are foreseen

at this place to reach a high measurement accuracy of $< 5\%$ for the ion beam [73]. In the last characterization step, the energy deposit of the beam within the phantom or patient has to be monitored preferably online.
The perspective of this thesis is to prepare for a reliable online proton-range verification with (few) mm spatial resolution in a small-animal irradiation geometry, as envisaged for the new CALA facility in Garching. This goal will be targeted by implementing a spatial and temporal resolved prompt γ-ray detection via a Compton camera.

Chapter 4

Photon detection techniques for medical imaging

Starting from radiation detectors like scintillators and semiconductors, this section gives a short overview of the positron emission tomography (PET) technique and introduces the principle of a Compton camera system as a potential future candidate for medical imaging, in particular for ion beam range verification in hadron therapy. Additionally, a combination of PET and the Compton camera method, the so-called γ-PET technique, applicable for a specific class of β^+ emitters, is explained.

4.1 Properties of radiation detectors

In general, radiation detectors can be based on solid, liquid or gaseous media, exploiting the same detection principle: within an active detector volume ionizing particles or γ rays create free charge carriers or carrier pairs mainly via photo-absorption, Compton scattering or pair production processes. Subsequently, those free charge carriers can be collected, amplified and converted into measurable signals. The number of created free charge carriers N_{eh} (electron-hole pairs or electron-ion pairs) amounts from the deposited energy E_{dep}, divided by the energy needed to create a pair E_{pair}

$$N_{eh} = E_{dep}/E_{pair} \tag{4.1}$$

Typically, in gases $\approx$ 30 eV, in semiconductors 1 - 5 eV and in scintillators 10 - 1000 eV is required to create a pair [39]. In scintillators, the light yield Y, which is the number of created photons per deposited energy in MeV, is commonly used for material characterization. The theoretically achievable energy resolution is primarily determined by the statistical fluctuation of the number of free charge carriers. Applying Poisson statistics, the variance σ_{eh} of the energy resolution can be expressed as

$$\sigma_{eh} = \sqrt{F N_{eh}} \tag{4.2}$$

Here the Poisson statistics has to be corrected by the Fano factor F [39]. The Fano factor results from the fact, that the energy loss creating free charge carrier in collisions is not purely statistical. The process leading to the individual charge carriers is not independent,

since the number of ways an atom may be ionized is limited by the discrete electron shells. The net result is a better energy resolution than predicted by purely statistical considerations [39]. For scintillators is $F \approx 1$, unlike gas detectors and semiconductor detectors, where $F < 1$. The relatively small energy of the band gap between valence and conduction band in the case of semiconductor detectors, which means the energy needed to create a free charge carrier pair, together with the relatively low Fano factor (Si: F = 0.12, Ge: F = 0.13) explains the superior energy resolution of semiconductor detectors. Much less energy is needed to create one information carrier, this results correspondingly in a much lower impact of statistical fluctuations. This sets the fundamental limit on the energy resolution achievable for any type of detectors based on ionization processes (commonly expressed via the Full Width at Half Maximum (FWHM) of the respective photopeak)

$$R_{Statistical\ limit} = 2.35\ \sigma_{eh} = 2.35\ \sqrt{F E_{dep}/E_{pair}} \tag{4.3}$$

Besides statistical fluctuations, also thermal noise (velocity fluctuation) and other noise effects influence the overall energy resolution of a radiation detector. All these uncertainty inducing fluctuations will add up quadratically to the overall energy resolution $R^2_{Overall}$ [39, 48]

$$\Delta R^2_{Overall} = R^2_{Statistical\ limit} + R^2_{noise} + ... \tag{4.4}$$

An 'ideal' detector should convert ionizing particles or radiation very fast into detectable electronic signals, have an excellent energy resolution, a small spatial resolution, a high stopping power and should be commercially available at reasonable costs. Especially the last point is often contradicting the others. Solid state detectors offer the possibility of a smaller detection volume compared to gas-filled detectors, due to their higher material density. Considering the focus of this thesis, only solid state scintillation detectors and semiconductor detectors will be discussed in the following sections.

4.1.1 Scintillation detectors

One advantage of scintillation detectors is that they can be manufactured with large volumes (e.g. compared to semiconductor detectors), enabling to stop also energetic photons. A disadvantage is their significantly reduced energy resolution compared to semiconductor detectors. Scintillator materials are distinguished into the classes of inorganic and organic materials, they can be solid, liquid or even gaseous. The basic principle of a scintillator is to convert ionizing particles or energetic radiation into visible photons. Scintillation conversion can be divided into three subsequent processes: the conversion, the transport and the luminescence process (see Fig. 4.1). In the conversion process, an energetic photon interacts with the scintillation material through photo-absorption, Compton scattering or pair production. During the process free electron-hole pairs are created and thermalized afterwards. Subsequently, in the transport stage, the electron-hole pairs diffuse through the material, here it is possible that (repeated) unwanted trapping at scintillation material defects and non-radiative recombination occurs. The last stage is the luminescence process, where the free charge carriers are trapped in the luminescence center and radiative recombination finally occurs [76].

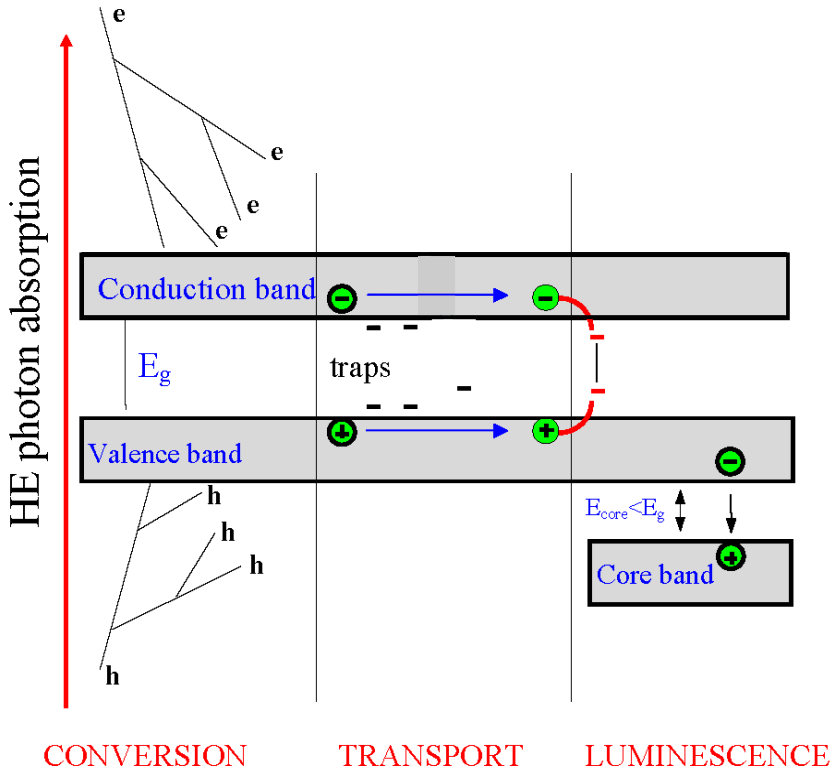

Figure 4.1: Schematic illustration of the three stages of the scintillation process: Conversion of an energetic photon to electron-hole pairs, their transport through the material and the luminescence produced by their recombination [76].

Subsequently, a scintillation light distribution will be created which spreads out, depending on the incident photon energy, over some cm of the scintillator volume. With segmented light guides [77] or segmented photomultipliers (PMT) [150], it is possible to achieve also a millimetric spatial resolution from the readout of a monolithic detector [79]. In detail, incident radiation or particles excite electrons from the valence band into the conduction band of the scintillator material. In order to guarantee that a scintillator is sufficiently transparent for its own light, it should be a single crystal. Doping of the scintillator material with activation centers adds transitions to the electronic structure within the band gap (e.g Tl^+ in case of NaI or Ce^{3+} in case of $LaBr_3$). Exceptions are crystals with exciton luminescence, like bismuth germanate $Bi_4Ge_3O_{12}$ (BGO), where electron-hole pairs form an exciton, or self-activated scintillating crystals like $PbWO_4$ or $CdWO_4$. In case of doping, these elements add additional transitions to the electronic band structure and act as luminescence centers by emitting visible photons, which then are detected and converted into electric signals using, e.g., a photomultiplier tube (PMT), avalanche photo-diodes (APD) or silicon photomultipliers (SiPM). Especially Ce^{3+} is a very efficient luminescence center, and Ce-doped scintillators show a very high light yield, which corresponds to the proportionality constant between the deposited energy and the average

amount of scintillation photons. The doping with Ce^{3+} provides shallow transitions between valence band and conduction band. The produced holes and electrons are trapped in states of the same cerium ion, particularly in the 4f state in case of holes, and the 5d state in case of electrons. The orbital overlap between these two states leads to annihilation and the emission of light with typical wavelengths in the blue or near UV ($\approx$ 350 - 450 nm, see also Tab. 4.1). The short decay time of these states of only approximately 30 ns leads to a fast timing behavior of a Ce^{3+}-doped scintillator [48].
In general, a scintillator should fulfill the following criteria: The conversion should be over a wide energy range linear proportional to the deposited energy. The decay time of the induced luminescence should be short, in order to produce fast signals. Also the scintillator material should be transparent to the wavelength of the luminescence and the refraction index should be close to glass (1 - 1.5), for an effective optical coupling of the scintillator to the photomultiplier [39]. Unfortunately, no scintillator material fulfills all of these criteria and a compromise has to be found for specific applications.
The density ρ, the decay time τ, the light yield Y, the relative energy resolution ΔE/E, the wavelength of maximum emission λ_{max} and the refractive index n of some commonly used scintillators are listed in Tab. 4.1. The upper part lists inorganic scintillators, which are interesting candidates for medical imaging and nuclear instrumentation in general. The lower part lists some organic scintillators, useful for time measurements (their names indicate brand names from different manufacturers, BC and NE (Pilot) stands for St. Gobain [80] (originally Bicron and Nuclear Enterprises, respectively), EJ for Eljen [81]. Choosing the right scintillator for an application also requires to consider properties like the 'afterglow' (delayed luminescence), potential intrinsic radioactivity or a hygroscopic nature of the crystal [39, 78].
Inorganic scintillators in general provide a high light yield and have a linear conversion of the deposited energy. Organic scintillators are in general very fast, but the output of light is less. Especially the higher density of inorganic scintillators prioritize them for spectroscopy, in contrast, time measurements favor organic scintillators, because of their fast decay time. When focusing on timing behavior, organic (i.e. plastic) scintillators are outstanding, therefore they are commonly used for time-of-flight measurements, as counting detectors or as reference detectors in coincidence measurements to determine the time resolution of a detector of interest.
Compared to the other inorganic scintillators, it can be seen that $LaBr_3$ exhibits a superior time response, light yield and energy resolution. Its density, showing the ability to efficiently absorb photons, is with 5.29 g/cm^3 in the upper range. Altogether, this makes $LaBr_3$:Ce^{3+} an interesting detector material for many applications. Especially in the context of this thesis, using $LaBr_3$ as an absorber of a Compton camera, applied for medical imaging, appears advantageous (see Sec. 5.2).

4.1.2 Semiconductor detectors

In contrast to scintillation detectors, where a light distribution is created, which spreads out over a rather large volume of the detector crystal, semiconductor detectors offer the great advantage that the interaction of an incident photon or charged particle is locally confined to a small volume. This results directly in a high spatial sensitivity. By using

Material	ρ [g/cm^3]	τ [ns]	Y [ph/MeV]	ΔE/E [%]	λ_{max} [nm]	n
Inorganic						
NaI:Tl$^+$	3.67	230	38000	5.6	415	1.85
$Bi_4Ge_3O_12$ (BGO)	7.13	300	8200	12	480	2.15
Lu_2SiO_5:Ce^{3+} (LSO)	7.40	47	25000	10	420	1.82
Gd_2SiO_5:Ce^{3+} (GSO)	6.71	60	9000	10	440	1.85
Y_2SiO_5 (YSO)	4.54	70	24000	10	420	1.8
$LaCl_3$:Ce^{3+}	3.79	28	46000	3	350	1.9
$LaBr_3$:Ce^{3+}	5.29	26	63000	3	380	2.1
Organic						
BC-404, EJ 204, NE 104	1.03	1.8	$\sim$10000	-	408	1.58
BC-408, EJ 200, Pilot F	1.03	2.1	$\sim$10000	-	425	1.58
BC-418, EJ 228, Pilot U	1.03	1.4	$\sim$10000	-	391	1.58

Table 4.1: Scintillation properties of some commonly used materials, showing the density ρ, the decay time τ, the light yield Y, the relative energy resolution at 662 keV, the wavelength of maximum emission λ_{max} and the refractive index n. The upper part lists inorganic scintillators, which are interesting candidates for medical imaging and nuclear instrumentation in general. The lower part lists some organic scintillators, useful for time measurements [39, 78].

highly segmented electrodes, it is possible to achieve a position resolution down to some μm. Semiconductor detectors also provide a much better energy resolution compared to scintillators, because of the relatively small energy needed for creating free charge carrier pairs, and also because their Fano factor is < 1. Scintillators, in contrast, can be produced with large volumes, able to fully absorb energetic photons. Many different semiconductor detector designs are existing, e.g., cylindric true-coaxial germanium detectors can have volumes up to one liter. Silicon detectors, in contrast, are only available in planar geometries, because of the required high resistivity for low-noise, fully depleted operation. The electrodes of planar detectors can be unsegmented or segmented, the latter is offering not only a spatial resolution, but also a higher rate acceptance of incoming photons and particles. Additionally, segmented semiconductor detectors show a lower noise, resulting from the decreased capacitance of the segmented electrodes.

Semiconductors form a crystalline lattice structure via covalent bonds to the closest neighbor, establishing allowed energy bands for the electrons, i.e valence band and conduction band, separated by a gap of forbidden energies, the so-called band gap (E_{gap}), whose size distinguishes between a semiconductor ($E_{gap} \approx$ 1 - 5 eV) or an insulator ($E_{gap} >$ 5 eV). The conduction band is a region of energies, where electrons are delocalized, able to freely move within the atomic lattice. Incident ionizing particles or γ rays excite electrons within the semiconductor from the valence band to the conduction band, leaving vacancies, thus creating electron-hole pairs, where the holes are regarded as pseudo particles, able to freely move inside the valence band. The number of pairs is proportional to the energy of the ionizing radiation, they get separated in an applied electric field $\vec{E}$,

drifting towards the (segmented) electrodes of the semiconductor detector. The direction of the externally applied electric field is selected to deplete the semiconductor volume from intrinsic charge carriers, called reverse biasing, thus considering the semiconductor detector as a diode. At the electrodes, electrons as well as holes induce a signal, which then will get amplified and registered. A high purity of the material is necessary to ensure that the signal originates from ionization, and not from internal free charge carriers. The charge carrier transport to the electrodes is described by the drift velocities for electrons and holes

$$\vec{\nu_e} = \mu_e \vec{E} \tag{4.5}$$

$$\vec{\nu_h} = \mu_h \vec{E} \tag{4.6}$$

An applied electric field $\vec{E}$ accelerates electrons and holes towards the electrodes, due to collisions a constant drift velocity $\vec{\nu}$ will be reached. The material dependent parameter μ corresponds to the mobility of the free charge carriers. A high mobility of the free charges leads to a small collection time, which is preferred to obtain a fast timing behavior of the detector and allows for high incident particle or photon rates.
Electron-hole pairs can also be thermally created, with a probability given by

$$p(T) = CT^{3/2} exp(-E_{gap}/2k_BT) \tag{4.7}$$

where C is a material constant, k_B the Boltzmann constant and T is the temperature. This leads to a thermal noise (also known as Johnson-Nyquist noise). At $T = 300$ K the k_BT term in the exponential amounts already to 0.026 eV. Thus, a small band gap is favored for achieving a good energy resolution (compare also Eq. (4.1)), but on the other hand the thermal noise and, with it, the energy resolution will increase.
Table 4.2 shows a comparison of the most commonly used semiconductors in nuclear instrumentation silicon, germanium and cadmium zinc telluride (CdZnTe) [48].
CdZnTe is a dense, high-Z detector material, having a band gap large enough to allow for operation at room temperature, while still providing a good energy resolution. However, the disadvantage of this material is the very small $\mu\tau$ product, which is about two orders of magnitude smaller compared to Si or Ge. The lifetime of the electrons and in particular the lifetime of the holes is for many applications too short, i.e. trapping and recombination of the charge carriers will occur, before registering a signal at the electrodes can be achieved.
Already in Sect. 2.1.1 it has been shown that germanium is in general a better absorber material, due to its higher density of 5.33 g/cm^3, compared to silicon (2.33 g/cm^3). As shown in Fig. 2.3, already beyond photon energies of 60 keV, silicon exhibits a larger probability of Compton scattering compared to photo-absorption. For germanium this crossover occurs around 150 keV. This qualifies silicon as the better scatter detector material. Additionally, in germanium the average stopping range for a 200 keV electron is $\approx$ 110 μm, which is only half compared to $\approx$ 210 μm in the case of silicon (see Fig. 2.14). This will turn out to be beneficial when aiming at a Compton camera with electron tracking capability. The band gap of Si is 1.12 eV, resulting in a low thermal noise, low enough to allow for room temperature operation of a silicon detector compared to germanium detectors (E_{gap} = 0.67 eV), which have to be operated at liquid nitrogen temperature. However, cooling of a detector requires additional technical efforts and an operation of the detector in vacuum. For selecting the proper material for the scatter component of a

	Silicon Si	Germanium Ge	Cadmium Zinc Telluride CdZnTe
Z	14	32	49.1
E_{gap}	1.12 eV	0.67 eV	1.57 eV
E_{pair}	3.62 eV	2.95 eV	4.64 eV
ρ	2.33 g/cm^3	5.33 g/cm^3	5.78 g/cm^3
μ_e	1200 cm^2/Vs	3600 cm^2/Vs	1000 - 800 cm^2/Vs
μ_h	250 cm^2/Vs	1700 cm^2/Vs	80 - 30 cm^2/Vs
τ_e	100 - 1000 μs	$\simeq$ 100 μs	1 - 5 μs
τ_h	100 - 1000 μs	$\simeq$ 100 μs	0.1 - 1 μs
F	0.12	0.13	0.1

Table 4.2: Properties of the three different semiconductor materials Si, Ge and CdZnTe are displayed. Z is the atomic number, E_{gap} the band gap energy, E_{pair} describes the pair-creation energy, ρ is the density, μ_e, μ_h and τ_e, τ_h are the mobilities and lifetimes, respectively, of the free electrons and the free holes. F denotes the Fano factor [48].

Compton camera (see Sect. 5.2), the Doppler broadening, which is the limit of the spatial resolution of a Compton camera, has to be considered. Silicon provides a smaller Doppler broadening of 0.4° at 1 MeV, compared to Ge with 0.65° at 1 MeV [26].

4.2 Compton Camera

The Compton camera technique exploits the well-defined kinematics of the Compton-scattering process (see Sect. 2.1.2) in order to allow for a reconstruction of the initial γ-ray source position. A Compton camera consists of two components, a scattering part and an absorber part. In the scattering part an incident photon undergoes Compton scattering, here the point of interaction needs to be measured with high position resolution. The red-shifted scattered photon is then absorbed in the second stage of the Compton camera, again also the corresponding position has to be determined in addition to the energy measurement. No mechanical collimator is needed for the source reconstruction, a Compton camera can instead be regarded as an electronically collimated detector system, resulting in a promising imaging sensitivity. Already in 1973, the detection of γ rays via Compton scattering (in the atmosphere) was proposed by V. Schoenfelder [82]. The first Compton camera for medical applications was built by M. Singh and D. Doria in 1985, consisting of an array of germanium detectors [83]. Aiming for an optimized Compton camera design for in vivo-dosimetry, simulations have been performed by various groups [84, 85, 86]. Actual projects studying the Compton camera concept for medical imaging follow two complementary routes: in a first approach, solid state detectors are used for the scattering and absorption part of the Compton camera. A Compton camera prototype using CdZnTe (20 x 20 x 5 mm^3, 16 x 16 pixels) as a scatter detector and LSO (54 x 54 x 20 mm^3,

13 x 13 pixels) as absorber detector was realized in Dresden, achieving a spatial image resolution of 5° at 0.5 MeV and 2.2° at 3 MeV, respectively, and a simulated efficiency of 0.7% at 1 MeV [48]. A second approach for a Compton camera design pursued by the Nantes group uses liquid xenon (LXe) as simultaneous scatter and absorber material in a time projection chamber (TPC) setup, exhibiting an active volume of 25.4 x 25.4 mm^2 with 120 mm length, resulting in 130 kg of LXe [112, 91]. At IFIC, Valencia, a prototype based on a continuous $LaBr_3$ crystal acting as a scatterer (16 x 18 x 5 mm^3) and a continuous LYSO crystal (16 x 18 x 5 mm^3), both coupled to SiPM arrays, has been developed within the European ENVISION project [88]. Another Compton camera project has been designed in Lyon, using 10 double-sided silicon strip detector (DSSSD) scatterer modules (80 x 80 x 2 mm^3, strip pitch 0.5 mm) and LYSO scintillators (300 x 300 x 40 mm^3), or alternatively, BGO (300 x 300 x 45 mm^3) as absorber. The spatial image resolution has been simulated for both scintillators to reach 7 mm at 10 cm γ source distance, with an efficiency of $3{\cdot}10^{-4}$ at 1 MeV [87]. The Compton camera concept has also been pursued in γ astronomy for the purpose of localizing cosmic γ-ray point sources. In this context, a prototype was developed, capable not only of tracking the incident photon, but also the recoiling Compton-scattered electron [25, 89, 90]. Based on this prototype design, simulations for in-vivo dosimetry for hadron therapy have been performed by M. Frandes [28].
So far, only the OncoRay project in Dresden is perspectively aiming for in-vivo proton beam range verification in laser-driven hadron therapy. In this scenario it can be exploited that a high-power, short-pulse laser system can provide a very fast trigger signal (< 1 ps), allowing to accurately apply the time-of-flight technique for the suppression of (mainly neutron) background. Therefore, an optimized Compton camera system in such an environment should preferably exhibit a fast time resolution well below 0.5 ns.

4.2.1 Gamma tracking

Figure 4.2 explains the basic principle of the Compton camera detection technique, here restricted to a measurement of photon properties only ('γ-tracking'). The energy loss $\Delta E_{\gamma,1}$, the residual energy $E_{\gamma,2}$ and the interaction positions of the Compton scattering process of the incident photon are measured in a scatter detector and a subsequent absorber detector, respectively. The initial photon energy $E_{\gamma,1}$ can be obtained by summing $\Delta E_{\gamma,1}$ and $E_{\gamma,2}$. The opening angle θ of the Compton-scattering cone can be derived from the known initial photon energy $E_{\gamma,1}$ and the measured energy of the second interaction $E_{\gamma,2}$, considering energy conservation, according to

$$\cos\theta = 1 - m_e c^2 \frac{E_{\gamma,2}}{E_{\gamma,1}(E_{\gamma,1} - E_{\gamma,2})} \tag{4.8}$$

which is a rearrangement of Eq. (2.4). Due to this Compton kinematics, the origin of the incident photon can be restricted to a cone surface ('Compton cone'). Superimposing different Compton cones from several events reduces the reconstructed source distribution in 3 dimensions to the few-millimeter range [25]. This formula is not taking into account the effect of Doppler broadening, arising from the momentum of the bound electron. In contrast, it assumes the electron to be at rest before Compton scattering. The MC

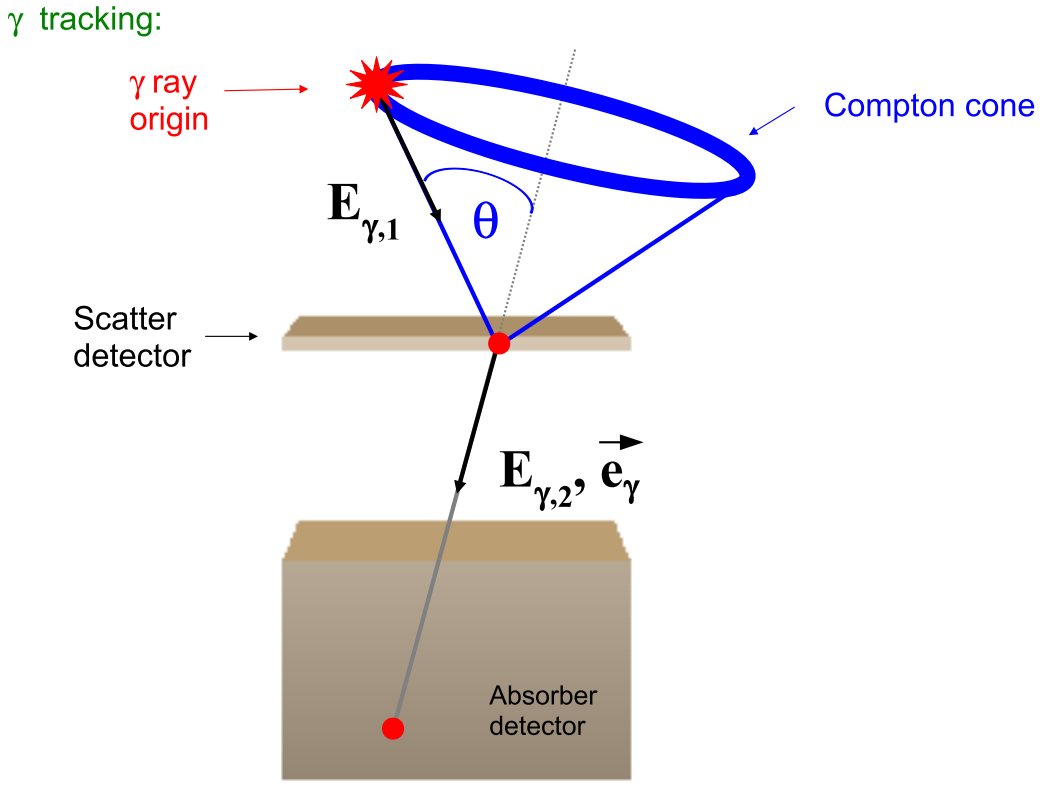

Figure 4.2: Basic principle of the Compton camera detection technique. A Compton camera consists in general of a scatter detector and an absorber detector. An incident γ ray will first be Compton scattered in the scatter part, where the position and energy deposition of the interaction is measured. Then the γ ray will subsequently be absorbed in the absorber detector, where again position and energy are measured. Due to the Compton kinematics, the γ-ray origin can be restricted to a cone surface ('Compton cone').

simulations performed within this thesis (see Chapt. 5), instead, explicitly take the non-zero momentum of a bound electron correctly into account.

4.2.2 Gamma + electron tracking

An advanced method for Compton camera-based photon imaging adds the capability to track the recoiling electron to the previously described technique. In this scenario, the so far monolithic scatter detector is replaced by several layers of thin detectors, allowing to measure the electron energy E_e and its direction $\vec{e_e}$. Now the reconstructed position of the incident photons can be restricted from the full Compton cone surface to a cone segment (Fig. 4.3). The length of the 'Compton arc' will depend on the precision of the measurement of the recoiling electron.
However, also this technique has its limits. The interaction of the Compton electron with the Coulomb potential of the scatter detector atoms leads to many small-angle scatterings while passing through the detector material. The deviation of the electron direction is

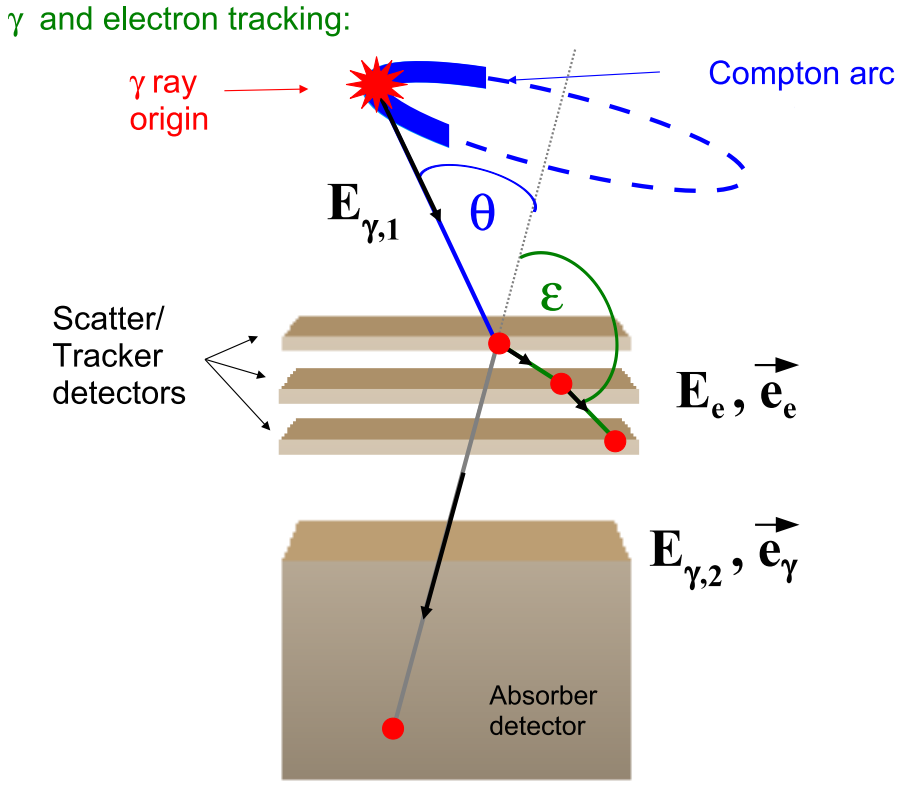

Figure 4.3: Basic principle of an advantaged Compton camera with additional electron tracking capability. Several thin scatter detectors are used for tracking the recoiled electron. Therefore, the origin of the γ ray can be restricted from a cone to an arc segment.

described by Molière theory (for an overview see [92]). This Molière scattering of the electrons inside the tracker detector is limiting the precision achievable for electron tracking in a Compton camera. The distribution of the scatter angle can be approximated by a Gaussian [93], the width of the angular distribution, projected on a scattering plane, is given by

$$\delta_{proj} = \frac{13.6\ \mathrm{MeV}}{\beta cp}\sqrt{\frac{r}{R_0}}\left(1 + 0.038\ \ln\frac{\mathrm{r}}{\mathrm{R_0}}\right) \tag{4.9}$$

where R_0 is the radiation length in the material (e.g. 9.35 cm for Si), r is the straight path length between start and end point of the electron in the material, and
$\beta cp = (E_e^2 + 2E_eE_0)/(E_e + E_0)$ is the product of the velocity and the momentum of the electron (E_0 is the rest mass of the electron). From Eq. (4.9) follows, that by decreasing the electron energy E_e, the width of the angular distribution δ_{proj} is increasing.
A MC simulation (Geant3) of the scattering angle distribution of electrons passing through 500 μm of Si is shown in Fig. 4.4. The Molière distributions for incident photon energies E_i of 1 MeV (top left panel) and 5 MeV (top right panel) are displayed (under normal incidence $\alpha = 90°$). Both distributions can be approximated by a Gaussian, while the distribution for 1 MeV already contains events, which no longer follow the Gaussian

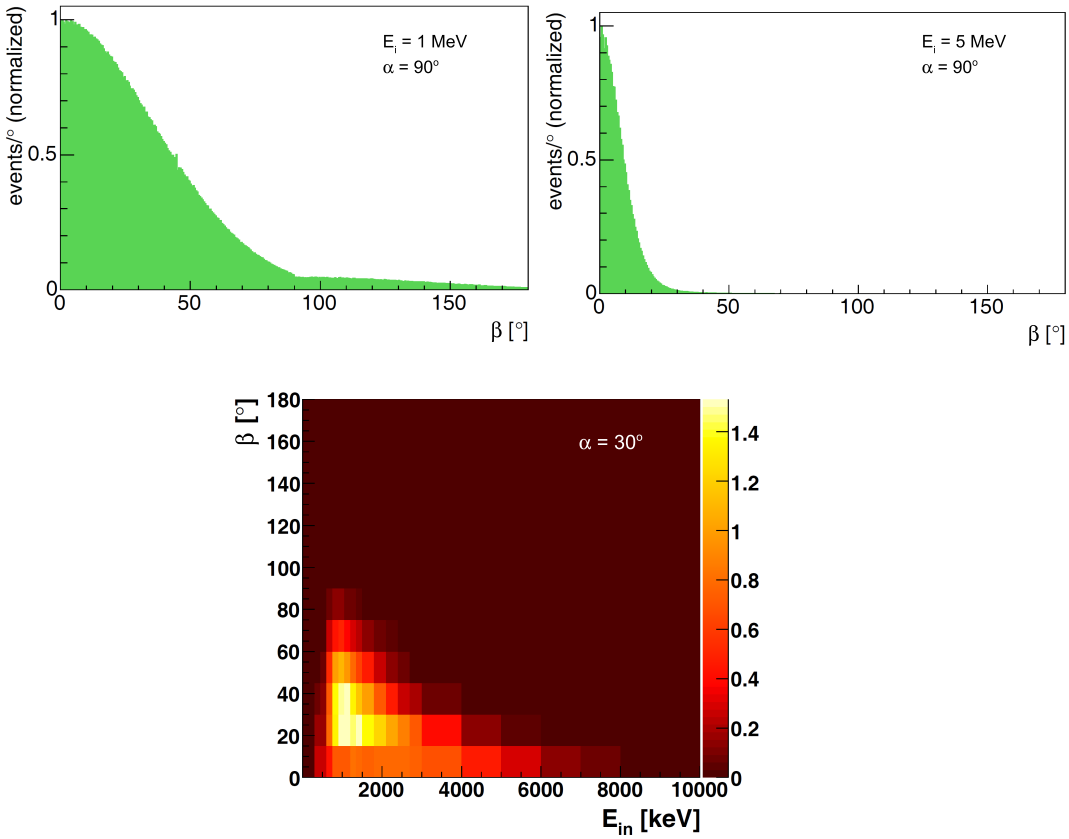

Figure 4.4: MC simulation (Geant3) of the scattering angle distribution of electrons passing through 500 μm of Si. The Molière distributions for incident photon energies E_i of 1 MeV (top left panel) and 5 MeV (top right panel) are displayed (under normal incidence $\alpha = 90°$). Both distributions can be approximated by a Gaussian, while the distribution for 1 MeV already contains events, which no longer follow the Gaussian shape (scatter angles $> 90°$). There the electron direction was reversed. The angular distribution β as a function of the incident photon energy E_{in} can be seen in the bottom panel. Here the incident angle was chosen to a more realistic value of $\alpha = 30°$, resulting in a slightly larger path in Si and also a slightly higher energy deposit. In agreement with Eq. (4.9), the width of the angular distribution is larger for smaller incident photon energies [26].

shape (scatter angles $> 90°$). There the electron direction was reversed. The angular distribution β as a function of the incident photon energy E_{in} can be seen in the bottom panel. Here the incident angle was chosen to a more realistic value of $\alpha = 30°$, resulting in a slightly larger path of the electron in Si and also a slightly higher energy deposit. In agreement with Eq. (4.9), the width of the angular distribution is larger for smaller incident photon energies [26].

For tracking the electron and determining its direction, the Molière scattering has the following consequences. Considering a Compton camera geometry with 1 cm distance between the scatterer layers and a pitch of the strip detector of 390 μm, the direction of an electron can be resolved up to 2.2°. Therefore, Molière scattering is the limiting factor. Because the scattered electron loses energy while passing through the Si layers, the average Molière scattering angle is increasing along the path of the electron. However, the initial Compton scattering interaction will leave the recoil electron with a remaining path length inside the corresponding silicon layer, which is obviously smaller than the larger thickness itself. Therefore the resulting width of the angular distribution relative to the direction of incidence, induced by (multiple) Molière scattering, is reduced in this primary interaction layer relative to the subsequent ones. This angular distribution will successively widen for all following tracker layers, therefore the reconstruction algorithm is limited to use only the first and second electron interaction position for the trajectory reconstruction. More information about the Molière scattering and the Compton electron tracking can be found in the PhD thesis of A. Zoglauer [26].

As already shown in Sect. 2.1.1, silicon provides a better Compton scattering to photo-absorption ratio compared to germanium. Additionally, silicon offers a smaller Doppler-broadening (0.4° at 1 MeV) compared to germanium (0.65° at 1 MeV), which limits the angular resolution of the Compton camera [26]. The availability of highly segmented, thin double-sided silicon strip detectors (DSSSD), allowing for a precise measurement of photon energy and interaction position at room temperature, together with the electron tracking capability, qualifies silicon as scatter detector in a Compton camera. For the absorber detector, in our case $LaBr_3$(Ce) was chosen as the most suitable detector material. This scintillation material shows a superior time response, capable to suppress neutron background via the time-of-flight technique. Its high light yield will result in a high energy resolution, while its high density enables the full absorption of energetic photons, resulting in a high detection efficiency.

4.3 Positron emission tomography

Considering the context of this thesis, the following discussion focuses on positron emission tomography as medical imaging technique, while single photon emission tomography (SPECT), X-ray computed tomography (CT) or magnetic resonance imaging (MRI) lie beyond the scope of the present work.

After M.E. Phelps, M.M. Ter-Pogosssian and T.F. Budinger built the first PET scanner in 1975 [95, 94], this medical imaging technique has received an amazing gain of interest over the last decades. Since the 1990's, the number of installed PET systems worldwide is exponentially growing, from 70 PET centers in 1996 to 400 in 2006, up to over 1000 in

2013 [96]. Positron emission tomography (PET) is a nuclear medical imaging technique for measuring the position- and time-dependent concentration of radioactively labeled tracer molecules in an organism. It permits a functional understanding of the underlying causes of diseases and had its breakthrough as an imaging instrument for clinical application studies (e.g. bone metabolism, myocardial perfusion and viability, lung embolism, tumours, thyroid function or even neurological disorders) in the last decade due to the large variety of different tracers and due to the significant improvement of the imaging performance [97]. These tracers are chemical compounds, carrying a positron emitting isotope to, e.g., a tumor site. Annihilation of the positron into two (almost) back-to-back emitted 511 keV photons allows to restrict the source origin in 2 dimensions onto a line of response (LOR).

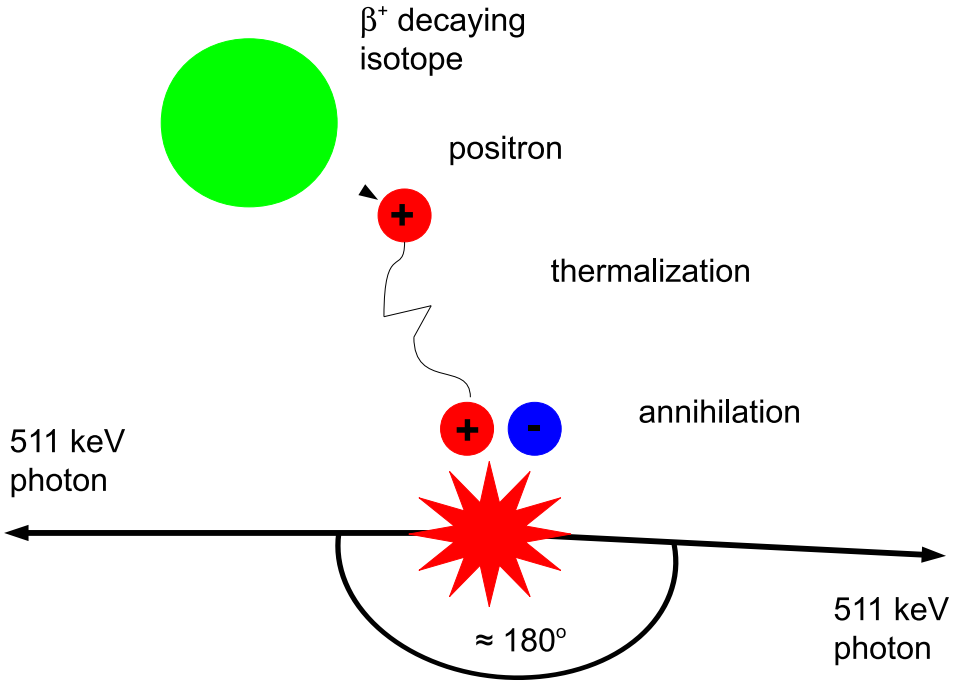

Figure 4.5: Sketch of the positron annihilation process. After the production from a β^+ decaying isotope (together with an electron anti-neutrino), a thermalization of the positron occurs. Finally, annihilation with a bound electron from the surrounding medium will occur, where the momentum of the electron gives rise to an angular acollinearity, i.e. the annihilation occurs not exactly into two photons emitted at 180°, but exhibits a smaller annihilation angle by about 0.3° [98].

Figure 4.5 shows a sketch of the annihilation process of a positron. An inherently limiting factor of PET is the acollinearity of the positron annihilation, i.e. the angular deviation from 180° between the two annihilation photons, originating from the momentum dis-

tribution of the annihilating electron-positron pair, after thermalization of the positron (within a few ps) and positronium formation. Because of the thermalization of the positron prior to its annihilation, the acollinearity is mainly caused by the significantly higher momentum of the bound orbital electrons. In a recent study [98], the acollinearity describes the angular deviation $\Delta\Theta$ from 180° by two components: a broad main component originating from orbital electrons with $\Delta\Theta = 0.633(8)^\circ$ and a narrower component with $\Delta\Theta = 0.27(10)^\circ$ resulting from positronium annihilation. This corresponds to a spatial deviation of 2 mm in an average PET-ring radius of 40 cm and thus represents the dominant limiting factor for the spatial resolution of whole-body PET systems [99]. Another effect arising from the momentum distribution of the annihilating electron-positron pair is the Doppler broadening of the annihilation spectrum. The actual broadening depends on the annihilation medium and can be used as a measure for the longitudinal component of the momentum distribution [100, 101].

Figure 4.6 shows the basic principle of the positron emission tomography (PET) technique. The source image reconstruction is determined by the accuracy of the localization of the photon interaction position in the detector. Two almost collinear 511 keV photons, produced by an annihilating positron from a β^+-decaying isotope inside a patient, get registered in a detector ring assembly, forming a back-projected line of response (LOR). Superimposing the LORs of different decay events locates the source distribution of the emitter, i.e. the concentration of the tracer molecules, in a patient in 3D. The two LORs marked in yellow in Fig. 4.6 correspond to correctly reconstructed events, their intersection defines the source volume. The blue LOR indicates a situation, where scattering in the sample/patient distorted the (almost) 180° correlation between the two annihilation photons, thus resulting in an erroneous reconstruction of the LOR. The green LOR shows the parallax error induced by the depth of interaction (DOI) uncertainty, which occurs for off-center source positions. Such parallax errors can be avoided by correcting for the depth of interaction in the scintillator via measuring the spatial distribution of the scintillation light to estimate the entry point of the photon on the crystal front surface [102]. Modern whole-body systems are combined PET/CT scanners, where CT provides the anatomical information for a reference frame and also data for the attenuation and scattering correction, while PET provides the molecular information. Such scanners, like the Philips Gemini TF [103] or the GE Healthcare Discovery ST [104], are able to reach a spatial resolution of 4.7 mm or (on average) 5.7 mm, respectively, which is a substantially larger value than the sub-millimeter spatial resolution attainable with computed tomography (CT, several hundred micrometer) or magnetic resonance imaging (MRI, 5-10 μm). This disadvantage of PET results in a limited localization of, e.g., lesions and lesion borders [105]. The performance of new generation PET/CT, the Siemens Biograph mCT [106], with point-spread-function (PSF) correction, can go down to 2.0 mm for the PET modality. An improvement of conventional PET imaging is the Time-of-Flight (TOF) PET technique, where the flight time difference (t_2 - t_1) of the two annihilation photons registered in the responding pair of detectors is taken into account for achieving an improved spatial information. Annihilation events can be restricted to a certain area of the LOR, thus achieving an improved image quality by an improved signal-to-noise ratio. Moreover, the patient dose and the examination time can be reduced. So far, the GEMINI TF and the Siemens Biograph mCT are the only PET/CT scanner on the market,

where the TOF technology has been implemented with a coincidence resolving time CRT $\approx$ 500 ps, resulting in a positioning uncertainty of $\pm$ 7.5 cm for a PET scanner with 80 cm diameter. It has even been shown that the TOF technique is capable of reaching a

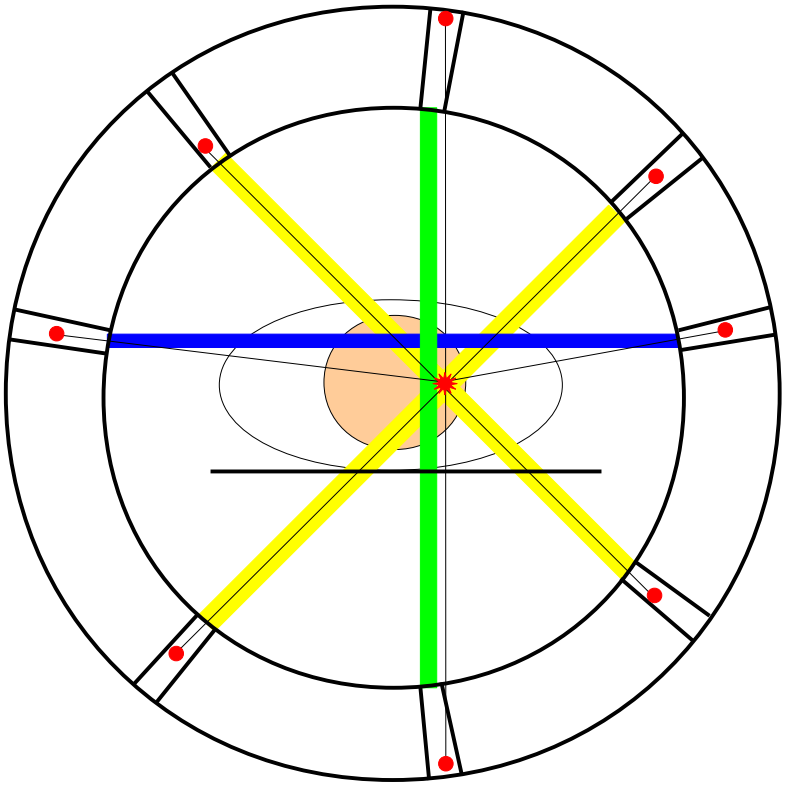

Figure 4.6: Basic principle of the positron emission tomography (PET) technique. Two almost collinear 511 keV photons, produced by an annihilating positron from a β^+-decaying isotope inside a patient, get registered in a surrounding detector ring, thus allowing to reconstruct the back-projected line of response (LOR). The two LORs highlighted in yellow denote two annihilation events with correctly reconstructed LOR. In contrast, the LOR marked in blue corresponds to a situation, where scattering inside the patient distorted the 180° correlation between the two annihilation photons, thus leading to an erroneous reconstruction of the LOR. The green LOR illustrates the parallax error induced by the depth of interaction (DOI) uncertainty, occurring for off-center source positions.

spatial resolution of about 1 mm, using a monolithic 24 x 24 x 10 mm^3 LSO:Ce scintillator, attached to a digital silicon photomultiplier (SiPM) [107]. In Fig. 4.7, a comparison of the LOR reconstruction with and without exploiting the time-of-flight information is displayed.

Besides the clinical diagnostic use of PET in whole-body scanner systems, another class of PET scanning systems is devoted to biomedical studies using small animals. Biomedical research, using animal models of metabolism and disease mechanisms, would profit from high-resolution, small-animal PET devices [109]. Presently, the microPET II de-

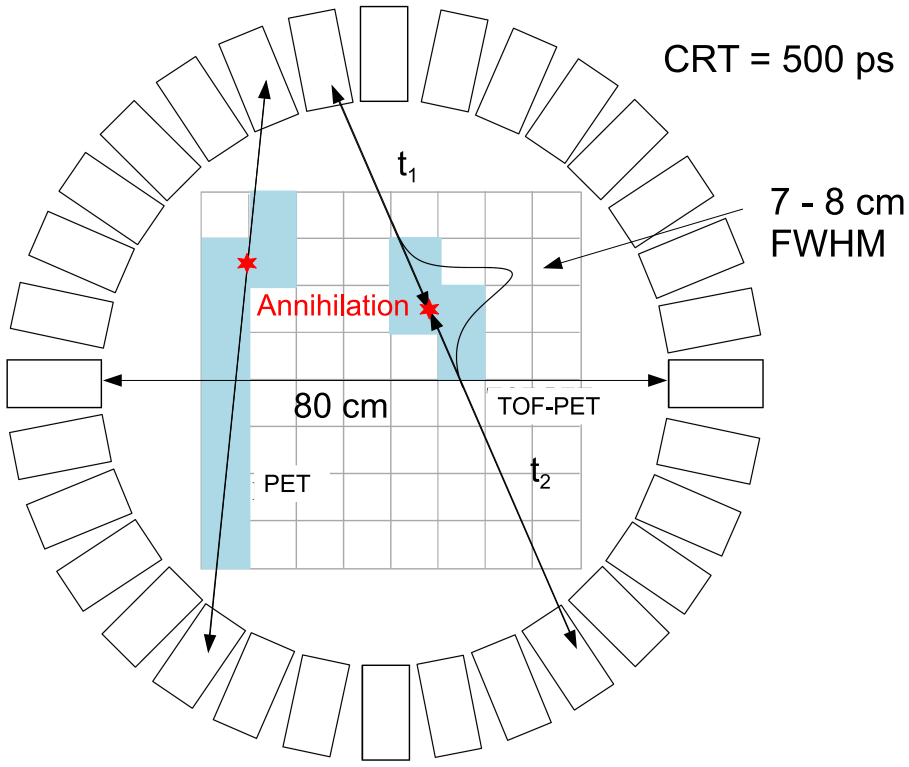

Figure 4.7: Comparison of the LOR reconstruction between the conventional PET technique and the TOF-PET technique. The TOF-PET technique reduces the uncertainty of the source reconstruction on the LOR to typically 7-8 cm (assuming a coincidence resolving time (CRT) of 500 ps and a radius of 40 cm of the PET ring) [108].

vice is a state-of-the-art small-animal PET. Moreover, especially biomedical research, using animal models of metabolism and disease mechanisms, would profit from a high-resolution small-animal PET device, where presently a resolution of 1.1 mm (FWHM) in the center of the field-of-view (FOV) has been reported, which degrades to 2.2 mm (FWHM) at a position with 2 cm radial offset [109, 110]. Even sub-millimeter spatial resolution may be reachable, as, e.g., first tests with continuous LYSO crystals coupled to a silicon photomultiplier matrix have shown [111]. Also the concept of a Compton camera has been investigated for its applicability with the PET technique, however, so far only at the laboratory development level [112]. In this case, position and energy information of the Compton scattering kinematics are measured in a scatter and an absorber detector, together allowing for a reconstruction of the direction to the source position on the surface of the Compton cone. In general, the spatial resolution of a PET device is limited by several effects. Limiting factors are the spatial, temporal or energy resolution of the detectors, random coincidences or the resolving power of the source image reconstruction algorithm. Moreover, there are also inherent physical limits to the achievable image resolution, like the above-mentioned acollinearity or Compton scattering of

the 511 keV photons within the patient or biological sample or the diffusion range of the positron before its annihilation, presenting the dominant limitation in small-animal PET imaging.
Besides the achievable spatial source reconstruction resolution, also the applied radioactive dose to the patient or sample, as well as the corresponding examination time, has to be taken into account when discussing medical imaging techniques. The applied radioactivity typically used in human PET studies is tracer specific and ranges from about 185 to 1850 MBq [113], while in small-animal PET even higher activities are applied. A typical human PET examination using the radioisotope ^{18}F takes 10-45 minutes, depending on scanner, tumor and image reconstruction method. While on the one hand such long examination times limit the number of patients' access to PET devices, they are prohibitive for real-time metabolism studies, due to, e.g., organ movements. Therefore, this study was motivated not only by aiming at an improved spatial resolution for PET examinations, but, perhaps even more attractive, by targeting a higher sensitivity via a lower reconstruction statistics required per voxel of the examination volume. Moreover, the technique described in the following also bears the potential to be applicable for ion beam range monitoring in hadron therapy [13, 8], exploiting the online generation of β^+ emitting isotopes.

4.4 γ-PET

After introducing the Compton camera and PET as imaging techniques, a combination of both concepts will be described. This 'γ-PET'-method combines the performance of a Compton camera with the additional ability to detect a line of response (LOR), defined by the two 511 keV annihilation photons from a β^+ decay.

4.4.1 Decay properties of PET isotopes

Table 4.3 compares the decay properties of various presently used or potential future PET radioisotopes.
The two isotopes ^{10}C and ^{14}O have been included here, despite of their short halflives of 19.3 s and 70.6 s, respectively, since both can be produced during hadron therapeutic irradiations using a carbon or proton beam [51, 52]. Thus they qualify as candidates for online ion-beam range monitoring during therapy treatment. Moreover, proposals have been presented to directly use positron emitter beams, such as ^{11}C [53, 54, 55], ^{10}C [56] or ^{15}O [57] as therapeutic beams, allowing for fast online ion-beam range verification. In Tab. 4.3, in particular the positron diffusion range in water has been simulated with Geant4 (last column) and benchmarked against measured values (column 6), showing good agreement. Geant4 (9.4) was used with the QGSP-BIC-HP physics list for hadronic interactions and the Livermore physics list for electromagnetic interactions [116]. In case of the positron range simulations, the detector was placed as close as possible to a water sphere of 6 cm diameter, thus ensuring to be in the regime where diffusion of the positron prior to its annihilation is the dominant factor for the position resolution, like in small-animal PET devices. ^{22}Na is the only non-medical radioisotope listed in Tab. 4.3, due to

Isotope	Decay mode	$E_{e^+}^{max}$ [MeV] [114]	I_β [%] [114]	E_γ [MeV] [114]	Mean range in water [mm] (experiment, [115])	Mean range in water [mm] (simulation, this work)
^{22}Na	$\beta^+ + \gamma$	0.54	100	1.27		1.5 ± 0.1
^{18}F	β^+	0.63	96.7		1.4	1.4 ± 0.1
^{94}Tc	$\beta^+ + \gamma$	0.81/1.83	10.5/70.8	0.87		1.4 ± 0.1
^{11}C	β^+	0.96	99.8		1.7	1.8 ± 0.1
^{13}N	β^+	1.20	100		2.0	1.9 ± 0.1
^{44}Sc	$\beta^+ + \gamma$	1.47	94.3	1.16		2.1 ± 0.1
^{15}O	β^+	1.73	99.9		2.7	2.6 ± 0.1
^{14}O	$\beta^+ + \gamma$	1.81	99.2	2.31		2.6 ± 0.1
^{68}Ga	$\beta^+ + \gamma$	1.90	88.0	1.08		2.7 ± 0.1
^{124}I	$\beta^+ + \gamma$	1.53/2.14	11.7/10.8	0.60		2.9 ± 0.1
^{10}C	$\beta^+ + \gamma$	2.93	98.5	0.72		2.6 ± 0.1
^{152}Tb	$\beta^+ + \gamma$	2.62/2.97	5.5/6.2	0.34		3.6 ± 0.1
^{86}Y	$\beta^+ + \gamma$	1.22/1.55/ 1.99/3.14	11.9/5.6 3.6/2.0	1.08		2.3 ± 0.1
^{76}Br	$\beta^+ + \gamma$	0.87/0.99 3.38/3.94	6.3/5.2 25.8/6.0	0.56		4.1 ± 0.1
^{82}Rb	$\beta^+ + \gamma$	4.39	100	0.78		4.9 ± 0.1

Table 4.3: Decay properties of presently used or potential future PET isotopes. The positron diffusion range has been simulated with Geant4 (last column) and compared to experimentally measured values, where available.

its use in our laboratory as test source for the later-on discussed γ-PET technique.

4.4.2 The γ-PET imaging technique

The novel γ-PET imaging technique presented here draws on specific e^+ sources, simultaneously emitting an additional photon with the β^+ decay from the deexcitation of the daughter nucleus. Exploiting the triple coincidence between the positron annihilation and the additionally emitted photon, it is possible to efficiently separate the reconstructed true events from background [112, 117]. Therefore, the image reconstruction sensitivity can be significantly increased by an improved signal-to-noise ratio, achieved via exploiting the spatial and temporal coincidence with the additionally emitted photon. Radioisotopes like $^{94(m)}$Tc, ^{67}Br, ^{124}I, ^{86}Y, ^{152}Tb, ^{52}Mn, ^{82}Rb and ^{44}Sc are suitable candidates for the γ-PET technique (see Tab. 4.3 for details). Especially ^{44}Sc is of interest, which β^+-decays into the stable ^{44}Ca, emitting an 1157 keV photon. It has already been tested clinically [118]. With a short half-life of 3.9 h, it has to be produced from a ^{44}Ti generator ($t_{1/2}$ = 60.4 a) [119], which presently cannot be performed in clinically relevant quantities. However, this may change with the soon expected availability of highly brilliant γ beams [117]. Due

to the kinematics of the Compton scattering process and subsequent photon absorption, a Compton camera allows for reconstructing the origin of a primary photon on the surface of the Compton cone. Superimposing different cones from different events reduces the reconstructed source distribution in 3 dimensions to the few-millimeter range [25]. The γ-PET technique is different, as it will intersect the Compton cone with the line of response (LOR) from the same β^+ annihilation γ coincidence event, thus allowing to reconstruct the source distribution in 3 dimensions from individual events. The principle of the γ-PET technique can be seen in Fig. 4.8.

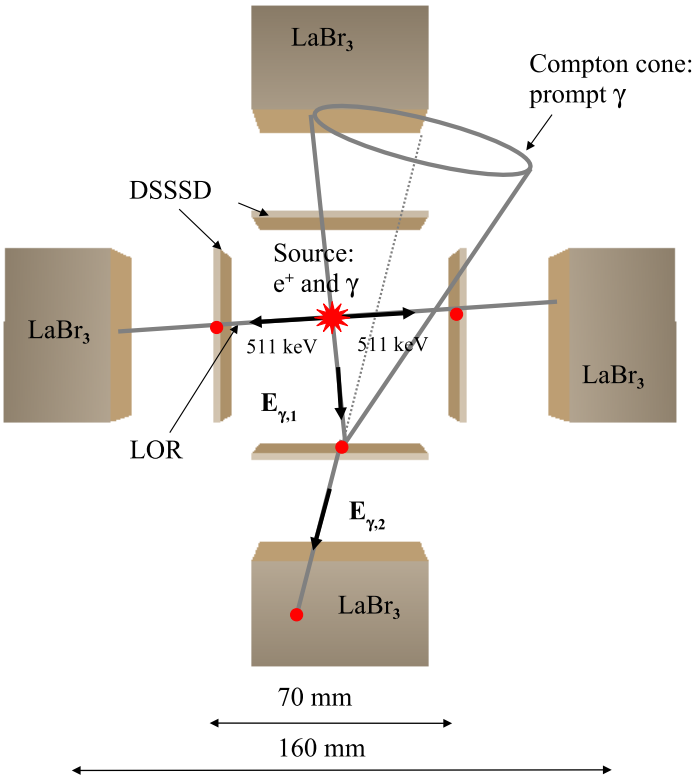

Figure 4.8: Principle of the γ-PET technique. The decay of certain radioisotopes produces a positron and a γ ray quasi-simultaneously. The emitted γ ray will first be scattered in a double-sided silicon strip detector (DSSSD), where the position and energy deposition of the interaction is measured. Then the prompt γ ray will subsequently be absorbed in a $LaBr_3$ scintillator, where again position and energy are measured. Due to the Compton kinematics, the γ-ray origin can then be restricted to a cone surface. The e^+ annihilation into two back-to-back 511 keV photons defines the line of response (LOR).

The emitted γ ray will first be Compton scattered in a position-sensitive double-sided silicon strip detector (DSSSD). Subsequently, the γ ray will be absorbed in a position-sensitive $LaBr_3$ scintillator, again measuring position and energy of this final interaction. The e^+ annihilation into two (almost) back-to-back 511 keV photons defines the LOR. The intersection of the Compton cone with the LOR restricts the source origin in 3 di-

mensions within one $\beta^+\gamma$ coincidence event. Figure 4.8 displays the schematical geometry of a γ-PET setup as used in our simulations (for results see Sect. 5.3), consisting of four Compton cameras, placed around a β^+ source isotope emitting a positron and a prompt γ ray. The intersection of the Compton cone and the LOR strongly suppresses background and restricts the reconstructed events to those belonging to the same $\beta^+\gamma$ coincidence event, originating from a volume defined by the displacement between the positions of the β^+ decay and the positron annihilation, depending on the time resolution of the detector system. In contrast to the restriction of the photon emission volume, the acollinearity effect cannot be removed by the γ-PET technique. Also Compton scattering of the 511 keV photons within the patient limits the performance. A further improvement of the γ-PET technique (so far not implemented in our reconstruction code) would take attenuation and scatter corrections of the annihilation photons, defining the LOR, into account [120, 121] (while scattering effects have been correctly simulated).

Chapter 5

Simulation of design specifications and performance of a Compton camera

This section is describing simulations that were performed in order to determine the design specifications and the performance of a Compton Camera and the feasibility of the γ-PET technique. Monte-Carlo simulations and image reconstruction have been performed using the 'Medium Energy Gamma-Ray Astronomy' library MEGAlib [89].

5.1 MEGAlib as simulation tool

MEGAlib is a software framework designed to simulate and analyze data from Compton cameras. The library consists of a Monte-Carlo (MC) simulation package, which utilizes the ROOT and Geant4 (9.4) software library, an event reconstruction and an image reconstruction section based on a list-mode maximum likelihood expectation maximization algorithm (LM-ML-EM) [26]. This algorithm is an iterative method to reconstruct the most probable γ-source distribution. For the requirements of the γ-PET technique, MEGAlib has been modified to realize an event reconstruction from the intersection between the Compton cone of the third, prompt photon and the LOR from the positron annihilation. The modifications are documented in the Appendix E. Subsequently, after successful event reconstruction, this information serves as starting point for an iterative image reconstruction of the γ-source positions.
Fig. 5.1 shows the basic layout of the MEGAlib software package, which consists of different modules with over 300000 lines of C++ source code in total. MEGAlib offers the two possibilities either to analyze real data measured with a Compton camera system or to analyze data originating from the MC simulation package "Cosima", which utilizes Geant4. The event reconstruction part is provided by the Revan library, which analyzes the individual hits, finds Compton scattering events with or without Compton electron tracks or pair creation events, even with time-of-flight suppression. The Mimrec library performs a high-level data analysis, this implies an event selection of all performance-relevant parameters of Compton camera systems, and a back-projected reconstruction of an image, based on a list-mode maximum likelihood expectation maximization algorithm. Additionally, a general Compton camera system analysis for angular resolution,

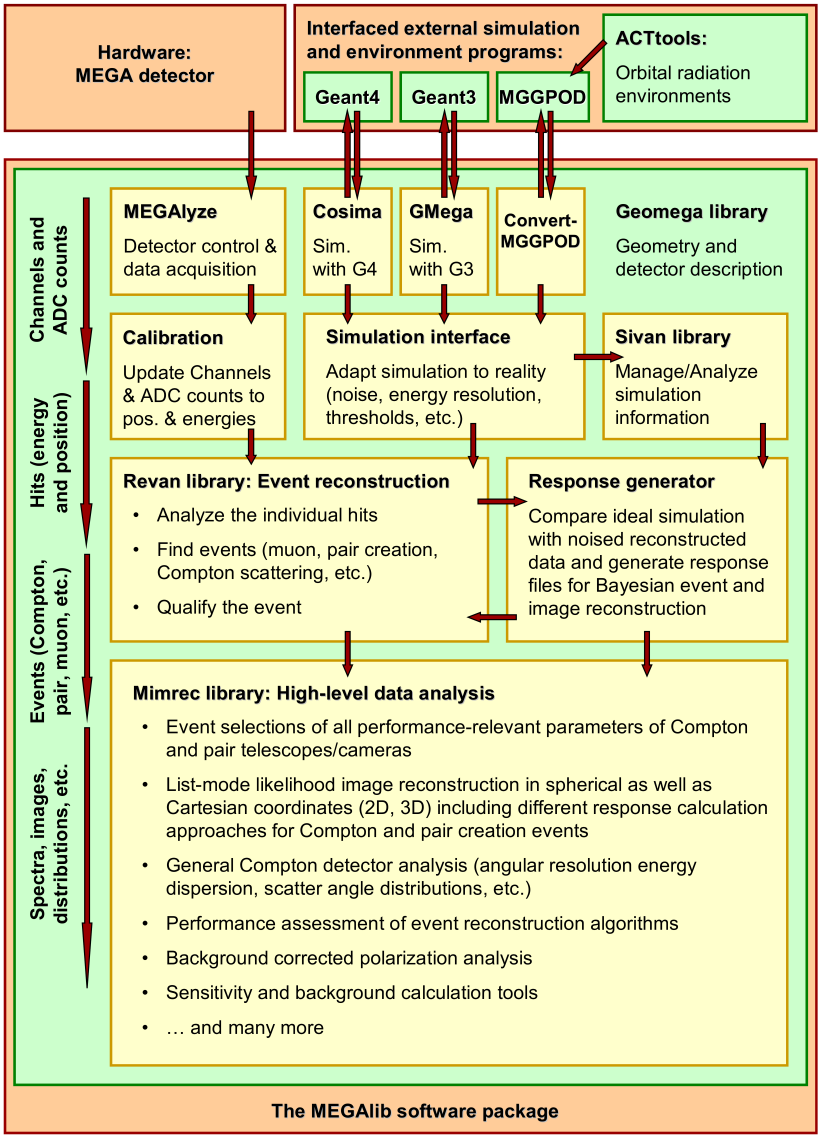

Figure 5.1: Overview of the various components of the MEGAlib software package for simulation and image reconstruction of Compton camera data [26]. MEGAlib offers the two possibilities either to analyze measured data or to analyze data originating from MC simulations. The event reconstruction (e.g. Compton event) is performed by the Revan library, the image reconstruction and high level analysis is performed by the Mimrec library.

energy dispersion or scattering angle distribution, etc., is included. For a detailed description of the MEGAlib software package, the reader is referred to the dissertation of A. Zoglauer [26].

5.1.1 The List-Mode Maximum-Likelihood Expectation-Maximization (LM-ML-EM) algorithm

The imaging algorithm implemented in MEGAlib is the List-Mode Maximum-Likelihood Expectation-Maximization (LM-ML-EM). Only a short introduction and the basic functioning of the algorithm will be given here, since a precise explanation, especially on the implementation in MEGAlib, can be found in [122].
For the image reconstruction, the so-called inverse problem has to be solved, meaning that from the knowledge of the effects (measured events), the cause (γ-source activity distribution) has to be inferred (Fig. 5.2). Given a certain cause C_j, the probability of observing a particular event E_i is called conditional probability $P(E_i \mid C_j)$.

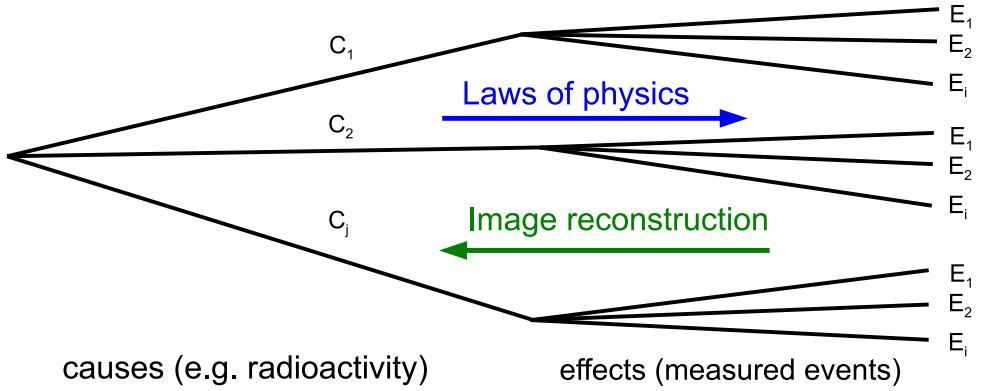

Figure 5.2: Sketch of the "inverse problem". From the knowledge of the effects (measured events), which are driven by the laws of physics, the causes (e.g. γ-source activity distribution) have to be inferred for image reconstruction. Given a certain cause C_j, the probability of observing a particular event E_i is called conditional probability $P(E_i \mid C_j)$.

The inverse problem is a general framework, which can as well be used for image reconstruction of γ-activity distributions. Where the causes C_j would be, e.g. in case of PET, the accumulated activity in a voxel j, and the events E_i the number of detected LORs.
To reconstruct the image J (Fig. 5.3), meaning the origin of the photons, the likelihood function $\mathcal{L}$ has to be found, which describes the probability that the individual measurements $E = \{E_i\}$ have been generated by the image J with the emissions $C = \{C_j\}$.

$$\mathcal{L}(C) = \prod_i P(E_i, C) \tag{5.1}$$

The radioactive decay events are independent from each other (besides of a few exceptions such as decay cascades) and showing therefore a Poisson nature, meaning that the occurrence of any event has no effect on the occurrence of any other event. For this reason, the Poisson probability density can be calculated:

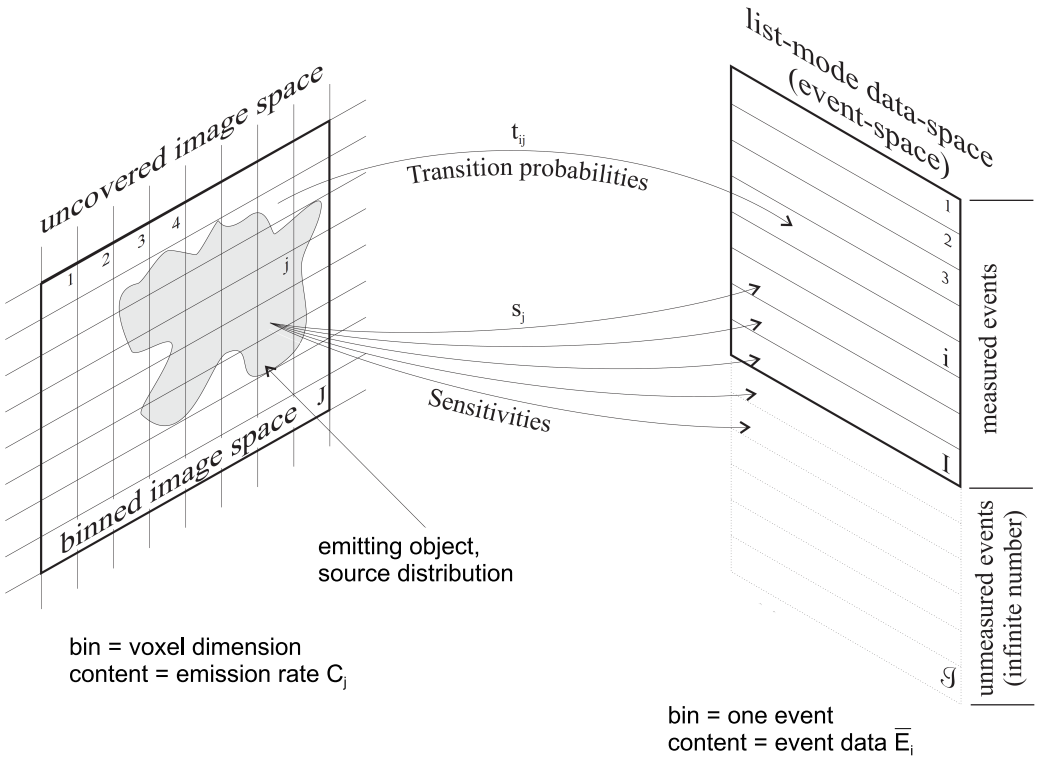

Figure 5.3: The data space and their relations, where I is the data space with all measured events, $\mathcal{I}$ is the data space of all not measured events, i is the event index, J is the image space, j is the image-bin index, C_i^l is the image-bin content at iteration level l, v_i is the "visibility", meaning the probability that the event i came from within the image-space, t_{ij} is the response matrix or transition matrix, which shows the probability of a photon emitted from the image space bin j that is measured with the parameters of event i, and s_j is the sensitivity, which is the probability that an event emitted from j is measured [26].

$$\mathcal{L}(C) = \prod_i P(E_i, C) = \prod_i \frac{\bar{E}_i^{N_i} e^{-\bar{E}_i}}{N_i!} \tag{5.2}$$

with $\bar{E}_i$ as the expectation of the Poisson distribution and N_i as the number of entries in data space bin i. In logarithmic description:

$$ln\ \mathcal{L}(C) = \sum_i \left[-\bar{E}_i + N_i\ ln\ \bar{E}_i - ln\ N_i!\right] \tag{5.3}$$

The $(-ln\ N_i!)$ term does not depend on C_j, therefore it can be neglected. The log-likelihood function has one maximum, the mathematical derivation can be found in [123]. To find now the highest probability of the source distribution, respectively the image J, the maximum of the likelihood function has to be found:

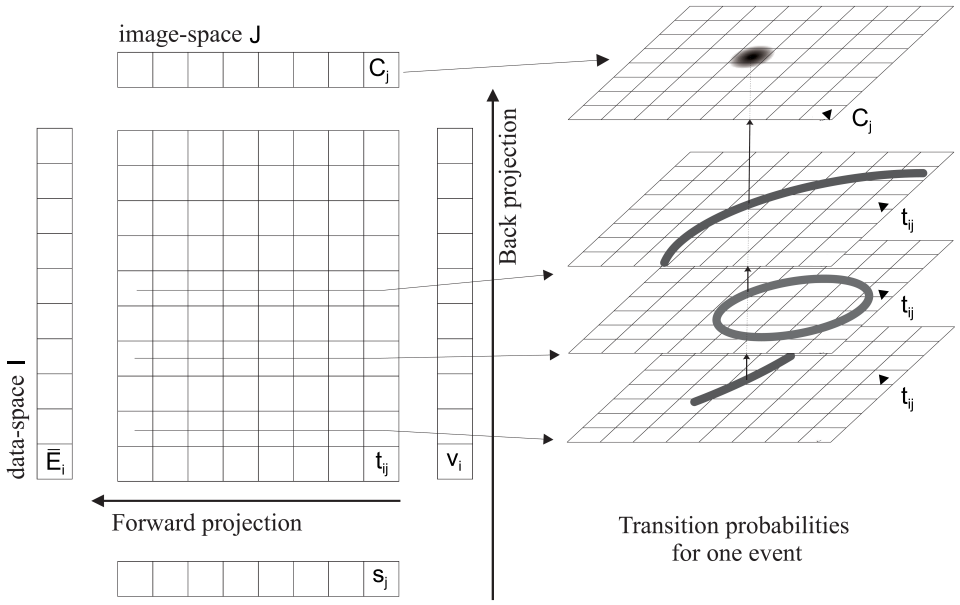

Forward projection (calculate expectation):

$$\bar{E}_i = \sum_k t_{ik} C_k$$

Back projection (maximization of expectation):

$$C_j^{(l-1)} = \frac{C_j^{(l)}}{s_j} \sum_i \frac{v_i t_{ij}}{\bar{E}_i}$$

Figure 5.4: The sketch is showing how the ML-EM algorithm is applied in MEGAlib. The algorithm is using five matrices: A matrix for the image C_j, a second matrix for the response of the individual events t_{ij} (so-called response matrix or transition matrix), a third matrix for the efficiency s_j, a fourth matrix for the expected data space content $\bar{E}_i$ and a fifth matrix for the Compton events, the visibility v_i. Each bin in the row of the response matrix t_{ij} represents the probability, that the event originates from the the given bin. "In a visual representation, Compton cones and arcs would appear. The iterative algorithm maximizes the expectation in two steps. First, given the current estimate of the image C_j and the response t_{ij}, the expectation that this event is measured, $\bar{E}_i$, is calculated. This step basically is a forward projection from image into data space. The second step maximizes the expectation and corrects the old image. This step is basically a backprojection from data into image space" [26].

$$\frac{\partial ln\ \mathcal{L}}{\partial C_i} = 0 \tag{5.4}$$

Solving this equation is not possible in the general case, therefore Lange and Carson suggested 1984 to maximize the expectation of the likelihood function instead, by reconstructing the image J with an iterative algorithm they derived [123]. Wilderman transformed this algorithm 1998 for medical imaging into list-mode [124]:

$$C_i^{(l+1)} = \frac{C_j^{(l)}}{s_j} \sum_i^l \frac{v_i\ t_{ij}}{\sum_k t_{ik}\ C_k} \qquad \forall j \in J \tag{5.5}$$

An explanation and derivation of the algorithm can be found in [122]. A sketch of the implementation of the algorithm in MEGAlib can be seen in Fig. 5.4. The algorithm developed by Wilderman did not contain any criteria to stop the iterations, and simply converges asymptotically. Therefore for obtaining the best reconstructed image, the iterations have to be stopped by hand, when the width of a reconstructed point source corresponds to the intrinsic angular resolution of the detector [26].

5.2 Design specifications of a Compton Camera

Let us summarize the design specifications of a Compton Camera with the capability of electron tracking, which have been determined so far:
For the scattering part of the Compton camera we choose double-sided silicon strip detectors (DSSSDs), because silicon is the better scattering material, while Ge is advantageous as absorbing material (Sect. 2.1.1). Additionally, for selecting the proper material for the scatter component of a Compton camera, the Doppler broadening has to be considered, which is limiting the spatial resolution of a Compton camera. Silicon provides a smaller Doppler broadening of 0.4° at 1 MeV, compared to Ge with 0.65° at 1 MeV. Furthermore, semiconductors, like DSSSDs, offer the great advantage that the interaction of an incident photon or charged particle is locally confined to a small volume. This results directly in a high spatial sensitivity compared to scintillation detectors. And finally, DSSSDs allow to track the direction of the Compton recoil electron, provided that the initial photon energy is high enough and the silicon detector thickness is sufficiently small to allow the electron to penetrate at least one detector layer. In general, microstructured silicon detectors provide a better energy resolution compared to scintillators, and can be operated at room temperature, in contrast to HPGe detectors (Sect. 4.1.2). For the absorbing part of the Compton camera, a scintillation detector has been chosen, because scintillators can be manufactured in larger volumes compared to semiconductors, thus enabling to efficiently absorb also energetic photons. In particular, $LaBr_3$ was selected for our Compton camera prototype due to the unique properties of this material: it exhibits a rather high density ($\rho_{\mathrm{LaBr_3}} = 5.29$ g/cm^3) and thus high detection efficiency (see Sect. 4.1.1) and provides both excellent energy and time resolution. The latter is especially promising to allow for suppressing background originating from neutrons occurring in hadron therapy irradiations, applying the time-of-flight technique (Sect. 3.1).

5.2.1 Optimization for multi-MeV photon detection

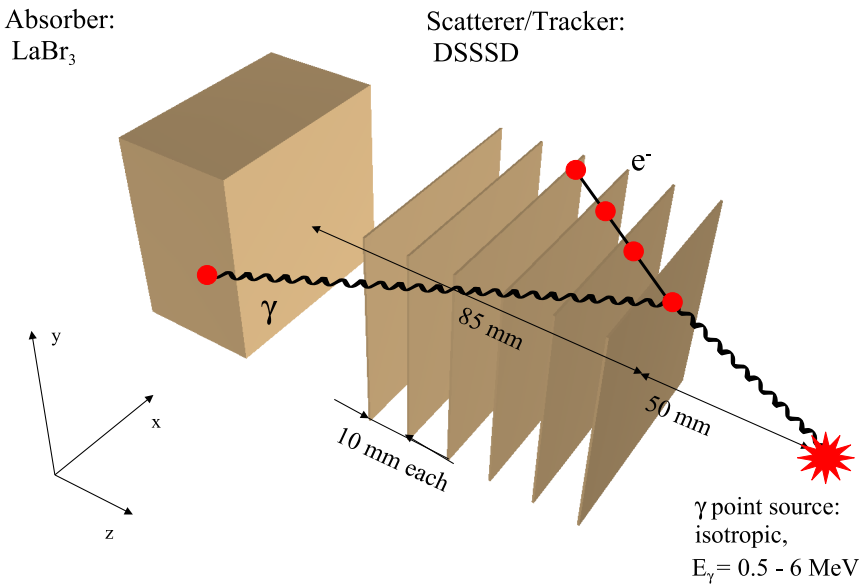

Figure 5.5: 3D view of the simulated Compton camera geometry, as optimized for the tracking of energetic (multi-MeV) photons. It consists of 6 DSSSDs, acting as scatter and Compton electron tracker (each with 10 mm distance), and a $LaBr_3$ scintillator, acting as absorber. The volume of the scintillator crystal amounts to 50 x 50 x 30 mm^3, while two different thicknesses of the DSSSDs (active area: 50 x 50 mm^2) have been simulated for comparison: 300 μm and 500 μm. In front of the detector system, a γ point source has been placed in a distance of 50 mm to the first Si detector, isotropically emitting photons with adjustable energies of E_γ = 0.5 - 6 MeV.

Fig. 5.5 shows a 3D view of the simulated Compton camera geometry, as optimized for the tracking of energetic (multi-MeV) photons, additionally allowing to track the Compton recoil electron. 6 DSSSDs acting as scatter detectors and Compton electron tracker. The distance of the $LaBr_3$ scintillator (acting as absorber) to the DSSSDs has been optimized to find a compromise between the detection efficiency of the Compton camera and the reconstructed image quality. Ideally, the distance between the photon source and the scatter position as well as between the scatter and absorption positions should be equal, since spatially measured uncertainties of the Compton interactions translate directly into spatial uncertainties of the reconstructed image analogue to a mechanical lever arm magnifying uncertainties. For tracking the electrons efficiently, a distance of 10 mm between each DSSSD was chosen. This distance is a compromise between typical Compton electron recoil angles and geometrical constraints from the detector mounting. In front of the de-

tector system, a γ point source was placed, isotropically emitting photons with adjustable energies E_γ = 0.5 - 6 MeV. The distance in z direction between the absorber surface and the first DSSSD was 85 mm, while the first DSSSD was placed in a distance of 50 mm to the γ source (corresponding to the situation of a small animal irradiation as envisaged in our Garching laser particle acceleration facility). This results in an equal distance of 75 mm from the center of the 6-fold scattering stack to the center of the absorber, as from the Si array center to the γ source, respectively. A scintillator crystal thickness of 30 mm was chosen, while two different thicknesses of 300 μm and 500 μm of the DSSSDs have been investigated in more detail. Also the response of the Compton camera for two different spatial resolutions of the absorbing $LaBr_3$ scintillator crystal (50 x 50 x 30 mm^3), with 64 pixels (6 x 6 mm^2 each) or 256 pixels (3 x 3 mm^2 each), as achievable with the readout via a multi-anode PMT has been explored during the simulations. An energy threshold of 10 keV (i.e. exceeding the electronic noise level) and an energy-dependent energy resolution were applied. The DSSSDs have 128 strips on each side and an active area of 50 x 50 mm^2. The pitch size of 390 μm, correspondingly, leads to a spatial resolution of 390 μm (FWHM). An energy resolution of 10 keV (FWHM) and a detection threshold of 10 keV was chosen in the Monte-Carlo simulations (due to the assumed electronic noise level of the DSSSD).

Spatial resolution

The spatial resolution, or more precise, the angular resolution of a Compton camera can be described by the angular resolution measure (ARM) as defined in [26], as

$$\Delta\varphi_{ARM} = \arccos(\vec{e_i} \cdot \vec{e_s}) - \theta \tag{5.6}$$

The distribution $\Delta\varphi_{ARM}$ can be determined by the directions of the known origin of the incoming photon $\vec{e_i}$ and the measured Compton-scattered γ-ray directional vector $\vec{e_s}$ and the Compton scattering angle θ (which can be calculated from the Compton formula according to Eq. (2.5)). The width of the distribution $\Delta\varphi_{ARM}$ is mainly influenced by the energy and position measurements in the scatter and absorber detector, negative values of $\Delta\varphi_{ARM}$ indicate incompletely absorbed Compton scattered photons, while the tail towards positive values of $\Delta\varphi_{ARM}$ corresponds to incompletely absorbed recoil electrons [26].

Two exemplary ARM distributions for γ energies of 2 MeV and 4 MeV, respectively, obtained with MEGAlib, are shown in Fig. 5.6. The fit function (as implemented in MEGAlib), consists of a Gaussian combined with Lorentzian tails [26]. For E_γ = 2 MeV and 4 MeV a width of 2.1° (FWHM) and 2.0° (FWHM), respectively, is obtained. The $\Delta\varphi_{ARM}$ distributions have been determined with the Compton camera geometry of Fig. 5.5, with a thickness of the DSSSD scatterer of 500 μm and a pixelation of 256 for the $LaBr_3$ absorber. These exemplary γ energies have been chosen, because the corresponding $\Delta\varphi_{ARM}$ distributions exhibit a similar width, however, for E_γ = 4 MeV already a strong contribution of a tail towards positive $\Delta\varphi_{ARM}$ values appear, indicating incompletely absorbed recoil electrons.

Further results of the investigation of the angular resolution can be seen in Fig. 5.7. The γ source energy as been adjusted to 7 different energies between 0.5 and 6 MeV and the

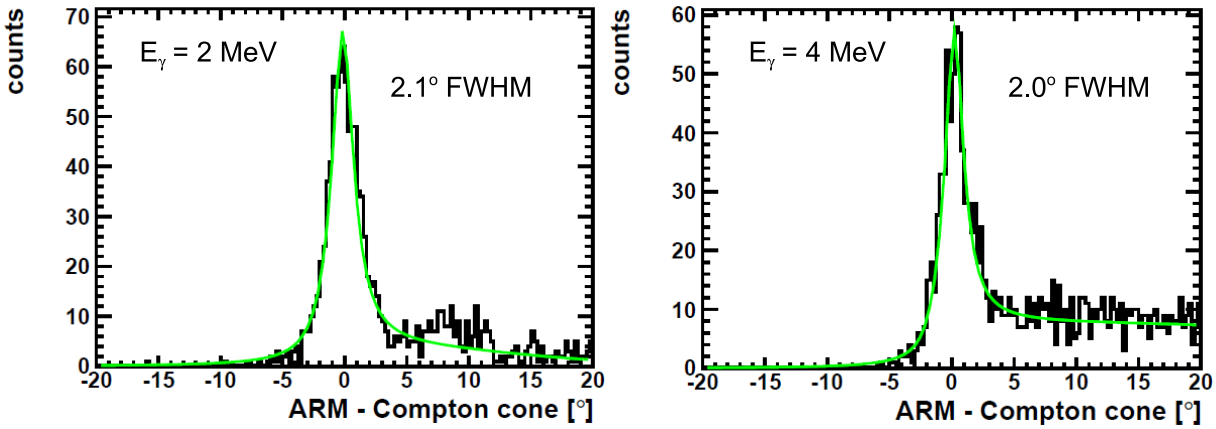

Figure 5.6: Exemplary Angular Resolution Measure (ARM) distribution for two γ energies of 2 MeV and 4 MeV. The width of 2.1° (FWHM) and 2.0° (FWHM), respectively, has been determined by a fit using a function consisting of a combination of a Lorentz and a Gaussian component, as implemented in MEGAlib.

image reconstruction was based on the photon detection only representing ('γ tracking'). Four curves are plotted, representing two different thicknesses of the DSSSD scatterer/-tracker (300 μm and 500 μm) and two different spatial resolutions of the $LaBr_3$ scintillator (6 x 6 mm^2 and 3 x 3 mm^2, corresponding to a multi-anode PMT readout via 64 pixel and 256 pixel, respectively). The y axis on the right-hand side indicates the corresponding spatial resolution of the Compton camera for a γ source distance of 50 mm to the first scatterer/tracker (as envisaged for our planned small-animal irradiation scenario). While the different thicknesses of the DSSSDs reveal no significant impact on the spatial resolution of the Compton camera, quadrupling the pixelation results in an improvement of the spatial resolution by about 40%. In proton-induced hadron therapy, the prompt γ emission from nuclear reactions exhibits dominant transitions in the energy range of 4-6 MeV (compare Fig. 3.1). The angular resolution of the Compton camera in this energy region is expected to be $\approx$ 2.7°-3.7° (corresponding to a spatial resolution of about 2.5 - 3 mm for a source distance of 50 mm) in the case of a $LaBr_3$ scintillator with 64 pixel, and can reach $\approx$ 1.5° - 2.5° (spatial resolution $\approx$ 1.5 - 2 mm for 50 mm source distance) when using a fourfold higher segmentation with 256 pixel. The trend of the curves reveals an improving angular resolution with increasing photon energy up to about 3 MeV, where an optimum can be observed. This trend follows the improving energy resolution of the absorbing $LaBr_3$ scintillator as a function of the photon energy. At higher photon energies, the then increasing number of incompletely absorbed photons is limiting or even decreasing the angular resolution [26]. Figures B.1 - B.3 (Appendix B) show the corresponding simulated energy spectra as expected to be registered by the Compton camera geometry of Fig. 5.5 for the four different scenarios investigated in Fig. 5.7. Besides the Compton continuum and the single and double escape peaks appearing at higher energies, the photopeak is visible. It can be seen that the full absorption of the photopeak is strongly decreasing for higher photon energies. In case of a γ energy of 6 MeV, the peak

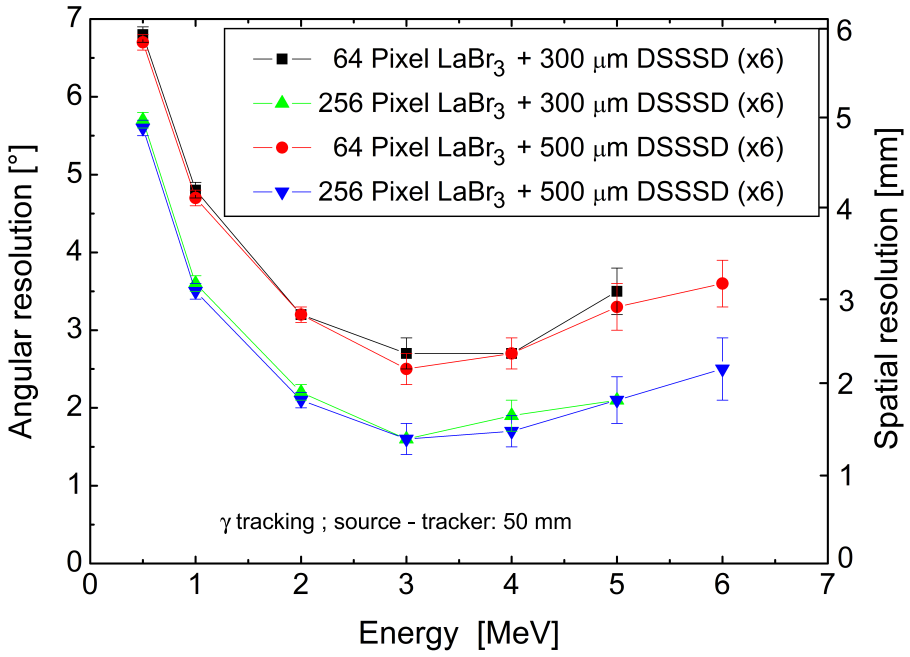

Figure 5.7: Angular resolution of the Compton camera (based on the geometry depicted in Fig. 5.5) for γ tracking only. The y axis on the right-hand side represents the corresponding spatial resolution for a distance of 50 mm between the γ source and the first tracking detector. The red and the black curves show the same trend, they correspond to a segmentation of the $LaBr_3$ absorber via multi-anode PMT readout of 6 x 6 mm^2 (64 pixel), while the green and the blue curves illustrate the situation for a segmentation of 3 x 3 mm^2 (256 pixel). In the interesting prompt γ energy range of 4 - 6 MeV (compare Fig. 3.1), the spatial resolution of the Compton camera is thus expected to be $\approx$ 2.5 - 3 mm in case of a $LaBr_3$ scintillator with 64 pixel, and can reach $\approx$ 1 - 2 mm in the case of 256 pixel. The different thicknesses of 300 μm and 500 μm of the 6 DSSSD scatter/tracker detectors do not affect the achievable spatial resolution.

has almost vanished, resulting in a very limited detection efficiency.

Photon source image reconstruction efficiency

In the following, the impact of the two simulated DSSSD scatter/tracker thicknesses on the photon source image reconstruction efficiency of the Compton camera will be investigated in detail together with the influence of an additional electron tracking capability. In Fig. 5.8, the image reconstruction efficiencies of the Compton camera for four different cases are plotted. The black and the red data show the reconstruction efficiencies for a setup with six 500 μm thick DSSSDs. The green and the blue data explore the efficiencies using six 300 μm thick DSSSDs, while the red and blue data points represent the reconstruction efficiency achievable with γ tracking only. The complementary black and green symbols belong to simulations, where the additional tracking of the Compton

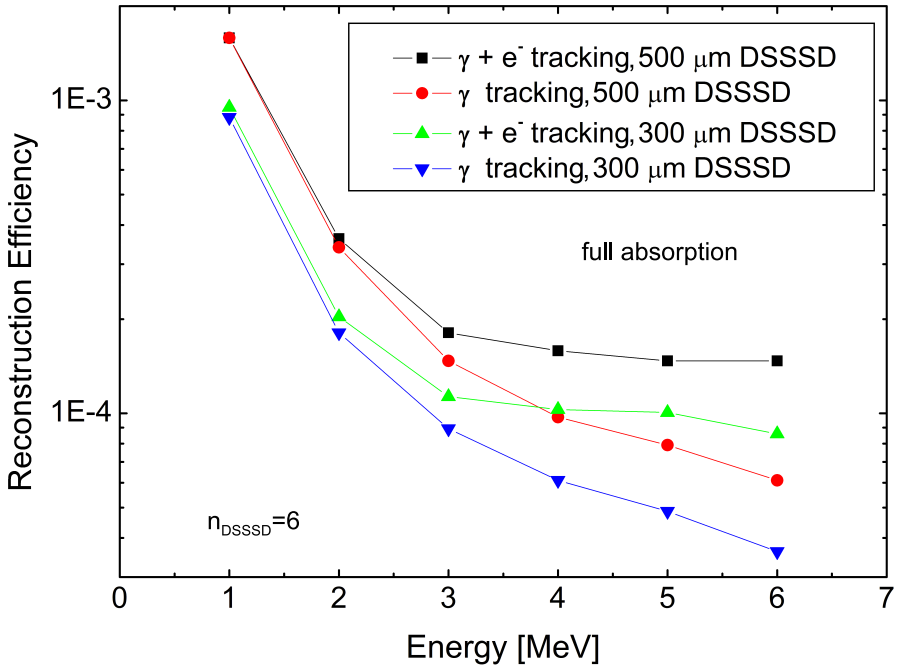

Figure 5.8: Simulated photon source image reconstruction efficiencies of the Compton camera.. The black and red data show the efficiency when using of six 500 μm thick DSSSD scatter/tracker detectors, while the green and blue data points correspond to a Compton camera using six 300 μm thick scatter detectors. Red and blue data represent an image reconstruction exploiting only the information from photon scattering ('γ tracking'), while the black and green data in addition make use of the information from the Compton scattered electron ('γ + electron tracking').

electron was exploited. Due to the larger scattering probability, a higher reconstruction efficiency is obtained for thicker scatter detectors, as can be seen in Fig. 5.8 up to photon energies of $\approx$ 4 MeV. Moreover, examining the trend of the black/red and blue/green data points clearly exhibits an enhanced reconstruction efficiency when electron tracking is applied. This enhancement increases as a function of the initial photon energy. Beyond $\approx$ 4 MeV, electron tracking even allows to achieve a higher reconstruction efficiency with the thinner (300 μm) scatter detectors compared to the thicker ones, operated only with γ tracking. The plotted efficiencies were obtained using an energy cut requiring full absorption of the photon energy. In this case, a maximum efficiency of $\approx 1.5 \cdot 10^{-4}$ in the energy range between 4 - 6 MeV can be obtained using 500 μm thick DSSSDs and an image reconstruction based on electron tracking.

The next two figures illustrate the tradeoff that can be achieved between optimizing the reconstruction efficiency or the angular resolution. In Fig. 5.9, two different sets of reconstruction efficiencies are plotted (based on 256 segments of the $LaBr_3$ absorber and a thickness of 500 μm for each of the DSSSD scatterer/tracker modules). The black curve shows the efficiency for an energy cut requiring full absorption of the photopeak energy plus electron tracking, while the red curve displays the efficiency without electron

tracking obtained by applying additional cuts to the accepted Compton angle (5 - 6 MeV: accepted Compton angle $\Theta = [1°; 90°]$), the maximum number of interaction points of the Compton scattering sequence (4 - 6 MeV: maximum of 3 hits). The red curve corresponds to Fig. 5.7.

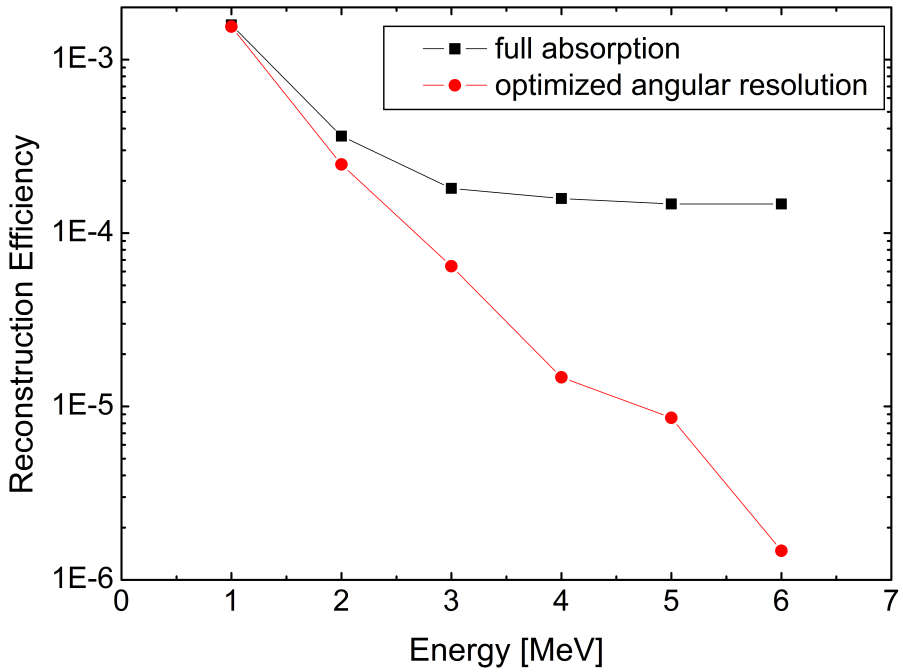

Figure 5.9: Simulated photon source reconstruction efficiencies of the Compton camera for two cases: full absorption of the photopeak energy (black curve) and additional cuts on the accepted Compton scattering angle and the maximum number of interaction points of the Compton scattering sequence for an optimized angular resolution (red curve).

Fig. 5.10 displays the angular resolution of the Compton camera. The black curve corresponds to the requirement of full absorption of the photon energy without electron tracking, while the red curve depicts the case with electron tracking and the additionally applied cuts mentioned above. It can be seen, that it is possible to obtain an angular resolution of 1.5° - 2.5° (spatial resolution $\approx$ 1.5 - 2 mm for 50 mm source distance) for a photon energy range of 4 - 6 MeV. For an optimized reconstruction efficiency (only requiring an energy cut on the photopeak energy) an angular resolution of 5° - 8° (spatial resolution $\approx$ 4.5 - 7 mm for 50 mm source distance) for the photon energy range of 4 - 6 MeV can be obtained.

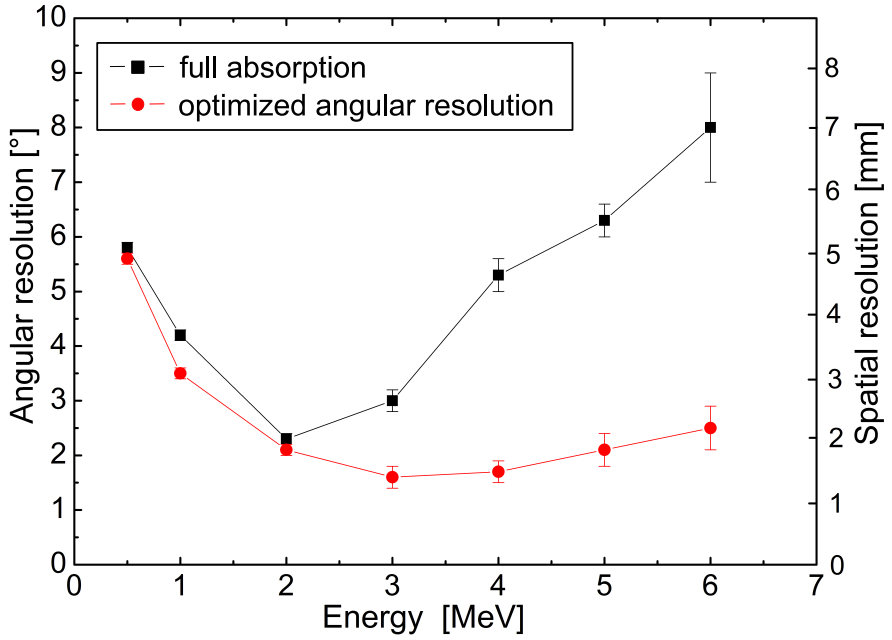

Figure 5.10: Angular and spatial resolution of the Compton camera geometry (Fig. 5.5) for two cases: full absorption of the photopeak (black curve) and additional cuts on the accepted Compton scattering angle and the maximum number of 6 interaction points of the Compton scattering sequence for an optimized angular resolution (red curve).

Image reconstruction

At the beginning of this chapter, the principle of the List-Mode Maximum Likelihood Expectation Maximization (LM-ML-EM) algorithm was introduced, here it will be applied to the reconstruction of photon sources. Results from a point source reconstruction in 0^{th} iteration in Cartesian coordinates are shown in Fig. 5.11. In the left column, intersections of Compton cones with the z = $\pm$ 1cm plane are displayed for the case of N_γ = 1, 2 and 10 reconstructed events, respectively. For one reconstructed event a ring appears in Cartesian coordinates, its width is determined in the 0^{th} iteration by a start parameter, which should be chosen reasonably by considering the expected angular resolution of the Compton camera geometry. However, too large values of the starting parameter just lead to longer calculation times of the ML-EM algorithm, while too small parameter values result in fragmented images. The angular resolution of the camera is not affected, its value is determined differently, see Sect. 5.2.1.

The right column shows the corresponding situation when allowing for additional electron tracking: the Compton cone is reduced to an arc segment. The more Compton cones/arcs of reconstructed events intersect with each other, the better the distribution of the photon source can be confined. It can be seen that already after few reconstructed Compton events the most probable source origin can be accurately determined. In the simulation, the photon source was placed at (0, 0, 0) in a distance of 50 mm from the first DSSSD

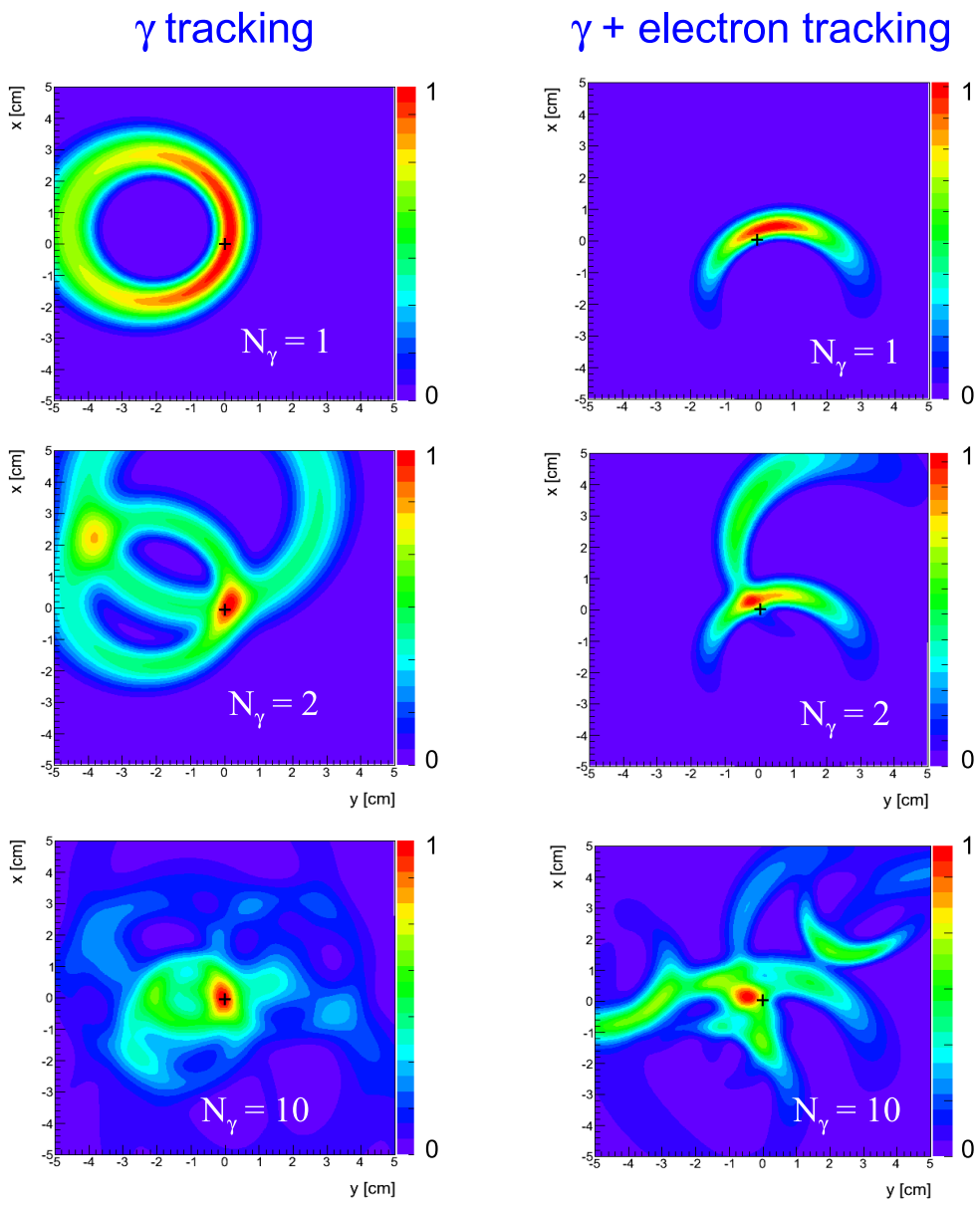

Figure 5.11: Reconstruction of the γ-ray source position determined with the Compton camera geometry of Fig. 5.5. The image reconstruction was performed using the LM-ML-EM algorithm in the 0^{th} iteration of the MEGAlib software package. Left column: reconstruction based solely on γ tracking. Right column: reconstruction including additional tracking of the Compton electron. Each scenario is shown for the case of 1, 2 and 10 reconstructed Compton events, respectively.

scatter detector. The centroid of the reconstructed image distribution typically shows a small offset from the simulated source position, which is < 0.5 mm, this behavior is documented in [26]. Fig. 5.12 shows two reconstructed source distributions (E_γ = 1 MeV and E_γ = 5 MeV) after 30 iterations of the LM-ML-EM algorithm, containing 30 Compton events. The projection onto the x axis shows a width of $\approx$ 0.26 mm (FWHM) for E_γ = 1 MeV and $\approx$ 0.12 mm (FWHM) for E_γ = 5 MeV, respectively, in agreement with the respective values for the ARM shown in Fig. 5.7. It should be clearly stated that the width of the reconstructed source distribution obtained by this iterative procedure is not a quantitative measure for the angular/spatial resolution of the Compton camera, since the iteration process has to be stopped by hand when reaching the expected ARM value for this energy.

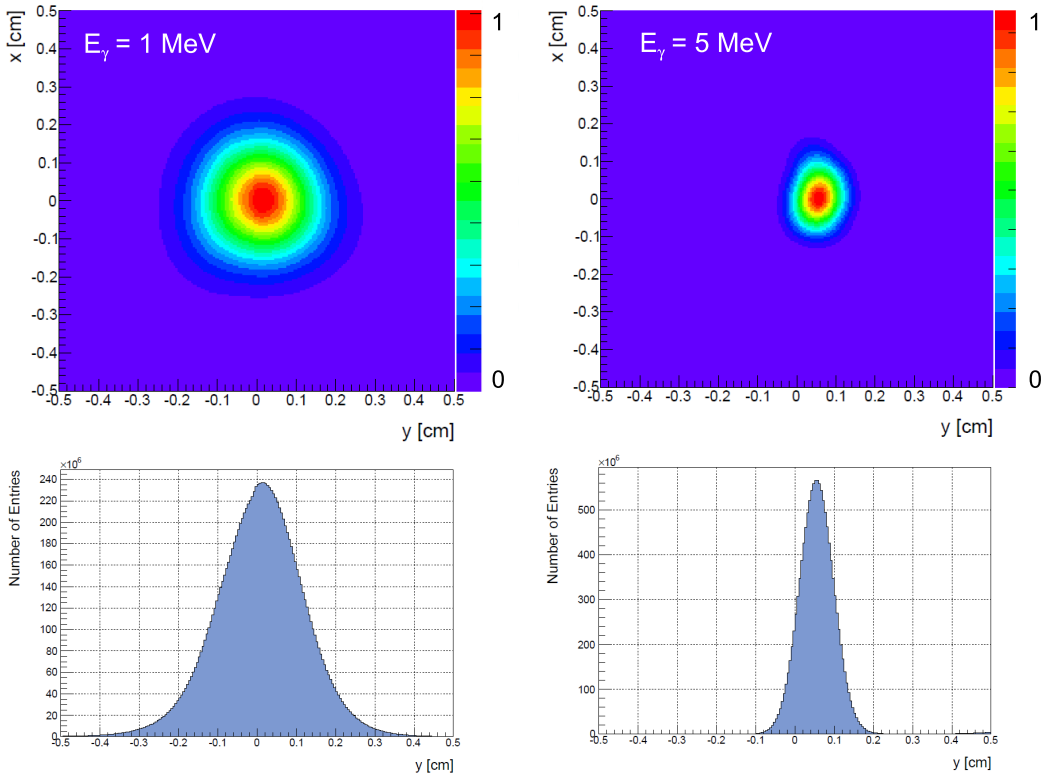

Figure 5.12: Top row: Reconstructed distribution of a photon point source after 30 iterations of the LM-ML-EM algorithm for E_γ = 1 MeV (left) and E_γ = 5 MeV (right). The distributions show the most probable origin of the photons (with the initial source position located at (0,0)). Bottom row: projections of the 2D-distributions onto the y axis. The distribution of the E_γ = 5 MeV photons is smaller, compared to the situation with E_γ = 1 MeV. The projections on the x axis exhibit a width of $\approx$ 0.12 mm (FWHM) and $\approx$ 0.26 mm (FWHM), respectively, in agreement with the respective values for the ARM in Fig. 5.7.

After several (here 30) iterations of the LM-ML-EM algorithm, the most probable origin

of the photon point source can be determined. The number of required iterations depends on the starting parameters and also on the number of reconstructed Compton events.

5.2.2 Optimization for low-energy photon detection

Motivated by the strong influence of the position resolution realized in the absorbing component of the Compton camera onto the angular resolution (as visible in Fig. 5.7), an alternative detector geometry has been investigated. In order to provide an improved spatial accuracy for detecting low energy γ rays, e.g. E_γ = 511 keV annihilation photons from β^+ decaying isotopes emitted during hadron therapy, a complementary solution for the absorber component was studied.

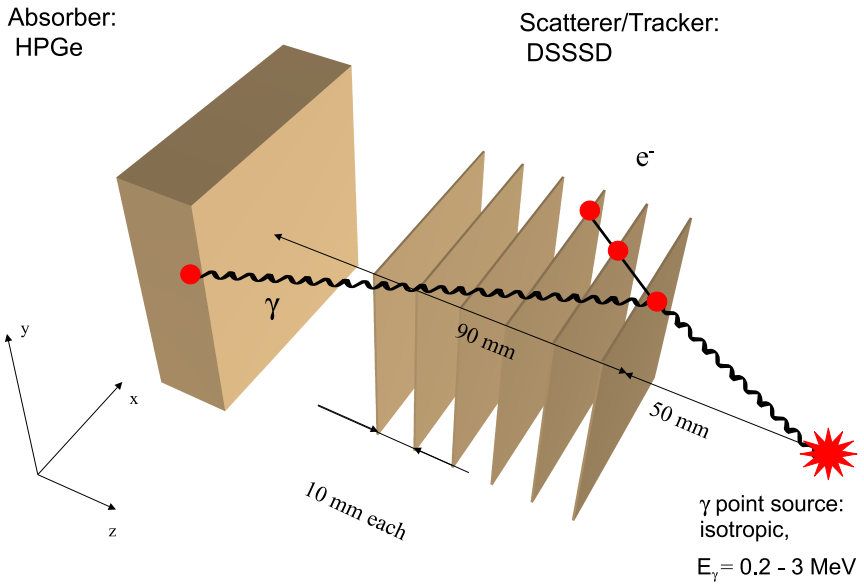

Figure 5.13: 3D view of an alternative Compton camera geometry. Compared to the Compton camera geometry of Fig. 5.5, the $LaBr_3$ absorber has been replaced by a 2D segmented planar high-purity Germanium detector (HPGe). The simulated geometry consists of six DSSSD modules with 500 μm thickness each, arranged in a tracker stack with 10 mm distance between adjacent detectors, and a 2D segmented planar Ge detector with an active volume of 64 x 64 x 20 mm^3, acting as absorber.

An 3D sketch of the alternative geometry, which has been simulated, can be seen in Fig. 5.13. The $LaBr_3$ scintillator, so far acting as absorber, has been replaced by a 2D segmented planar high-purity Germanium detector (HPGe). The active volume of the semiconductor amounts to 64 x 64 x 20 mm^3, segmented with 64 strips (width 1 mm) on the front and back side of the Ge block, resulting in a spatial resolution of 1 mm^2 for

the Compton camera absorber. Such a detector presently represents the limit of technical feasibility of 2D segmented planar Ge detectors. In addition, a spatial resolution in depth of 1 mm was included in the simulations, which could be realized via pulse shape analysis of the detector signals. An energy resolution of 2.4 keV has been assumed.

The same scatter detectors were used as included in the Compton camera geometry discussed before in Fig. 5.5. Their thickness was assumed to be 500 μm, arranged in a stack with 10 mm distance between the individual modules.

In Fig. 5.14, the resulting angular resolution of this alternative Compton camera geometry can be seen. For comparison, the results (brown data points) have been added to the data already shown in Fig. 5.7. While the alternative geometry without depth information of the absorber exhibits only a slightly improved angular resolution (dashed brown line) compared to the geometry of Fig. 5.5, additional depth information of the absorber would lead to a significantly improved resolution (solid brown line).

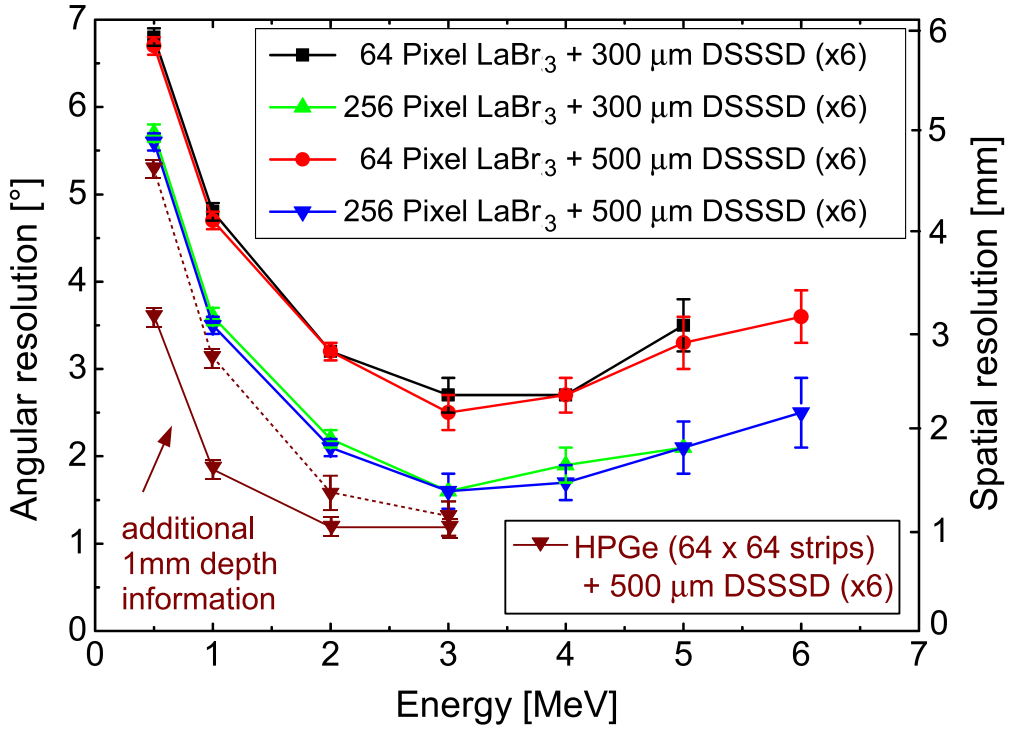

Figure 5.14: Angular resolution of the alternative Compton camera geometry based on a 2D planar germanium detector as Compton camera absorber. For comparison, the results have been added to the data shown in Fig. 5.7. While the alternative geometry without depth information of the absorber exhibits a slightly improved angular resolution (dashed brown line) compared to the geometry of Fig. 5.5, additional depth information of the absorber would lead to a significantly improved resolution (solid brown line). The drawback is the inferior efficiency of the thinner absorber, which limits the capability to reconstruct Compton cones to initial photon energies $\lesssim$ 3 MeV.

In the range of γ energies of 1 - 3 MeV, a resolution of $\approx$ 1.0° - 1.5° ($\approx$ 1.5 mm in 50 mm source distance) can be obtained. The 511 keV annihilation photons can be reconstructed down to an angular/spatial accuracy of 3.6° (3 mm), this is significantly more precise than achievable with the $LaBr_3$ absorber with a segmentation of 256 pixel ($\approx$ 5.5° ($\approx$ 5 mm in 50 mm source distance)). The simulation showed, that a higher spatial resolution of the Compton camera absorber of 1 mm^2 instead of 3x3 mm^2 only slightly improves the angular resolution obtainable with the Compton camera, while an additional depth information of the absorber would help to overcome the depth-of-information problem, originating from the unknown interaction point along z direction of the 30 mm (20 mm) thick absorber.

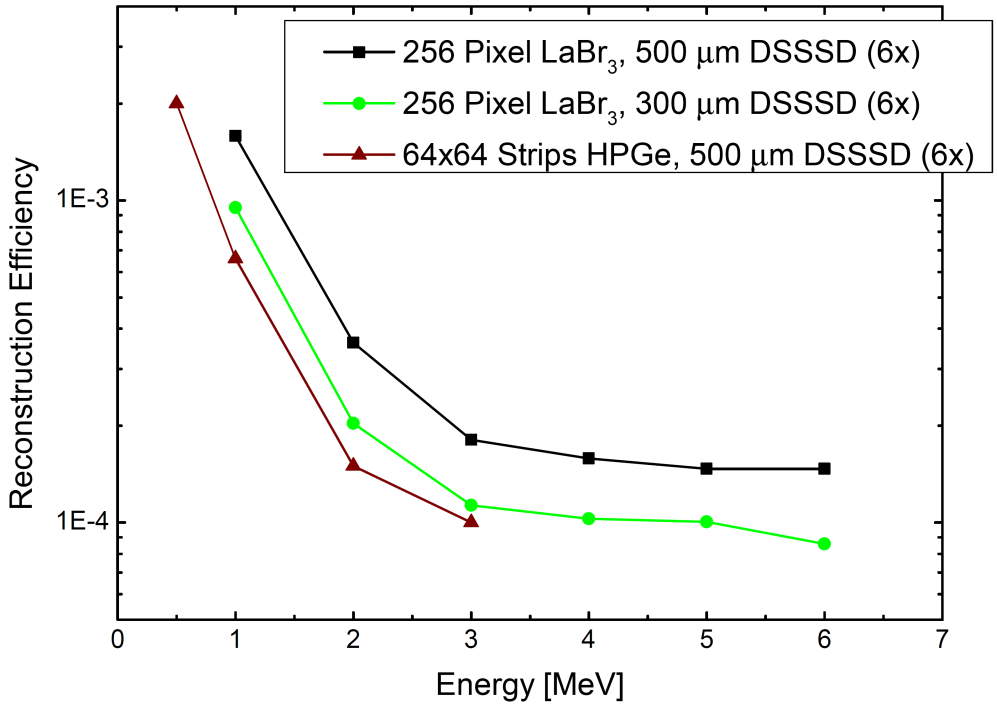

Figure 5.15: Reconstruction efficiency of the alternative Compton camera geometry (Fig. 5.13). For comparison, the results of the simulations with the $LaBr_3$ detector with 256 pixel has been added to the data (see Fig. 5.8). The alternative geometry with the 2D HPGe detector acting as absorber component exhibits a lower image reconstruction efficiency compared to the geometry with the $LaBr_3$ detector.

The corresponding image reconstruction efficiency is shown in Fig. 5.15. The Compton camera with the HPGe absorbing detector exhibits a lower reconstruction efficiency in the studied energy range below 3 MeV, compared to the detector system with a scintillator as absorber. Here it becomes obvious, that although an improvement of the image reconstruction performance can be expected from a finer segmentation of the absorber component, still the decisive feature is the photopeak detection efficiency. While the density of both studied absorber materials is almost equal (ρ_{Ge} = 5.33 g/cm^3, $\rho_{\mathrm{LaBr_3}}$ = 5.29

g/cm^3), the larger thickness of 30 mm ($LaBr_3$) compared to 20 mm (HPGe) finally decides on the superior efficiency of the scintillator-based Compton camera. Moreover, it should be mentioned that also from practical reasons the use of the 2D HPGe absorber poses some challenges, since this detector requires permanent cooling to liquid nitrogen temperature. Also a scaling to larger fields of view cannot be realized in an economically affordable way on the basis of such a detector.

5.3 Quantitative design considerations for realizing a γ-PET detector system

After showing the concept of the γ-PET technique in Sect. 4.4, followed by the design specifications of a Compton camera, quantitative design considerations for realizing a detector system that allows to apply the γ-PET technique will be described here. The basic element is a Compton camera, additionally the full system has to be capable to detect the 511 keV annihilation photons from β^+ decaying isotopes, where the daughter isotopes emit a third prompt photon from an excited state. The minimum configuration to fulfill this requirement would be three Compton camera modules, two of them placed at 180° to each other. In order to optimize the detection and reconstruction efficiency, an arrangement of 4 Compton camera modules in a cubic arrangement was studied, as already introduced in Fig 4.8.

5.3.1 Simulation of image reconstruction properties

For the requirements of the γ-PET technique, MEGAlib was modified to realize an event reconstruction from the intersection between the Compton cone and the LOR. A documentation of the modifications can be found in the Appendix E. In an upcoming new release of MEGAlib, these modifications will be included into the official version [125].
In Fig. 5.16, the image reconstruction of a γ-ray point source with the LM-ML-EM algorithm in 0^{th} iteration can be seen. For this sketch, extra long LORs have been drawn to illustrate the technique. In general, the thickness of the LOR is determined by the spatial resolution of the scatterer (here 0.390 μm (FWHM)), its length is determined by the thickness of the Compton cone ($\approx$ 1 cm). In case of a measurements with low statistics, the dimensions of the LOR can be adjusted to larger values, enabling the ML-EM algorithm to reconstruct an image of the most probable source distribution, while the spatial resolution of such an image will be reduced. The top left panel shows the principle of the intersection between the Compton cone and the LOR for one event ($N_{3\gamma}$ = 1), where two intersections (marked in red) will be created during the reconstruction process. Top right: Zoomed view of one of the two interactions between the LOR and the trajectory of the 3^{rd} prompt photon within one $\beta^+\gamma$ event ($N_{3\gamma}$ = 1). Bottom left: Superposition of the intersections from two $\beta^+\gamma$ events ($N_{3\gamma}$ = 2). Two $\beta^+\gamma$ events are already strongly confining the spatial source distribution. Bottom right: after only ten $\beta^+\gamma$ events ($N_{3\gamma}$ = 10), the origin of the photons is already well located.
Subsequently, after successful event reconstruction, this information serves as starting point for an iterative image reconstruction of the γ-source positions.
In order to characterize the spatial resolution of a PET scanner, a Derenzo phantom is commonly used [126]. Here a quasi-Derenzo phantom was simulated (see Fig. 5.17 for a sketch of the source geometry), consisting of twelve ^{22}Na point sources with 100 kBq activity each. Point sources were chosen for this exploratory study, while in a later stage it is foreseen to extend this to the realistic scenario of an extended source. Four equilateral triangles are arranged in four sections, containing 3 point sources each, with a separation of 0.2 mm, 0.4 mm, 0.6 mm and 0.8 mm, respectively. This source arrangement was placed

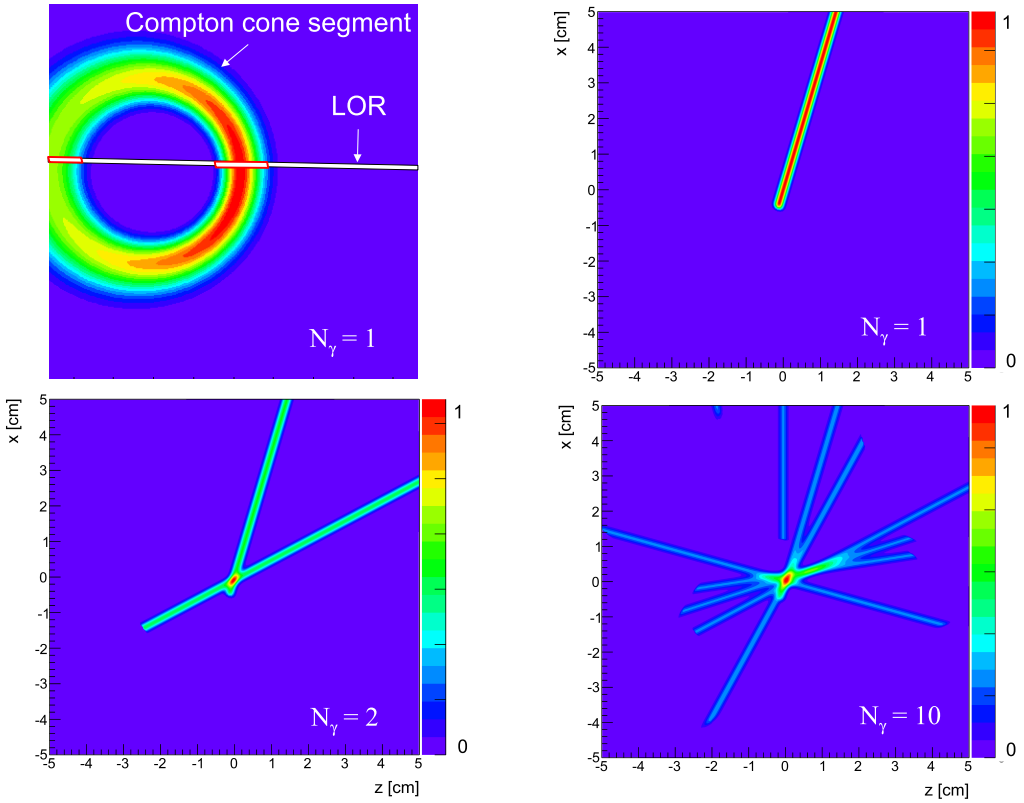

Figure 5.16: Reconstruction of the γ-ray source position determined with the γ-PET technique. The underlying detector geometry was introduced in Fig. 4.8. For this sketch extra long LORs have been drawn to illustrate the technique. The image reconstruction was performed using the modified version of the MEGAlib software package (see Appendix E), utilizing the LM-ML-EM algorithm in the 0^{th} iteration step.

inside a water sphere of 6 cm diameter to imitate a medical or biological sample and to take into account photon scattering effects in the sample during the source reconstruction. Each of the four Compton camera modules consists of a $LaBr_3$ scintillator crystal (50 x 50 x 30 mm^3), read out by a 2D-segmented photomultiplier with 64 pixels (6 x 6 mm^2 each). An energy threshold of 5 keV (i.e. exceeding the electronic noise level) and an energy resolution varying from Δ E / E = 4.7% at 500 keV to 3.5% at 1 MeV were used. Furthermore, the previously used array of six rather thin silicon strip detectors was replaced by a scatter module consisting of just one double-sided silicon strip detector with 128 strips on each side, an active area of 50 x 50 mm^2 and a thickness of 2 mm (representing the maximum thickness presently commercially achievable for microstructured silicon detectors). The pitch size of 390 μm correspondingly leads to a width of the LOR of 390 μm (FWHM). An energy resolution of 10 keV (FWHM) and a detection threshold of 10 keV was chosen in the Monte Carlo simulation (due to the assumed electronic noise level of the DSSSD). For the detector system a time resolution of 1 ns was (conservatively) assumed. According to the findings during the characterization measurements, the signal

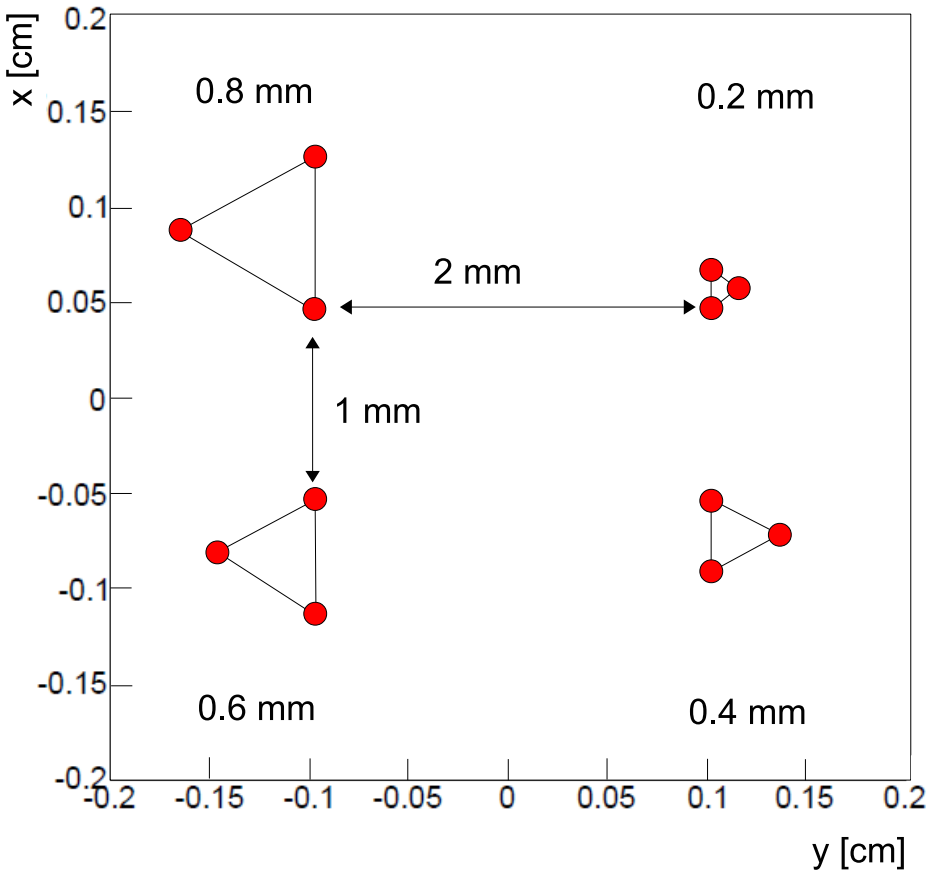

Figure 5.17: Sketch of the simulated photon source geometry, representing a quasi-Derenzo phantom [126], consisting of twelve ^{22}Na point sources with 100 kBq activity each. Four equilateral triangles are arranged in four sections, containing 3 point sources each, with 0.2 mm, 0.4 mm, 0.6 mm and 0.8 mm separation, respectively.

rise time from the $LaBr_3$ scintillator is about 8 ns, resulting in a time resolution of 273 ps for our 50 x 50 x 30 mm^3 crystal. In order to test the feasibility of the γ-PET technique, Monte-Carlo simulations and image reconstructions have been performed using the Medium Energy Gamma-Ray Astronomy library (MEGAlib) as introduced in Sect. 5.1.

5.3.2 Results

In the following, we address the potential of the proposed γ-PET imaging technique by separately discussing the main issues of spatial resolution, detection efficiency and reconstruction sensitivity for different arrangements of the detection system and imaged isotope.

Spatial source reconstruction resolution

The γ-ray energy spectrum, as emitted from the twelve ^{22}Na point sources of the quasi-Derenzo phantom and detected by one of the four Compton camera modules (taking into account the energy resolution), placed outside a water sphere of 6 cm diameter, is shown in Fig. 5.18. The spectrum was obtained from a Monte-Carlo simulation using Geant4 (9.4).

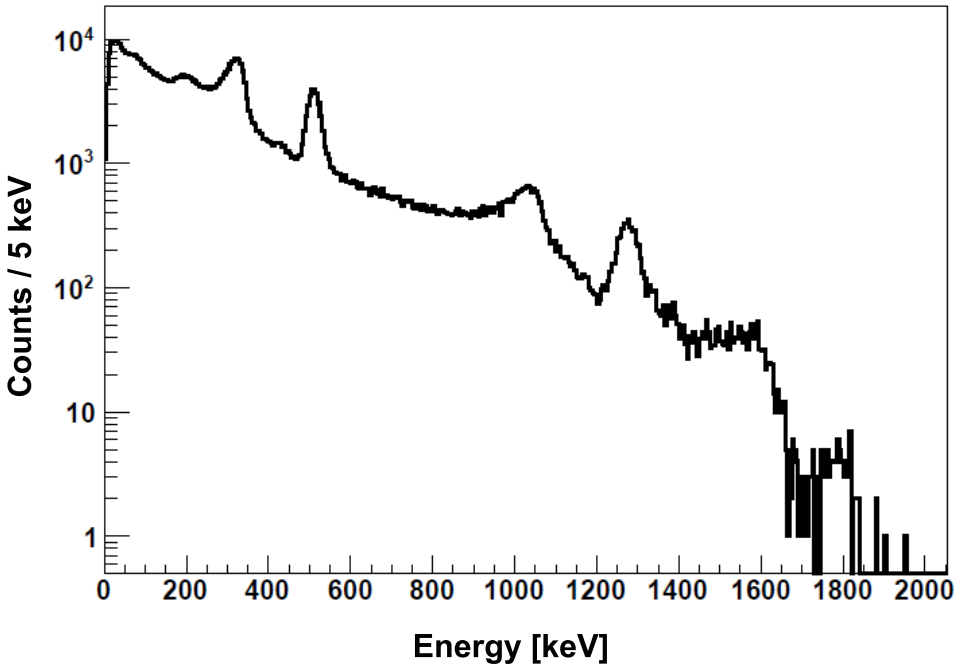

Figure 5.18: γ-ray energy spectrum emitted from the twelve ^{22}Na point sources, as detected in one of the 4 Compton camera modules placed around a water sphere of 6 cm diameter. For the Geant4-based Monte-Carlo simulations, the point sources were arranged in a geometry as indicated in Fig. 5.17. The trigger condition in these simulations required three hits in three of the DSSSD modules and one hit in one of the $LaBr_3$ absorbers. The decreasing yield with increasing energy is due to incompletely absorbed γ rays. Visible are the 511 keV positron annihilation line, as well as the 1275 keV line from the γ ray of the β^+ decay of ^{22}Na. Strong contributions at around 340 keV and around 1062 keV arise from electrons of the Compton backscattering of the 511 keV and the 1275 keV γ rays, respectively. Also visible at 1786 keV is the pileup of 511 keV and 1275 keV γ rays.

The decrease of the γ-ray yield with energy is due to incompletely absorbed γ rays. Clearly visible are the 511 keV positron annihilation line, as well as the 1275 keV line from the γ ray following the β^+ decay of ^{22}Na. The strong contribution at 340 keV originates from the Compton-backscattered electrons of 511 keV photons, while the peak at

1062 keV stems from Compton-backscattered 1275 keV photons. The trigger condition in these simulations required three hits in three of the DSSSD modules and one hit in one of the $LaBr_3$ absorbers. The line at 1786 keV is due to pileup between the 1275 keV transition and one of the 511 keV annihilation photons. Based on the geometrical arrangement of the ^{22}Na sources (Fig. 5.17) and detector modules (Fig. 4.8), the underlying data of the detected γ-ray energy spectrum (Fig. 5.18) are first used for a kinematical event reconstruction. The event reconstruction identifies Compton events in an energy window of 1275 ± 50 keV, corresponding to the γ-ray energy from the ^{22}Na decay, also identifying simultaneous hits above the detection threshold in the DSSSD for reconstruction of the LOR. In Fig. 5.19, the resulting image of the reconstructed γ-source geometry is shown, as obtained from exploiting the γ-PET technique. It was possible to clearly resolve the two largest triangles with spacings of 0.8 mm and 0.6 mm, respectively. The triangle with 0.4 mm spacing still could be resolved sufficiently well, while the 0.2 mm spaced triangle could not be resolved at all. The black crosses indicate the original source positions in the simulation. Due to the γ-PET technique, the imaging sensitivity for positron annihilation significantly displaced from the initial decay spot via thermalization and diffusion is strongly suppressed, and only positron annihilation photons emitted in spatial and temporal coincidence with the third (prompt) γ are included for image reconstruction. While the acollinearity of annihilation photons in our close detector geometry (distance 50 mm to the source) contributes only about 0.3 mm to the position uncertainty, Fig. 5.20 shows the correlation between the spatial resolution (as estimated via the above described quasi-Derenzo phantom) and the β end-point energy $E_{e^+}^{max}$ for the three isotopes ^{22}Na, ^{44}Sc and ^{10}C. Isotopes with $E_{e^+}^{max} < 4$ MeV are promising candidates for sub-millimeter imaging in our geometrical detector arrangement.

5.3.3 Efficiency considerations

After having shown that the γ-PET technique allows for sub-millimeter spatial resolution in the position reconstruction of the underlying radio-tracer independent of its β^+ energy, we address a further major advantage of this method, which is the acquisition time reduction achievable with the highly sensitive triple-γ coincidence measurement.
During the analysis of the 511 keV annihilation photons, no energy conditions have been applied. The simulations showed that there is no necessity for a stricter event definition than requiring an energy deposit (within a coincidence time window of 1 ns) above a threshold of 10 keV in three DSSSD detectors (two of them diametral) and a (completely absorbed) 1275 keV (prompt gamma from ^{22}Na decay) signal from the summed signal of the third scatterer and its scintillator to generate the LOR and still reach sub-millimeter spatial resolution. This can mainly be attributed to the capability of the event reconstruction algorithm to provide a reliable reconstruction even on the basis of an incomplete photon energy absorption. Additional energy conditions would discard this latter class of events (containing $5.8 \cdot 10^{-2}$ ($3.4 \cdot 10^{-3}$) of all events for one (two) completely absorbed 511 keV photon(s)) and unnecessarily lead to a drastic reduction of the reconstruction efficiency (see below). Here, reconstruction efficiency denotes the ratio of the number of identified intersections between the LOR of the positron annihilation photons and the Compton cone derived from the detection of the third prompt photon and the number of

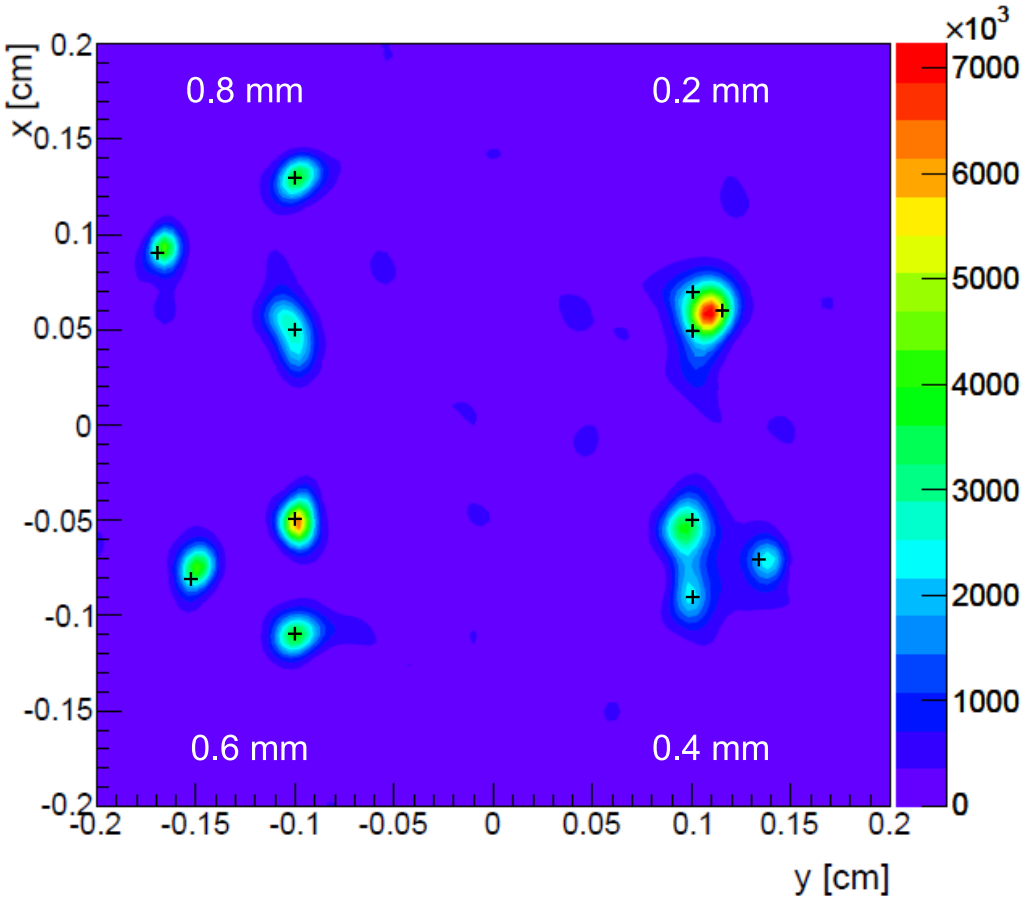

Figure 5.19: Image of the reconstructed γ-source geometry of the quasi-Derenzo phantom introduced in Fig. 5.17, using the γ-PET technique after 100 iterations (depending on start parameters) using a maximum-likelihood algorithm. The two largest triangles with spacings of 0.8 mm and also the 0.6 mm, respectively, are clearly resolved. In case of the 0.4 mm spaced triangle, the resolution is sufficient, however not as conclusive as for the previous two cases, while the smallest triangle with distances of 0.2 mm could not be resolved. The black crosses indicate the original source positions.

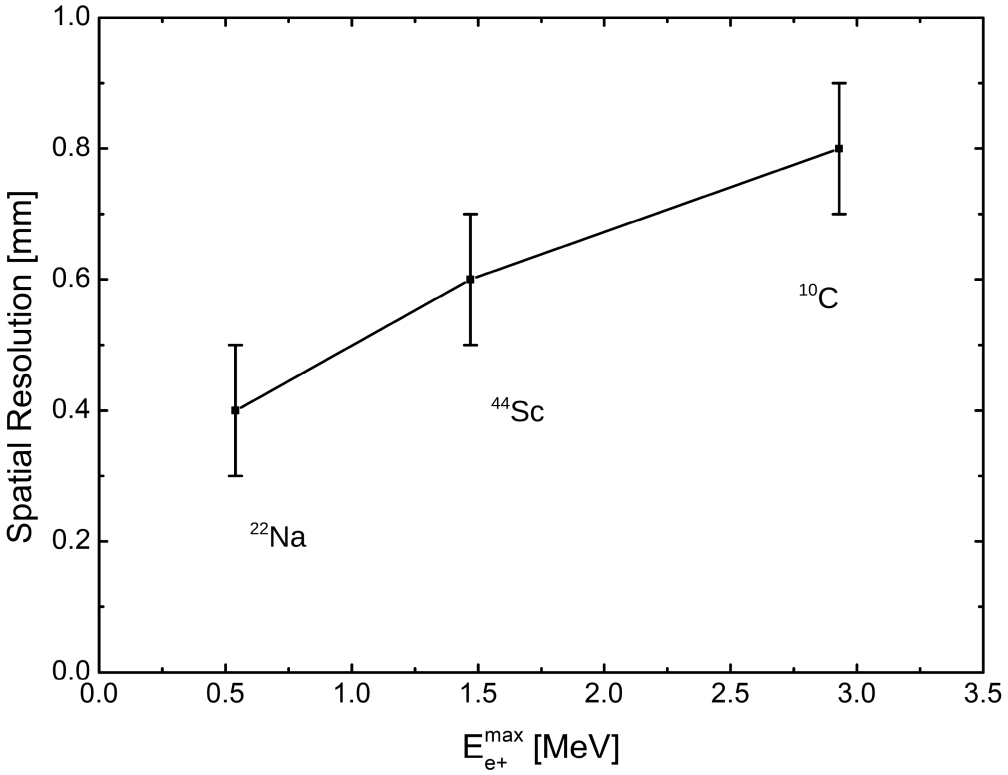

Figure 5.20: Correlation between the spatial resolution (as estimated from an image reconstruction using the quasi-Derenzo phantom described before) and the β end-point energy $E_{e^+}^{max}$ for the isotopes ^{22}Na, ^{44}Sc and ^{10}C.

initial decay events. It comprises contributions from the photon detection efficiency as well as from the image reconstruction sensitivity. Moreover, the narrow timing coincidence of 1 ns significantly helps to remove random background. One individual Compton camera module simulated here provides an event reconstruction efficiency of $3.3 \cdot 10^{-5}$. Thus the geometry studied with 4 camera modules exhibits an overall reconstruction efficiency for the Compton cone of $1.3 \cdot 10^{-4}$. Moreover, a 5 (8) times thicker scatterer (or a stack of 5 (8) scatter detectors with a summed thickness of 10 (16) mm) per Compton camera module would increase the reconstruction efficiency of the Compton cones by an additional factor of 4.4 (5.8) to a value of 5.7 (7.5) $\cdot 10^{-4}$. Similar scatter detector thicknesses have been favoured in [30]. In the case of thicker scatterers, where no depth information of the scattering point is measured, the spatial resolution increases from 0.4 mm (for 2 mm scatterer) to 0.6 mm (for 16 mm scatterer). This efficiency could be further increased by replacing our prototype geometry with a pyramidal arrangement of a scatter detector and a larger absorber, covering the opening angle of the cone seen from the photon source at the top of the pyramid. For our detector geometry, this would require an absorber with an area of 114 x 114 mm^2, about 5 times larger than the one used in our study. Finally, when extending the Compton camera to a γ-PET device, the temporal and

spatial coincidence with the annihilation LOR has to be considered. The simulated triple-coincidence detection efficiency for the γ-PET technique (assuming the detector setup of Fig. 4.8)) amounts to $7.0 \cdot 10^{-8}$ reconstructed intersections per ^{22}Na decay between the LOR of the annihilation photons and the Compton cone of the third photon. This reduction of the above given Compton camera efficiency is on the one hand due to the solid angle acceptance of the scatter detectors entering the LOR reconstruction, in our scenario resulting in a geometrical coincidence probability of 0.026. Moreover, a loss of those events has to be considered, where due to the diffusion of the positron before its annihilation no intersection between its reconstructed LOR and the Compton cone of the third photon, i.e. a spatial and temporal coincidence, could be found. This fraction amounts to ca. 91.8%, in total resulting in the above given overall γ-PET reconstruction efficiency of $7.0 \cdot 10^{-8}$ for ^{22}Na. This value would be further reduced to a prohibitively low value of $1.1 \cdot 10^{-10}$, if in addition to the condition set to the energy deposition of 1275 keV in the scatterer and absorber from the third photon also conditions on the energy of the two diametral 511 keV annihilation quanta (besides their temporal coincidence within 1 ns) would have been required. In a pyramidal arrangement of a scatter detector and a larger absorber, covering the full opening angle of the scatterer as seen from the emission point, such an additional energy condition would not reduce the efficiency, but would reduce random coincidences. For an optimized detector system consisting of 4 Compton camera modules, each with 8 x 2 mm thick scatter detectors and geometrically matched sizes of the absorber crystals, a triple reconstruction efficiency of $9.7 \cdot 10^{-5}$ (for ^{22}Na) can be expected. The efficiencies of other isotopes are different, due to the individual γ energies E_γ, the different positron endpoint energies $E_{e^+}^{max}$ and the branching ratio of γ/β^+. The simulated reconstruction efficiencies for various $\beta^+\gamma$ emitters are listed in Tab. 5.1.

Isotope	^{22}Na	^{44}Sc	^{14}O	^{68}Ga	^{124}I	^{10}C	^{76}Br	^{82}Rb
$\epsilon_{\mathrm{rec},1}$ [10^{-8}]	7.0	6.0	1.6	0.093	20	6.8	47	2.6
$\epsilon_{\mathrm{rec},2}$ [10^{-5}]	9.7	8.0	5.1	0.13	22	2.8	89	3.3

Table 5.1: Simulated reconstruction efficiencies for various $\beta^+\gamma$ emitters. In case of ^{124}I and ^{76}Br, which emit several prompt γ rays with considerable branching ratio, the individual efficiencies have been summed up (^{124}I: 0.60 MeV, 0.72 MeV, 1.5 MeV and 1.7 MeV. ^{76}Br: 0.56 MeV, 0.66 MeV, 1.13 MeV, 1.22 MeV and 1.85 MeV). The upper line corresponds to the detector system shown in Fig. 4.8, while the lower line represents the reconstruction efficiency for an optimized system with thicker scatter and larger absorber detectors (see text).

Sensitivity considerations

A minimum of 40 reconstructed intersections between the LOR and the reconstructed emission direction of the third photon is sufficient for a reliable image reconstruction of a point source with a ratio of true-to-false reconstructed events allowing for a correct reconstruction of the (submillimeter) point-source position without fragmentation of the source image. Choosing a typical injected activity of 400 MBq and taking into account

our intersection reconstruction efficiency $\epsilon_{\mathrm{rec},2}$ for ^{76}Br, 40 intersections can be identified after an examination time of about 140 seconds, which is sufficient for a reliable sub-millimeter image reconstruction of a point source contained within a voxel volume of about 1 mm^3 (high-resolution mode). In a standard PET iterative reconstruction analysis (without exploiting time-of-flight information, i.e. ordered subset expectation maximization (OSEM) [127]), about 6000 true coincidences acquired with a Siemens Biograph mCT PET scanner [106] are necessary to localize a ^{22}Na point source in the center of the scanner field-of-view using the smallest voxel volume of 2 x 2 x 3 mm^3. In order to compare the performance of the γ-PET technique with conventional PET, we determined the imaging sensitivity of the method based on a comparable width of the LOR of ca. 2 mm (in contrast to the previously used value for ^{22}Na of 0.4 mm). In such a case, also about 40 reconstructed intersections per voxel (derived without iterative reconstruction procedure) lead to a reliable localization of the ^{22}Na point source. This sensitivity can be evaluated and compared to standard PET by quantifying the examination time required to localize a point source as described above. The minimum number of β^+-emitter decays per voxel N_{decay}, required for localizing a point source, relates to the imaging sensitivity, expressed by the minimum number of reconstructed intersections N_{inter} and the corresponding reconstruction efficiency ϵ_{rec} as well as to the activity concentration $C(i)$ of each voxel i, the examination time Δt and the voxel volume V_{vox} according to

$$N_{\mathrm{decay}}(i) = N_{\mathrm{inter}}(i)/\epsilon_{\mathrm{rec}} = C(i) \cdot \Delta t \cdot V_{\mathrm{vox}}(i). \tag{5.7}$$

For a given activity concentration and tumor size, the required examination time for localizing a point source only depends on the imaging sensitivity N_{inter} and the reconstruction efficiency ϵ_{rec}. While the γ-PET method described here features a clear advantage in terms of sensitivity expressed by N_{inter} compared to standard PET, it falls behind when comparing the corresponding efficiencies ϵ_{rec}, where values of about 0.1 are reported for small-animal PET scanners [128], while similar values are found for whole-body scanners [129].

Isotope	$t_{1/2}$ [min]	γ/β^+ [%]	Tracer	h_T [μSv/MBq]	Ref.	E^{exam} [mSv]	τ^{exam} [s]
^{14}O	1.2	99	Water	0.88	[131]	0.33	2420
^{124}I	6013	90	MIBG	250	[132]	92	558
^{76}Br	16.2	100	MAb-38S1	410	[134]	150	138
^{82}Rb	1.3	13	Chloride	1.28	[133]	0.46	3740
^{44}Sc	236	100	DOTATOC	n.a.	[119]		1100

Table 5.2: γ-PET examination time τ^{exam} for the localization of a point source of selected $\beta^+\gamma$-decaying radioisotopes, assuming an injected activity of 400 MBq and a tumor activity concentration of 25 kBq/ml. τ^{exam} reflects the imaging sensitivity of the γ-PET method based on the minimum requirement of 40 reconstructed intersections and the isotope-specific reconstruction efficiencies $\epsilon_{\mathrm{rec},2}$. Column 7 shows the corresponding effective dose E^{exam}, based on the associated equivalent dose coefficients h_T (for adult males). The first columns list decay properties and suitable tracers of the respective isotopes

Tab. 5.2 lists in the last column the examination times τ^{exam} required for the localization of point sources of selected γ-PET radioisotopes, where information of tracer and associated equivalent dose coefficients (h_T) were available. τ^{exam} reflects the imaging sensitivity of the γ-PET method based on the minimum requirement of 40 reconstructed intersections and the isotope-specific reconstruction efficiencies $\epsilon_{\mathrm{rec},2}$ (see Tab. 5.1). Here we assume a typical value for the activity concentration accumulated in a tumor of 25 kBq/ml, corresponding to a PET examination of a patient with a body weight of 80 kg with an injected dose of 400 MBq and an average SUV (standard uptake value) of 5. Column 7 shows the corresponding effective dose values (calculated with h_T values derived for adult males). The rather wide spread of τ^{exam} values, reflecting the corresponding isotope-specific spread of the reconstruction efficiency ϵ_{rec}, exhibits no clear correlation with any of the isotopic properties like the β^+ endpoint energy or the energy of the third prompt photon. Thus it may rather represent a correlated interplay between different factors that makes it difficult to predict the performance of a specific radioisotope when applying the γ-PET technique. In case of small-animal PET, where even higher effective doses are injected, real-time imaging of the metabolism or organ motion, or a study of biological washout diffusion processes in animal experiments with implanted radioisotopes [130], appears feasible with the γ-PET technique

Chapter 6

Characterization of the medical imaging detector components

In this chapter, the experimental detector characterizations of the Compton camera components will be discussed, comprising measurement results of energy, time and spatial resolution as well as efficiencies for the different detector types, acting as scatterer or absorber in the Compton camera. Two different kinds of $LaBr_3$ scintillators were investigated: one with a surface finishing with absorptive wrapping was characterized within the scope of this thesis, while the same crystal was lateron modified to a reflective surface wrapping and was mainly studied within the parallel thesis work of S. Aldawood [135]. In order to allow for a direct comparison of the two detectors, both datasets are shown here. The scintillator with absorptive wrapping is designed for optimized photon position detection, while the scintillator with reflective wrapping for photon energy detection. Additionally, measurements at two synchrotron light facilities with the $LaBr_3$ scintillator, as well as with a 2D segmented planar germanium detector, will be discussed.

6.1 Compton camera absorber: $LaBr_3$:Ce scintillator

Since the availability of $LaBr_3$:Ce crystals for about one decade, this novel material has attracted growing interest in the context of a variety of applications, from nuclear spectroscopy to the field of medical imaging. This interest is rooted in the very attractive properties of $LaBr_3$:Ce scintillators, exhibiting a very high light yield of
63000 photons/MeV in combination with an excellent energy resolution and a fast timing behavior. All these properties together advocate $LaBr_3$:Ce for medical imaging applications, compared to conventional scintillators like BGO or LSO (see Sect. 4.1.1), especially in the quest for laser-accelerated particle therapy, where the short-pulse laser can provide a fast trigger signal. Figure 6.1 shows a photograph of the $LaBr_3$:Ce scintillator, as it is presently used as an absorber detector in the Compton camera prototype. It is a rectangular block crystal with an active volume of 50 x 50 x 30 mm^3, of type Brilliance 380 from Saint Gobain [136], attached to a multi-anode photomultiplier tube (PMT, Hamamatsu H9500C [137]). According to the manufacturer information, the scintillator Ce doping level is between 2.4% and 10%.

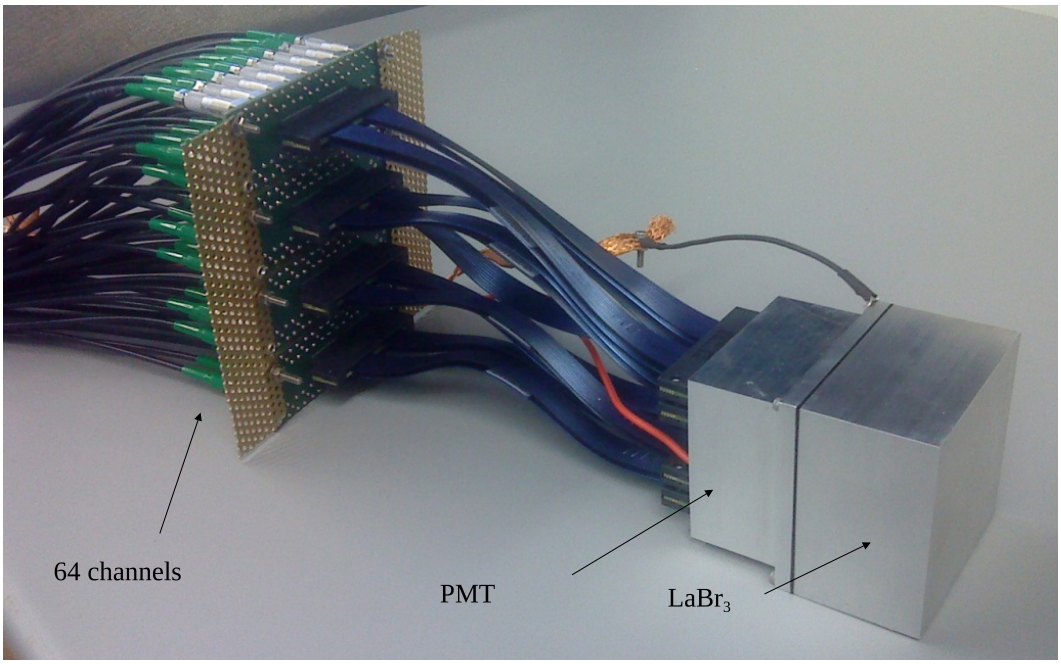

Figure 6.1: $LaBr_3$:Ce scintillator (active volume: 50 x 50 x 30 mm^3), attached to a 256-fold multi-anode photomultiplier (Hamamatsu H95000C). In this initial setup, each four pixel are combined to one readout channel, resulting in 64 signal channels, each with a pixel size of 6 x 6 mm^2.

6.1.1 Intrinsic radioactivity of $LaBr_3$:Ce

Besides its favourable light yield, timing and energy resolution properties, $LaBr_3$:Ce scintillators exhibit a small, yet not negligible intrinsic radioactivity of about 2 Bq/cm^3. This results in a count rate of $\simeq$ 140/s for our scintillator volume of 50 x 50 x 30 mm^3. A summed photon energy spectrum of a 1 h long measurement is shown in Fig. 6.2. The activity is due to the β-unstable constituents ^{138}La and ^{227}Ac and their daughter products. Intrinsic radioactivity is a typical feature of all lanthanum halide scintillators [144]. While Milbrath et al. measured a ^{227}Ac concentration of $1.3 \cdot 10^{-13}$ ^{227}Ac per La atoms [145], a reduction of the ^{227}Ac concentration achieved by crystal processing refinements in the growth technique was reported by Quarati et al. [146], resulting in a decrease of the alpha contamination, visible in the energy range between 1700 keV and 2700 keV, from 0.6 counts / (s cm^3) to 0.04 counts / (s cm^3). However, no simple solution has been found yet for reducing the concentration of ^{138}La, being the only naturally occurring isotope of lanthanum (with 0.0902% abundance and $1.05 \cdot 10^{11}$ yr half-life) [144], because this would require isotopic separation techniques. ^{138}La has two decay modes: electron capture to ^{138}Ba (66.4%), emitting a 1436 keV γ ray in coincidence with a 37.4 keV ^{138}Ba X-ray, and

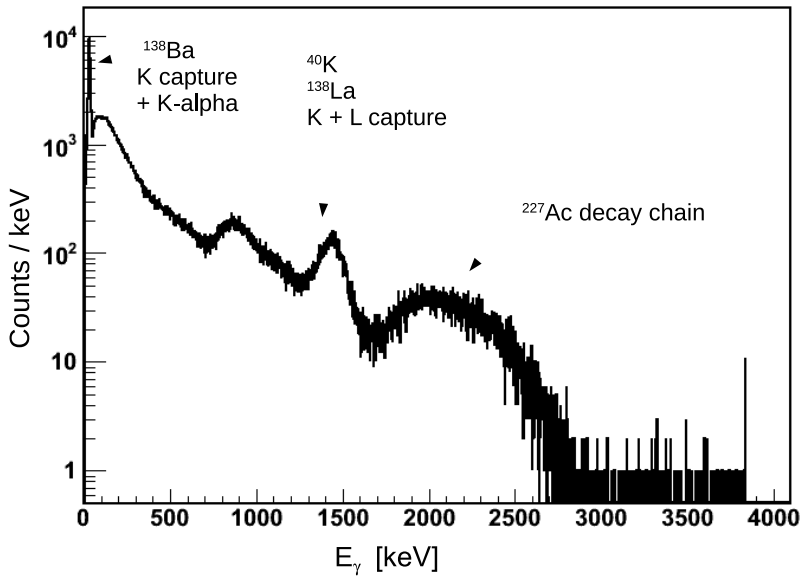

Figure 6.2: γ-ray energy spectrum originating from the intrinsic radioactivity of the $LaBr_3$:Ce scintillator crystal. Starting from lower energies, the strong line at $\simeq$ 35 keV originates from the ^{138}La K-shell electron capture into ^{138}Ba, emitting a 37.4 keV X-ray photon, and from the K_α transition of ^{138}Ba, emitting a 32.2 keV X-ray photon. The detector's energy resolution is not capable to resolve the two lines. The subsequent region with a strong decrease of transition intensity stems from the β decay of ^{138}La. Between around 800 keV and 1200 keV, γ and β decays of ^{138}La form a broad distribution. Around 1400 keV, several overlapping transitions are unresolved. This peak contains the 1440 keV line from the K-shell capture and the 1472 keV line from the L-shell capture of ^{138}La, together with the 1461 keV line of the M-shell capture from ^{40}K (emitted from the surrounding concrete walls). The high-energy part in this histogram shows a broad distribution, originating from the ^{227}Ac decay chain.

β decay (33.6%) with a 255 keV endpoint energy, in coincidence with a 789 keV γ ray. The continuum between $\sim$ 1700 - 3000 keV stems from α decays from the ^{227}Ac decay chain [39, 147]. Additionally, the K_α transition of ^{138}Ba, emitting a 32.2 keV X-ray, gets excited. This transition energy cannot be separated from the line of the electron capture to ^{138}Ba of 37.4 keV within the energy resolution of the $LaBr_3$:Ce detector. The broad line around 1400 keV also contains the room background contribution of the 1461 keV transition from ^{40}K. It is possible to take advantage from the intrinsic radioactivity, by using the X-ray and γ lines to calibrate the low energy detection characteristics of the detector and, additionally, to correct the spatial light amplitude distribution (see Sect. 6.1.6).

6.1.2 Electronic Signal Processing

The multi-anode photomultiplier tube is 256-fold segmented, allowing for position sensitive readout (pixel size: 3 x 3 mm^2), providing an additional sum signal for the energy measurement. In order to reduce the amount of signal processing electronics, the detector was commissioned by combining four PMT pixels to one readout channel, resulting in 64 PMT segments, each with a pixel size of 6 x 6 mm^2. Fig. 6.1 (left side) displays the adapter board that reduces the initial 256 PMT signals (fed in via 4 flat ribbon cables with high-density connectors (socket: Samtec QSE-040-01-F-D-A, cable assembly: Samtec EQCD-040-06, 00-SEU-TEU-1) to 64 Lemo output connectors. In an already completed upgrade, this reduction was recently removed and all 256 PMT channels can be individually processed and digitized [135]. In a first step, all photomultiplier signals are amplified by a factor of 3. In order to allow for optimum timing for each individual channel, Constant-Fraction Discriminator modules have been chosen to derive precisely timed logic signals from the PMT outputs. Both, amplification and timing, are provided by the 16-channel NIM module MCFD-16 from MESYTEC [138]. Besides the amplified charge pulse, the module provides a trigger signal and a gate. Finally, the amplified signals and gates are fed into VME-based charge-to-digital converter (QDC) units (Mesytec MQDC-32 [139]). The MQDC-32 consists of capacitors with 500 pC/ 100 Ω, together with an applied high voltage of -1100 V to the PMT and a gain of 3 of the MCFD-16, a dynamic range of 1 MeV can be achieved. A gain of 1 of the MCFD-16 will result in a dynamic range of 4 MeV. A logical trigger from the PMT sum dynode is starting the readout procedure, afterwards the data are recorded and analyzed on a PC, utilizing the ROOT [140] based software library Marabou [141].

The MQDC-32 can be operated with individual gates for each signal channel, or alternatively, with one or two master gates. The present measurements have been performed using individual gates, which have to precede the signal by at least 6 ns, while the Master Gate should precede the individual gates by at least 2 ns. In order to realize these timing requirements, the length of the twisted-pair ribbon cables connecting the MCFD-16 and MQDC-32 modules have been properly adjusted (based on a signal transmission speed of 5 ns/m). The following cable connections have to be considered:

L_0 = Lemo cable length from 'Fast OR' output of the MCFD-16 modules to the 'Gate' input of the MQDC-32 module
L_1 = (34-pin) twisted pair cable from the ECL pulse output of the MCFD-16 to the 'Gate' input of the QDC
L_2 = (34-pin) twisted pair cable from the MCFD-16 analog signal output to the QDC signal inputs

Resulting cable lengths with correct timing behavior:

$L_1 = L_0 + 2$ m
$L_2 = L_1 + 2$ m + (CFD delay [ns] * (1 + CFD fraction [%]) / 5 [m/ns])

For calculating the cable length L_2, the processing time of the CFD has to be

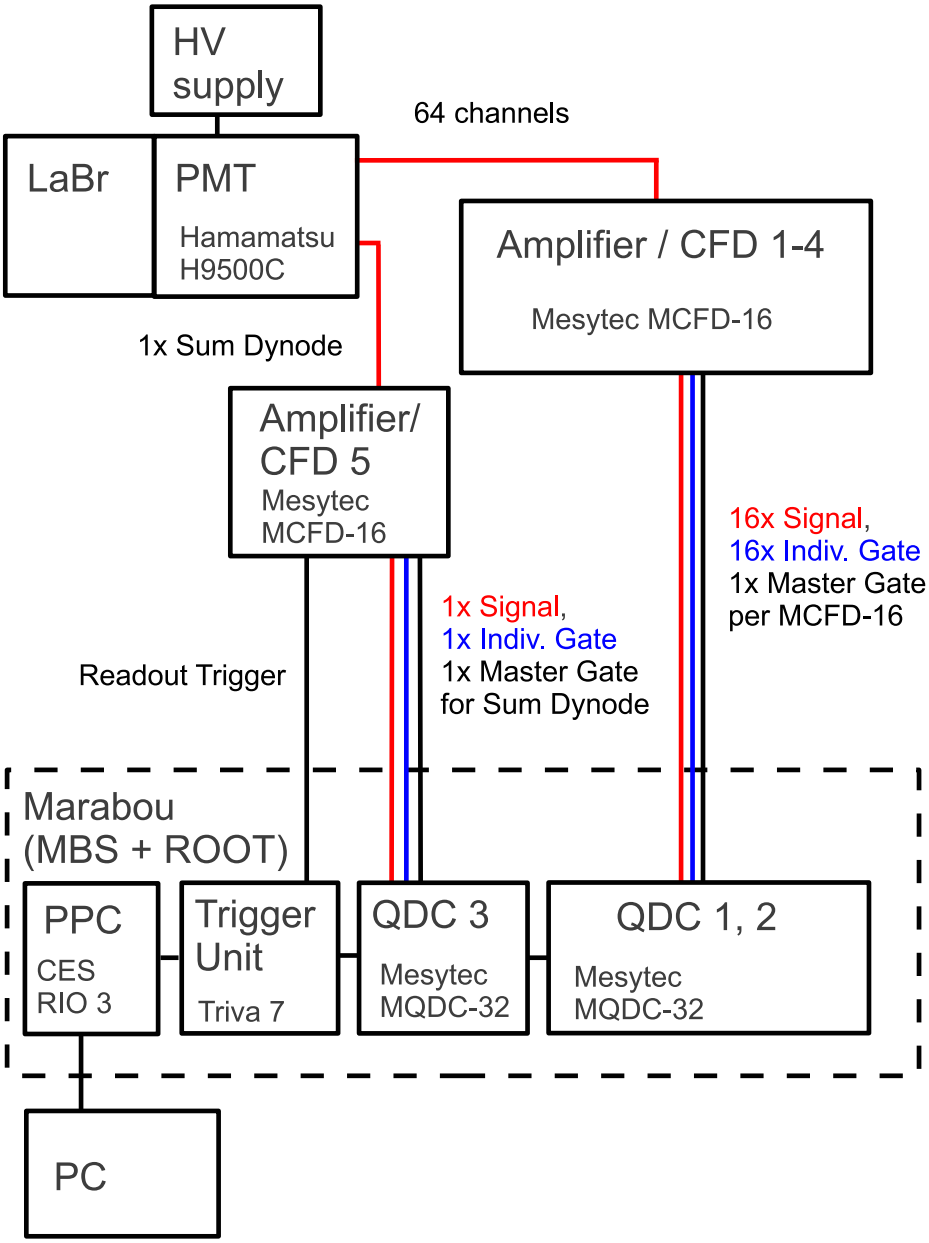

Figure 6.3: Schematics of the signal processing electronics of the $LaBr_3$:Ce scintillator. The scintillator crystal is attached to a multi-anode photomultiplier (Hamamatsu H9500C). The 64 channels (red lines) from the PMT are evenly distributed to four MCFD-16 amplifier plus Constant Fraction Discriminator modules, the sum signal goes to an additional 5th MCFD-16 module. The output of the four MCFD-16 modules (each: 16x analog signal (red), 16x individual Gate (blue) and a Master Gate (black)) was connected to two Charge-to-Digitial converters (MQDC-32), the 5th MCFD-16, processing the sum signal, was connected to an extra MQDC-32 (using only 1 channel). Data acquisition was performed using the VME-based Marabou system [141].

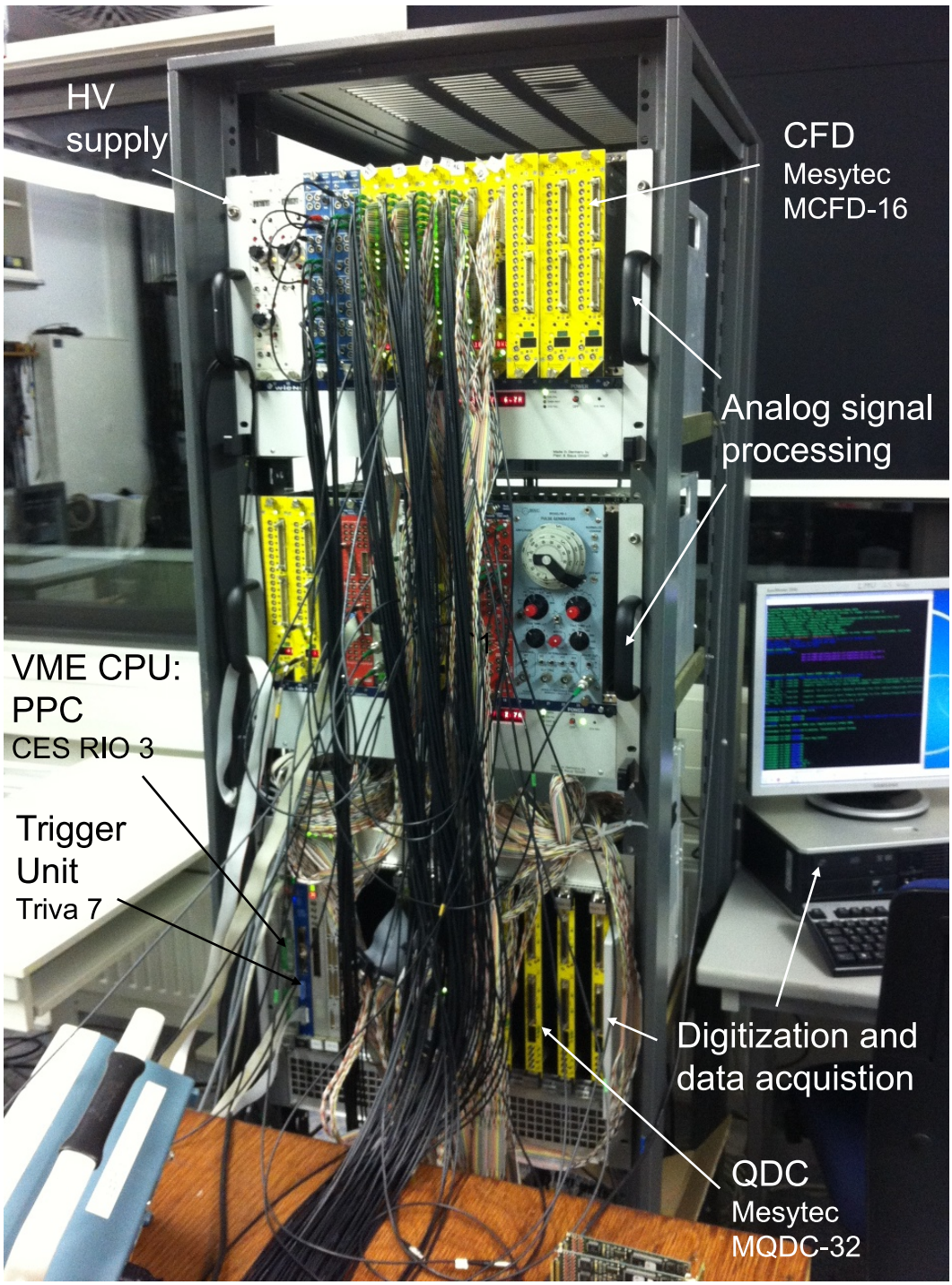

Figure 6.4: Photograph of the signal processing and data acquisition electronics used to characterize the $LaBr_3$:Ce detector with 64-fold (by combining 4 segments of the inital 256-fold segmentation) multi-anode PMT readout.

considered. According to its functional principle, a CFD is summing a delayed incoming signal (with a delay smaller than the signal risetime) with an inverted (constant) fraction of it, in order to derive an amplitude-independent logical signal from the resulting zero crossing. Therefore, the time delay of the analog signals has to be appropriately chosen. We used a CFD fraction of 20% and a CFD delay of 5 ns, taking into account the rise time of the $LaBr_3$:Ce scintillator signals of 8 ns. With L_0 = 1 m, L_1 and L_2 result to 3 m and 7 m, respectively. Figure 6.3 shows the schematics of the signal processing electronics of the $LaBr_3$:Ce scintillator in detail. The 64 channels (red lines) from the PMT are evenly distributed to four MCFD-16 modules, the sum energy signal is fed to an additional MCFD-16 module. The output of the four MCFD-16 units (each: 16x analog signal (red), 16x individual Gate (blue) and a Master Gate (black)) was connected to two MQDC-32 units, while the 5th MCFD-16 module, processing the sum signal, was connected to an extra MQDC-32 unit (using only 1 channel).

6.1.3 Energy Resolution

The $LaBr_3$:Ce scintillator is designed to act as an absorber in a Compton camera, where the energy resolution of the absorber will directly affect the spatial resolution of the Compton camera and is therefore, besides of the spatial resolution of the absorber, the most important property [89]. Typical values for the energy resolution of a (cylindric)

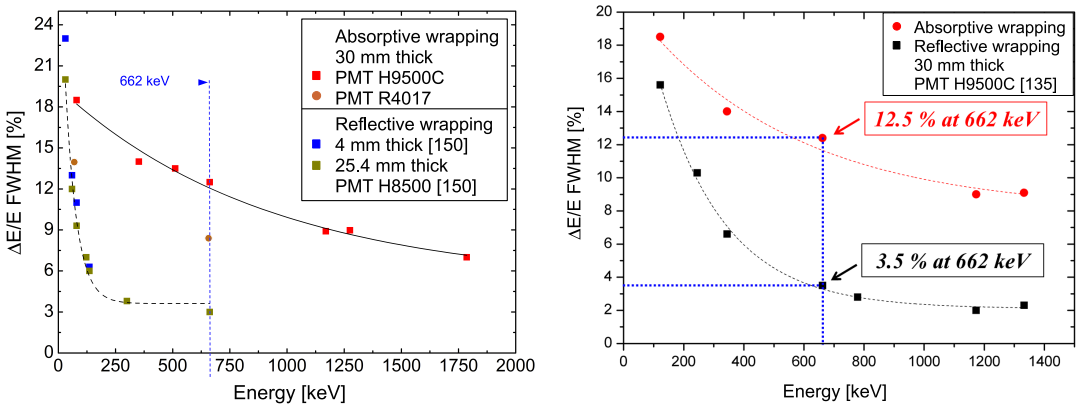

Figure 6.5: Calibrated energy spectrum of a ^{137}Cs point source, detected with the $LaBr_3$:Ce scintillator and read out with the Hamamatsu photomultiplier H9500C. ^{137}Cs β^- decays in 94.4% into the metastable ^{137m}Ba, which then decays into the ground state, emitting a 662 keV photon. The FWHM of the photopeak of the 662 keV transition amounts to ΔE/E = 12.5% in case of absorptive wrapping (left) and 3.5% in case of reflective wrapping [135] (right). Besides of the Compton continuum of this line, the peak at 32.2 keV originates from the K_α X-ray transition of ^{138}Ba, which is an intrinsic isotope in $LaBr_3$:Ce scintillators, and from a ^{137}Ba component contained in the ^{137}Cs source.

2" $LaBr_3$:Ce crystal with reflective wrapping range at about ΔE/E = 3% (FWHM) for the 662 keV photons emitted from a ^{137}Cs source [150]. The energy spectrum displayed in Fig. 6.5, showing the calibrated photon energies registered from a ^{137}Cs source (plus

the K_α X-ray peak at 32.2 keV from the internal ^{138}Ba contribution within the $LaBr_3$:Ce crystal, and from ^{137}Ba contained in the ^{137}Cs source), reveals in contrast a (spatially integrated) relative energy resolution of ΔE/E = 12.5% (FWHM) for the crystal with absorptive wrapping (left panel), derived from the sum dynode of the multi-anode PMT. The crystal with reflective wrapping (right panel) exhibits instead a relative energy resolution of ΔE/E = 3.5% (FWHM) at 662 keV.

The spatial dependence of the energy resolution at 662 keV has been investigated with a collimated ^{137}Cs source (collimator diameter: 1 mm, activity: 110 MBq). The center position of each of the 64 pixel was irradiated and the relative energy resolution was determined, leading to the energy resolution maps displayed in Fig. 6.6. The projections onto the X- and Y-axes, respectively, (also shown in Fig. 6.6) clearly reveal a gradual decrease of the energy resolution from its optimum of about 8% in the crystal center to about 16% in the crystal corners, in case of the scintillator with absorptive wrapping (a). In contrast, the scintillator with reflective wrapping (b) exhibits an almost constant energy resolution of 3.5% over the whole crystal area.

In order to study the energy dependence of the energy resolution, a ^{152}Eu source was used to provide γ transitions between 121 keV and 1408 keV. The resulting calibration curve for the scintillator with absorptive wrapping is shown by the red squares in the left panel of Fig. 6.7. For comparison, the brown circles indicate the values provided by the manufacturer, however, obtained by coupling the crystal to a single-anode PMT. About 30% difference between specified and measured energy resolution can be already attributed to the choice of the PMT. However, still the manufacturer's values were in clear contradiction to typical published detector properties of (cylindrical) crystals of similar size, as indicated by the green and blue circles in Fig. 6.7, stemming from Ref. [150], assuming the originally delivered $LaBr_3$ to be reflectively wrapped as ordered.

As it turned out, in contrast to ordering specifications, the side surfaces of our $LaBr_3$:Ce crystal were delivered with a diffusive finish and a black absorptive wrapping. Thus internal scintillation light reflections, particularly in the crystal corners, will be reduced, however, at the expense of energy resolution by the resulting losses of scintillation light. This effect dominates in the crystal corners and explains the drastic decrease of the energy resolution in these areas as visible in Fig. 6.6. Being a reasonable choice in cases when only spatial resolution needs to be optimized, this type of surface treatment is prohibitive in our situation, where the envisaged use of the scintillator as absorber of a Compton camera requires an optimum energy resolution on top of the spatial resolution. Therefore, the manufacturer agreed to modify the crystal to the initially ordered polished side surfaces with reflective wrapping.

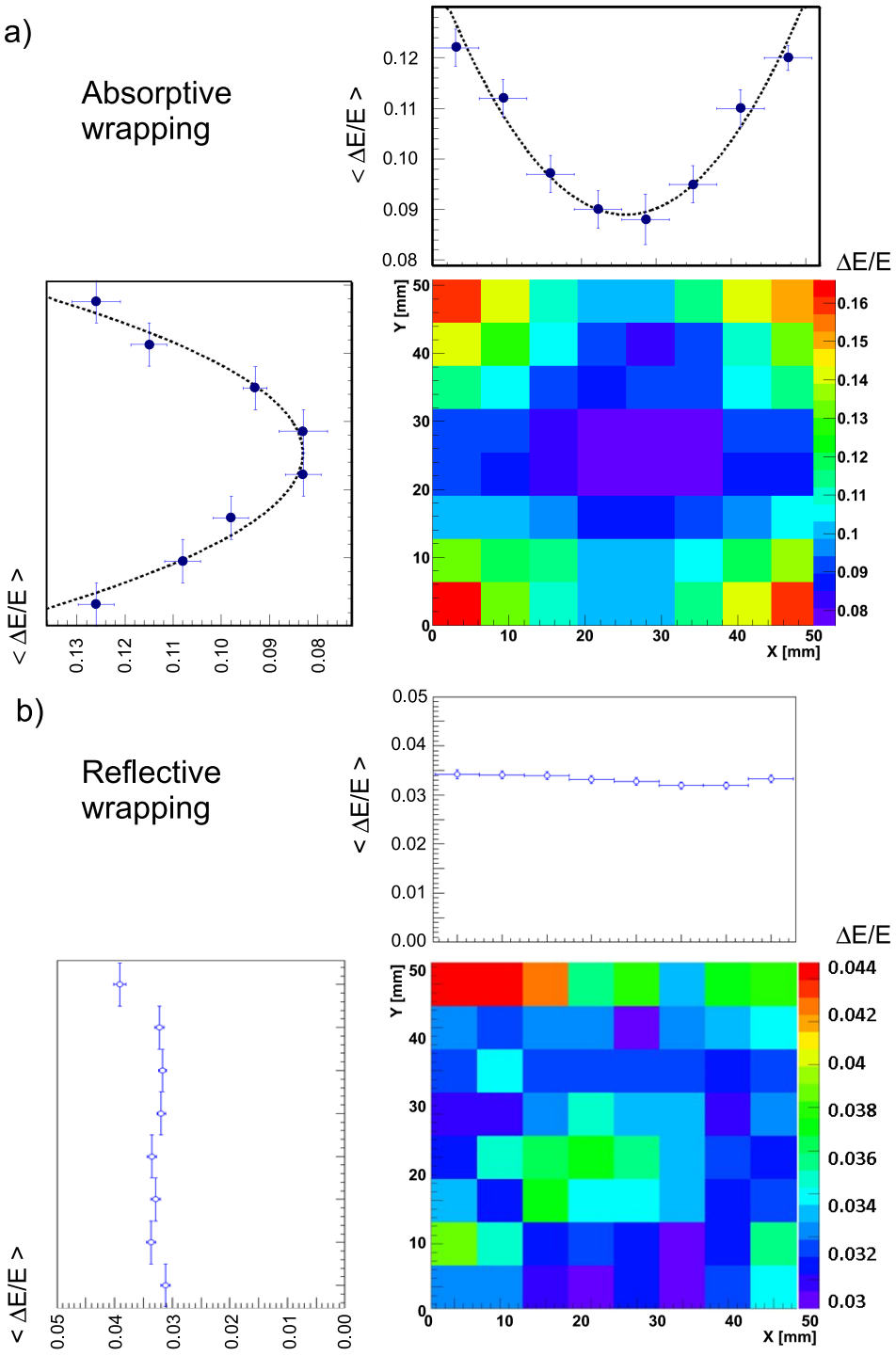

Figure 6.6: Energy resolution map of the two $LaBr_3$:Ce scintillators with (a) absorptive wrapping, b) reflective wrapping [135], measured with a collimated ^{137}Cs source (662 keV) of 1 mm diameter, irradiating the center of each of the 64 pixels. In case of the absorptive wrapping, the x- and y-projections reveal a gradual decrease of the energy resolution from the central region (ca. 8%) towards the corners (ca. 16%). The scintillator with reflective wrapping exhibits an almost constant energy resolution of about 3.5% over the whole crystal area.

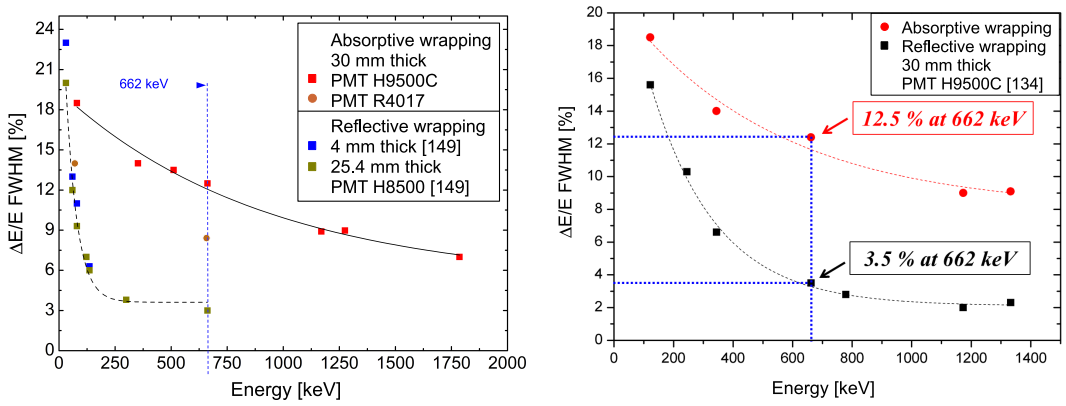

Figure 6.7: Relative energy resolution ΔE/E of the $LaBr_3$:Ce scintillator as a function of the photon energy. Left panel: the red squares indicate the relative energy resolution for the $LaBr_3$:Ce scintillator studied here in the version with absorptively wrapped side surfaces, coupled to its multi-anode PMT H9500C. The two brown circles are manufacturer's data for the same $LaBr_3$:Ce crystal, however, coupled to a single-anode PMT R4017. In this case, the relative energy resolution is lower by about 30% (8.5% at 662 keV). Significantly lower relative energy resolutions have been reported for comparable crystal dimensions of 2" x 2" with reflective surface finishing (3% at 662 keV [150]). Right panel: direct comparison of the relative energy resolution of the two investigated $LaBr_3$:Ce scintillators with absorptive and with reflective wrapping. The expected superior energy resolution of the reflectively coated crystal is clearly visible.

6.1.4 Time Resolution

In the context of range verification of (laser-)accelerated proton beams for use in hadron therapy, a fast timing detector is favored to allow for an efficient discrimination of background radiation, mainly arising from neutrons, which are produced by nuclear interactions of the protons in tissue.

One of the main advantages of $LaBr_3$:Ce as scintillation material is its superior timing behavior compared to more conventional materials like NaI or BGO. In order to determine the time resolution of our $LaBr_3$:Ce scintillator, we used fast-timing plastic scintillators as reference detectors, consisting of BC-418 from BICRON ([142]) (also known as NJ-228 from ELJEN Technology or Pilot U from Nuclear Enterprises). This type of plastic material (Polymer base: polyvinyl-toluene, Ø25 mm, thickness 3 mm) exhibits an excellent timing, with a rise time of 0.4 ns and a decay time of 1.4 ns. Two of such scintillators were coupled to fast PMTs (model XP2020/Q from Photonis). The signals of the plastic scintillators were fed into the same DAQ system as described before, adjusting only the delay of the CFD (MCFD-16) to 2 ns. The trigger was derived from the plastic scintillator and the relative timing between two such detectors was determined, using a time-to-digital converter (TDC) VME-unit (model CAEN V775 [143]). The measurement setup consisted of two identical BC-418 detector modules and the $LaBr_3$:Ce crystal, as shown in Fig 6.8. A ^{60}Co γ point source was used, which emits two γ photons in coincidence (1.173 MeV and 1.332 MeV). The measurement was performed in three steps: First the two BC-418

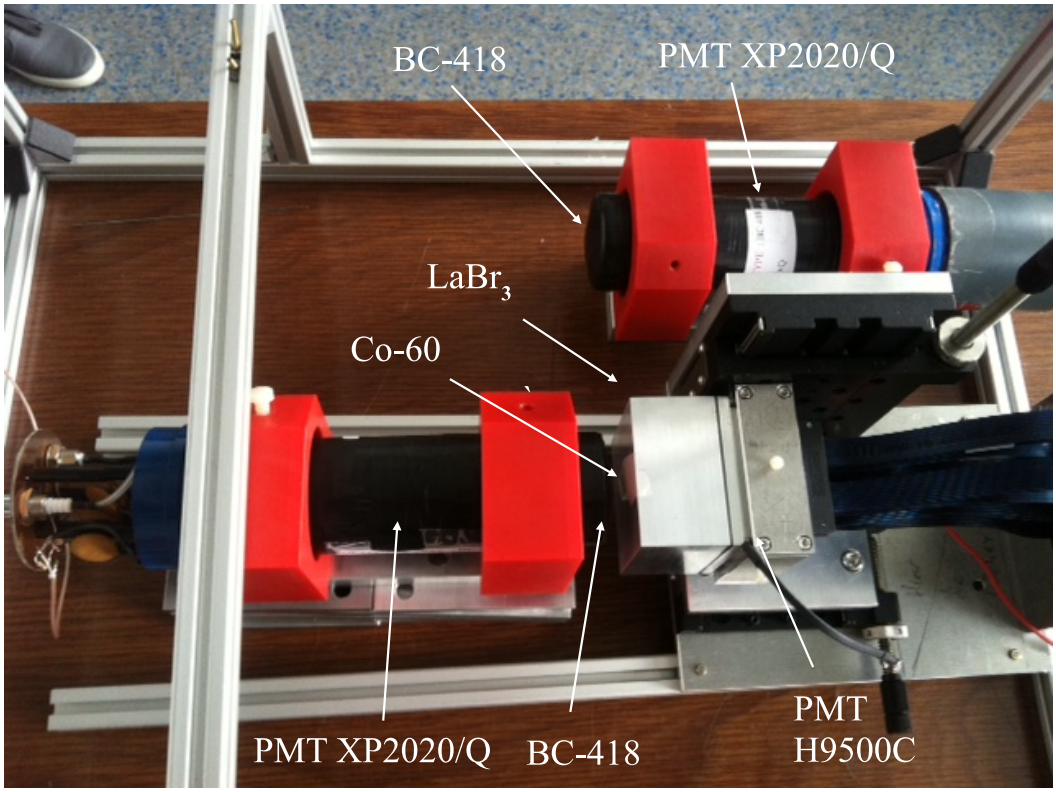

Figure 6.8: Experimental setup for the time resolution measurement of the $LaBr_3$:Ce scintillator. Two BC-418 fast plastic scintillators (rise time = 0.5 ns, decay time = 1.4 ns) are coupled to fast-timing PMTs (XP2020/Q). A ^{60}Co γ point source, emitting two γ photons in coincidence (1.173 MeV and 1.332 MeV) was used.

detectors were operated in coincidence, in order to determine the time resolution of this detector system and hence to derive the time resolution of an individual plastic detector module. As a result, the detector system of two BC-418 modules exhibits a combined time resolution of $\Delta t^{coinc}_{plastic}$ = 365 ps (as displayed in Fig. 6.9a)), allowing to determine the time resolution of an individual module according to:

$$\Delta t^{coinc}_{plastic} = \sqrt{\Delta t^2_{BC418,1} + \Delta t^2_{BC418,2}} \tag{6.1}$$

Considering that $\Delta t^2_{BC418,1} = \Delta t^2_{BC418,2}$, a time resolution of $\Delta t_{\mathrm{BC418}}$ = 258 ps was derived for each of the two BC-418 modules. In the second step, one of the BC-418 modules was replaced by the absorptively wrapped $LaBr_3$:Ce scintillator and the coincidence time measurement was repeated. The resulting time distribution can be seen in Fig. 6.9b). A combined time resolution of 595 ps was measured for this detector system, finally resulting in a time resolution of the $LaBr_3$:Ce scintillator of $\Delta t_{\mathrm{LaBr(abs)}}$ = 536 ps.
This time resolution of 536 ps is slow compared to published values of $\simeq$ 200 - 300 ps when using a ø25.5 mm x 30 mm $LaBr_3$ crystal coupled to a fast single channel PMT

of type XP2/D0 [151]. As it can be seen in panel c) of Fig. 6.9, the time resolution is significantly affected by the side surface finishing and can be improved by a reflective wrapping of the $LaBr_3$ crystal, resulting to a timing of $\Delta t_{\mathrm{LaBr(refl)}}$ = 275 ps [152].

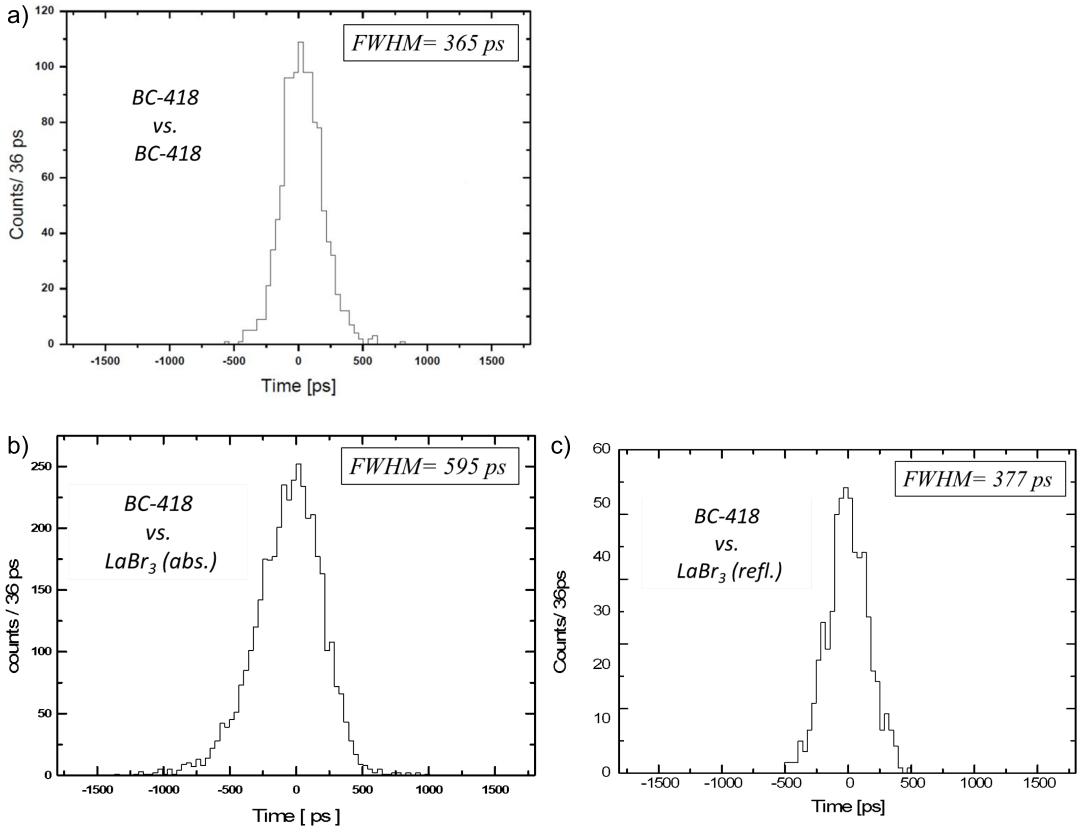

Figure 6.9: a) Time difference between two BC-418 plastic scintillators, operated in coincidence mode using a ^{60}Co source ($\Delta t^{coinc}_{plastic}$ = 365 ps). The resulting time resolution of one BC-418 module is Δt_{BC418} = 258 ps. b) Time difference between the absorptively wrapped $LaBr_3$:Ce scintillator, measured against one of the previous fast-timing BC-418 plastic scintillators. The resulting time resolution of this detector amounts to $\Delta t_{\mathrm{LaBr(abs)}}$ = 536 ps. c) the time resolution is significantly affected by the side surface finishing and can be improved by a reflective wrapping of the $LaBr_3$ crystal, resulting to a timing of $\Delta t_{\mathrm{LaBr(refl)}}$ = 275 ps [152].

The time resolution of scintillator-based detectors are directly driven by the density of photoelectrons, created in the photodetector at the detection threshold [18]. Main influencing factors include the time structure of the pulse, the light yield of the scintillator and the light transport, which can affect the pulse shape, the photon statistics and the light yield. As the same $LaBr_3$ crystal has been investigated, the light yield of the detector material has been assumed to be the same for both experiments. Affected by the different crystal wrapping, the number of scintillation photons that arrive at the PMT is different for the absorptively and reflectively coated $LaBr_3$. Mainly the spread in transit time of

photoelectrons in the PMT contribute to the time resolution of the system. Assuming Poisson statistics to hold for the distribution of possible transit times of photoelectrons in the PMT, the relative spread in transit times will be inversely proportional to the square root of the number of photoelectrons per event: $\Delta t \propto 1/\sqrt{N_{\mathrm{ph}}}$ [39] .
Therefore, the measured improvement in the time resolution for the reflectively wrapped $LaBr_3$ crystal compared to the absorptively wrapped crystal, can be explained by the increased number of photoelectrons N_{ph} in the PMT.

6.1.5 Absolute Photopeak Efficiency

In order to derive the energy dependence of the absolute (solid-angle and dead-time corrected) photopeak efficiency $\epsilon_{ph}(E_\gamma)$ for the $LaBr_3$:Ce scintillator, two methods were used: The first method is based on the known activity of the γ source. For the measurement we used ^{152}Eu and ^{137}Cs calibration sources with activities of 125.8 $\pm$ 0.02 kBq and 268.1 $\pm$ 0.08 kBq, respectively. The other method for deriving the absolute photopeak efficiency $\epsilon_{ph}(E_\gamma)$ is by exploiting coincident deexcitation cascades in ^{152}Eu, where the 121 keV line is emitted in coincidence with the 1408 keV line, the same holds for the

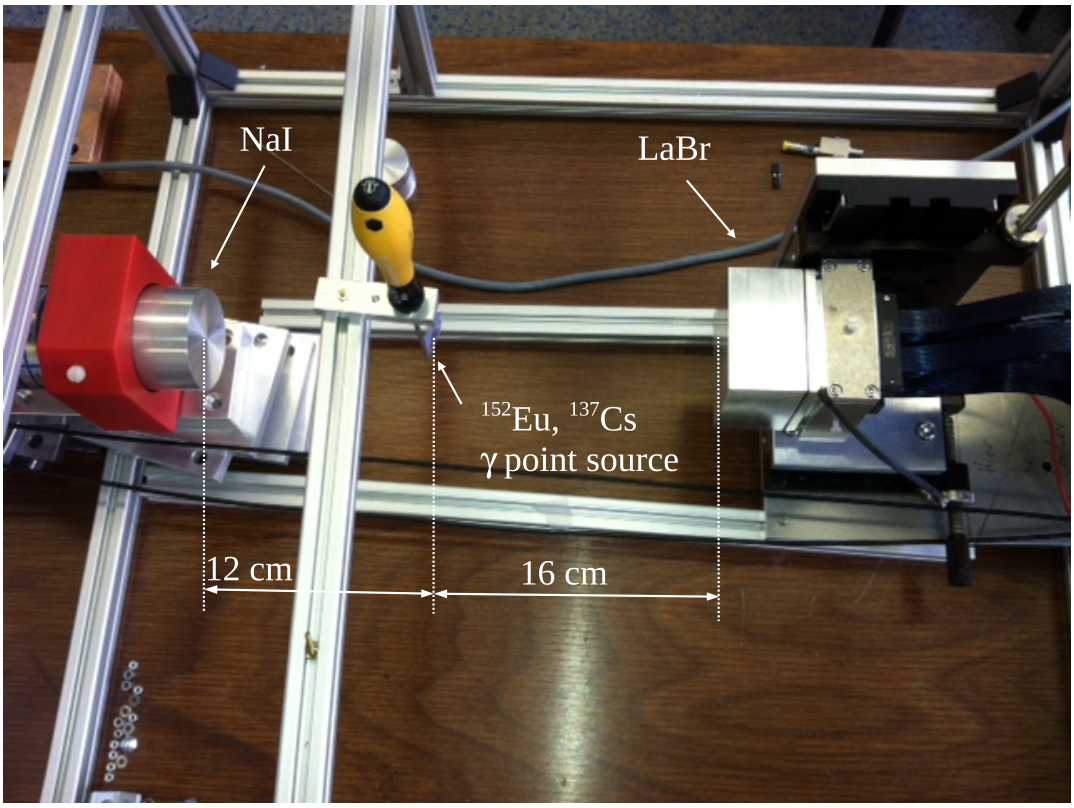

Figure 6.10: Setup used for the efficiency measurement. A γ point source, ^{152}Eu or ^{137}Cs, was placed 16 cm away from the front surface of the $LaBr_3$:Ce scintillator. For reference measurements, a NaI scintillator was positioned in a distance of 12 cm from the γ point source.

transitions at 344 keV and 779 keV, respectively. In this case a second detector, here a 2" NaI scintillator, has to be used to register one of the two members of the deexcitation cascade as trigger, while subsequently the amount of the second photon registered in the $LaBr_3$:Ce detector allows to derive the corresponding absolute efficiency after solid-angle and deadtime correction.

A picture of the efficiency measurement setup can be seen in Fig. 6.10. A γ point source, ^{152}Eu or ^{137}Cs, is placed 16 cm away from the front surface of the $LaBr_3$:Ce scintillator. A 2" NaI scintillator is positioned in a distance of 12 cm from the γ point source as trigger detector. In order to suppress background radiation, the NaI scintillator was operated in a Pb shielding (not shown).

The resulting absolute photopeak efficiency $\epsilon_{ph}(E_\gamma)$ as a function of the photon energy is displayed in Fig. 6.11, revealing a good agreement between the two methods. Starting from an efficiency of $\epsilon_{ph}(E_\gamma)$ = 76 $\pm$ 2 % at 121 keV, the absolute photopeak efficiency $\epsilon_{ph}(E_\gamma)$ decreases to about 7 $\pm$ 1 % at 1408 keV.

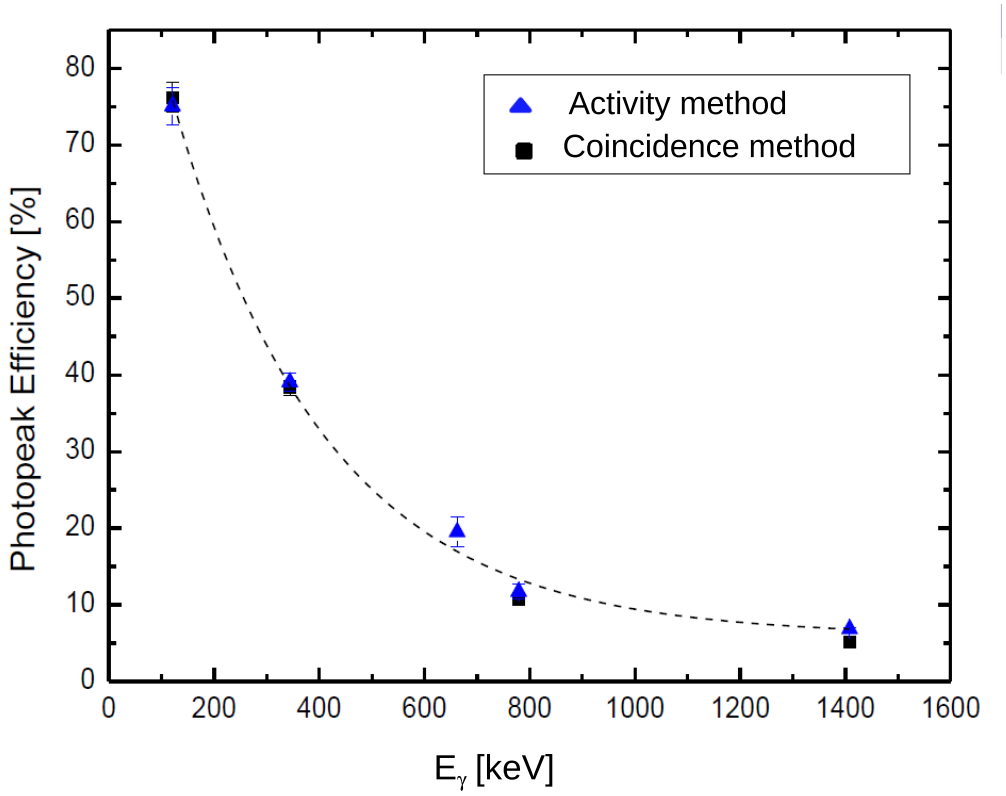

Figure 6.11: Energy dependence of the absolute (solid-angle and dead-time corrected) photopeak efficiency $\epsilon_{ph}(E_\gamma)$ for the $LaBr_3$:Ce scintillator. Two methods have been used, the activity method and the coincidence method (see text), both are in good agreement. The data points at 121 keV, 344 keV, 779 keV and 1408 keV were measured with a ^{152}Eu source, the 662 keV transition originates from ^{137}Cs.

6.1.6 Spatial Resolution and Point-Spread Function

The spatial resolution of the $LaBr_3$ detector, read out via a position-sensitive PMT, is another key property, considering its use as an absorber in a Compton camera system. The achievable spatial resolution of a Compton camera is directly affected by the spatial resolution of its absorber [89].

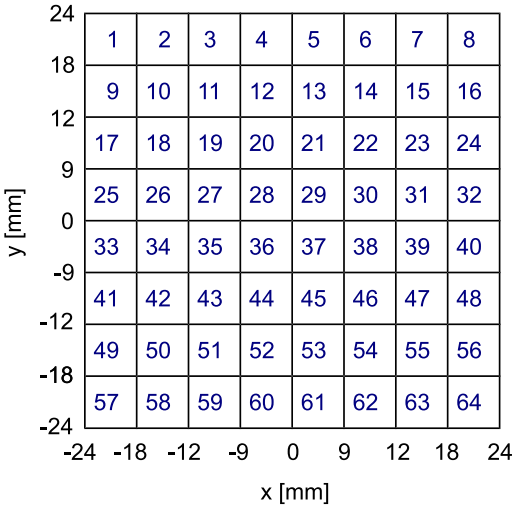

Figure 6.12: Matrix of the PMT pixel number mapping in front view.

While the lateral interaction position in pixelated detectors is straightforward obtained by segment identification, the determination of the interaction position of a γ or X-ray photon in a monolithic scintillator crystal is more complex. Here, the scintillation photons, produced by photo-absorption and subsequent luminescence, spread over the entire PMT volume [39]. In order to derive the correct information on the initial γ interaction point from the measured charge (i.e. light yield) distribution of the scintillation event, several correction steps have to be applied. The spatial resolution of the $LaBr_3$:Ce scintillator has been studied with a collimated ^{137}Cs γ source (E_γ = 662 keV, 1 mm collimator diameter) with an activity of 110 MBq, sequentially positioned to irradiate each pixel (6 x 6 mm^2) in its center. Fig. 6.12 shows a matrix of the PMT pixel number mapping in front view. The light distribution on the PMT anode plane was measured for each of the 64 pixel during a measurement time of 300 s at a counting rate of about 3500/s. Figure 6.13 shows exemplarily the response of the continuous crystal to the irradiation of three different pixels (top left, center and bottom right, corresponding to the three columns of the figure), while the 5 rows contain the respective light yield distributions resulting from subsequently applied correction steps during the data analysis. The black dots indicate the corresponding position of the collimated γ source. In row a) the uncorrected light amplitude distributions on the anode plane are displayed. Initially, it is not possible to see any clear correlation between the real source position and the light yield distribution. In row b), the data have been corrected for their individual different electronic amplifier gains via pulser signals, by using two different pulser signal heights, additionally the energy pedestal (= QDC

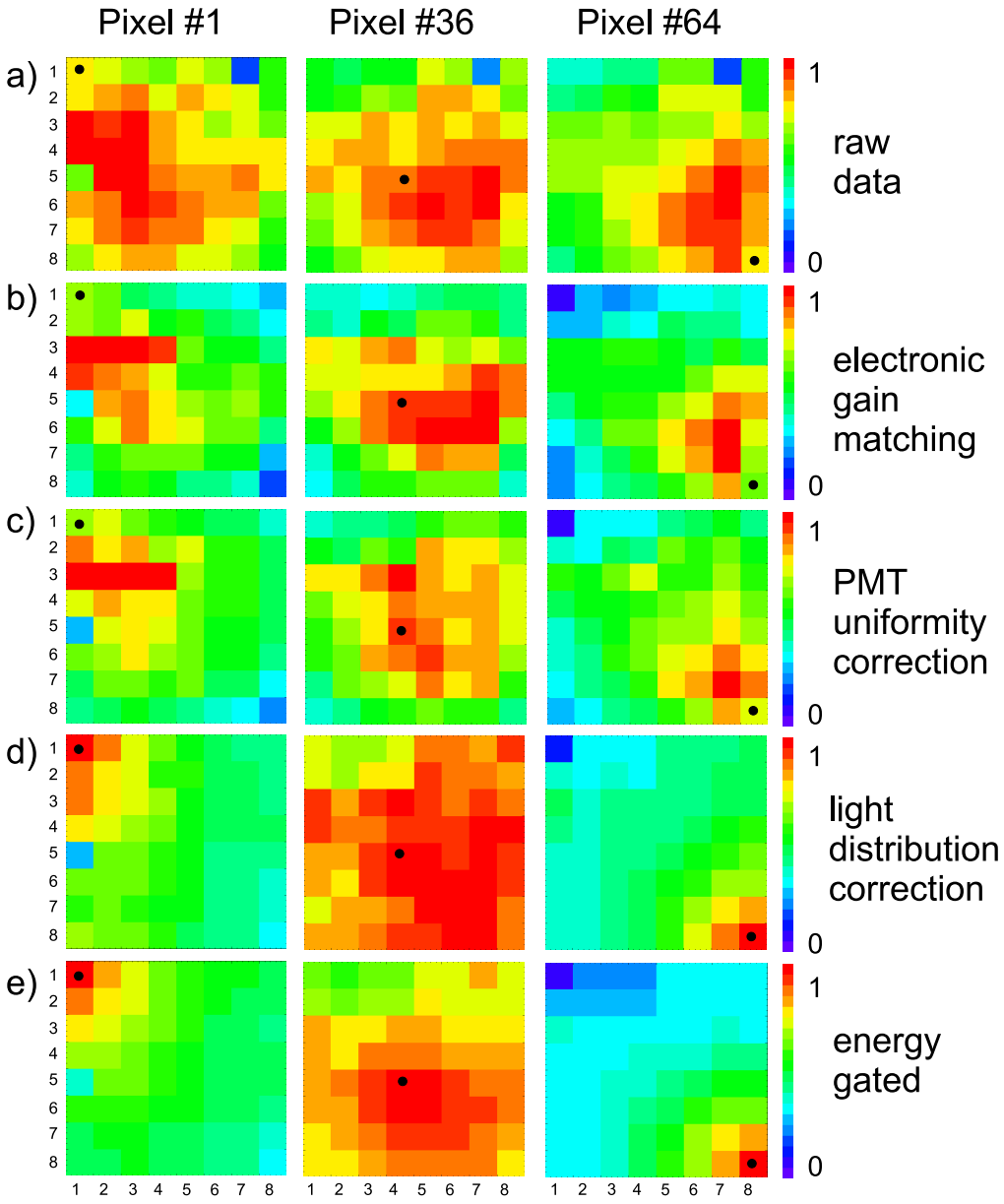

Figure 6.13: Response of the $LaBr_3$:Ce scintillator to a collimated ^{137}Cs γ source (662 keV) with an activity of 110 MBq (collimator diameter 1 mm). The charge distribution was corrected in different steps during the data analysis. The data in row a) shows the uncorrected raw data, followed in row b) by a gain matching of the electronics (with pulser signals), additionally the energy pedestal was shifted to QDC channel zero. Row c) shows the effect of correction of the PMT uniformity (using the manufacturer's gain uniformity matrix). In row d), finally a light distribution correction was performed (see text). The last row e) shows the energy gated (662 keV photo-peak in the sum signal spectrum) light distribution. The position of the γ source is indicated by a black dot.

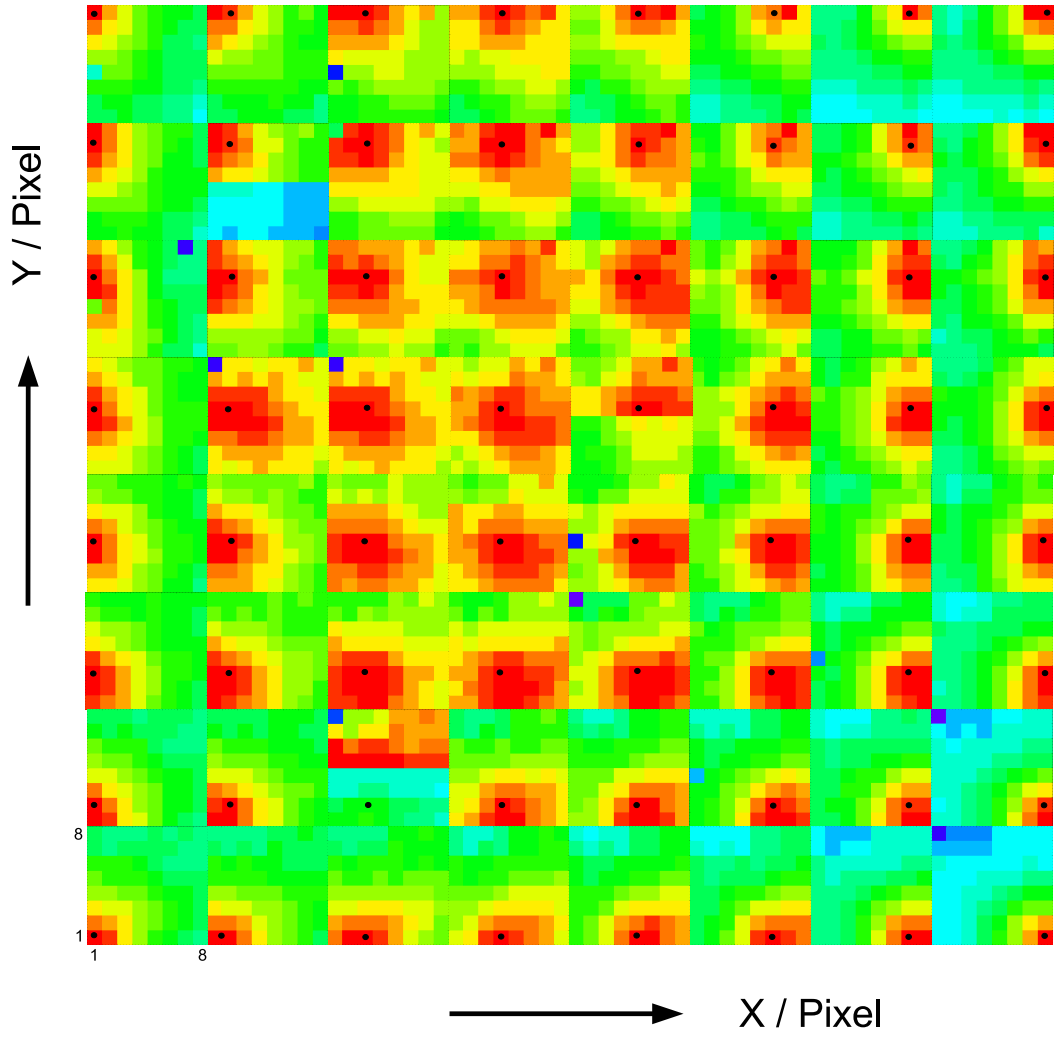

Figure 6.14: Map of 64 light amplitude response matrices of the (absorptively wrapped) $LaBr_3$:Ce scintillator to a collimated ^{137}Cs γ source, irradiating in each case the pixel in the center, marked by a black dot. The charge distribution was fully corrected and gated on the ^{137}Cs 662 keV line. A clear correlation of the actual source position and the resulting light yield response is visible.

dark current) has been shifted to QDC channel zero. In row c), the individual gains of the segments of the multi-anode PMT were matched according to the gain uniformity matrix provided by the manufacturer. In order to account for the combination of 4 PMT pixel into 1 readout channel, the respective entries of the matrix have been averaged. Row d) shows the result of the light distribution correction. By irradiating the detector with a far field γ source, a homogenous γ distribution on the crystal is expected.
Mostly due to not fully absorbed photons at the edges and in the corners and incomplete registration of the scintillation light (absorptive wrapping of crystal), the measured light distribution is not uniform.
This correction step compensates the spatial difference between irradiating position and reconstructed position at corner and edge positions. Finally, in order to obtain the data shown in row e), an energy gate on the 662 keV photopeak of the ^{137}Cs γ source was applied. The values of the different correction steps can be found in Appendix C. A clear correlation between the source position and the resulting detector response is visible in Figure 6.14. The map shows 64 fully corrected and energy-gated light yield responses of the $LaBr_3$:Ce scintillator to a collimated ^{137}Cs γ source, irradiating in each case the corresponding pixel (marked by a black dot) in its center.
Figure 6.15 shows three prototypical γ energy spectra of the $LaBr_3$:Ce scintillator, measured with the sum dynode, responding to the irradiation of two diagonal corner pixels (panel a) and c)) and a central pixel (panel b)) by the collimated ^{137}Cs γ source. The spectra show the 662 keV γ line, a strong Compton back-scattering contribution, the X-ray lines of the Pb collimator material and the intrinsic X-ray lines of barium contained inside the crystal. The 662 keV line is strongly distorted, broadened and shifted in the corner pixels (panels a) and c)), due to incomplete registration of the scintillation light.
In Fig. 6.16, the 2D light-yield (i.e. charge) distribution is displayed for a central irradiation of the $LaBr_3$ scintillator (position (0,0)). In addition, the projections onto the x and y axes are shown, the corresponding mean values $<X>$ and $<Y>$ (calculated using Eq. (6.2) and (6.3)) are indicated, exhibiting a small offset of the calculated irradiation centroid relative to the crystal center at (0,0).
Fig. 6.17 displays the corresponding radial projection of the 2D charge distribution together with a fit curve indicating the point spread function (PSF) with a width (FWHM) of 29.5 mm. The mean values ($<X>$ and $<Y>$), utilizing Eq. (6.2) and (6.3), are displayed and indicated with dotted lines. A radial projection shows the point spread function with a FWHM of 29.5 mm. Tab. 6.1 lists all 64 irradiation positions X_0, Y_0 and the resulting maximum values X^{max}, Y^{max} as well as the mean values $<X>$, $<Y>$ of the charge distribution on the anode plane of the PMT. It can be seen that the maximum of the charge distribution is ambiguous (e.g. pixel 5 - 8 corresponds to different irradiation positions X_0, however, they result in the same maximum value X^{max}, while the mean values differ from each other).
The most common method of reconstructing the interaction point of an incident γ ray inside a continuous scintillator crystal is the center of gravity (CoG) algorithm [149], also known as weighted means. However it is well known, that this method reaches its limits when being applied to asymmetric distributions or distributions with a light offset [149], as it is the case for the spatial measurements with the $LaBr_3$ detector. Here, the CoG method cannot be expected to give optimum results and a more sophisticated reconstruc-

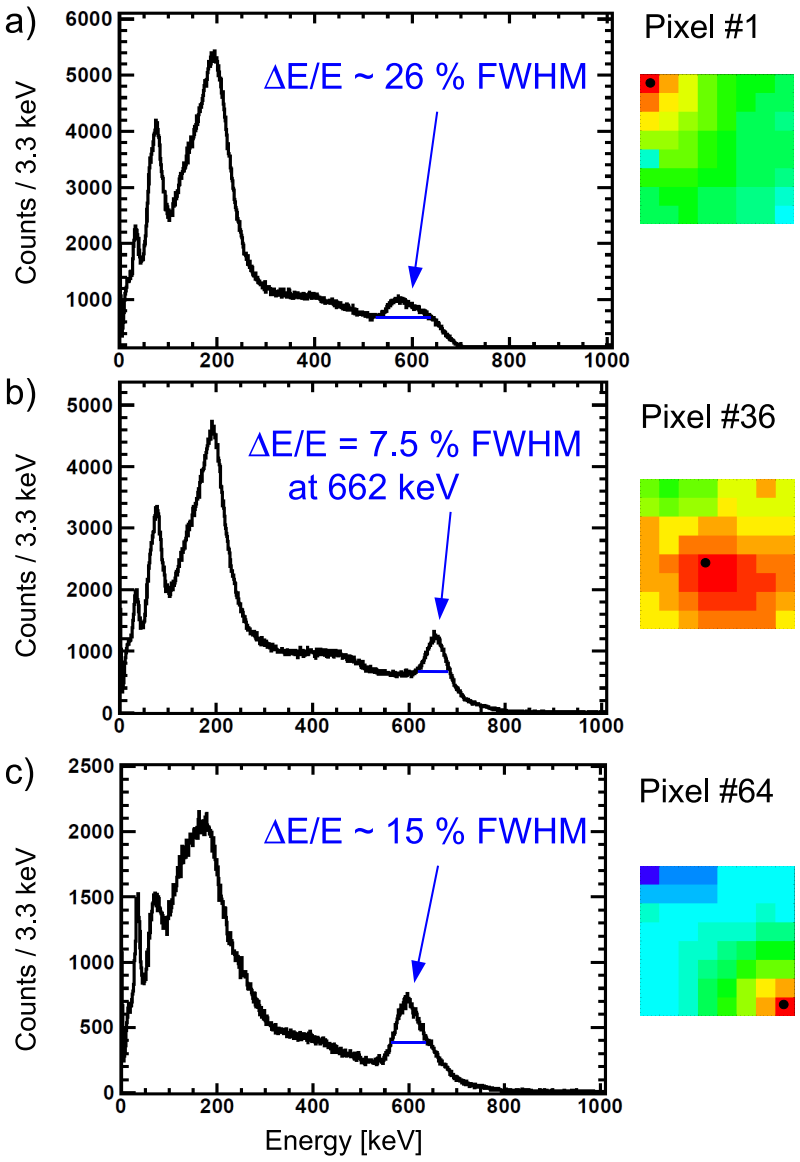

Figure 6.15: Three γ-ray energy spectra of the $LaBr_3$:Ce scintillator, measured with the PMT sum dynode, of a collimated ^{137}Cs γ calibration source, irradiating two diagonal corner pixels (panel a) and c)) and a central pixel (panel b)). The spectra show the 662 keV γ line, a strong Compton back-scattering contribution, the X-ray lines of the Pb collimator material and the X-ray lines of barium contained inside the LaBr crystal. The 662 keV line is strongly distorted and broadened in the corners, due to incomplete registration of the scintillation light by the absorptively wrapped crystal.

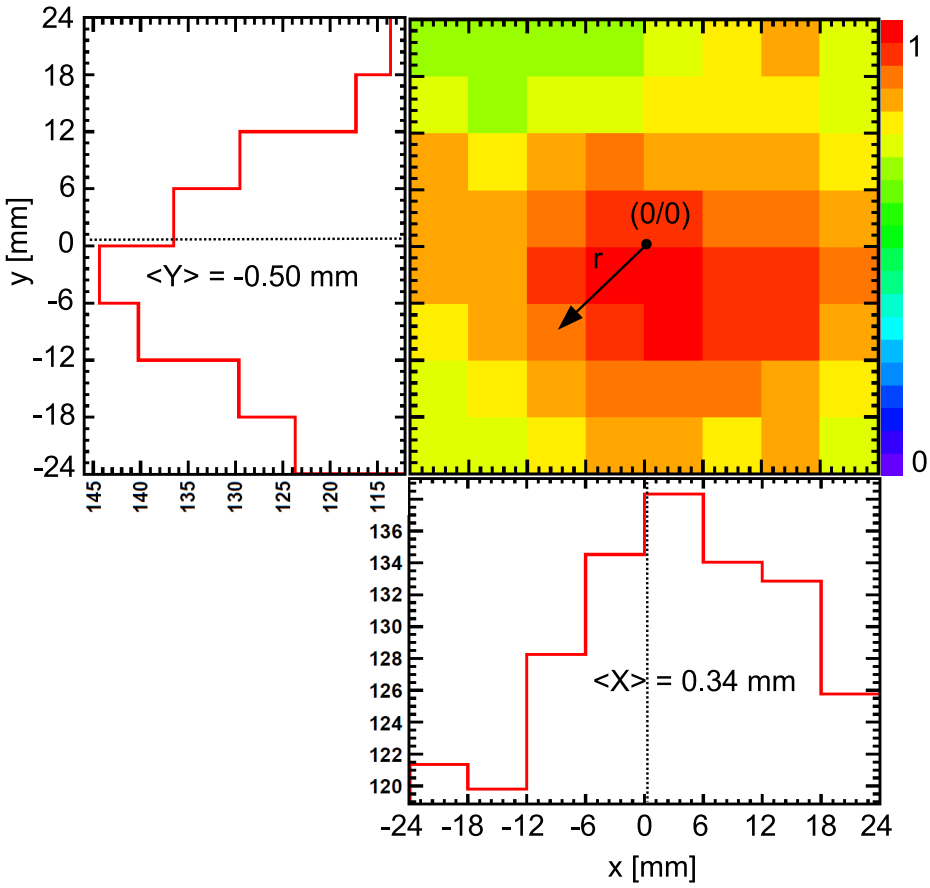

Figure 6.16: Charge distribution on the anode plane of the PMT and the corresponding projections on the X and Y axes, obtained from a collimated ^{137}Cs γ source irradiating the center of the scintillator. A slight offset with respect to the central irradiation position at (0,0) is noticeable. The dotted lines in the X and Y projections indicate the calculated mean values.

tion algorithm for a obtaining a reliable assessment of the spatial resolution should be applied. A promising example is the "k-nearest-neighbor" algorithm developed at TU Delft [79]. Work in this direction has started after the completion of the experimental work of this thesis. Nevertheless, as a first approach, the CoG algorithm has been applied to the present data. By applying Eq. (6.2) and (6.3), the (X, Y) position of the photon incidence can be determined for each primary photon interaction:

$$< X > = \sum_{i=1}^{8} \sum_{j=1}^{8} \frac{Q_{ij} x_{ij}}{Q} \tag{6.2}$$

$$< Y > = \sum_{i=1}^{8} \sum_{j=1}^{8} \frac{Q_{ij} y_{ij}}{Q} \tag{6.3}$$

Pixel	X_0 [mm]	Y_0 [mm]	X^{max} [mm]	Y^{max} [mm]	<X> [mm]	<Y> [mm]	Pixel	X_0 [mm]	Y_0 [mm]	X^{max} [mm]	Y^{max} [mm]	<X> [mm]	<Y> [mm]
1	-21	21	-21	21	-2.1	1.3	33	-21	-3	-21	-3	-2.3	-0.87
2	-15	21	-21	21	-1.4	1.3	34	-15	-3	-21	-3	-1.6	-0.92
3	-9	21	-9	21	-0.15	1.5	35	-9	-3	-9	-3	-0.58	-1.3
4	-3	21	-3	21	0.66	1.4	36	-3	-3	-3	-3	0.54	-1.1
5	3	21	15	21	1.6	1.6	37	3	-3	3	-3	1.8	-1.2
6	9	21	15	21	2.1	1.8	38	9	-3	9	-3	2.1	-1.3
7	15	21	15	21	2.4	2.4	39	15	-3	15	-3	2.7	-1.3
8	21	21	15	21	2.5	2.5	40	21	-3	21	-3	3.0	-1.2
9	-21	15	-21	21	-2.3	1.1	41	-21	-9	-21	-9	-2.3	-1.5
10	-15	15	-21	21	-1.7	5.1	42	-15	-9	-21	-9	-1.5	-1.7
11	-9	15	-9	15	-0.34	1.1	43	-9	-9	-9	-9	-0.51	-1.8
12	-3	15	-3	15	0.54	1.3	44	-3	-9	-3	-15	0.65	-1.9
13	3	15	15	21	1.5	1.4	45	3	-9	3	-9	1.7	-2.3
14	9	15	15	21	2.1	1.6	46	9	-9	9	-15	2.2	-2.2
15	15	15	15	21	2.4	1.9	47	15	-9	15	-9	2.8	-2.4
16	21	15	15	21	2.8	2.0	48	21	-9	21	-15	3.1	-2.4
17	-21	9	-21	9	-3.6	-0.61	49	-21	-15	-21	-21	-2.3	-2.0
18	-15	9	-21	9	-1.7	0.53	50	-15	-15	-21	-21	-1.5	-2.2
19	-9	9	-9	9	-0.61	0.59	51	-9	-15	-9	-21	0.21	4.1
20	-3	9	-3	9	0.53	0.61	52	-3	-15	-3	-21	0.65	-2.5
21	3	9	3	9	1.4	0.60	53	3	-15	3	-21	1.5	-2.7
22	9	9	15	21	2.1	0.68	54	9	-15	9	-21	2.4	-2.9
23	15	9	15	9	2.5	1.0	55	15	-15	21	-21	2.7	-3.1
24	21	9	21	9	2.9	1.1	56	21	-15	21	-21	3.3	-3.6
25	-21	3	-21	-3	-2.4	-0.17	57	-21	-21	-21	-21	-2.0	-2.1
26	-15	3	-21	-3	-1.5	-0.25	58	-15	-21	-15	-21	-1.3	-2.4
27	-9	3	-9	-3	-0.29	-0.54	59	-9	-21	-9	-21	-0.30	-2.6
28	-3	3	-3	-3	0.58	-0.28	60	-3	-21	-3	-21	0.78	-2.7
29	3	3	3	3	1.5	1.5	61	3	-21	3	-21	1.6	-3.0
30	9	3	15	-3	2.1	-0.30	62	9	-21	9	-21	2.2	-3.2
31	15	3	15	-3	2.6	-0.12	63	15	-21	21	-21	2.5	-3.4
32	21	3	21	3	2.9	-0.077	64	21	-21	21	-21	3.0	-3.6

Table 6.1: All 64 irradiation positions X_0, Y_0 and the resulting maximum values X^{max}, Y^{max} as well as the mean values <X>, <Y> of the charge distribution on the anode plane of the PMT. It can be seen that the maximum of the charge distribution is ambiguous (e.g. for pixel 5 - 8, corresponding to different irradiation positions X_0, but resulting in the same maximum value X^{max}, while the mean values <X> differ from each other).

The pixel positions x_{ij} and y_{ij} are weighed with the corresponding position-dependent charge Q_{ij} and normalized to the total charge Q.

On the basis of error propagation, it is possible to derive an estimate of the spatial resolution of the $LaBr_3$ scintillator [153], using the CoG algorithm, by

$$\sigma_{<X>} = \frac{1}{\sqrt{N_{ph}}} \sqrt{\sum_{i=1}^{8} (\sum_{j=1}^{8} (x_i - x_j) f_i)^2 f_i} \tag{6.4}$$

where f_i is a form factor of the projected charge distribution on the anode plane, roughly representing the spatial extension of the light amlitude distribution. Eq. (6.4) can be simplified according to Pani [153] as

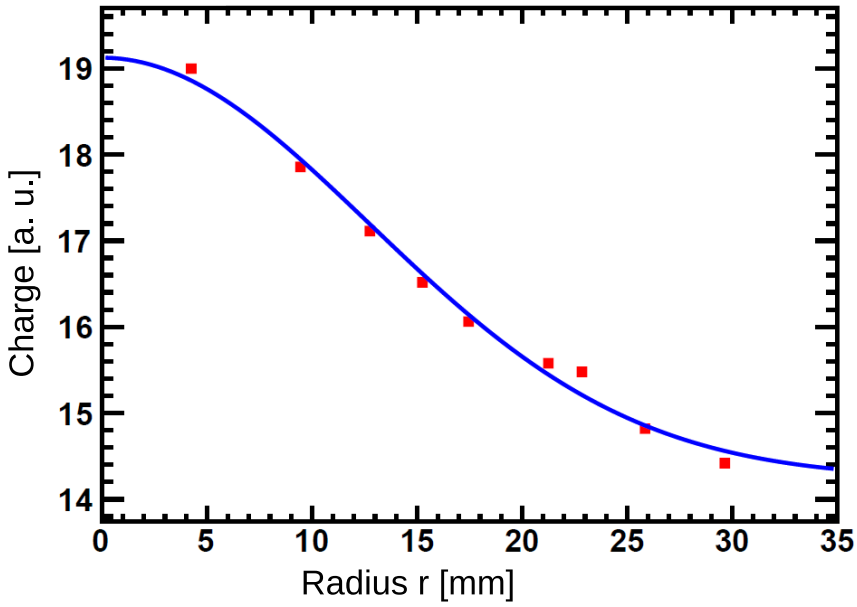

Figure 6.17: Charge distribution on the anode plane of the PMT as a radial projection, showing the point spread function with a FWHM of 29.5 mm for the absorptively wrapped $LaBr_3$ crystal.

$$\mathrm{SR} = \mathrm{PSF}\,\frac{\Delta E}{E} \tag{6.5}$$

where PSF (Point Spread Function (FWHM)) represents the charge distribution registered at the anode plane of the PMT as shown in Fig. 6.17. According to Eq. (6.5) and using the energy resolution map of Fig. 6.6 together with a PSF of 29.5 mm (FWHM), the theoretical spatial resolution is expected to be roughly 3 mm in the crystal center, and 5 mm in the crystal corner, for 662 keV incident photon energy.
Figure 6.18 shows the resulting CoG reconstruction for 64 light distribution response matrices of the $LaBr_3$ scintillator to the collimated ^{137}Cs γ source in one plot. The 64 irradiation positions (6 mm distance each) are indicated by black circles in the upper panel of the figure, the lower part shows a zoomed view of the central CoG reconstruction region. A common feature of the algorithm is the constrained projection of the position reconstruction, reasonably considering this as a plot of mean values. These mean values have to be assigned to the real irradiating positions for the determination of the photon interaction. In the center part of the crystal is it possible to distinguish the different irradiating positions, in contrast to the edge and the corner of the crystal, which show, as expected, a worse spatial resolution compared to the center. It should be considered that Eq. (6.5) is only a coarse estimate of the expected spatial resolution. The implementation of the k-nearest-neighbor algorithm developed at TU Delft [79] for the position reconstruction of absorbed photons, is presently in progress, but beyond the scope of this thesis.

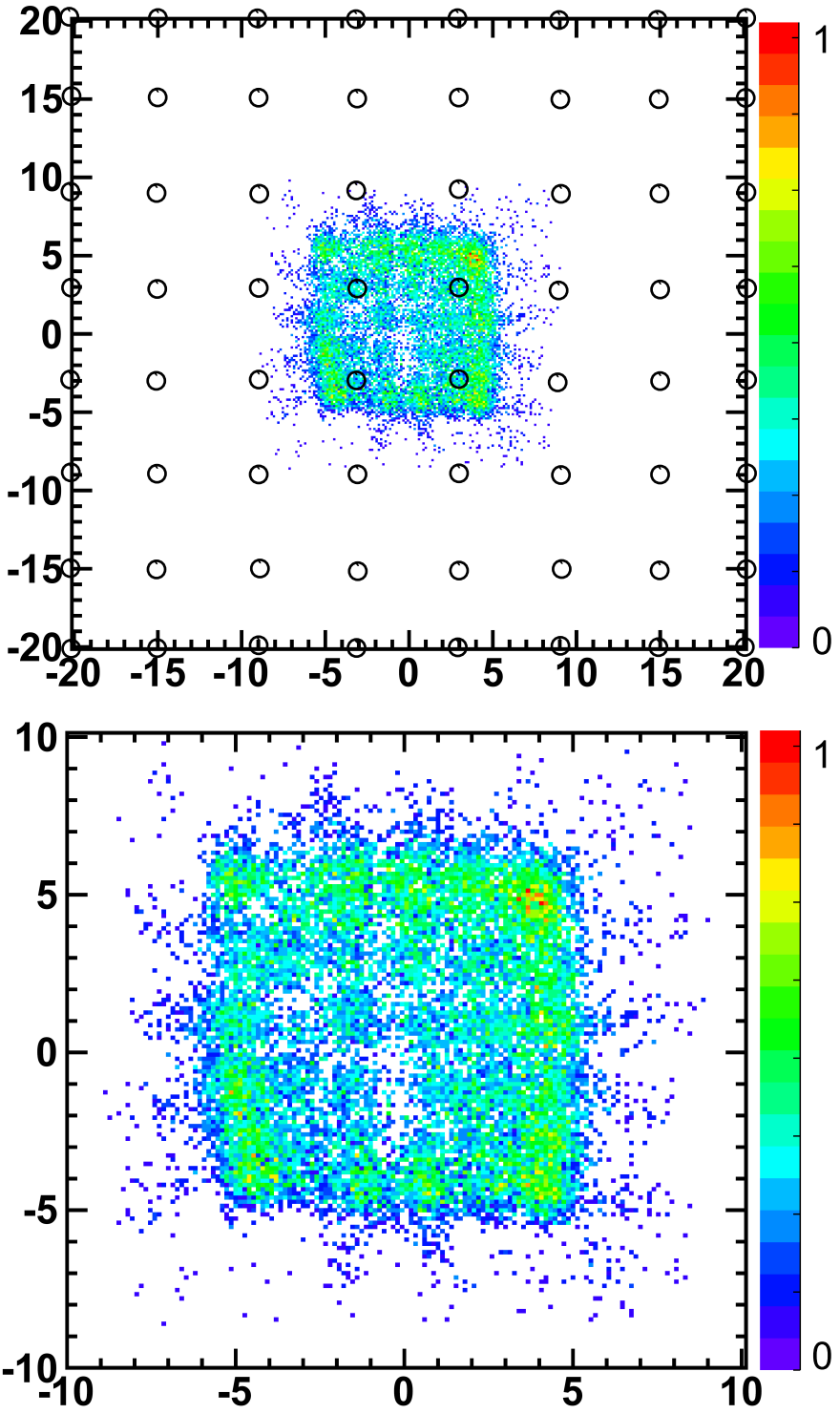

Figure 6.18: Center-of-Gravity reconstructions for 64 light amplitude response matrices of the (absorptively wrapped) $LaBr_3$ scintillator to a collimated ^{137}Cs γ source. In the upper part, the 64 irradiating positions are indicated by black circles, the lower part shows a zoomed view of the central region of the CoG reconstruction.

6.2 Compton camera scatterer: double-sided silicon strip detectors (DSSSD)

As introduced in Sect. 5.2, the optimized scatter/tracker detector of the Compton camera, enabling tracking of the Compton-scattered electrons, consists of a stack of 6 double-sided silicon strip detectors (DSSSD) with a thickness of 500 μm each, an active area of 50 x 50 mm^2 and a segmentation of 128 strips per side (pitch size 390 μm). In this section, the design considerations of the DSSSDs will be explained more specifically, in terms of design considerations for the scatter/tracker detector, its operational conditions and first characterization measurements of the DSSSD array.

6.2.1 Design of the DSSSD

The double-sided silicon strip detectors have been manufactured according to customer specifications by CiS in Erfurt (CiS Forschungszentrum für Mikrosensorik and Photovoltaik GmbH [156]). The detector assembly was manufactured by CiS, being specialized in semiconductor sensor design. Consequently, the connecting printed circuit board had to be designed according to our detailed specifications. Fig. 6.19 shows the layout as a technical drawing of the board and the wafer. The wafer exhibits a thickness of 500 μm, an active area of 50 x 50 mm^2 and consists of 256 strips, with 128 strips on the p side and 128 perpendicular strips on the n side (each with a pitch size of 390 μm). Four connector pads with 64 channels each are foreseen to position the 68 pin high-density connectors (type: BLR 4 100 (female), SLR 4 100 (male) [157]) to read out the 64 odd strips and the 64 even strips on the opposite sides of the p side and n side of the wafer, respectively. Thus all four connectors are placed on the p side (front side) of the detector, since the contacts to the strips of the n side are fed via through-going contacts towards their connector pads. A top view of one module of the scatter/tracker array can be seen in Fig. 6.20, the four additional 10-pin connectors in the corners provide electrical contacts for the chip border (metallized frame) and the guard ring of the detector (both on ground potential). Displayed in Appendix D are the technical drawings of the DSSSD board, showing the pin assignment.

The resistivity of the wafer was specified to be $>$ 10 kΩcm, with a depletion voltage of $\approx$ -75 V. The specified leakage current is $<$ 1 μA at a depletion voltage of -75 V.

For illustration, a photograph of the whole scatter/tracker array, consisting of 7 DSSSD modules, is visible in Fig. 6.21 (the photograph includes a spare detector module). The 6 detector modules are separated by a distance of 10 mm, as optimized in the MC simulations for a distance between the γ source and the first silicon detector of 50 mm. This geometry corresponds to the targeted scenario of small animal imaging at the upcoming Garching laser acceleration facility CALA, which is presently under construction [34] (see Sect. 3.2.1).

The stacked array of the 2D segmented detectors allows for tracking of the Compton recoil electrons, by detecting their trajectories and energies. Thus a reduction of the Compton cone to an arc segment will be enabled, allowing to reduce background and enabling to reconstruct incompletely absorbed Compton events. In turn, the reconstruction efficiency

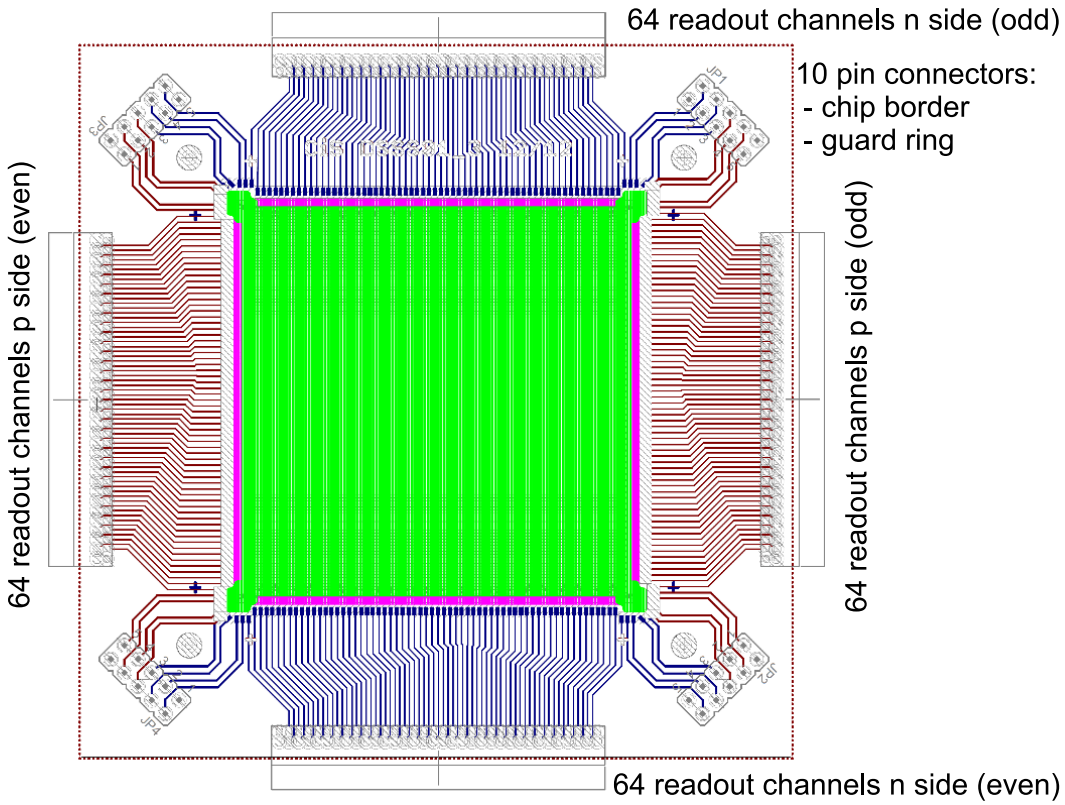

Figure 6.19: Technical drawing of a double-sided silicon strip detector used for the tracker array of the Compton camera prototype. The wafer exhibits a thickness of 500 μm, an active area of 50 x 50 mm^2 and consists of 128 strips on the p side and 128 perpendicular strips on the n side (pitch size 390 μm). On four sides of the board are the connector pads for the 4 x 64 channels (separated for even and odd channel numbers connecting on opposite sides of the sensor) for the readout of the p side and n side of the sensor, respectively. Four additional 10-pin connectors in the corners provide electrical contacts for the chip border (metallized frame) and the guard ring of the detector.

will be significantly increased by a factor of ≈ 2 for incoming photons with 5 MeV, compared to a Compton camera without electron tracking.

6.2.2 Operation and readout of the DSSSD

The scatter/tracker detector array, consisting of 6 DSSSD modules, comprises 6 x 256 electronic signal channels. This results in a significant electronic effort for processing these 1536 channels, solved by a readout with compact Application-Specific Integrated Circuits (ASICs), based on the GASSIPLEX chip [158].
Each GASSIPLEX-based readout board (so-called frontend (FE), see Fig. 6.24) can process 64 channels, and is connected via an AC coupler to the DSSSD detector, in order to protect the electronics from the high bias voltage applied to the detector (see Fig. 6.22). A sketch of the electrical network circuit of the AC coupler is displayed in Fig. 6.23. Each

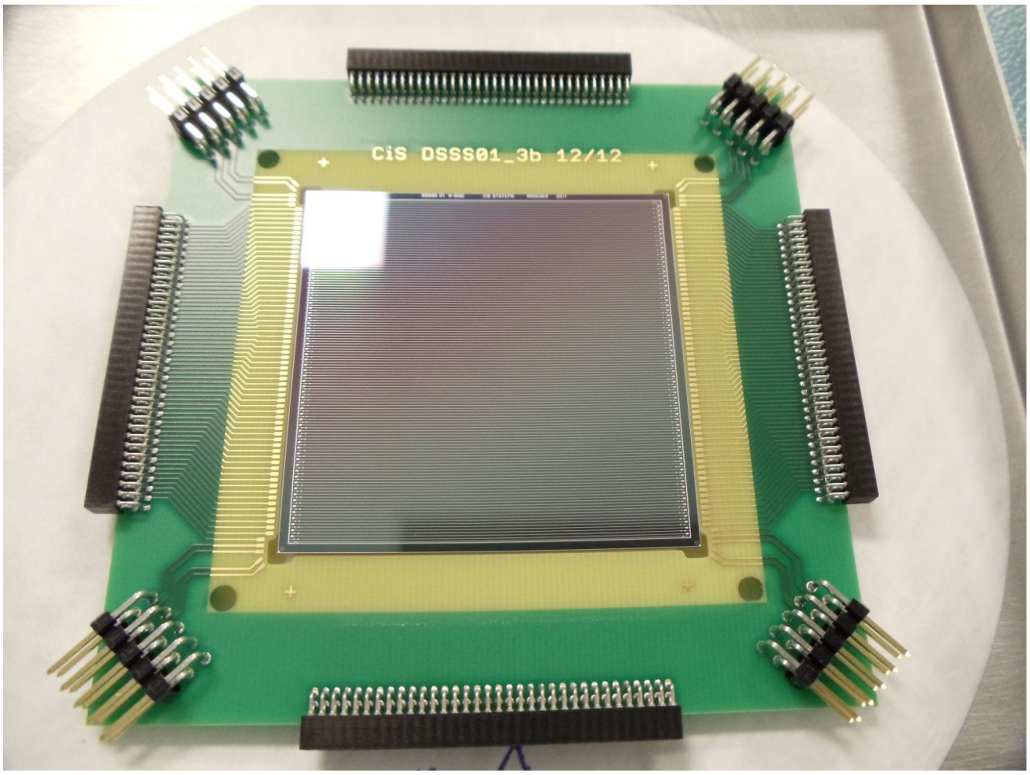

Figure 6.20: Top view of one DSSSD module of the scatterer array. Four high density connectors (68 pins) are positioned on the printed circuit board in order to read out the electrical signals of the 64 odd and 64 even strips of the n- and p sides of the silicon sensor on opposite sides of the p side (top side). Additional 10-pin connectors in the corners are foreseen for the electrical contact of the chip border (metallized frame) and of the guard ring (both on ground potential).

channel of the subsequent signal processing electronics is protected by a 10 MΩ and a 100 kΩ resistor from the reflux current of the bias voltage, limiting the current to μA during the bias voltage application. The detector side (in 1-64 in Fig. 6.23 (top)) is decoupled by a 1 nF capacitor from the frontend side (out 1-64). The p side of the detector is connected to negative bias voltage (typically -75 V), while the n side is coupled to ground potential.

ASIC-based readout

In the following, the silicon strip signal processing based on the frontend boards built around the charge integrating GASSIPLEX chips is described. Originally, the frontend boards were designed for the Ring Imaging Cherenkov detector (RICH) of the HADES experiment at GSI [159]. The frontend modules have been designed to process positive signals, due to their application in a multi-wire proportional chamber with cathode pad readout, where the cathode pads were operated on ground potential. A detailed description of the electronic readout system of the HADES RICH detector can be found in the diploma

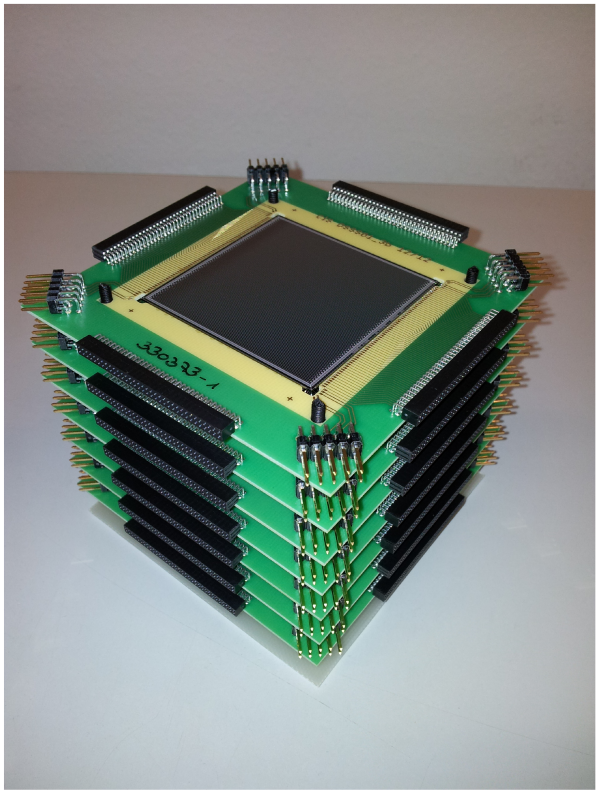

Figure 6.21: Photograph of the scatter array, consisting of 6 DSSSD modules, separated by a distance of 10 mm. Here 7 modules are shown, including one spare detector, not to be included in the final Compton camera assembly.

thesis of M. Böhmer [160].

Fig. 6.24 and Fig. 6.25 show a photograph and a block diagram, respectively, of the preprocessing frontend board. The most important electronic components are the four 16 channel GASSIPLEX ASIC chips, each consisting of a charge sensitive preamplifier, a shaper and a track & hold circuit for each channel. The shaper generates a nearly Gaussian shaped signal with a rise time of 550 ns. Therefore, the external readout trigger has to be delayed for the signal readout of the DSSSDs, which was chosen in the offline measurements as 600 ns for processing the maximum of the analog signal amplitude. The GASSIPLEX chips hold the actual analog values in their track & hold stage, initiated by an external TTL trigger, processed by a VME-based trigger unit (see Fig. 6.22). It is a disadvantage of the GASSIPLEX chip and the board built around it, that the GASSIPLEX chip is not capable of creating an internal trigger, also it is not possible to get access to the analog preamplified signals for monitoring purposes. Finally, the analog signals are amplified and multiplexed via a fast video multiplexing amplifier EL44441CS (for more information see the data sheet [163]) to the 20 MHz, 10 bit sampling analog-to-digital converter (ADC) ADS820 (data sheet [164]). In the logic part of the frontend module responsible for the data acquisition process, the data are compared to digital thresholds and

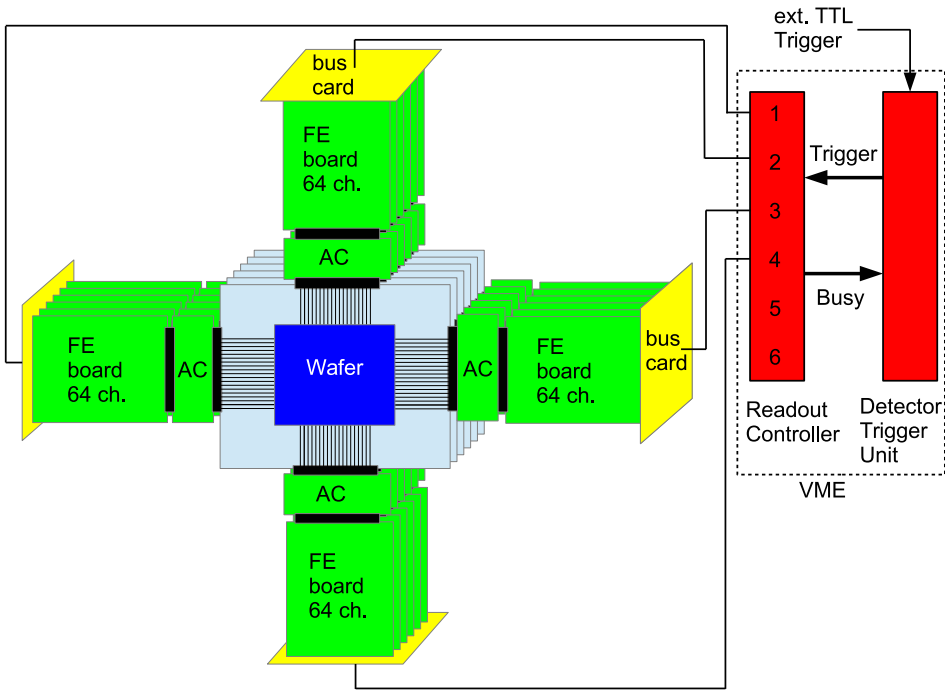

Figure 6.22: Sketch of the strip signal readout of an individual DSSSD detector module. Each readout module (so-called frontend board (FE)) built around the GASSIPLEX ASIC chip can process 64 channels, and is connected via an AC coupler to the DSSSD detector. In the stacked array of 6 DSSSD modules, each 6 frontend modules on one of the four sides of the stack are connected to four common bus cards, and only from there the signals are fed to the VME readout controller.

saved in the FIFO (First In First Out) memory storage bank together with a trigger tag, when exceeding the predefined individual channel specific thresholds. The FIFO memory chips are capable of buffering temporarily up to 15 full events (15 x 64 ADC values). Two different FIFO memory storage banks are implemented: an analog readout bank (ARD), which stores the digitized amplitude values of the event and a pattern readout bank (PRD), which stores the hit pattern of the event, originally implemented for direct Cherenkov ring identification in an Image Processing Unit (IPU) (not used here). The digital readout controlling part is handling the digital data transfer to the VME readout controller.

A sketch of the data readout chain for one quarter of the DSSSD array is displayed in Fig. 6.26. The readout system, in general, is capable of asynchronous data acquisition and data transfer. For the readout of 64 channels (out of 128) from one side of the DSSSD stack, 6 frontend modules (FE) are operated in a daisy-chained mode and connected via a bus card to the VME readout controller. The readout controller configures the (overall 24) frontend modules (by writing, e.g., threshold and mapping values) before starting the data acquisition. During data acquisition, the readout controller also transmits the (TTL) trigger signal received by the detector trigger unit to the frontends and controls the readout of the data temporarily stored in the FIFO memory banks on the frontend modules. The

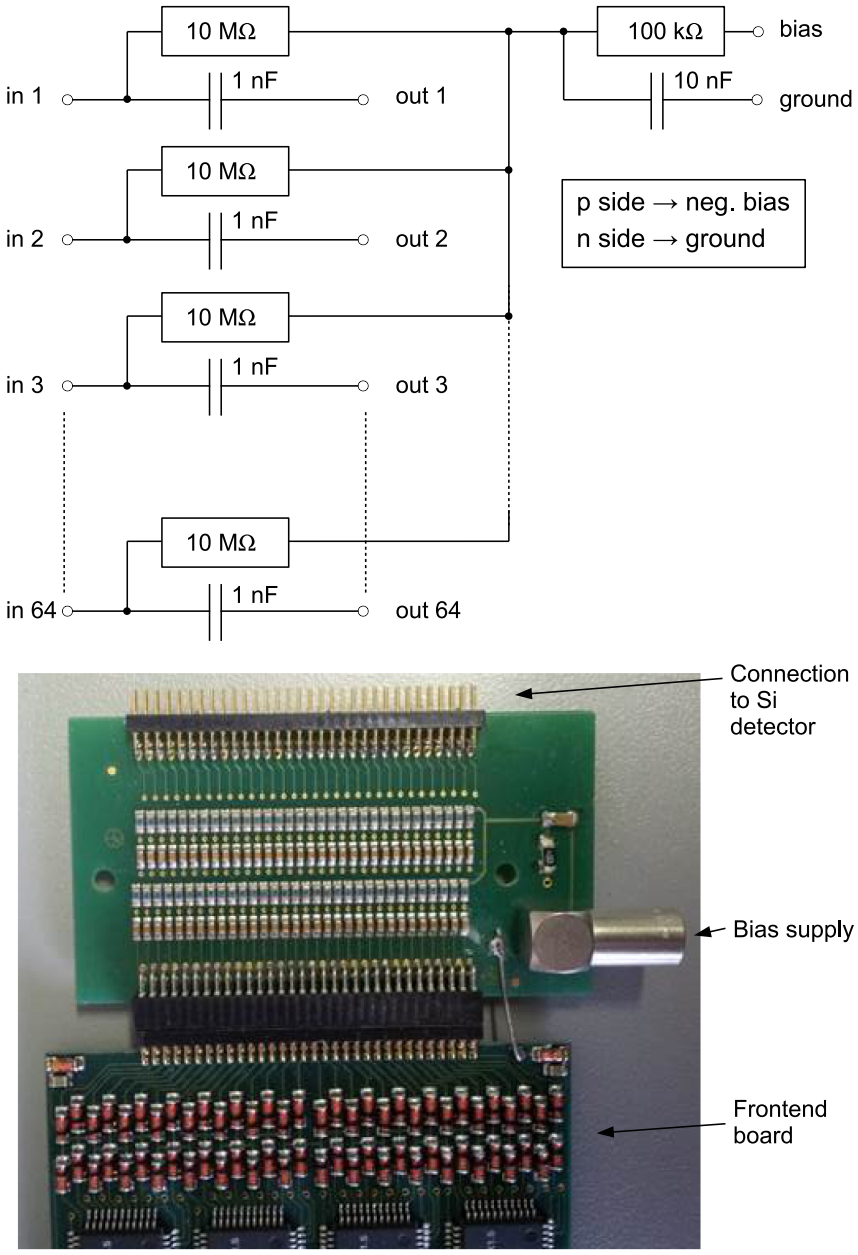

Figure 6.23: Top panel: Sketch of the electrical network of the AC coupling between individual strips of the Si detector and the subsequent signal processing electronics. Bottom panel: photograph of the AC coupler that serves to protect the subsequent signal processing electronics of the GASSIPLEX-based frontend module from the bias voltage applied to the DSSSD detector.

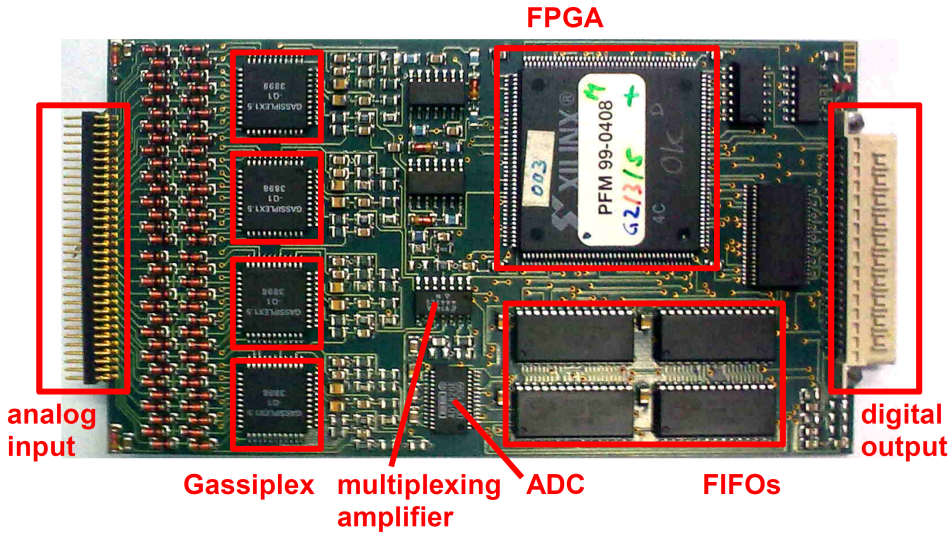

Figure 6.24: Photograph of the 64-channel readout frontend board (FE) based on the GASSIPLEX ASIC chip. Highlighted are the areas of the analog input, which is connected via the AC coupler to the detector strips, the four (16-channel) GASSIPLEX ASIC chips, the multiplexing amplifier and ADC stages, the FIFO registers for temporary event buffering, the FPGA, which is responsible for the data acquisition and transfer, and the digital output, which is connected to a common bus card that collects the data of up to 6 FE boards and transfers them to the VME-based readout controller [162].

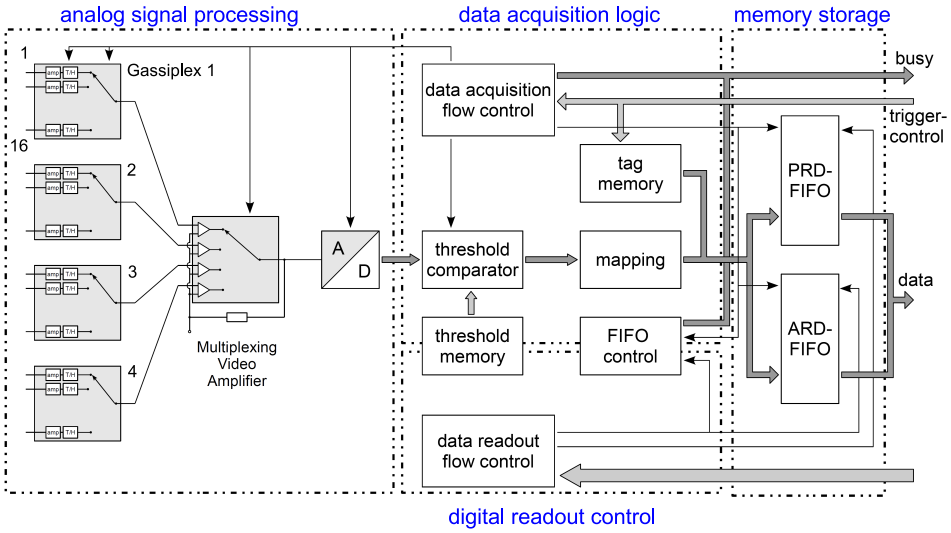

Figure 6.25: Block diagram of the 64-channel readout frontend boards based on the GASSIPLEX ASIC chip. The boards are divided in four processing blocks: (i) the analog processing part containing four GASSIPLEX chips, a multiplexing video amplifier and an ADC, (ii) the data acquisition logic consisting of a data acquisition flow control, threshold memory and threshold comparator, mapping unit and trigger tag memory, (iii) the PRD (pattern readout) and ARD (analog readout) FIFO memory storage banks (see text for details), (iv) and the block for the digital data readout flow control [160].

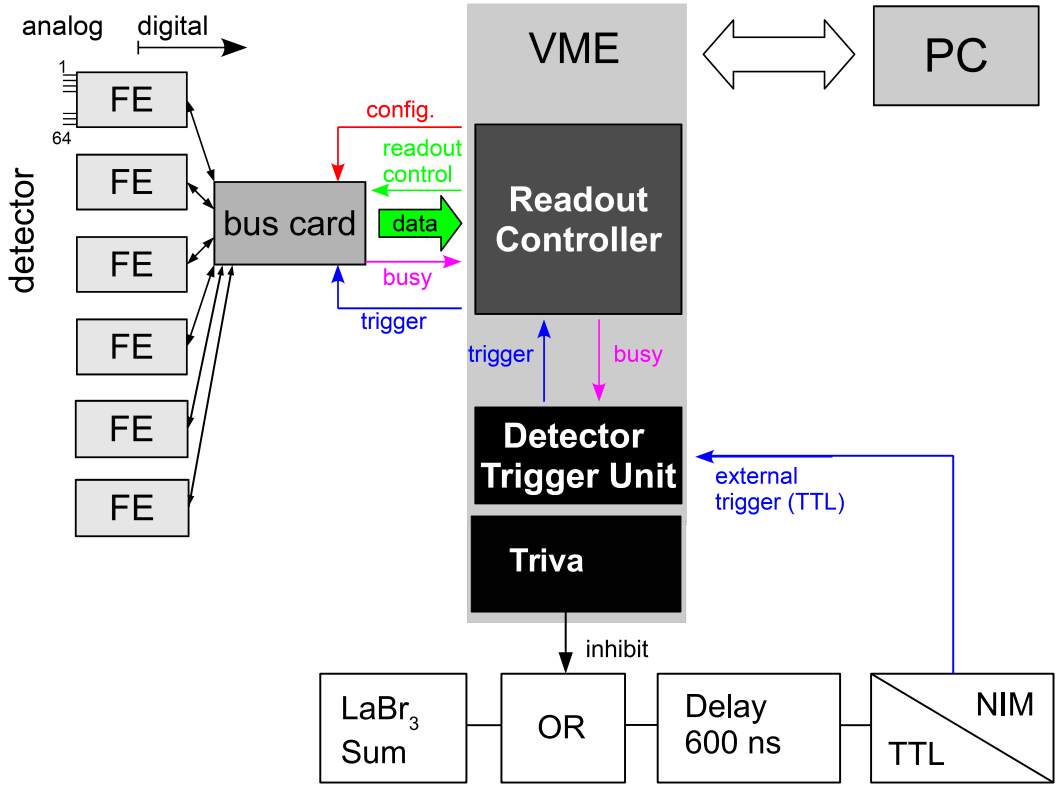

Figure 6.26: Sketch of the data readout chain, with a bus card connecting 6 frontend boards (FE) with the VME readout controller and the detector trigger unit . For the readout of the full DSSSD array of the Compton camera 4 bus cards are required. Figure adapted from [162].

readout controller communicates with the VME CPU and thus also with the PC. The detector trigger unit also accepts external trigger signals and takes care of the busy signal generated by the frontend modules or the readout controller.

Adaptation of the frontend modules for DSSSD signal readout

Originally, the frontend boards were designed for positive signal processing, due to their application in the RICH detector of the HADES experiment, where a multi-wire proportional chamber with cathode pad readout was implemented, with the cathode pads operated on ground potential. In contrast, the electronic signals to be received from the n- and p-side contacts of the DSSSD modules comprise both polarities. Hence, an adaptation of the frontend boards for the readout of the DSSSDs' positive and negative signals (in particular the latter originating from the n side) had to be performed. The procedure presented here for the adaptation of the frontend modules to negative signals follows the detailed description given in the diploma thesis of J. Bortfeldt [162].
The multiplexing video amplifier is built on four non-inverting voltage amplifiers, where the inverting (negative) inputs of the four operational amplifiers are connected, thus they

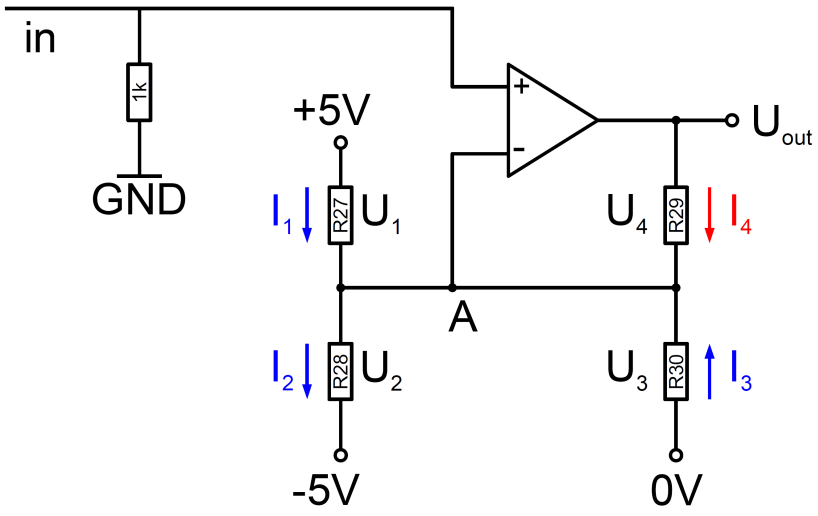

Figure 6.27: Electrical circuitry of the resistor configuration for the non-inverting operational amplifier at the multiplexing amplifier of the GASSIPLEX-based frontend board. The working point of the amplifier is denoted with A and can be altered by adjusting the values of the four resistors R27, R28, R30 and R30 [162].

are not individually accessible. The working point as well as the gain of these amplifiers can be commonly adjusted by choosing proper values of the four resistors R27, R28, R29 and R30 (see Fig. 6.27 for the resistor network).
The working point, i.e. the voltage at the inverting input, determines the lowest input voltage at the non-inverting input, resulting in a positive output signal for the input to the ADC (range +0.25 V to +4.25 V).
Based on the circuitry shown in Fig. 6.27, the resulting equations following Kirchhoff's voltage law are given by:

$$U_1 + U_2 - 10V = 0 \tag{6.6}$$
$$U_3 + U_2 - 5V = 0 \tag{6.7}$$
$$U_1 - U_4 - 5V + U_{out} = 0 \tag{6.8}$$
$$U_4 - U_3 - U_{out} = 0 \tag{6.9}$$

Applying Kirchhoff's current law for the currents flowing in and out of the node A gives:

$$I_3 + I_4 + I_1 = I_2 \tag{6.10}$$
$$\frac{U_3}{R30} + \frac{U_4}{R29} + \frac{U_1}{R27} = \frac{U_2}{R28} \tag{6.11}$$

Taking into account that an ideal behavior of an amplifier exhibits $U_{in+} = U_{in-}$ gives:

$$U_{in} = 5V - U_1 \tag{6.12}$$

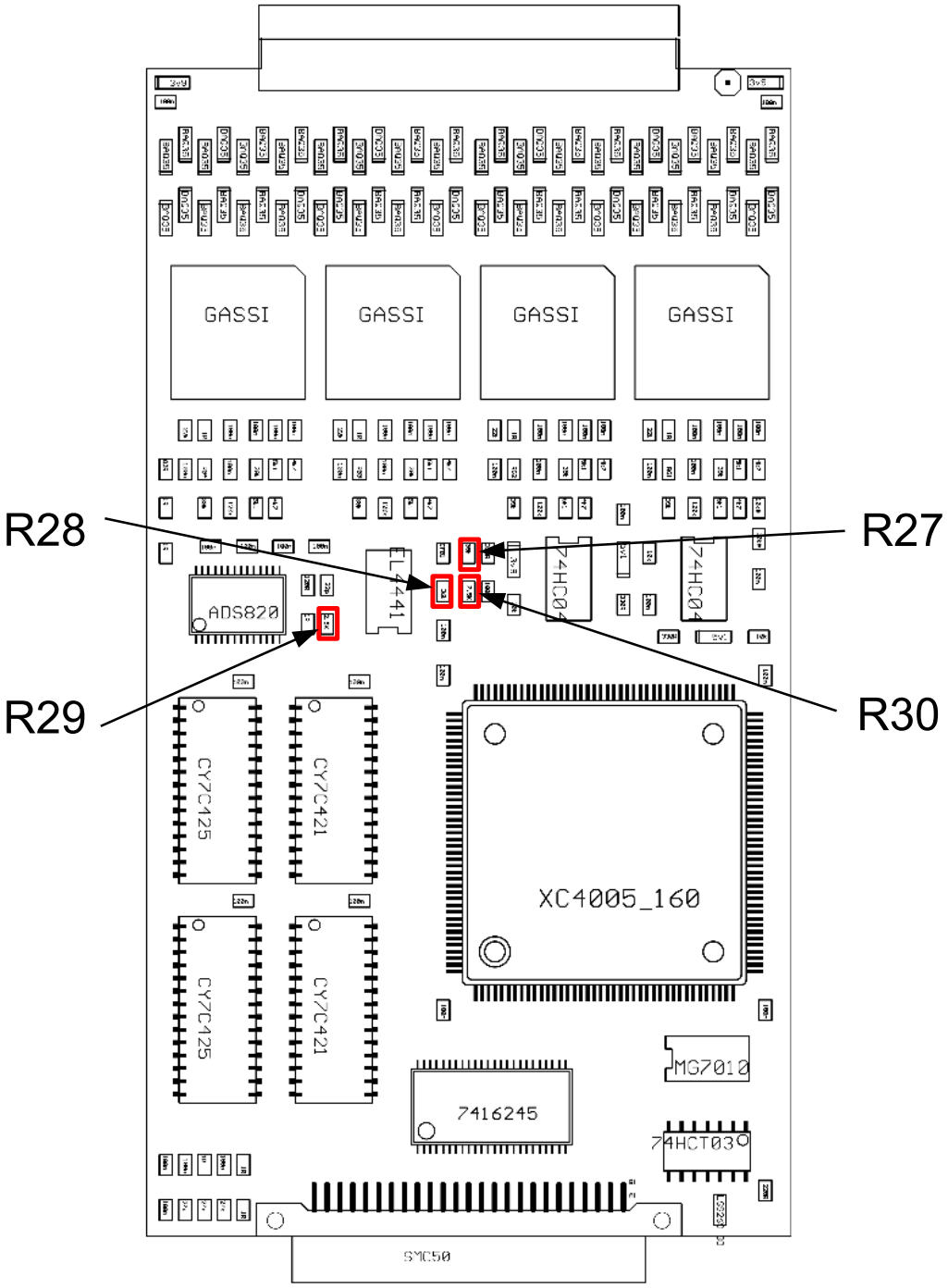

Figure 6.28: Schematic overview of the frontend readout board. The resistors that need to be adapted to be able to process negative signals (R27, R28, R29 and R30) are marked in red. Choosing proper values of the four resistors, the working point as well as the gain of the fast video multiplexing amplifier EL44441CS can be adjusted.

The output voltage U_{out} (baseline) of the amplifier can then be calculated from its input voltage U_{in}:

$$U_{out} = R29 \left(5V \left(\frac{1}{R28} - \frac{1}{R27} \right) + U_{in} \left(\frac{1}{R27} + \frac{1}{R28} + \frac{1}{R29} + \frac{1}{R30} \right) \right) \tag{6.13}$$

The gain factor of an operational amplifier can then be calculated by the definition:

$$G_U = \frac{U_{out1} - U_{out2}}{U_{in1} - U_{in2}} \tag{6.14}$$

with U_{in1}, U_{in2} and U_{out1}, U_{out2} as two different input and output voltages, respectively. Finally, the gain factor G_U can be expressed by the four resistors:

$$G_U = R29 \left(\frac{1}{R27} + \frac{1}{R28} + \frac{1}{R29} + \frac{1}{R30} \right) \tag{6.15}$$

Fig. 6.28 displays the schematic component layout overview of the frontend module. The resistors R27, R28, R29 and R30 that need to be adapted prior to processing negative signals are marked in red.

	HADES [160]	HERMES [165]	Micromegas [162]
R27 [Ω]	39k	33k	75k
R28 [Ω]	2.2k	4.5k	3.3k
R29 [Ω]	2.5k	3.3k	1.8k
R30 [Ω]	7.5k	8.2k	33k
baseline U_{out} [V]	0.47 ± 0.08	3.5 ± 0.11	2.85 ± 0.08
gain factor G_U	1.51	2.24	1.62

Table 6.2: Resistor configurations of three different experimental applications of the GASSIPLEX-based frontend boards together with the resulting U_{out} baseline voltage and gain factor.

	DSSSD p side (this work)	DSSSD n side (this work)
R27 [Ω]	75k	39k
R28 [Ω]	3.3k	2.2k
R29 [Ω]	1.8k	2.5k
R30 [Ω]	33k	7.5k
baseline U_{out} [V]	2.85 ± 0.08	0.47 ± 0.08
gain factor G_U	1.62	1.51

Table 6.3: Resistor configurations of the GASSIPLEX-based frontend boards together with the resulting U_{out} baseline voltage and gain factor for the readout of the DSSSDs' positive (p side) and negative signals (n side).

Table 6.2 shows different resistor configurations together with the resulting U_{out} baseline voltage and gain factor of three different experimental applications: for the original HADES experiment with positive signal readout of a multi-wire proportional chamber,

the modified configuration for the HERMES experiment at DESY [165] with first-time negative signal readout of a scintillating fiber detector and the resistor configuration for the readout of Micromegas tracking detectors (Micro-pattern gaseous detectors), developed for particle physics applications in the ATLAS collaboration at CERN [162]. Table 6.3 lists the resistor configurations realized for the readout of the positive and negative DSSSD signals studied within the present project. As a first approach, the same values for the baseline voltage and gain factor have been chosen for the readout of the negative (n-side) DSSSD signals, as applied for the Micromegas detectors, while for the readout of the positive (p-side) DSSSD signals the HADES resistor configuration has been adopted.

6.2.3 First characterization measurements

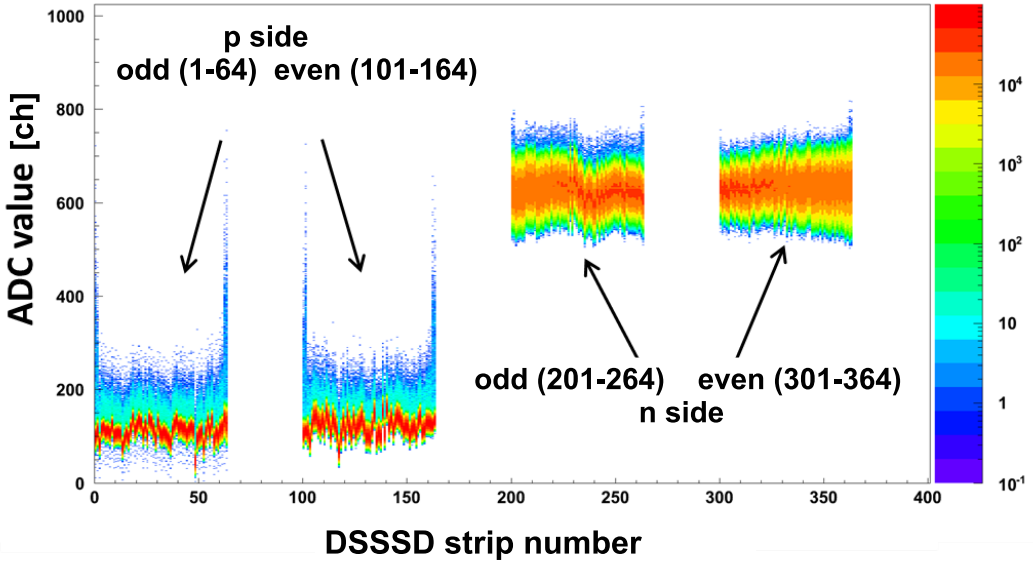

Figure 6.29: Measured energy spectra of all 256 strips of one of the silicon detectors, irradiated with a ^{60}Co γ source. Arranged on the horizontal axis are the 256 strips of the DSSSD and plotted on the vertical axis are the recorded ADC values. The intensity of the signal is displayed in a logarithmic color scale. Starting from the left, the first two structures belong to the p side of the DSSSD and represent the 64 even and 64 odd strips, respectively. The third and fourth structure correspond to the 64 even and 64 odd strips, respectively, of the n side of the DSSSD. The modification of the resistor configuration of the frontend modules resulted in the baseline shift of the n side to higher ADC values, thus enabling the handling of negative signals.

For the first characterization measurements, energy spectra for all 256 channels of one of the silicon strip detectors have been recorded, irradiated with a ^{60}Co γ source (activity: 32 kBq). The measurement was performed at atmospheric pressure, in a dark room. Fig. 6.29 shows the 256 strips of the DSSSD plotted on the horizontal axis (arranged such that each 64-channel block of even/odd strips from p- and n-side of the detector was sorted into an

increasing block of 100 spectral channels), while the recorded ADC value is depicted on the vertical axis and the intensity of the signal is indicated on a logarithmic color scale. Four structures are visible: starting from the left, the first two structures belong to the p side of the DSSSD and represent the 64 even and 64 the odd strips, respectively. The third and fourth structure correspond to the 64 even and 64 odd strips, respectively, of the n-side of the DSSSD.

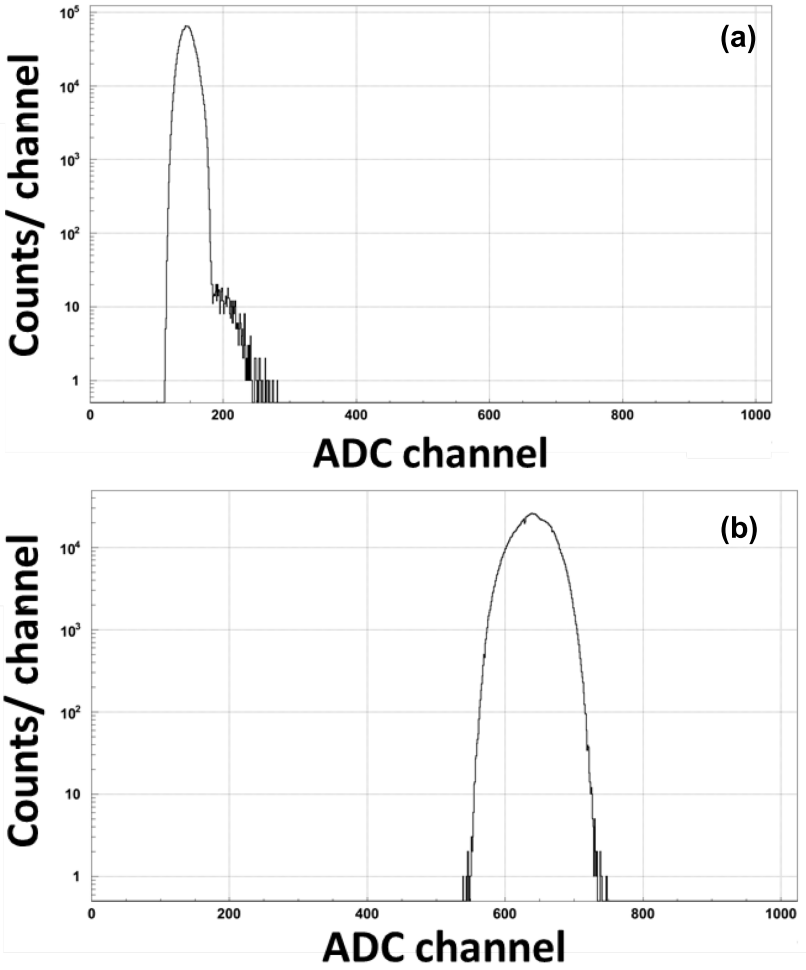

Figure 6.30: Two exemplary energy spectra of a p-side strip (a) and an n-side strip (b) of the silicon strip detector. The dominant peaks that can be observed in both spectra result from the dark currents ('pedestal') of the sensor (around ADC channel 150 for the p side and around channel 650 for the n side). The entries to the right from the pedestal peak on the p side can be attributed to the irradiation of the ^{60}Co γ source, whereas on the n side the pedestal was too broad to be able to identify the entries from the ^{60}Co source.

It can be seen that the baselines of the n-side strips have shifted to higher ADC values, due to the modification of the resistor network of the frontend modules. It should be noted that a further shift by about 200 channels would have been desirable to allow for

more efficient use of the ADC dynamic range. However, this is not feasible due to the multiplexing amplifier, which would run into saturation for a baseline value beyond +2.85 V. The measurements were performed with a set of prototype silicon detectors, which exhibited a higher dark current as specified, as can be seen in the broader distribution of the energy spectra of the n-side strips. These precursor modules were accepted from the manufacturer prior to the arrival of a second batch of modules, in order to be available for first characterization tests and for getting first operational experience with the readout of the silicon sensors. In Fig. 6.30, two exemplary energy spectra of a p-side strip (a) and an n-side strip (b) are shown. The dominant peaks on both strips result from the dark current of the detector (around ADC channel 150 for the p side and around 650 for the n side), while the structure to the right of the pedestal peak on the p side can be attributed to signals from the irradiation of the ^{60}Co γ source. As it can be seen, the large dark current on the n side completely covered the entries from the γ source. The delivery of the final batch of DSSSD detectors occurred after the completion of the experimental work of this thesis, so further characterization studies are subject to the PhD thesis of S. Aldawood [135].

6.2.4 Simulation of the energy deposition in the DSSSD stack

In order to obtain a quantitative prediction of the energy deposition in the DSSSD stack of the Compton camera from proton-induced prompt γ rays and to be able to optimize the gain of the multiplexing video amplifier of the frontend boards (see Sect. 6.2.2) according to the required dynamic range, MC simulations have been performed using GEANT4. The simulated geometry can be seen in Fig. 5.5. Fig. 6.31 displays the resulting energy deposition in the DSSSD stack for incident photons with an energy of 4.4 MeV, requiring a Compton scattering interaction with subsequent absorption of the scattered photon in the $LaBr_3$. The resulting energy spectra of the 6 DSSSDs show an increase of the registered intensity from the 1st (towards the calibration source) to the 6th (towards the $LaBr_3$ detector) DSSSD layer, together with an increasing peak at around 140 keV. This signature originates from the energy deposit of incident γ rays, being Compton scattered in one of the DSSSD layers, via their recoil electrons. In particular, the peak around 140 keV is indicating the resulting ΔE signal of electrons of $\gtrsim$ 1 MeV traversing 500 μm of Si (see also the energy loss plot for electrons in Si displayed in Fig 2.13).
The Compton electron energy from multi-MeV Compton-scattered photons are large enough to cross all six layers of DSSSDs, from it is evident that the increasing intensity of the ΔE peak with increasing depth of the Si stack reflects the accumulation of electron signals successively generated along the electron trajectory across the DSSSD stack. Almost no entries are registered in the DSSSD layers above 500 keV, thus providing an upper limit for the required dynamic range.

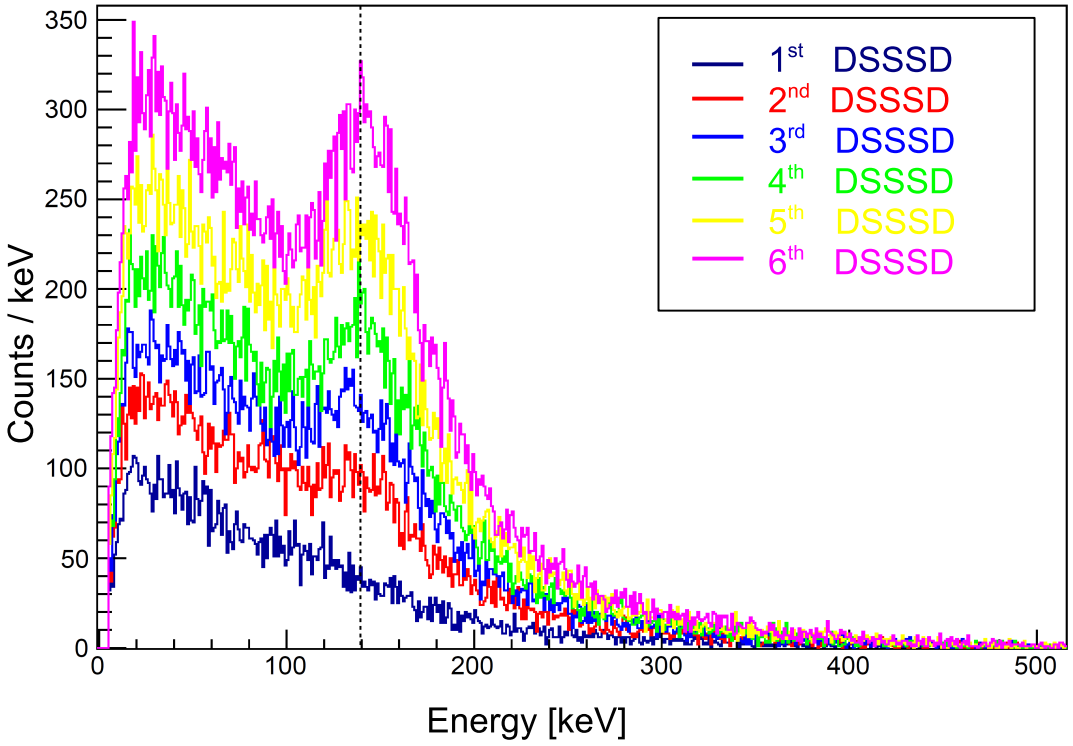

Figure 6.31: Monte-Carlo simulation (using GEANT4) of the energy deposition in the DSSSD stack for 4.4 MeV incident photons, where a Compton scattering interaction was required with subsequent absorption of the scattered photon in the $LaBr_3$ detector. The simulated geometry can be seen in Fig. 5.5. The registered intensity increases from the 1st (i.e. located towards the γ source) to the 6th (i.e. located in front of the $LaBr_3$ detector) DSSSD layer, originating from recoiling Compton electrons created in the previous DSSSD layers. Also an increasing peak at around 140 keV is visible, indicating the successively accumulating ΔE signal of electrons (with a energy of $\gtrsim$ 1 MeV) traversing 500 μm of Si.

6.3 2D segmented planar germanium detector

Semiconductor detectors exhibits a very good energy resolution compared to scintillation detectors. Detector materials, e.g. germanium, combine the ability of an excellent spatial (via segmentation) and energy resolution, together with a high material density (ρ_{Ge} = 5.33 g/cm^3), able to efficiently absorb energetic photons. High-purity germanium detectors (HPGe), cooled to liquid nitrogen temperature, show an excellent energy resolution of a few keV (typical: $\approx$ 2 keV at 1.3 MeV photon energy). A Compton camera consisting of a sufficiently thick, segmented semiconductor detector as absorber would profit in terms of spatial resolution of the reconstructed image (see Sect. 5.2.2).

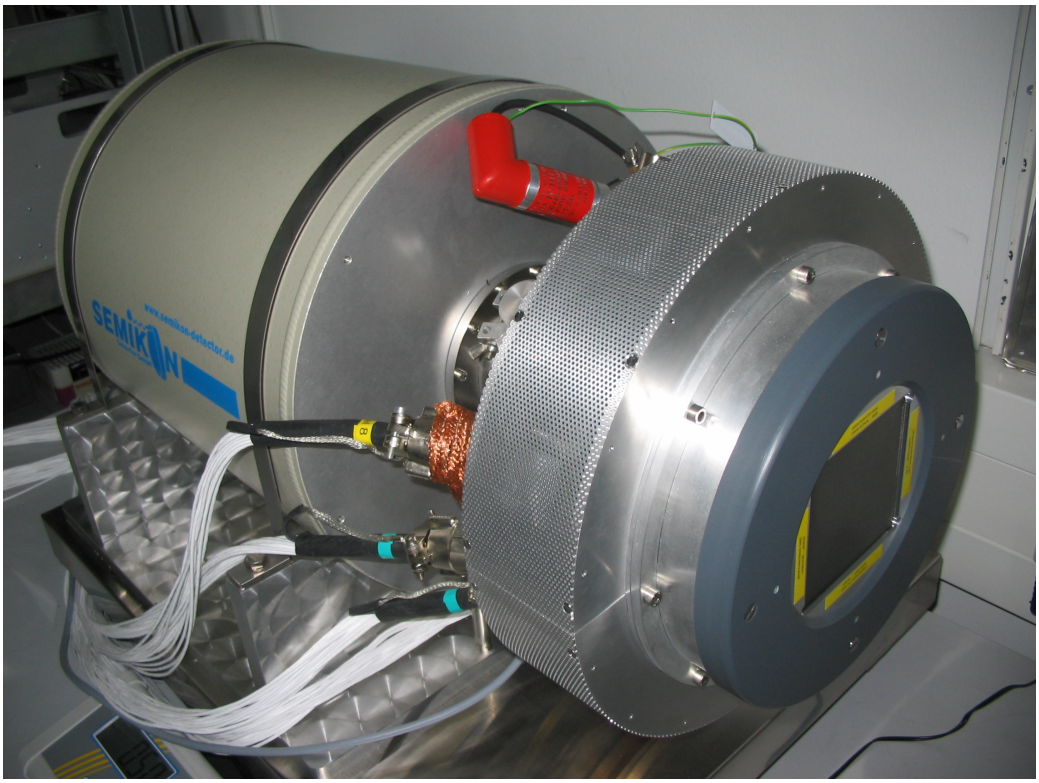

Figure 6.32: Photograph of the 2D segmented high-purity planar germanium detector. The circular aluminum housing contains 128 preamplifier boards, while the planar germanium crystal block is held behind a 0.5 mm beryllium entrance window under permanent vacuum. Attached to the housing is a dewar for cooling the crystal to liquid nitrogen temperature.

Figure 6.32 shows a photograph of a 2D segmented high-purity planar germanium detector, which could alternatively be used as absorber component in the Compton camera prototype. It consists of a rectangular block crystal (see Fig. 6.33) with an active volume of 64 x 64 x 15 mm^3 (in its first prototype version, later exchanged to the final crystal with 20 mm thickness) fabricated by the manufacturer SEMIKON [166]. The electrodes of the germanium crystal are 128-fold segmented with 64 parallel strips on each side, where

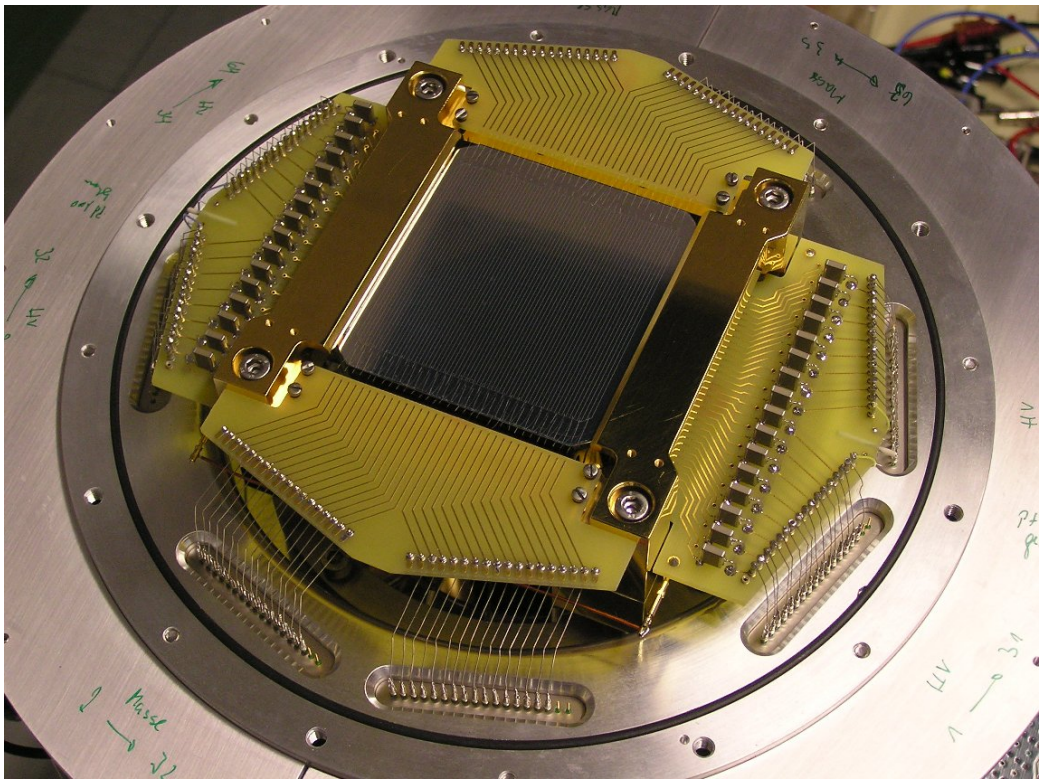

Figure 6.33: Photograph of the 128-fold segmented high-purity planar germanium crystal (thickness 15 mm). On each side, the wafer is segmented into 64 strips, with a width of 1 mm each, resulting in 128 signal channels for both sides. Visible are the boron implanted p^+ front-side contacts (p side). The even and odd channels lead to 2 boards, and branch out to 4x16 feedthroughs. On the boards of the amorphous Ge rear contacts (n side) capacitors and resistors are mounted, protecting the crystal from high currents.

the front-side strips are perpendicularly oriented with respect to the back-side strips, thus allowing for position sensitive readout. The strip width and pitch is 1 mm, resulting in a pseudo pixel size of 1 x 1 mm^2. The front-side contacts are boron implanted p^+-contacts (p side), the rear contacts consist of amorphous Ge contacts (n side). The amorphous Ge contact is realized by evaporating a germanium layer on to the crystal surface, followed by an aluminum layer [167]. The crystal is cooled to liquid nitrogen temperature and therefore has to be permanently kept under vacuum. The crystal surface is placed behind a 0.5 mm thick beryllium entrance window, resulting in a low photon energy threshold of approximately 5 keV. The detector discussed here represents a unique prototype, still suffering from some non-working strips and strips with increased leakage current, in particular at the edges of the (amorphous Ge) back-side contact, resulting in a reduced energy resolution. The 128 signals from the individual strip electrodes are separately preamplified in charge-sensitive preamplifier boards, directly mounted to the detector unit close to the Ge crystal (see Fig. 6.34).

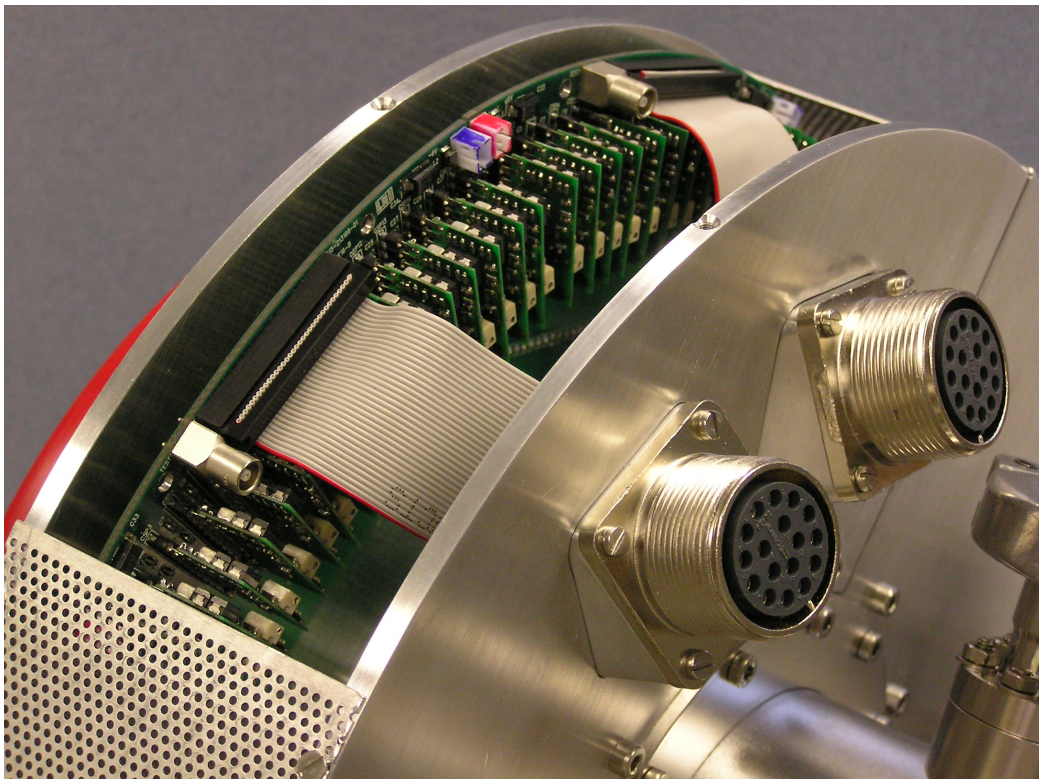

Figure 6.34: Photograph of the opened aluminum housing of the HPGe detector. Visible inside is a part of the 128 charge-sensitive preamplifier boards mounted close to the Ge crystal.

6.3.1 Electronic signal processing

While Fig. 6.35 shows a photograph of the signal processing and data acquisition electronics used to characterize the HPGe detector, Fig. 6.36 shows the corresponding schematics. After the preamplification of the 128 signals from the strip electrodes, the channels are evenly distributed to eight MSCF-16 modules from MESYTEC [168]. Each module contains 16 shaping amplifier channels with a selectable gain of 1, 3 or 10 for the analog signal processing and 16 timing filter amplifier together with 16 constant fraction discriminators for deriving precisely timed logical signals from the preamplifier output. An OR-trigger from the eight MSCF-16 modules is used for starting the data acquisition and for generating the ADC gate. Finally, the amplified signals and the gate are fed into VME-based analog-to-digital converter (ADC) units (Caen V785 [169]). The OR-trigger from the eight MSCF-16 modules is starting the readout procedure, afterwards the data are recorded via a VME CPU (PPC, RIO3 from CES) on a PC, and analyzed and visualized using the ROOT [140] based ”Marabou” acquisition system [141].

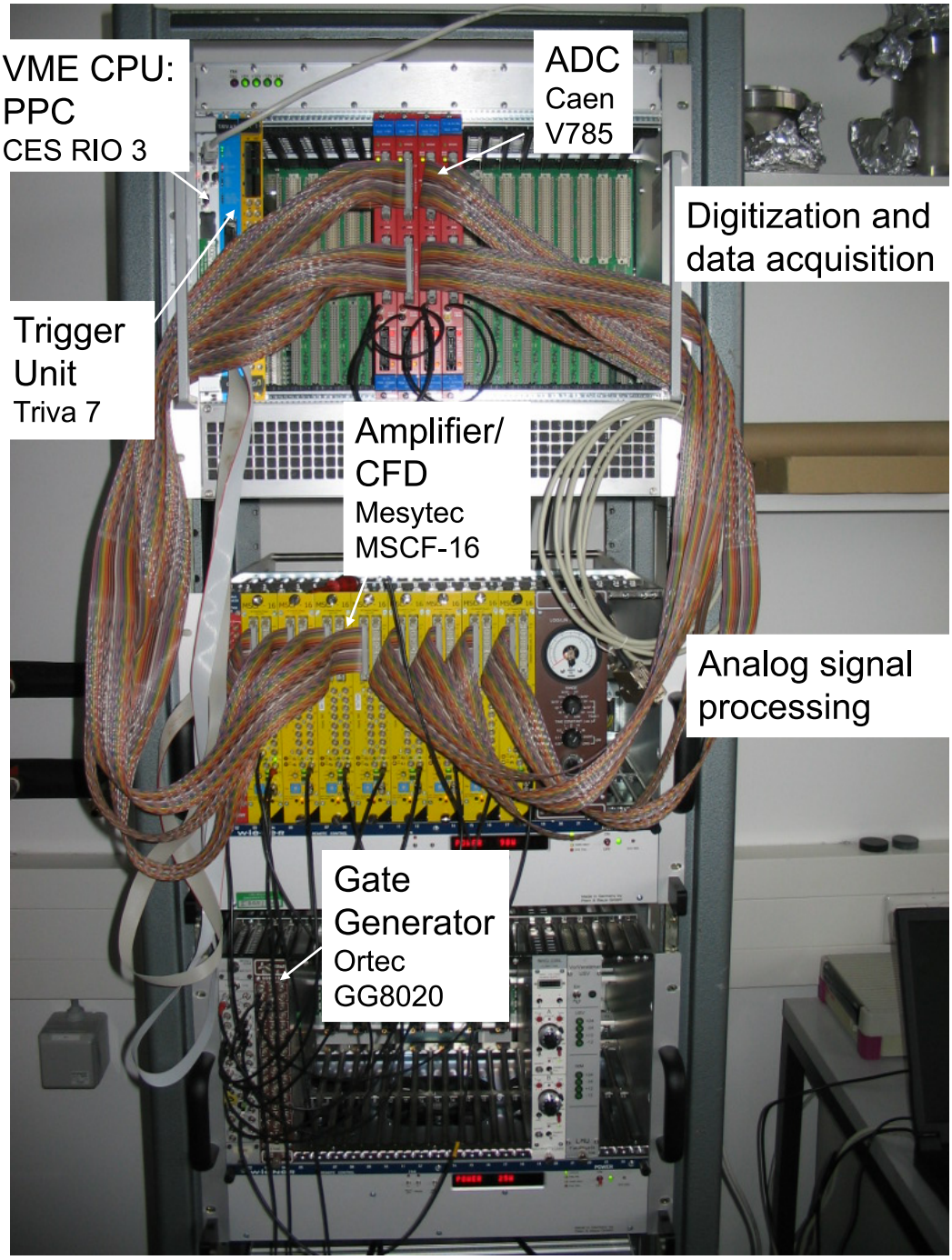

Figure 6.35: Photograph of the signal processing and data acquisition electronics used to characterize the high-purity planar germanium detector with 128-fold segmented electrode readout.

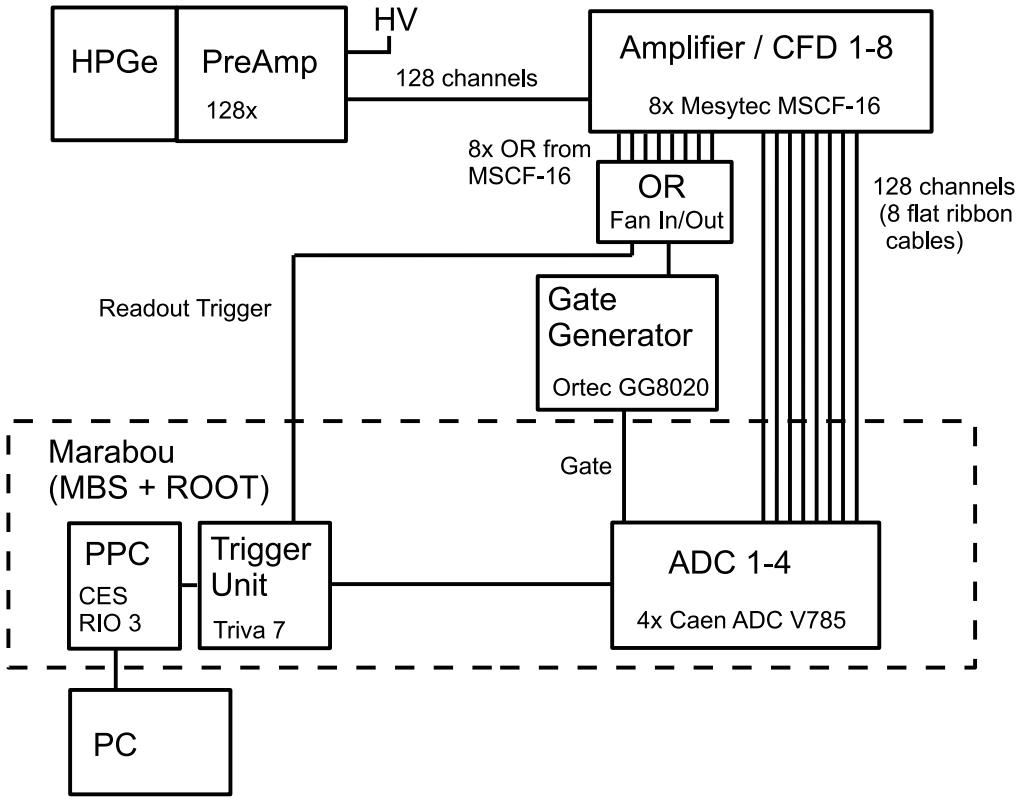

Figure 6.36: Schematics of the signal processing electronics used for the high-purity planar germanium detector. The energy signals from the 128-fold segmented electrodes (64 on each side) are first sent to a preamplification stage, afterwards the 128 channels are distributed to eight 16-channel shaping amplifier / Timing-Filter Amplifier and Constant Fraction Discriminator modules (MESYTEC MSFC-16). The output of the eight MSCF-16 modules was connected to four Analog-to-Digital converters (Caen V785). Data acquisition was performed using the VME-based Marabou system [141].

6.3.2 Energy Resolution

In order to determine the energy resolution of the high-purity planar germanium detector, two γ calibration sources (^{241}Am and ^{152}Eu) were placed in front of the HPGe detector in a distance of around 10 cm. The recorded energy spectrum of one typical strip on the p^+-side of the HPGe detector can be seen in Fig. 6.37. The 60 keV γ line of ^{241}Am and the 18 keV X-ray line from its daughter product ^{237}Np are visible in the dynamic range (up to $\approx$ 410 keV for an amplifier gain of 10), together with the 121 keV, 244 keV and 344 keV γ transition of ^{152}Eu. The 40 keV and 46 keV X-ray lines also visible in the spectrum originate from ^{152}Sm, which is the daughter product of ^{152}Eu. The shaping time of the amplifier was adjusted to 0.5 μs, and an energy threshold of 15 keV was chosen. The energy resolution at 121 keV was determined to be 2.5 keV (FWHM).

Fig. 6.38 shows the individual energy resolution at 121 keV for all strips and two values of the shaping time of 0.5 μs and 4.0 μs, respectively. Strips 1 - 64 correspond to the p^+-

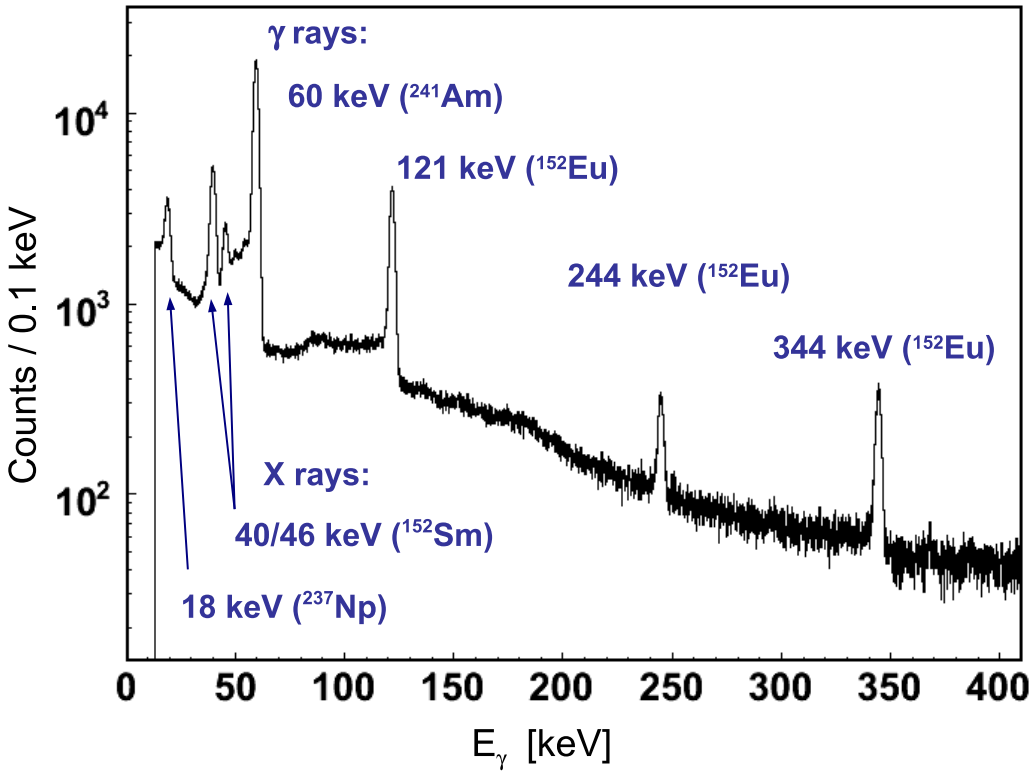

Figure 6.37: Measured γ-ray energy spectrum of one typical strip on the p^+-side of the HPGe detector, recorded from two different γ calibration sources (^{241}Am and ^{152}Eu). Visible in the dynamic range is the 60 keV γ line of ^{241}Am and the 18 keV X-ray line from its daughter product ^{237}Np, together with the 121 keV, 244 keV and 344 keV γ transitions of ^{152}Eu. Additionally visible are the 40 keV and 46 keV X-ray lines from ^{152}Sm, which is the daughter product of ^{152}Eu. The energy resolution at 121 keV is 2.5 keV (FWHM). An energy threshold of 15 keV was chosen.

contacts on the front side, and 65 - 128 correspond to the amorphous Ge contacts on the back side of the crystal. Caused by a higher leakage current, 5 strips in the center of the detector on the back side show a reduced energy resolution. Additionally, the strips at the edges of the back side exhibit a significantly reduced energy resolution, most likely caused by distortions of the electric field at the edges of the crystal. With increasing bias voltage, the depletion zone of this detector is expanding, starting from the boron implanted p^+ contacts on the front side to the amorphous Ge contacts on the back side by increasing the applied high voltage (here 2.1 kV, leakage current 27 nA). Therefore, the strips on the front side generally show a slightly better energy resolution compared to the strips on the back side. Two shaping times have been used: 0.5 μs (black dots) and 4.0 μs (red dots). In general, a shaping time of 4.0 μs provides a better energy resolution (front side: $\approx$2.0 keV, back side: $\approx$2.5 keV) compared to the shorter shaping time of 0.5 μs (front side: $\approx$2.7 keV, back side: $\approx$3 keV). Besides of an increased dead-time of the detector, the

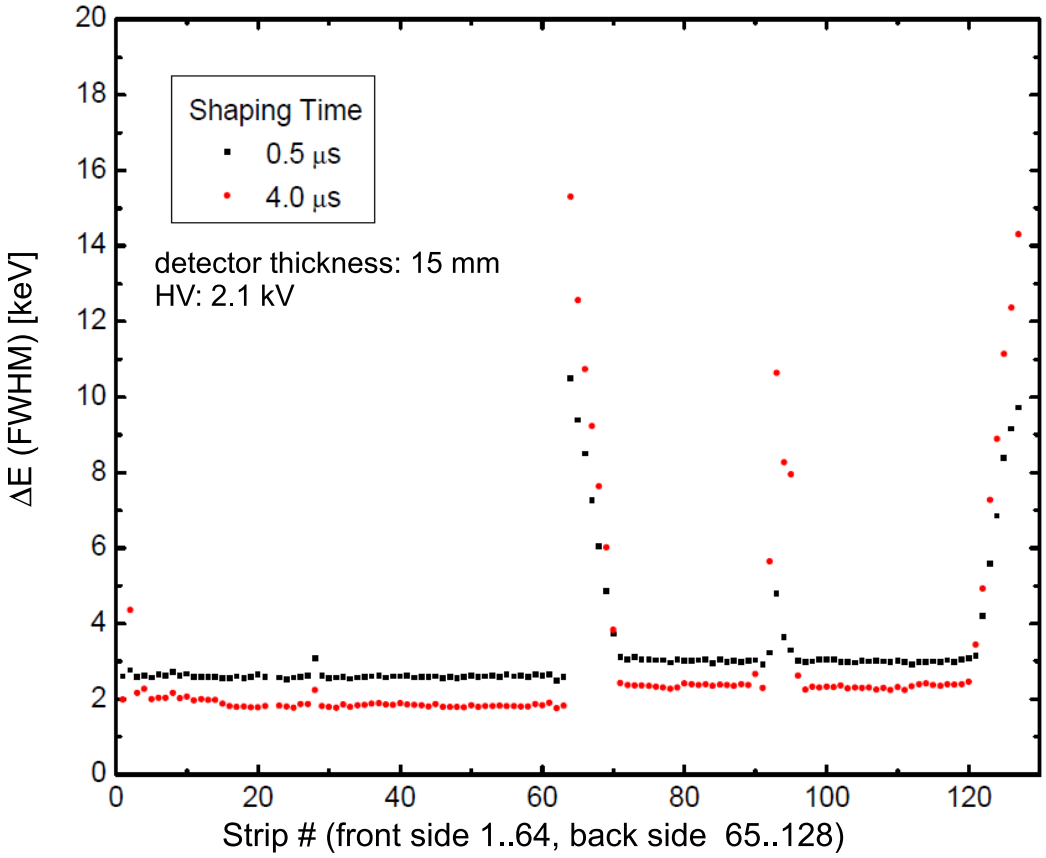

Figure 6.38: Individual energy resolution at 121 keV of all 128 strips for two options of the shaping time: 0.5 μs (black dots) and 4.0 μs (red dots). Strips 1 - 64 correspond to the p^+-side (front side), and 65 - 128 correspond to the amorphous Ge contact (back side).

disadvantage of the longer shaping time is a significantly degraded energy resolution of the center and edge strips on the back side in the case of this specific prototype detector crystal. Therefore, a shaping time of 0.5 μm has been chosen here as a compromise.

Different high voltages applied to the crystal have been investigated to study the effect of potential field distortions at the detector edges. The dependence of the energy resolution on three different high voltages of 2.1 kV (black dots), 2.2 kV (red dots) and 2.3 kV (blue dots) can be seen in Fig. 6.39. As expected, the energy resolution of the p^+-contacts on the front side (strip 1 - 64) shows no variation, however, the energy resolution of the amorphous Ge contacts (strip 65 - 128) was found to vary significantly. Fig. 6.40 shows an enlarged view of the data. The top and bottom panel display the edge strips, where an improvement of the energy resolution by almost a factor of 2 can be achieved by increasing the high voltage from 2.1 kV to 2.3 kV for about 7 strips at both edges of the back side, while the center strips (middle panel) significantly degrade for the same high voltage increase. (e.g. strip 96 and 94 degrade from $\approx$3 keV to $\approx$19 keV and from $\approx$5 keV to $\approx$14 keV, respectively). Additionally, the leakage current of the whole crystal

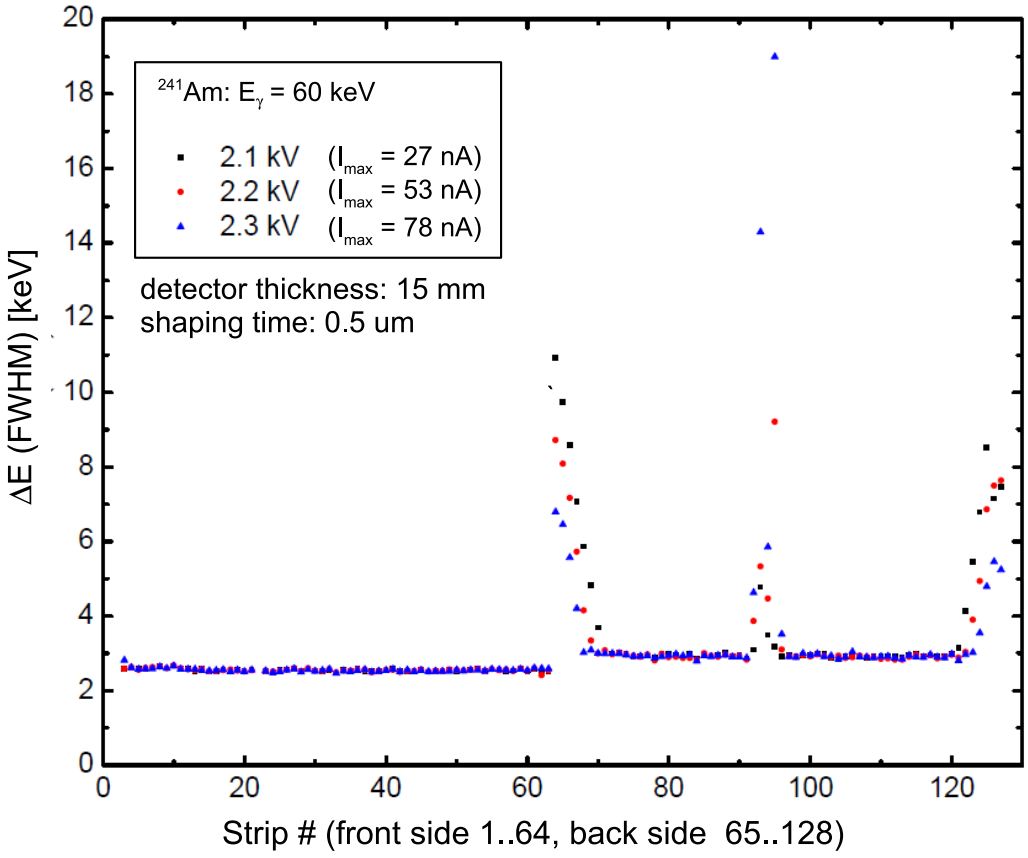

Figure 6.39: Individual energy resolution measured at 60 keV for all 128 strips as a function of three different detector bias voltages: 2.1 keV (black dots), 2.2 keV (red dots) and 2.3 keV (blue dots). Strip numbers 1 - 64 correspond to the p^+-side (front side), while strip numbers 65 - 128 belong to the amorphous Ge contact (back side).

strongly rises from 27 nA at 2.1 kV, over 53 nA at 2.2 kV, to 78 nA at 2.3 kV. After several iterative optimizations of the manufacturing process of this n-side contact, it is unlikely to blame the amorphous Ge contact itself being for the reason of this detector behavior. Rather, electric field distortions and charge carrier traps induced by crystal inhomogeneities and local impurities beyond specification could explain the poor quality at the edges of the n side. It should be noted that in the final version of the crystal (thickness 20 mm) these problems have been largely solved. The significantly degraded energy resolution of 5 central strips on the back side, potentially originating from local crystal defects or impurities, prevents the use of even higher bias voltages. Since these central strips critically influence the spatial event reconstruction, the applied high voltage was chosen as 2.1 kV to optimize the energy resolution in this area. The energy range up to 360 keV (full dynamic range is $\approx$ 410 keV for an amplifier gain of 10) of the HPGe is plotted in Fig. 6.41 for a shaping time of 0.5 μs and bias voltage of 2.1 kV (leakage current 27 nA). All 128 detector strips are visible, showing the individual differences of

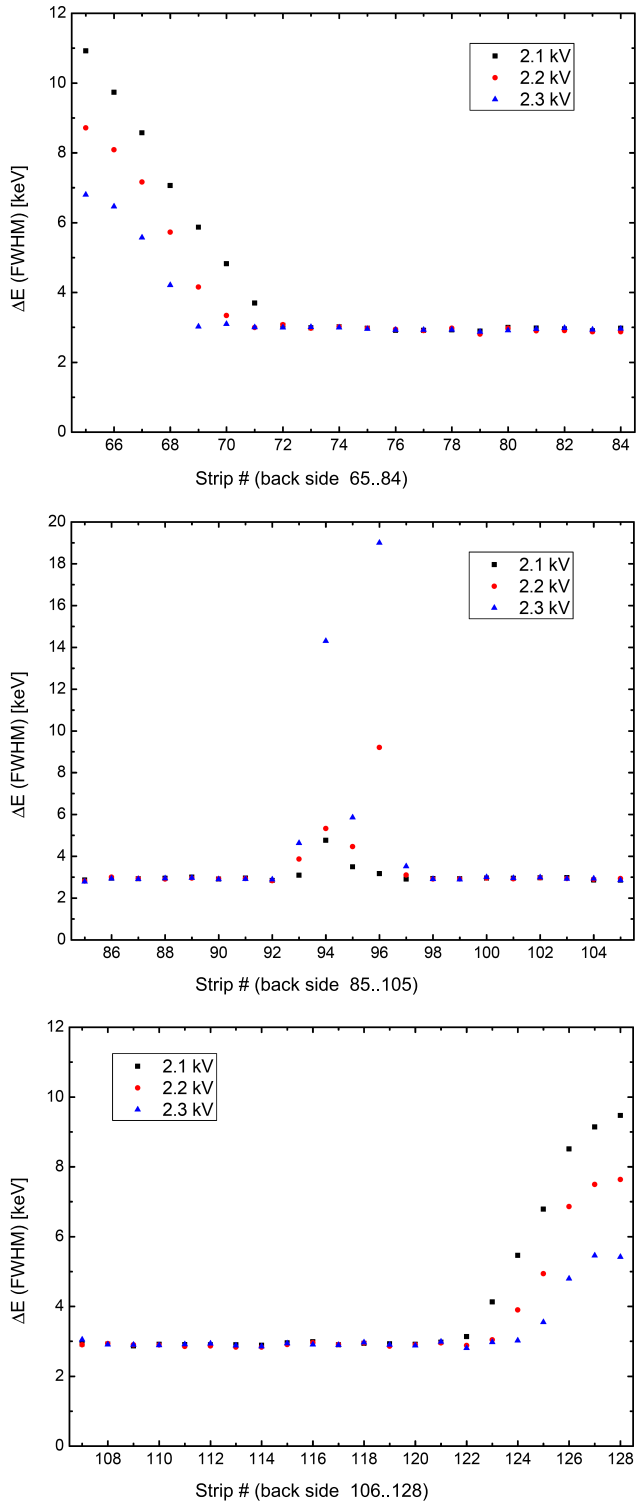

Figure 6.40: Individual energy resolution measured at 60 keV for all 64 back-side strips as a function of three different detector bias voltages: 2.1 kV (black dots), 2.2 kV (red dots) and 2.3 kV (blue dots). The 3 panels show an enlarged view on the n-side data of Fig. 6.39.

the energy resolution as discussed above. The front-side strip numbers 1 - 64 of the p^+ contact exhibit an (almost) identical intensity profile in response to the photons from the calibration sources ^{241}Am and ^{152}Eu, while the strips on the amorphous Ge (n)-side (strip numbers 65 - 128) show a reduced efficiency compared to the p^+-side.

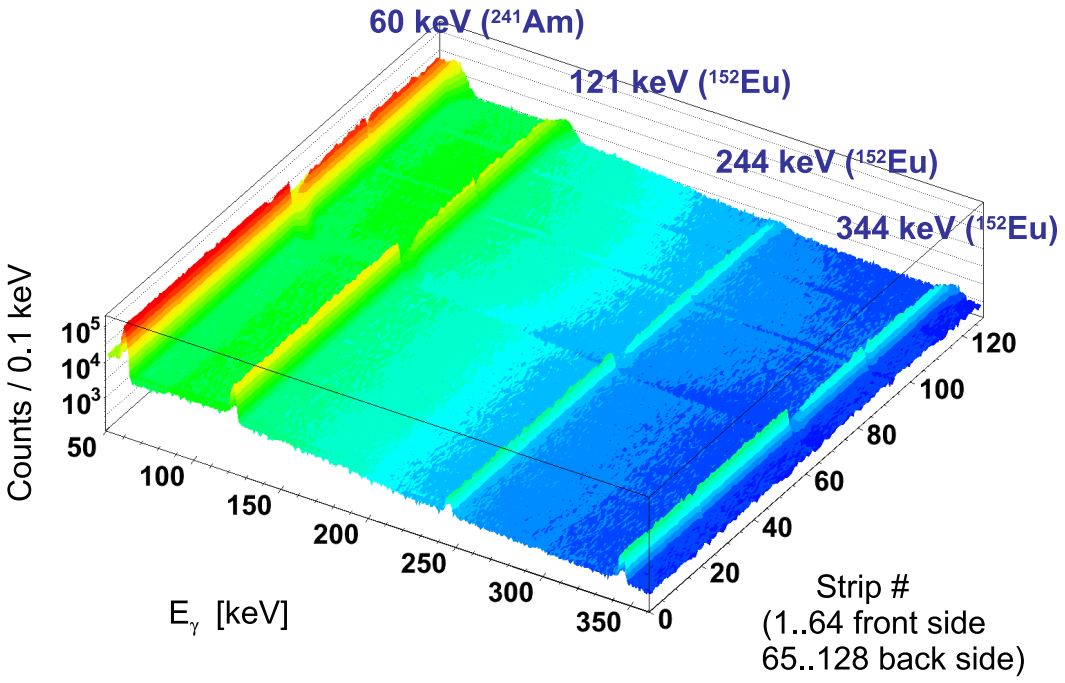

Figure 6.41: Energy range up to 360 keV of the 15 mm thick high-purity planar germanium detector: γ-ray energy spectra of all 128 detector strips for a shaping time of 0.5 μm and a bias voltage of 2.1 kV, resulting from a measurement using a ^{241}Am and ^{152}Eu calibration source. Strip numbers 1 - 64 correspond to the p^+-contacts (front side), strip numbers 65 - 128 belong to the amorphous Ge contacts on the (n) back side of the crystal.

6.3.3 Absolute Photopeak Efficiency

In order to derive the energy dependent absolute (solid angle and dead-time corrected) photopeak efficiency of the HPGe detector, the known activity of the two γ calibration sources ^{241}Am and ^{152}Eu was used with an activity of 352.3 $\pm$ 0.06 kBq and 143.9 $\pm$ 0.02 kBq, respectively. The sources were placed in a distance of 53 cm from the HPGe detector, a shaping time of 0.5 μm and a bias voltage of 2.1 kV were chosen. The resulting absolute photopeak efficiency as a function of the γ-ray energy is displayed in Fig. 6.42. The two curves indicate the absolute photo-peak efficiency of typical strips on the front side (black symbols) and on the back side (red symbols). The absolute photo-peak efficiency

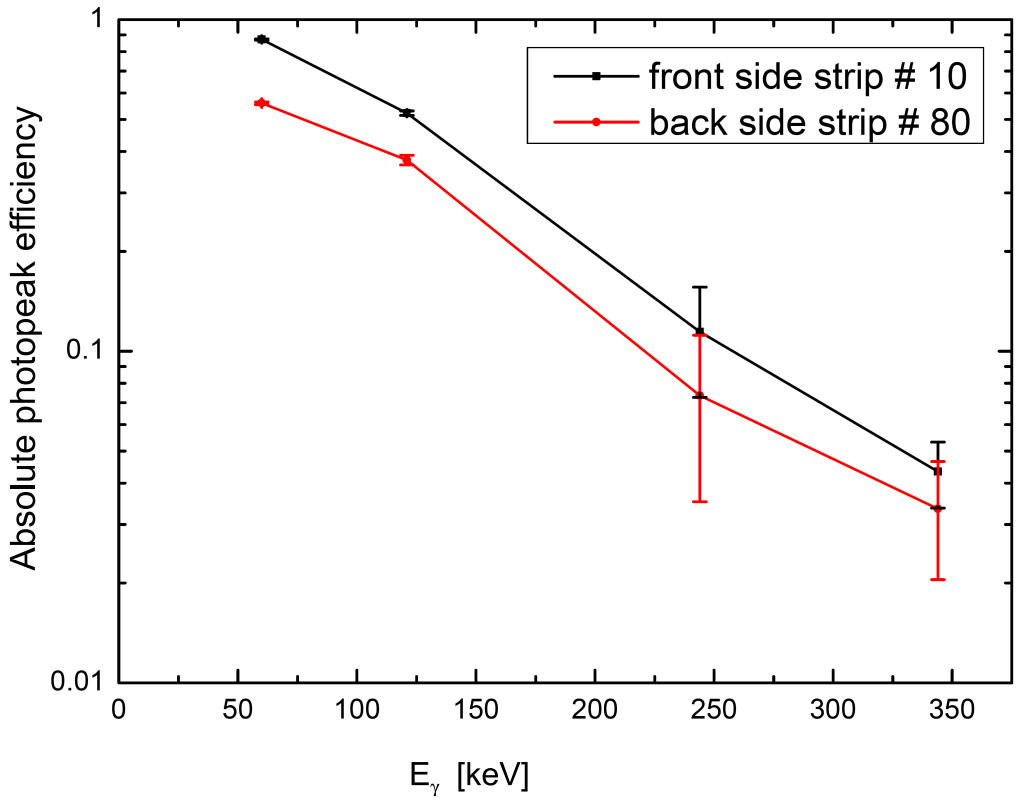

Figure 6.42: Energy dependence of the absolute photo-peak efficiency (deadtime and solid-angle corrected) of a typical strip of the HPGe detector of the front side (black symbols) and of the back side (red symbols). The data have been obtained with a ^{241}Am (60 keV) and ^{152}Eu (121 keV, 244 keV and 344 keV) γ source and were analyzed using the known activities of the calibration sources.

is exponentially decreasing from 87% $\pm$ 0.3% at 60 keV to 4.3% $\pm$ 1.0% at 344 keV for strip # 10 of the p^+-contact, and from 56% $\pm$ 0.5% at 60 keV to 3.3% $\pm$ 1.3% at 344 keV for strip # 80 of the amorphous Ge contact. The almost by a factor of two reduced efficiency of the back side compared to the front side is most likely caused by the quality of the Ge crystal, exhibiting areas of increased impurity levels and thus traps for the created charge carriers pairs. Fig. 6.43 shows the absolute photo-peak efficiency as a function of the photon energy for all 128 strips on the front (1 - 64) and back side (65 - 128). The efficiencies are shown with error bars for each strip and have been determined by individual Gaussian fits of the 3 γ transitions at 60 keV (^{241}Am source), 121 keV and 244 keV (^{152}Eu source), additionally corrected for deadtime and solid-angle coverage. Strips on the back side with a low energy resolution have been excluded from the analysis (see also Fig. 6.38 and Fig. 6.39). While the strips on the front side show an almost equal absolute photo-peak efficiency for each of the measured energies, the back-side strips reveal a variation of the efficiency towards the crystal edges with a strong reduction of the efficiency for about 6-7 strips at both edges of the crystal.

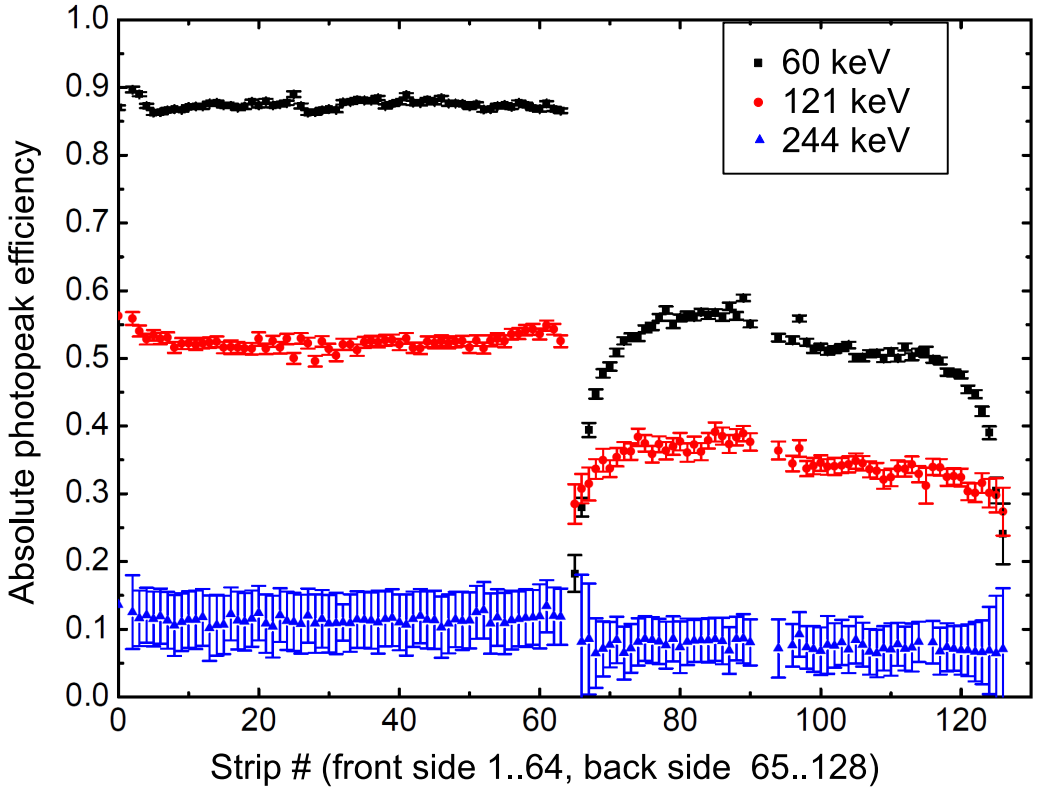

Figure 6.43: Energy dependence of the absolute photo-peak efficiency (deadtime and solid-angle corrected) for all 128 strips of the HPGe detector of the front (strip 1 - 64) and of the back side (strip 65 - 128). The data have been obtained with a ^{241}Am (60 keV (black dots)) and ^{152}Eu (121 keV (red dots) and 244 keV (blue dots)) γ source, respectively, using the known activity of the calibration sources.

6.3.4 Spatial event reconstruction and polarimetry

As mentioned in Sect. 2.1.2, the linear polarization of an incident photon can be determined by the Compton scattering process. A segmented germanium detector is capable of measuring the polarization of an incident photon, using simultaneously the detector as scatterer and absorber. The required polarimeter properties are provided by the multi-hit capability of the detector (enabled by the individual readout of each strip), the small volume of the created free charge carrier pairs (several tens of μm), and by the high energy resolution of the HPGe [41].

For an efficient use of germanium as absorber and scatter medium, the cross sections of these two processes have to be considered. Regarding Fig. 2.2, the optimum incident photon energy is around 150 keV for germanium, where the cross section of the Compton scattering process equals the one of the photo absorption process. For an incident photon energy of 150 keV, the maximum sensitivity for a polarization measurement is reached at a scattering angle of $\theta \approx 80°$ (see Fig. 2.12). Fig. 2.6 shows the corresponding kinematic correlation between the energies of the Compton scattered photon and the scattered (re-

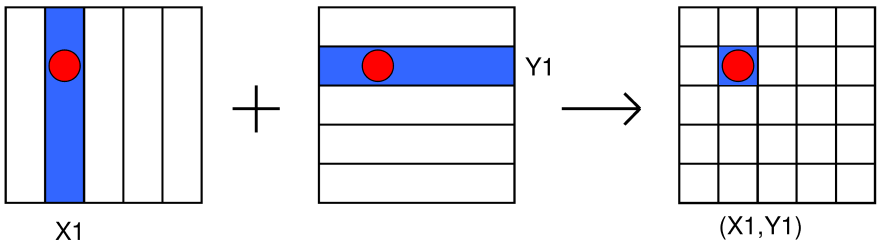

Figure 6.44: Sketch of the position reconstruction of the simplest case of a single photo absorption event (red dot) for a 2D segmented detector. A strip on one side of the detector is registering the energy deposition of the incident photon, e.g., via the electron signal component, simultaneously a strip on the other side of the detector is registering the corresponding hole component. Together, the signals deliver the X and Y position of the interaction [41].

coil) electron. For E_γ = 150 keV and $\theta = 80°$, the resulting energies are $E_{\gamma'}$ = 120 keV and E_e = 30 keV, respectively. For efficiently absorbing Compton scattered photons of this energy, a minimum thickness of 15 mm of germanium is required to absorb 90% of the incident photons (see Fig. 2.2).

For reconstructing a Compton event in a 2D segmented planar HPGe detector, the following considerations have to be taken into account. The signal from the scatter process is on the one hand created by the recoil electron, which has a short stopping range in Ge of several tens of μm (see Fig. 2.14). The complementary signal component from the final photon absorption is created by the scattered photon with a significantly larger absorption length (for, e.g., E_γ = 150 keV, the absorption length is resulting in $\approx$ 17 mm). To allow for an individual identification of the two signals from scattering and absorption, the distance between the positions of the scattering and absorption process of the incident photon have to be further apart than the segmentation of the detector, which in our case is 1 mm. Ambiguities arise, whenever Compton events are registered in neighboring strips, because they cannot be distinguished from charge sharing of the created electron-hole cloud on two (or more) strips.

In Fig. 6.44, a sketch of the simplest reconstruction pattern of an individual photo-absorption event is shown. A red dot is indicating the precise absorbing position on the respective X or Y strips from the two detector sides, highlighted in blue. Superimposing the position information obtained from the two perpendicularly segmented detector contacts allows to identify the pixelated position of the photo absorption, as can be seen in the right-hand panel of Fig 6.44. In case of a Compton scattering event (Fig. 6.45), the combination of the signals from the two X_1, X_2 and two Y_1, Y_2 strips does not unambiguously allow for distinguishing the interaction positions. Four possible interaction positions are resulting: (X_1, Y_1), (X_1, Y_2), (X_2, Y_1) and (X_2, Y_2). Due to the fact that a photon interaction will produce an equal charge of electrons and holes in the semiconductor, an additional energy condition ($E(X(i)) \stackrel{!}{=} E(Y(j))$) can be applied to correctly reconstruct the two interaction positions of the Compton event.

Further improvements of the event pattern identification could be achieved by requiring

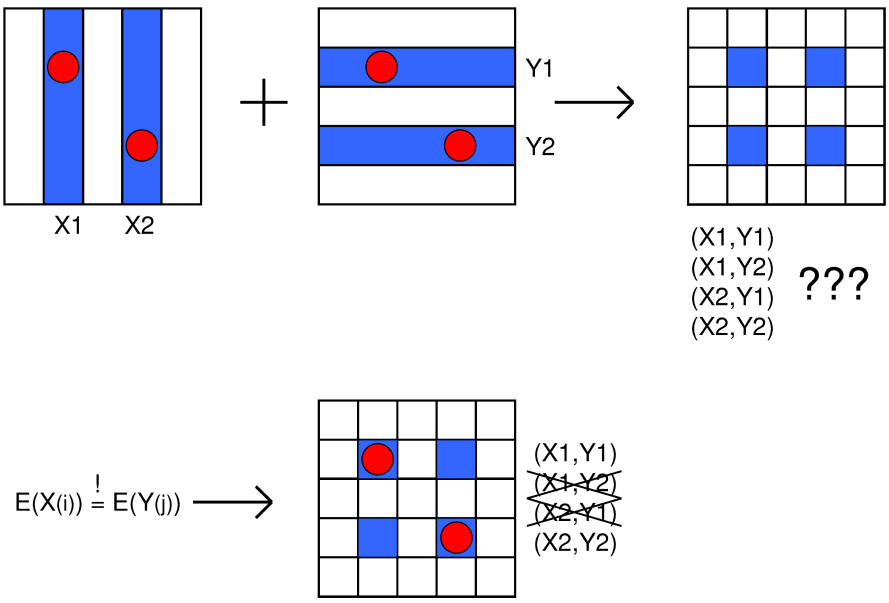

Figure 6.45: Sketch of the position reconstruction of a Compton event (red dots indicate the interaction positions). A combination of the signals from X and Y strips does not unambiguously allow for distinguishing the interaction positions. Only the additional energy condition $E(X(i)) \stackrel{!}{=} E(Y(j))$ allows to correctly reconstruct the interaction positions of the Compton event [41].

isolated hits, excluding events with neighboring hits, thus rejecting events with charge sharing and cross talk between adjacent strips. On the other hand, detectors with strips of 1 mm width would suffer from significant efficiency reduction when applying this strict analysis condition, therefore it has not been used in the following analysis. Moreover, events with small energy deposit (here < 5 keV) are particularly affected by the electronic noise, and have been suppressed in the analysis shown here.

In order to assess the response of the germanium detector to 100% horizontally polarized photons, a MC simulation utilizing Geant4 was performed. The resulting Compton scattering distribution for a scattering angle $\theta = 90°$ and for an incident photon energy of E_γ = 200 keV is shown in Fig. 6.46. This figure exhibits the typical dumbbell-shaped angular distribution of linearly polarized photons, with maximum emission perpendicular to the polarization plane. The registered scattered photons range up to a distance of about 30 mm from the interaction point. Considering the detector surface of 64 x 64 mm^2 (indicated as a black square), almost all of the scattered photons can be absorbed, provided that the scattering interaction occurs in the central area of the crystal.

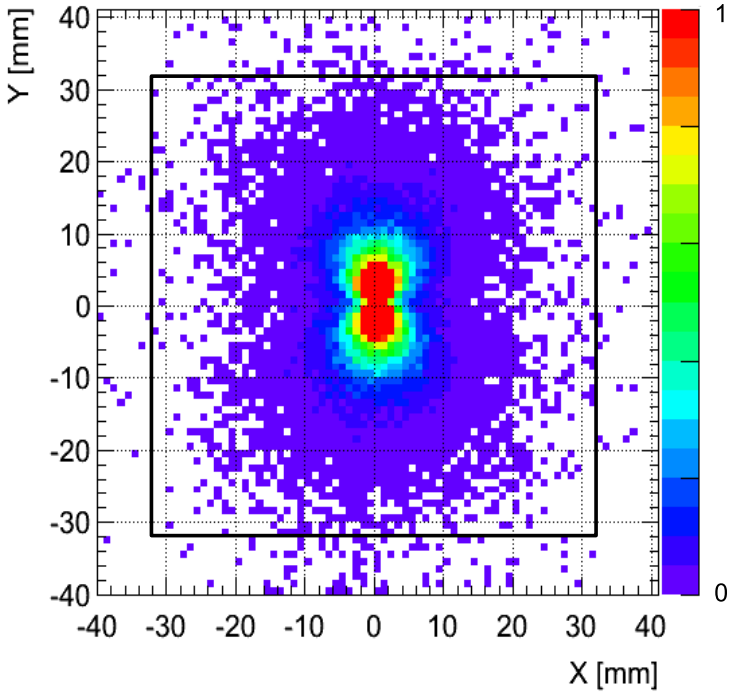

Figure 6.46: MC simulation utilizing Geant4 for the response of the 2D segmented planar germanium detector to horizontally polarized photons with E_γ = 200 keV. The resulting Compton scattered angular distribution for a Compton scattering angle $\theta = 90°$ ranges up to a distance of about 30 mm from the interaction point and exhibits the typical dumbbell-like distribution. The black rectangle is indicating the detector crystal dimensions.

6.3.5 Experimental characterization of the polarization sensitivity

For characterization and experimental calibration of the planar 2D segmented polarimeter properties of the HPGe detector, a measurement at the Deutsches Elektronen-Synchrotron (DESY) in Hamburg was performed. 92% horizontally linear polarized photons with an energy of 146 keV were accessible at the HASYLAB beamline BW5 at the electron storage ring DORIS III.

Deutsches Elektronen-Synchrotron (DESY)

The measurements were performed at the electron storage ring DORIS III, which is a part of the Deutsches-Elektronen-Synchrotron (DESY) in Hamburg, besides of other storage rings of DESY like PETRA III. DORIS III is the third generation of the DORIS storage ring, upgraded to 9 wiggler/undulator insertion devices and several dipole beamlines. Before injection of the electrons into DORIS III, they got accelerated in two steps: first by a linac to energies of 450 MeV, followed by the synchrotron DESY. In the storage ring DESY (II), a maximum electron energy of 4.5 GeV can be reached. Fig. 6.47 shows a sketch of the electron storage ring DORIS III, surrounded by 36 beamline stations. The

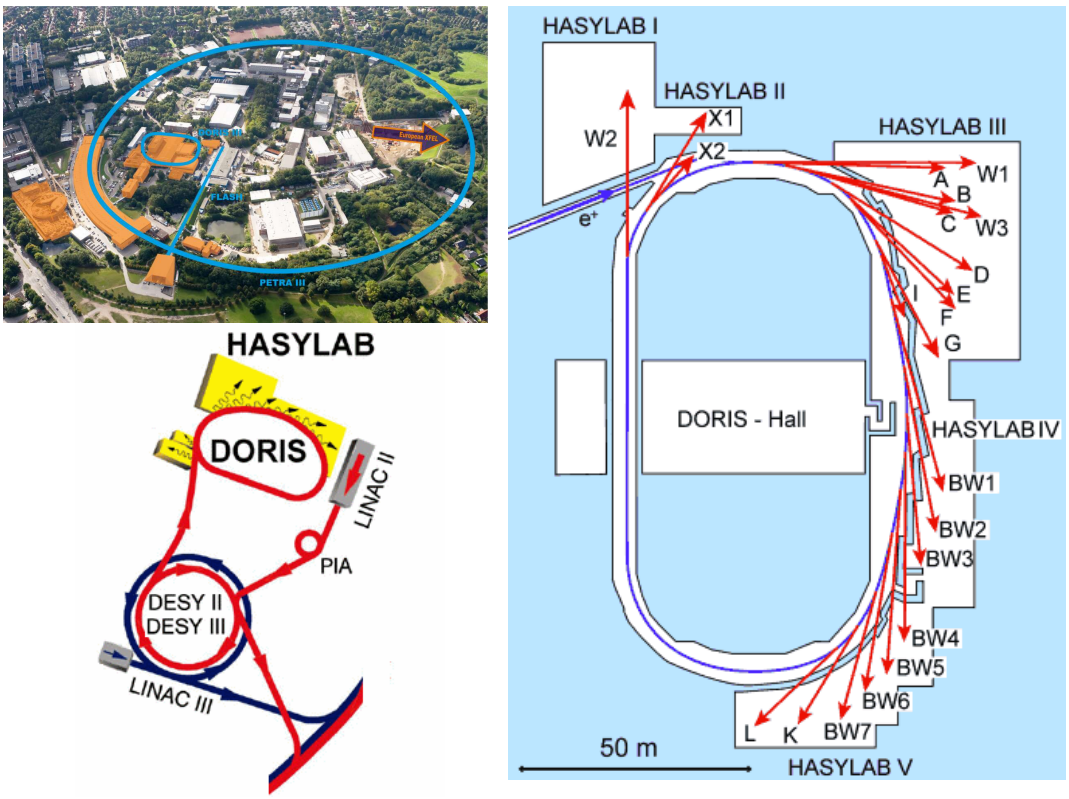

Figure 6.47: Sketch of the electron storage ring DORIS III, providing 36 beamline stations. The radiation in the extreme ultraviolet and X-ray regime is used in a broad range of applications from biology and chemistry to material science [170, 171]. The polarization calibration measurement was performed at the HASYLAB beamline BW5.

stored beam current is 140 mA of positrons in 5 bunches with a typical lifetime of 10 to 18 hours. The radiation in the extreme ultraviolet and X-ray regime is used in a broad range of applications from biology and chemistry to material science [171]. In Fig. 6.48, a comparison of the X-ray peak brilliance as a function of the photon energy of different photon sources operational or under construction at DESY is shown. Approximately 10^{17} photons/s mrad^2 mm^2 0.1% BW with an energy of 100 keV can be provided by DORIS III [171].

Polarization sensitivity measurement

The experiment was performed at the HASYLAB beamline BW5 of DORIS III, delivering 92% horizontally linear polarized photons produced by the wiggler HARWI 2, which consists of 34 dipole magnets. The synchrotron photon flux was roughly $5 \cdot 10^9$ ph / (s mrad^2 mm^2 0.1% BW). After collimation, a double-crystal monochromator is installed, capable to deliver photons with an energy between 60 keV to 150 keV, followed by a slit aperture. In our experiment, the X-ray beam was monochromatized to an energy of 146 keV and collimated to 0.5 x 0.5 mm^2 by the slit aperture. In a distance of 900 mm from

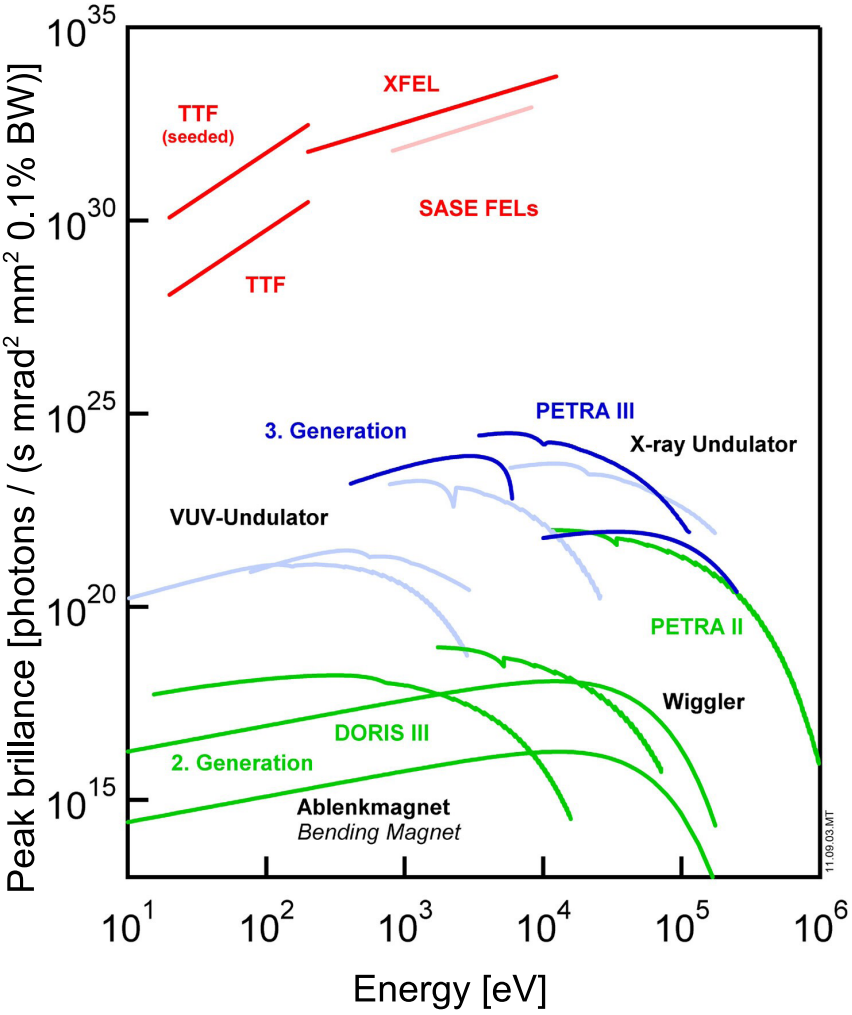

Figure 6.48: Comparison of the dependence of the peak brilliance of the synchrotron radiation on the photon energy for different synchrotron light sources operated at DESY. DORIS III exhibits a smaller peak brilliance compared to other DESY facilities, but can provide a broader photon energy range. At a photon energy of 100 keV, DORIS III is capable to deliver $\approx 10^{17}$ photons/s mrad^2 mm^2 0.1% BW [171].

the slit aperture, the HPGe detector was placed under 0° with respect to the X-ray beam axis. Between the monochromator and the slit aperture an attenuator with 48 mm Fe and 10 mm Pb was installed, in order to reduce the beam rate to 16 kHz (measured with a NaI scintillator, at the position of the HPGe detector). Because of the small dimensions of the scintillator, it was possible to completely shield the NaI detector. As it turned out, strong background radiation ($\approx$ 14 kHz) from scattered photons originating from the monochromator could be detected at the experimental position of the polarimeter detector and had to be mitigated by extensive shielding efforts. Due to the short beam time of 25 h and the dimensions of the HPGe detector, it was not possible to completely shield the background radiation.

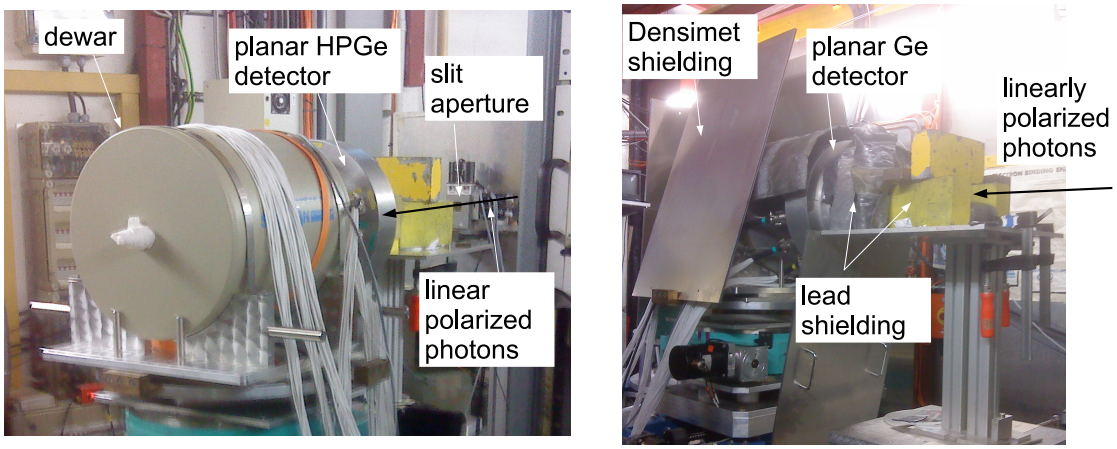

Figure 6.49: Experimental setup at the HASYLAB beamline BW5 of DORIS III, delivering 92% horizontally linear polarized photons. Left panel: the HPGe detector was placed under 0° downstream of the double-crystal monochromator, followed by a slit aperture. Right panel: the detector was properly shielded by heavy-Z material blocks and plates to minimize the registered background radiation.

Two photographs of the setup are shown in Fig. 6.49. The left panel shows the position, where the planar HPGe detector was placed. The right panel of Fig. 6.49 displays the substantial shielding efforts, which had to be applied to minimize the background radiation that could reach our polarimeter. In order to reduce the background counts and dead-time of the data acquisition system, the trigger was only derived from the central front-side strips (17 - 45). This choice reflects the central irradiation position of the photon beam.
In the course of the data analysis it could be shown, that even when operating in an environment with an enormous background radiation it is possible to clearly filter out the Compton events, by applying a multiplicity and an energy condition to the raw data.

Data acquisition and analysis

Prior to starting the data acquisition from the DORIS III polarized photon beam, an individual energy calibration of all 128 strips of the HPGe detector was performed, using a ^{133}Ba γ source. The resulting calibrated energy spectrum of all strips can be seen in

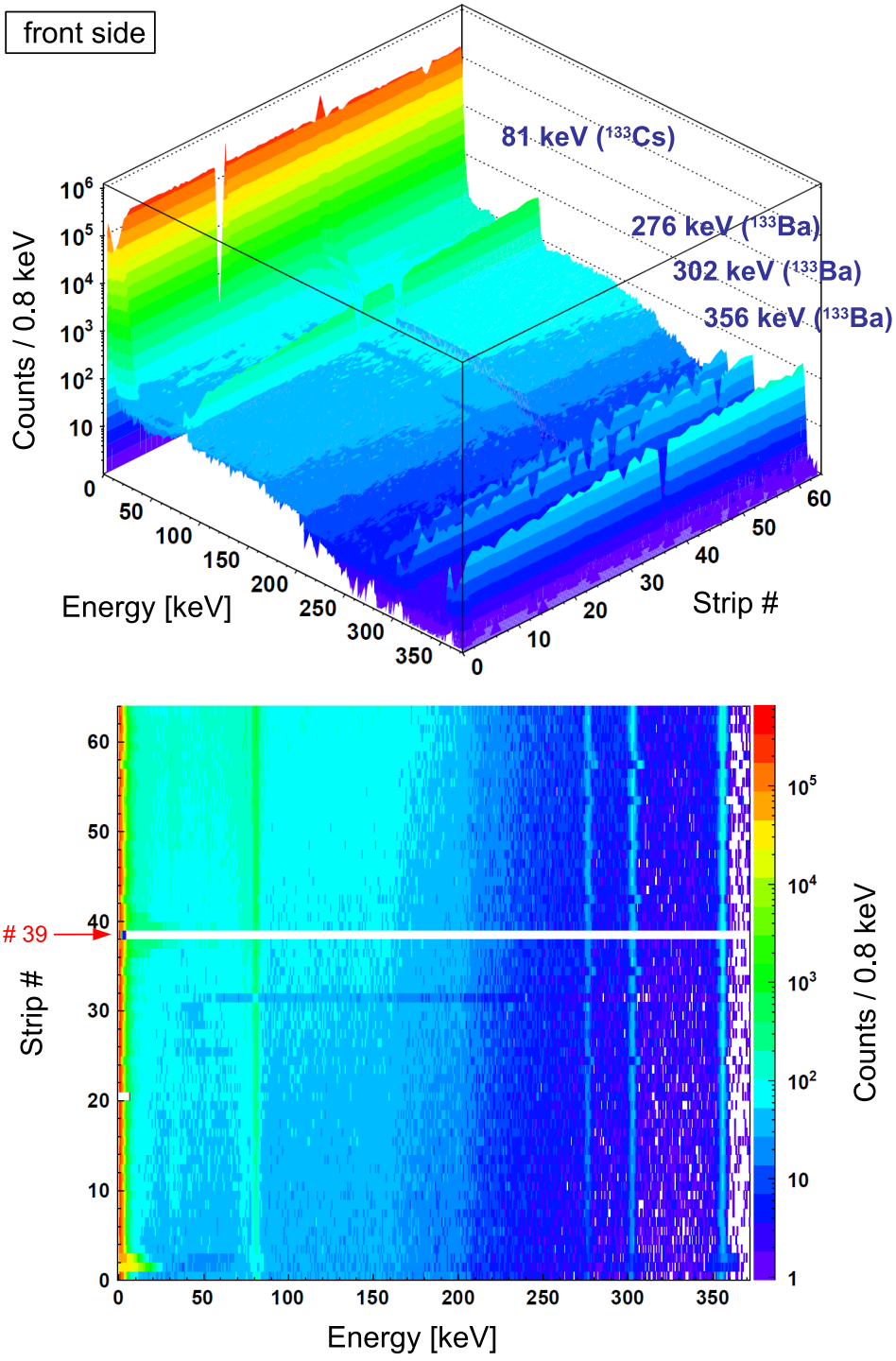

Figure 6.50: Calibrated γ-ray energy spectra of the 64 front-strips of the planar Compton polarimeter. The top panel shows an isometric perspective, while the bottom panel shows a top view. The 64 strips have been individually calibrated with a ^{133}Ba γ source, emitting photons with energies of 81 keV (X-ray from ^{133}Cs), 276 keV, 302 keV and 356 keV, respectively. The detector was operated at a bias voltage of 2.1 kV, with a shaping time of 0.5 μm. The red marked strip # 39 has been excluded from the subsequent data analysis.

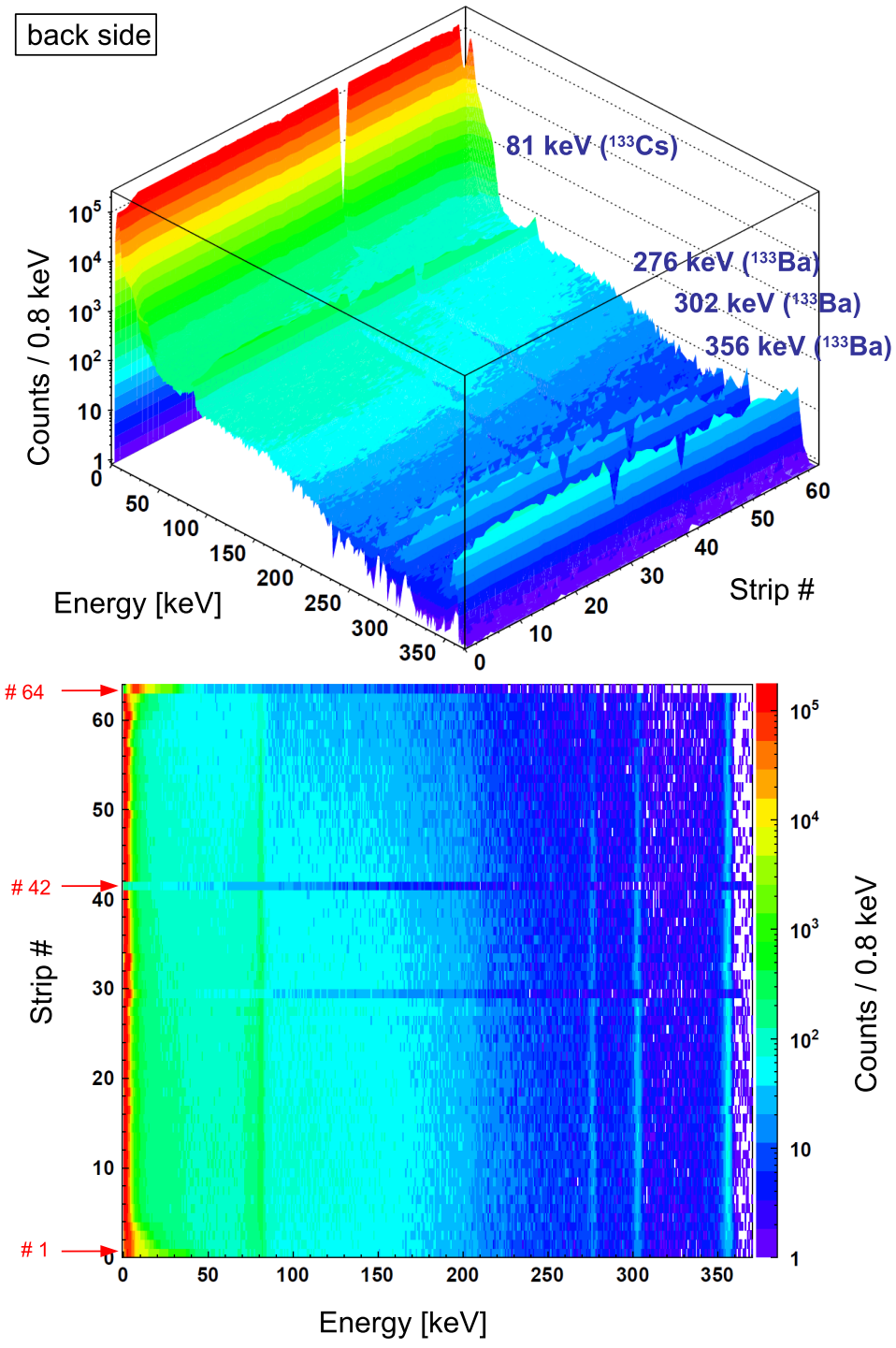

Figure 6.51: Calibrated γ-ray energy spectra of the 64 back-side strips of the planar Compton polarimeter. The top panel shows an isometric perspective, while the bottom panel shows a top view. The 64 strips have been individually calibrated with a ^{133}Ba γ source, emitting photons with energies of 81 keV (X-ray from ^{133}Cs), 276 keV, 302 keV and 356 keV, respectively. The detector was operated at a bias voltage of 2.1 kV, with a shaping time of 0.5 μm. The red marked strips # 1, # 42 and # 64 have been excluded from the subsequent data analysis.

Fig. 6.50 and 6.51 for front side and back side, respectively. The top panel shows an isometric perspective, while the bottom panel shows a top view.

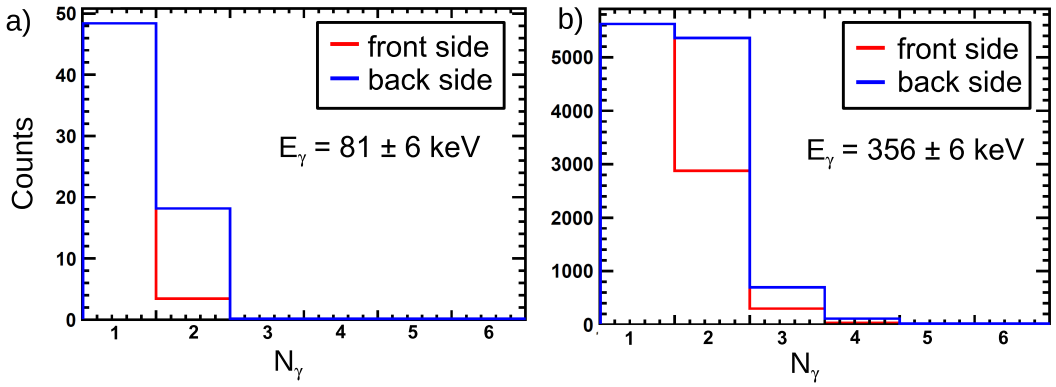

Figure 6.52: Strip hit multiplicity N_γ of the front-side strips (red lines) and back-side strips (blue lines) for γ energies of 81 keV (panel a)) and 356 keV (panel b)).

Besides the 81 keV X-ray emitted by the daughter β-decay product ^{133}Cs, the 276 keV, 302 keV and 356 keV γ rays from ^{133}Ba are visible. Due to limited statistics, only the 81 keV and 356 keV lines have been used for the individual energy calibration of the 128 strips. The registered intensity of the lines varies over the strips, due to the positioning of the γ calibration source in front of a corner of the crystal. It can be seen, that some strips from the front side (# 39) and back side (# 1, # 42 and # 64) had to be excluded from the subsequent analysis of the polarization measurement either because of their complete failure or extremely reduced efficiency. The charge sharing between adjacent strips has been investigated by applying an energy condition to complete photon absorption in the strips of one side of the detector, while counting the number of responding strips of the other detector side within one event. Fig. 6.52 shows the resulting photon hit multiplicity distributions for the case of photon energies of 81 keV (panel a)) and 356 keV (panel b)), respectively. In panel a), the front side (red line) exhibits a multiplicity N_γ = 1 of 92 % and N_γ = 2 of 6.2 % of the total number of events. The ratio between N_γ = 1 and N_γ = 2 results in a factor of $\approx$ 15. On the other hand, the back-side strips (blue lines) show a multiplicity N_γ = 1 in 72 % and N_γ = 2 in 27 % of all events, resulting in a ratio of 2.7. In panel b), the investigated photon energy was 356 keV, at this energy the front side (red lines) exhibits a multiplicity N_γ = 1 in 63 % and N_γ = 2 in 32 % of the total number of events, while the back side (blue lines) shows a multiplicity N_γ = 1 in 47 % and N_γ = 2 in 45 % of all events. At this energy, the ratio between N_γ = 1 and N_γ = 2 results in a factor of 2 and 0.5 for front side and back side, respectively. Obviously, charge sharing due to increased side-scattering increases as expected for higher photon energies. In combination with proper energy conditions, the initial hit pattern could be reconstructed by adding the scattered charge component (most likely the lower value of two adjacent hits) back to the neighboring strip. After the energy calibration and beam flux adjustment, the monochromatized horizontally polarized photon beam from DORIS III was irradiating the HPGe detector. The free count rate was $\approx$ 16 kHz, while the accepted rate was $\approx$ 1 kHz. Displayed in Fig. 6.53 are the recorded sum energy spectra

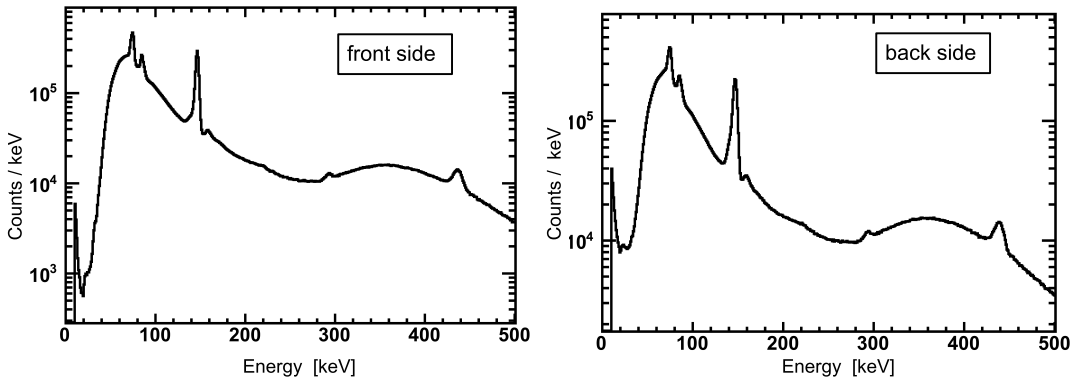

Figure 6.53: Recorded X-ray sum energy spectra of the 64 front-side strips (left) and the 64 back-side strips (right). The peaks at 75 keV and 85 keV are the K_α and K_β X-ray lines from the shielding material Pb. The strong line at the energy of 146 keV stems from the monochromatized photon beam. At an energy of about 160 keV, the pile up from the two X-ray transitions of Pb is visible. The small peak at 292 keV corresponds to the 2nd harmonic emitted at the double-crystal monochromator. Additionally, at 438 keV the 3rd harmonic is visible, overlapping with a pile up component at 452 keV between the 2nd harmonic of the photon beam energy and the Pb X-rays.

of the front-side strips (left panel) and the back-side strips (right panel), as derived from adding up all respective X-ray spectra of the individual strips. $5.07 \cdot 10^7$ events have been recorded in 45316 s (12.6 h) run time. Besides the dominant peak of the photon beam at 146 keV, the sum spectra contain predominantly the K_α and K_β X rays from Pb (which was used as shielding material) at 75 keV and at 85 keV, respectively. The small peak at $\approx$ 160 keV originates from pile up between the Pb X-ray transitions. The small peak at 292 keV corresponds to the 2nd harmonic of the monochromatized X-ray beam (2x 146 keV), emitted at the double-crystal monochromator. Additionally, at 438 keV the 3rd harmonic (3x 146 keV) is visible, partially overlapping with a pile-up component at 452 keV from the 2nd harmonic of the beam energy and the Pb X-rays. The energy resolution of the sum spectra at 146 keV is 4.2 keV (FWHM) and 5.6 keV (FWHM) for front- and back side, respectively. To get an impression of the quality of the individual energy calibration of the 128 strips, these values have to compared with the energy resolution derived from the irradiated strip on the front side (3.5 keV) and back side (4.6 keV), which turns out to be only about 20 % better.

An important criterion for selecting the Compton events during the data analysis is the photon hit multiplicity, i.e. the number of responding strips on the front or the back side within one event. Fig. 6.54 displays the multiplicity of the front side (a) and of the back side strips (b). In case of the front side (a), 48 % of all events exhibit a multiplicity N_γ = 1, for N_γ = 2 and N_γ = 3 the fraction is 33 % and 10 %, respectively. In comparison, in the case of the back side (b), 45% of all events exhibit a multiplicity N_γ = 1, for N_γ = 2 and N_γ = 3 the fraction is 38 % and 11 %, respectively. Additionally, in Fig. 6.54 the hit multiplicity gated with an energy condition of 146 $\pm$ 6 keV, requiring full absorption of the 146 keV photons for the front-side (c) and the back-side strips (d) is displayed. A hit

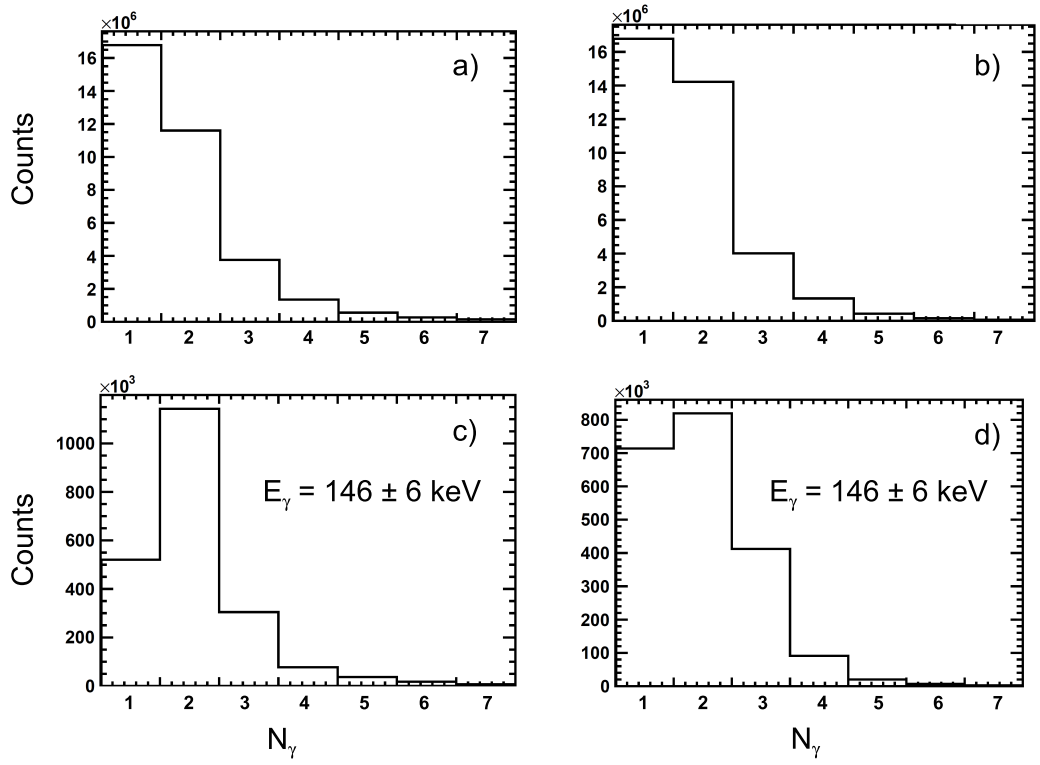

Figure 6.54: Strip hit multiplicity N_γ of the front-side strips (a) and back-side strips (b). Additionally, N_γ was determined requiring an energy condition on full absorption of the 146 keV photons from the X-ray beam, in panel c) displayed for the front-side strips and in panel d) for the back-side strips.

multiplicity of N_γ = 2 for the incoming 146 keV photons is now dominating, indicating an enhanced probability of Compton scattering compared to the ungated scenario (a) and (b). In case of the front side (c), 25 % of all events possess a multiplicity N_γ = 1, for N_γ = 2 and N_γ = 3 the fraction is 52 % and 14 %, respectively. In the case of the back side (d), 34 % of all events show a multiplicity N_γ = 1, for N_γ = 2 and N_γ = 3 the fraction is 39 % and 10 %, respectively. Requiring a hit multiplicity of N_γ = 2 in the raw data, the correlation between the X-ray energies of the two involved strips (here the two front-side strips) is plotted in Fig. 6.55 in logarithmic scale. Several correlations can be observed, with enhanced intensities at 75 keV, 85 keV and 146 keV, originating from simultaneously registered K_α and K_β lines from Pb and from the polarized photons of the beam. The dominance of the Pb lines while requiring N_γ = 2 indicates the presence of substantial background radiation. Most important are the photon hits on the interrupted diagonal line, for $E_{\gamma_1}+E_{\gamma_2} = 146$ keV (marked in red), indicating the energy distribution of the Compton-scattered photon and the corresponding recoil electron. These events can be assigned to the Compton continuum of a Compton scattering spectrum. These events have to be selected for the Compton-event reconstruction. The peak in the middle of the

diagonal line is originating not from Compton scattering but from the Pb lines and from sharing of the charge cloud between two neigboring strips. For the incident photon energy of E_i = 146 keV, the maximum energy transfer is about 90 keV and 56 keV to the scattered photon and electron, respectively, while the case of an evenly distributed incident photon energy is (almost) not observed (see Fig. 2.6).

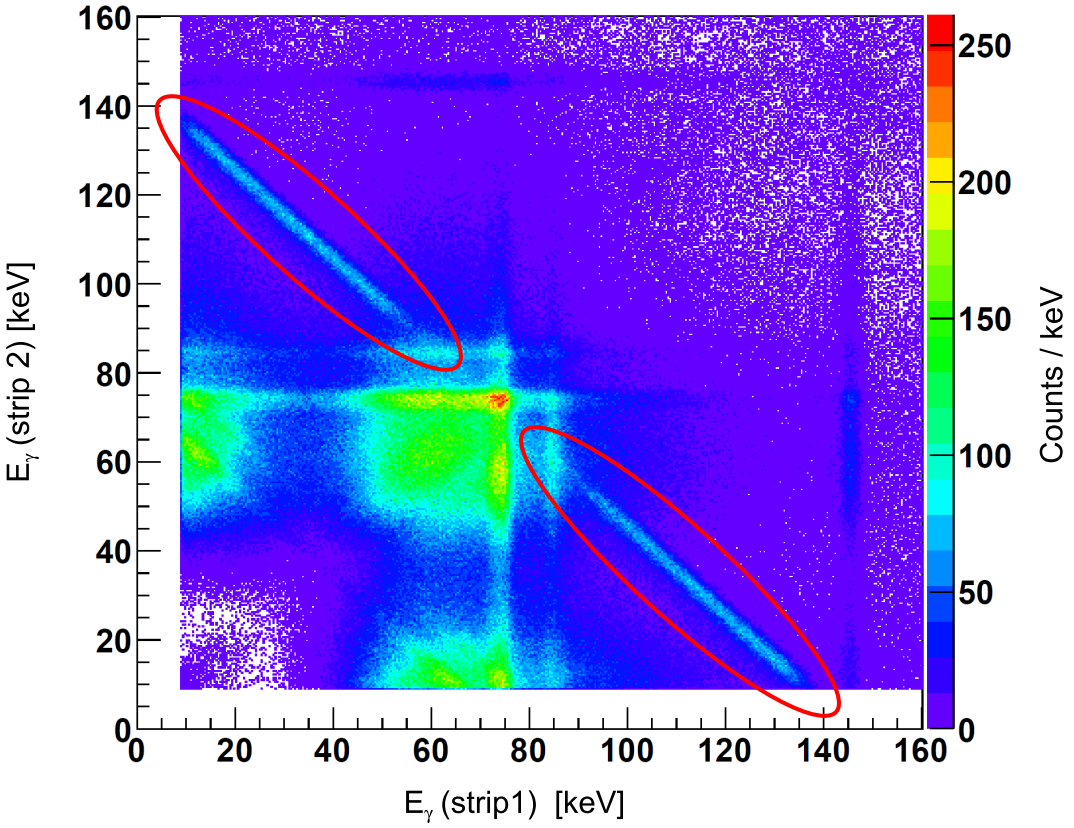

Figure 6.55: Requiring a hit multiplicity of N_γ = 2, the correlation between the X-ray energies of the two firing strips (here two front-side strips) is displayed. The strong enhancement of counts at 75, 85 keV and 146 keV originates from simultaneously registered K_α and K_β lines from Pb and from the polarized photons of the beam. The events on the interrupted diagonal line $E_{\gamma_1}+E_{\gamma_2} = 146$ keV (marked in red) correspond to the energy distribution of the Compton scattered photons and the correlated recoil electrons.

Applying an additional energy condition requiring full absorption of the 146 keV photons in both sides of the detector, the resulting detector response is displayed in Fig. 6.56 in an x-y plot, where the back-side strips are represented on the x-axis, and the front-side strips form the y-axis.
The azimuthal anisotropic Compton-scattering distribution can be identified. Panel a) displays the response of a parallel (front side), respectively perpendicular (back side), orientation of the strips relative to the incoming photon beam polarization. For recording the central panel b), the detector was rotated counterclockwise by 45°. Additionally,

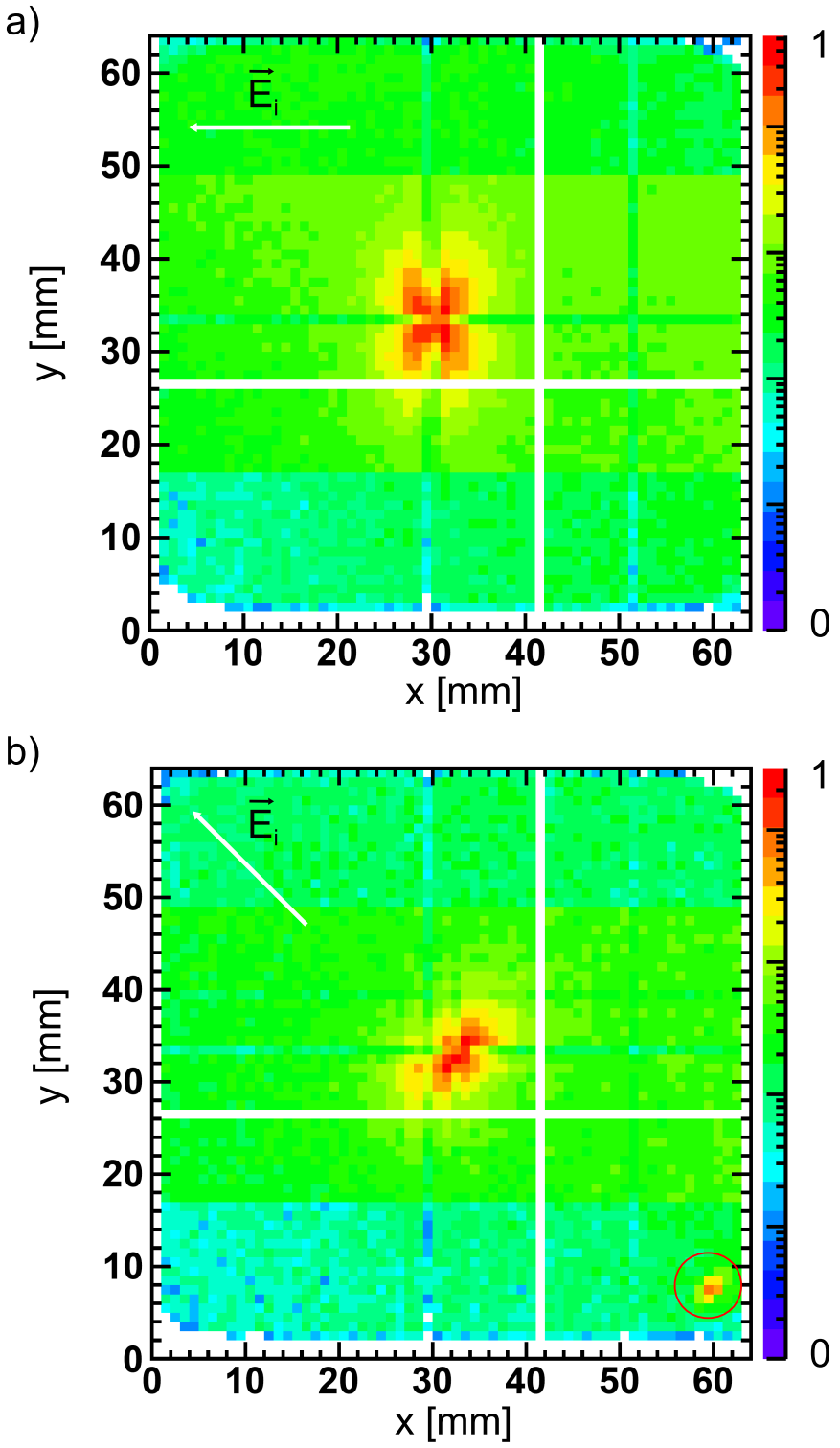
a)
$\vec{E}_i$
y [mm]
x [mm]
0
10
20
30
40
50
60
1
0
b)
$\vec{E}_i$
y [mm]
x [mm]
0
10
20
30
40
50
60
1
0

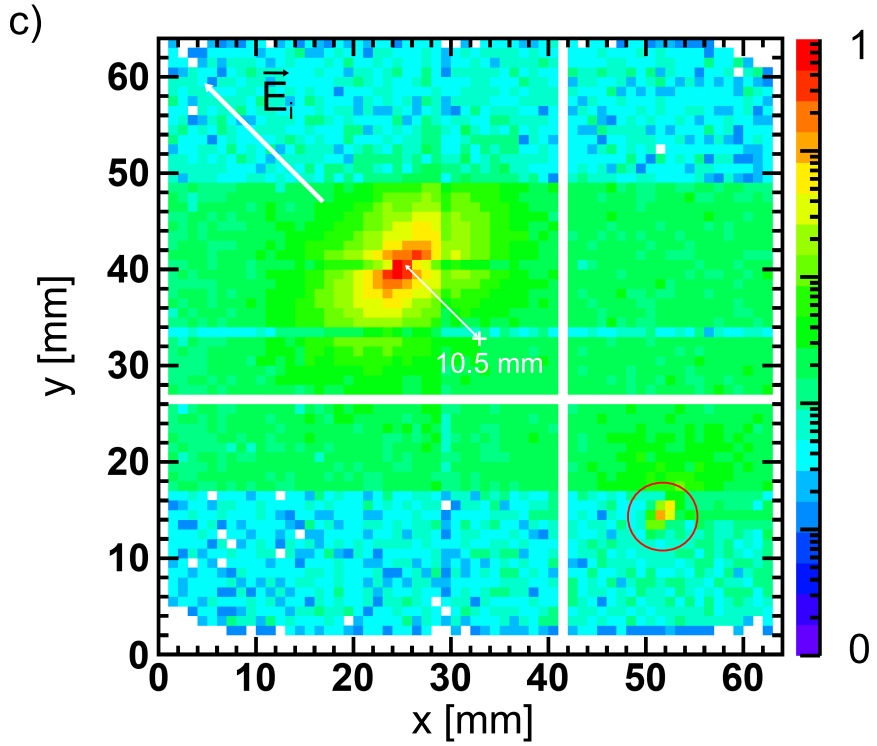

Figure 6.56: Azimuthal photon scattering distribution for all Compton scattering angles θ. Panel a) shows the reconstruction for a horizontal (front side), respectively perpendicular (back side), orientation of the strips relative to the incoming photon polarization. Panel b) displays the distribution after rotation of the detector by 45°, followed by a horizontal movement of the detector by 10.5 mm (panel c)). The white arrows indicate the polarization direction of the incoming photons with energy E_i relative to the orientation of the detector front face. The trigger condition was derived only from the central front-side strips (17 - 45), due to the remaining high rate from background radiation, resulting in a reduced intensity registered by the front side strips (y axis) 1-16 and 46-64 (see text for the reconstruction conditions).

resulting in panel c) of Fig. 6.56, the detector was moved horizontally to the right by 10.5 mm. The data were taking requiring a multiplicity of N_γ = 2 for the front-side and back-side strips, and an energy condition for the incoming photon of 146 keV $\pm$ 6 keV, registered as sum energy of the front-side and back-side strips, was applied. As discussed in Sect. 6.3.5, the trigger signal was derived only from the central region of the front-side strips (number 17 - 45), due to the remaining high count rate from background radiation. This results in less counts of the front-side strips (y-axis) 1-16 and 46-64. Also visible in panel b) and panel c) is a leakage of scattered X-ray beam photons through the shielding arrangement, resulting in a high statistics registered in the bottom right quadrant of the detector (marked with a red circle). Besides of the two corrupted strips (number 39 on the front side (y axis: 26 mm) and number 42 on the back side (x axis: 41 mm)), which failed during data acquisition (see Fig. 6.50 and 6.51), a less pronounced cross-like structure with reduced data intensity in the scattering distribution is visible in Fig. 6.56. This reflects the applied Compton scattering condition via the photon hit multiplicity N_γ = 2 both for back- and front-side strips. All events, where the scattered photon was registered in the same strip as the Compton electron, emerge as N_γ = 1 from the analysis and as such are excluded from the further analysis. Since the Compton electron is not always registered in the same strip, this cross-like structure, created by the multiplicity condition, is smeared out, which is especially visible in panel a), where the polarization vector of the incoming photon is parallel, respectively, perpendicular to the detector strips.

This cross-like feature appears more prominently, when the scattered photons are position corrected by the registered Compton electron position, as can be seen in Fig. 6.57. The position of the Compton electron can be derived by exploiting the fact that at photon energies below 511 keV the energy transfer to the Compton electron is smaller than the energy transfer to the scattered photon (see Fig. 2.6 and [41]). In Fig. 6.57, the azimuthal photon scattering distribution is shown for different Compton scattering angles θ = 20° - 180°, determined via the Compton kinematics through a condition to the photon energy of one of the registered Compton signals (while still obeying the sum energy requirements of 146 $\pm$ 6 keV). Superimposed in red onto two panels are the prototypical calculated differential Compton-scattering cross section distributions as a function of the azimuthal scattering angle φ for a vertically aligned photon polarization with energy $\vec{E_i}$ = 146 keV for θ = 50° and 90° (compare also to Fig. 2.10). The dipole character of the scattered photons is observed more or less pronounced in different regions of the Compton scattering angles θ, reflecting the theoretical polarization sensitivity discussed in Fig. 2.12. As expected, the maximum sensitivity for a photon energy of 146 keV is achieved at an angle θ of around 80°. At Compton angles θ of 20° - 40°, the deposited energy of the Compton electron is already very close to the electronic noise of the detector, also the energy of the scattered photon is close to the photo peak of 146 keV, resulting in a reduced Compton event reconstruction sensitivity. The distributions for the angular bins θ = 60° - 80° and θ = 80° - 100° seem to be truncated in the lower and upper region (green area), this occurs due to the increased background counts in the front-side strips 17 - 45 (see left panel of Fig. 6.56), serving to provide the trigger signal.

An even more obvious representation of the sensitivity on the azimuthal photon scattering distribution is shown in Fig. 6.58, where the intensity distribution of the azimuthal scattering angle φ for a Compton scattering angle θ = 90° $\pm$ 10° and a fixed radius of 4.5 -

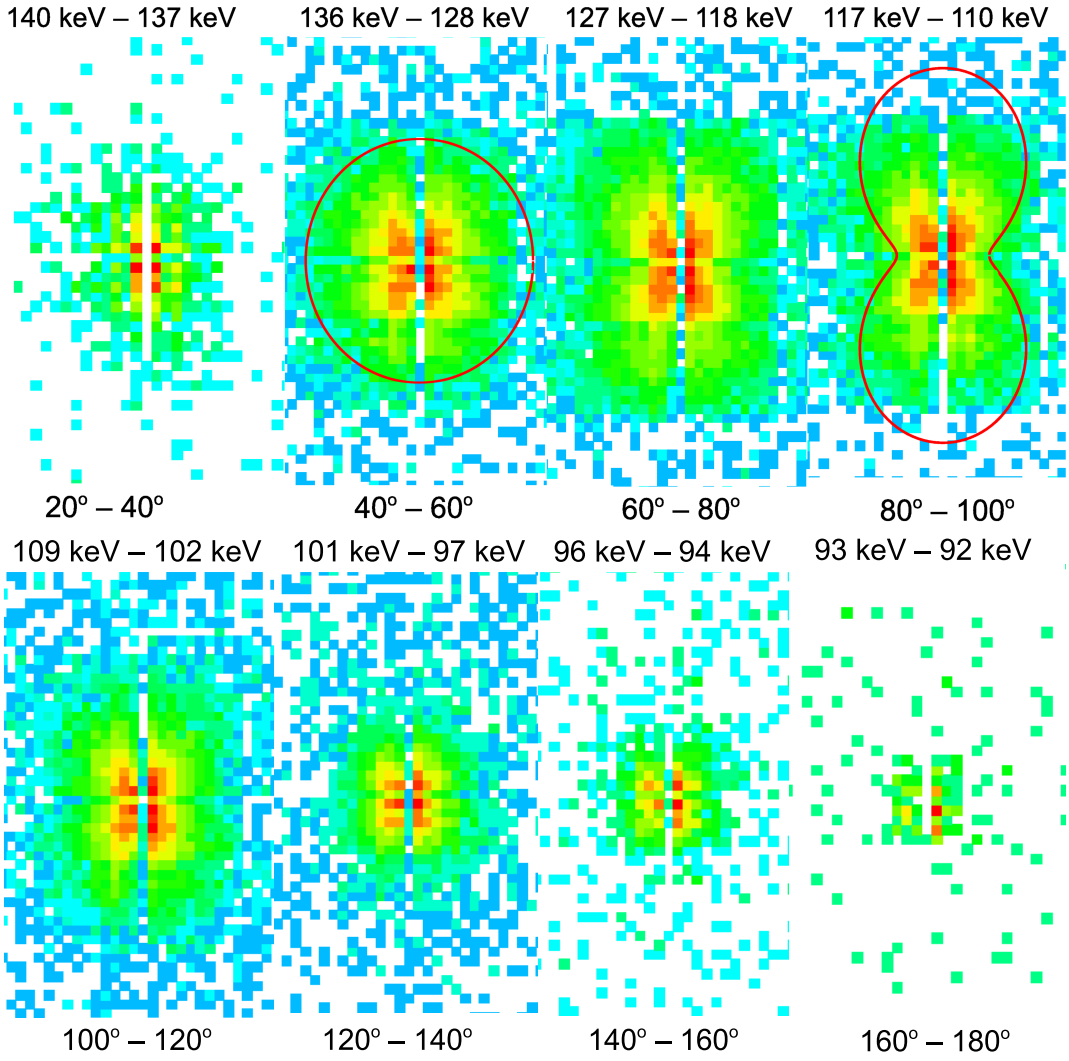

Figure 6.57: Azimuthal photon scattering distribution for different Compton scattering angles θ = 20° - 180°, determined via the Compton kinematics through a condition to the photon energy of one of the registered Compton signals (while still obeying the sum energy requirement of 146 $\pm$ 6 keV). Additionally, the scattered photons have been position corrected by the registered Compton electron position. Superimposed in red onto two panels are the prototypical calculated differential Compton-scattering cross section distributions as a function of the azimuthal scattering angle φ for a vertically aligned photon polarization with energy $\vec{E}_i$ = 146 keV for θ = 50° and 90°. The dimension of one pixel is 1 x 1 mm^2.

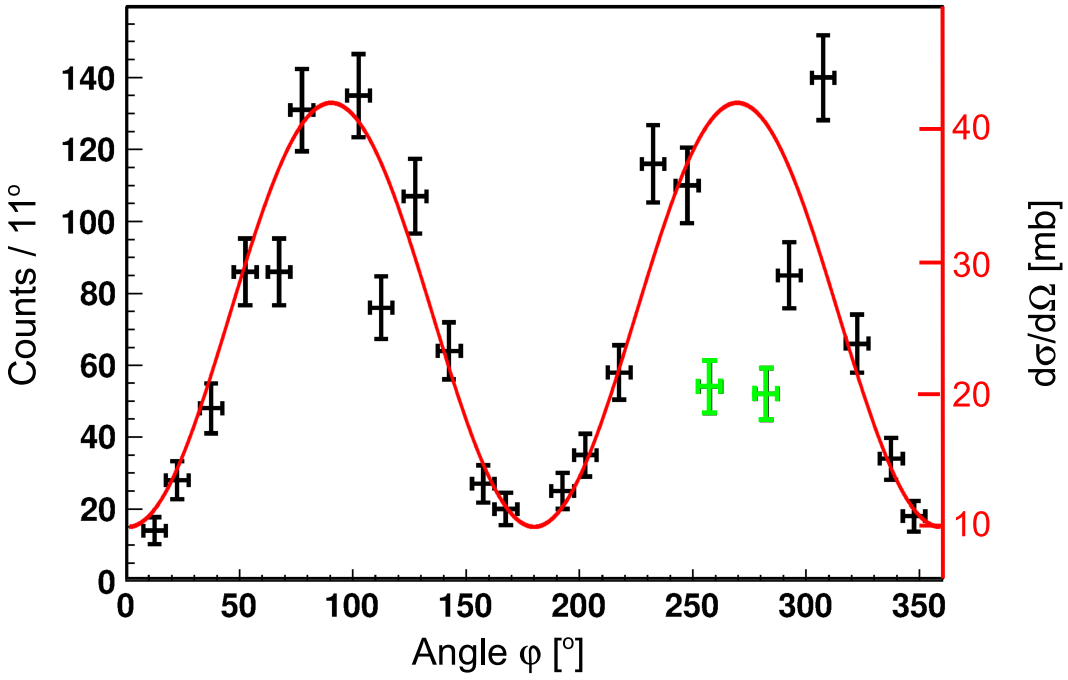

Figure 6.58: Azimuthal photon scattering distribution for a Compton scattering angle of θ = 90° ± 10° and a fixed radius of 4.5 - 5.5 mm around the Compton scattering point. Superimposed is the calculated differential Compton-scattering cross section distribution as a function of the azimuthal scattering angle φ in linear scale for a vertically aligned photon polarization with an energy E_i = 146 keV, for θ = 90°, as shown in Fig. 2.10. While most of the data points nicely follow the calculated curve, two green marked data points around ϕ = 270° exhibit reduced intensity, resulting from the non-working strip on the y axis (compare Fig. 6.56a)), which intersects the Klein-Nishina distribution at about 270°.

5.5 mm around the Compton scattering point is plotted. Also displayed is the calculated differential Compton-scattering cross section distribution as a function of the azimuthal scattering angle φ in linear scale, according to the calculation as plotted in Fig. 2.10 (there in polar coordinates). While most of the data points nicely follow the calculated curve, two green marked data points around ϕ = 270° exhibit reduced intensity, resulting from the non-working strip on the y axis (compare Fig. 6.56a)), which intersects the Klein-Nishina distribution at about 270°.

In conclusion, it could been shown that a highly segmented planar HPGe detector is capable to identify the polarization of linearly polarized photons, while acting simultaneously as a scatterer and an absorber of a Compton polarimeter. Even in an environment with copious background radiation, it is possible to reconstruct the Compton events by only applying an analysis condition on energy and multiplicity. Already in Sect. 5.2.2, the simulations showed that the HPGe can be used as an alternative absorber for a Compton camera for low-energy photons ($E_i < 2$ MeV). With the potential of the detector of po-

larization sensitivity, a Compton camera could profit from such an absorber in terms of selectivity.

Chapter 7

Medical imaging using nuclear resonance fluorescence

In the chapters before, a single Compton camera module or an arrangement of several cameras, allowing to apply the γ-PET technique, was used to study their prospects for medical imaging. The presented Compton camera prototype was optimized for registering prompt γ rays emitted by excited nuclei during hadron treatment, while the γ-PET technique takes advantage of specific PET isotopes, which emit a positron together with a prompt γ ray in coincidence. In the following chapter, an alternative method is presented, using nuclear resonance fluorescence to image the in-vivo function of medical relevant molecules via a tracer isotope.

We focus on the prototypical example of Lithium (Li), which is widely used as a mood-stabilizing drug. Following psychiatric medication, Li can be used to treat primarily bipolar disorders, in particular manic depression. However, still the location of the Li interaction inside the brain is not exactly known [172]. Monitoring the lithium atoms after injection would help to improve our knowledge on the functionality of antidepressant drugs. In addition, also non-medical applications of the nuclear resonance fluorescence technique are of interest, e.g., the imaging of Li ions inside Li batteries during charging and discharging could foster the development of more efficient batteries.

Experiments in the past primarily used bremsstrahlung to induce fluorescence from excited nuclear resonances [173, 174, 175]. However, a photon spectrum from bremsstrahlung exhibits an exponential decrease with energy and as such is far from being monoenergetic. This will result in a lot of unwanted γ-radiation background from scattering and excitation via atomic processes. On the contrary, a monochromatic photon beam is capable to selectively excite a certain nuclear transition of the isotope of interest. A γ beam energy with small enough energy spread would not excite or ionize other species, thus resulting in a harmless medical examination or material classification. In the following, a nuclear resonance fluorescence (NRF) measurement of ^{7}Li will be presented, which was recorded with the $LaBr_3$:Ce scintillator, previously characterized as absorbing component of the Compton camera. The experiment was performed at a high-energy X-ray synchrotron light source, the European Synchrotron Radiation Facility (ESRF in Grenoble) [176].

7.1 The European Synchrotron Radiation Facility (ESRF)

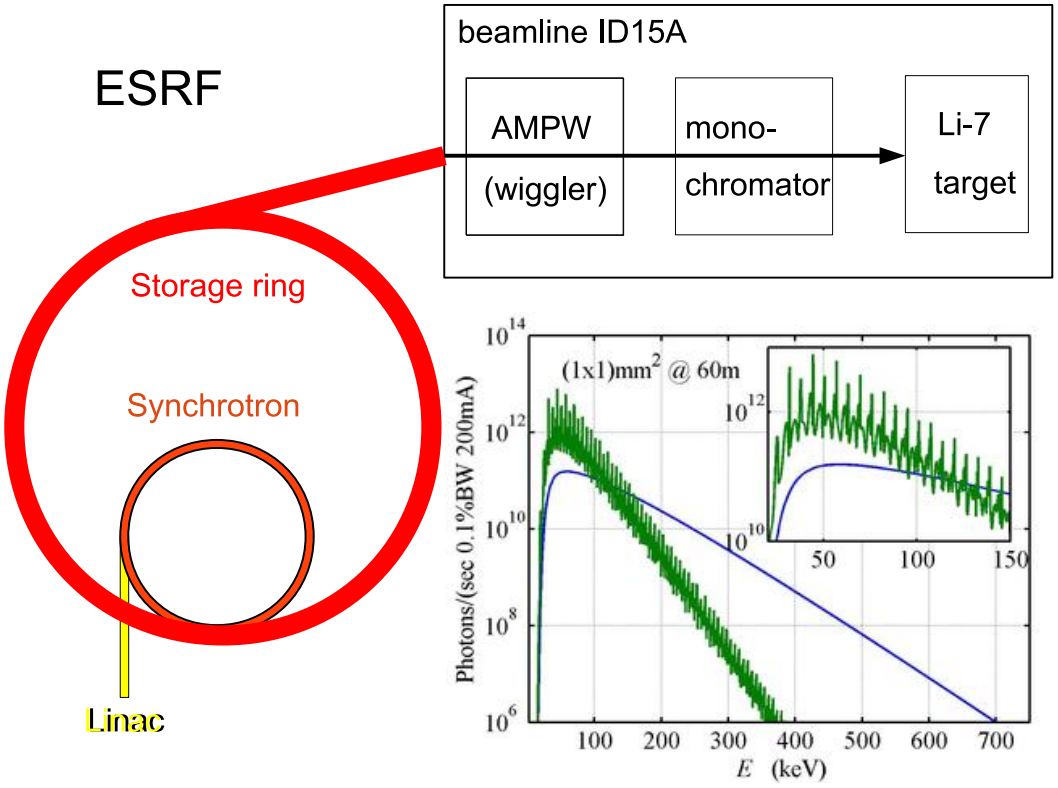

Figure 7.1: Layout of the electron beam acceleration, storage and extraction scheme realized at the ESRF (Grenoble). Electrons are accelerated up to 200 MeV in a linear accelerator (linac) and injected into a synchrotron, which boosts the electron energy to 6 GeV. Afterwards, the 6 GeV electrons are injected into a storage ring, ready to produce high-energy X-rays via an asymmetric multipole wiggler (AMPW) in a dedicated high-energy beamline (ID15A). In a last step, the X-ray beam passes a monochromator before irradiating the target. The inset shows the photon fluxes of the asymmetric multipole wiggler (blue) and the undulator (green) at the orbit through a ø1 mm^2 pinhole at 60 m distance (before the monochromator) [177].

The European Synchrotron Radiation Facility (ESRF) [176] is a high-energy X-ray source. It consists of a 200 MeV linear accelerator (linac) acting as a pre-injector, a 6 GeV synchrotron, increasing the electron beam energy from 200 MeV to 6 GeV, and a storage ring with a circumference of 844.4 meter to store the electron beam after injection from the synchrotron.
The experiment was performed at the high-energy beam line ID15A [177], which is dedicated to applications using high energy X-ray radiation from 30.1 - 750.0 keV. The straight section of this beam-line insertion contains a 7 pole (1.84 T) asymmetric multipole wig-

gler (AMPW) and an in-vacuum undulator. A layout of the electron beam acceleration, storage and extraction scheme at the ESRF (Grenoble), together with a scheme of the high-energy beamline ID15A is displayed in Fig. 7.1. The lower right panel shows the broad energy spectrum of the photon beam after the wiggler (blue line) and after the undulator (green line), respectively, before the monochromator. The photon beam flux at 478 keV is $\approx 10^8$ photons / (sec 0.1% BW) per 200 mA electron beam current (loaded into the storage ring), for the scenario of using the AMPW (in 60 m distance from it). The undulator is delivering a more than two orders of magnitude lower photon beam flux at this energy, but is favored for lower energies below 100 keV. For the excitation of the 477.6 keV nuclear transition of ^{7}Li in the present experiment, the AMPW has been used due to its higher photon flux in the relevant energy region. The double Ge-crystal monochromator configuration can be adjusted to the required energy for the experiment. The energy of the X-ray beam has been measured with a coaxial germanium detector, positioned downstream at 0 degrees relative to the beam axis.

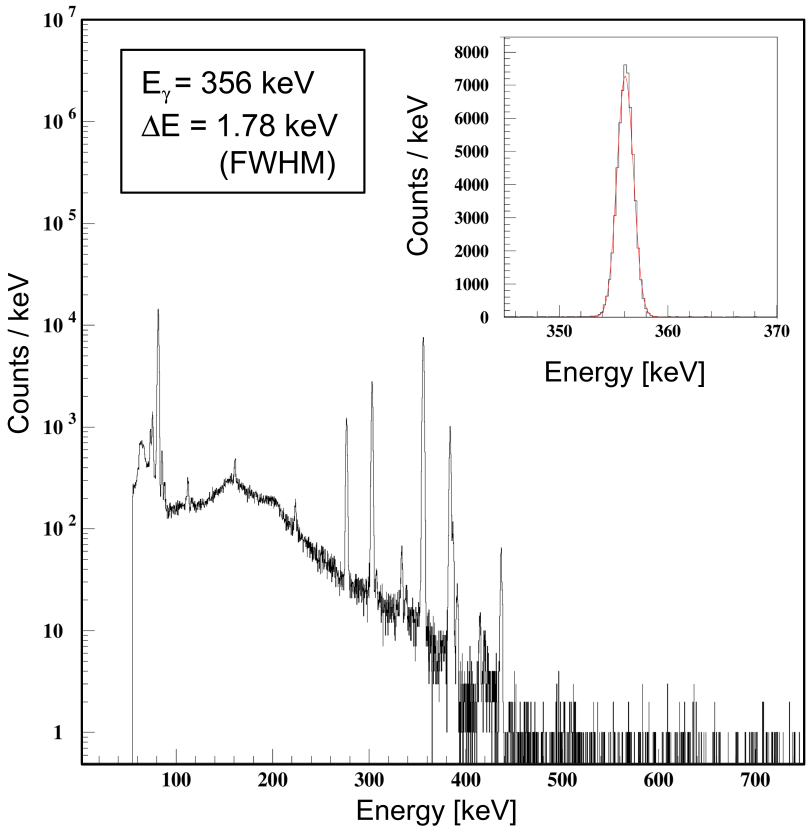

Figure 7.2: Calibrated energy spectrum of a ^{133}Ba point source, detected with a coaxial germanium detector. The width (FWHM) of the peak at 356 keV amounts to ΔE_{Ge} = 1.78 keV.

In Fig. 7.2, a calibrated γ-ray energy spectrum of a ^{133}Ba point source can be seen, which was detected with the germanium detector. The energy resolution of the detector amounts to ΔE = 1.78 keV at 356 keV. The detector resolution was not determined for the line

at 436 keV (seemingly more appropriate if finally aiming at E_γ = 478 keV), since this line originates from a pile up of the two ^{133}Ba emission lines at 80 keV and 356 keV, and therefore is broadened. Fig. 7.3 shows the energy spectrum of the X-ray beam, as measured downstream at 0 degrees relative to the beam direction. The energy of the beam has been adjusted with the monochromator as close as possible to the nominal energy of the targeted excitation of ^{7}Li (477.6 keV) to 477.1 keV. The FWHM of the peak at 477.1 keV amounts to ΔE_{meas} = 2.52 keV. To determine the energy bandwidth of the X-ray beam, the energy resolution of the photon beam can be disentangled from the (Ge-)detector resolution, according to:

$$\Delta E_{beam} = \sqrt{\Delta E_{meas}^2 - \Delta E_{Ge}^2} \tag{7.1}$$

This finally results in an energy spread of the X-ray beam after the monochromator of 1.78 keV, which is equivalent to a narrow energy bandwidth of $\Delta E/E \approx 4 \cdot 10^{-3}$.

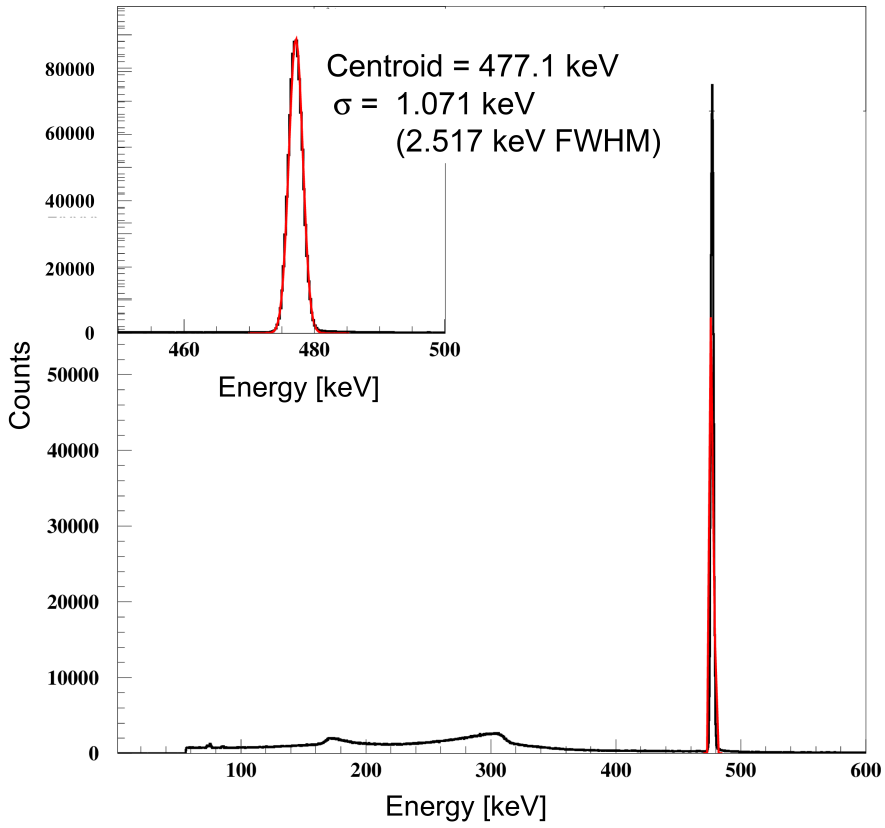

Figure 7.3: Recorded energy spectrum of the X-ray beam after the monochromator, measured with a coaxial germanium detector. The energy of the beam has been adjusted to 477.1 keV. The width (FWHM) of the peak at 477.1 keV amounts to ΔE_{meas} = 2.52 keV. Together with the energy resolution of the germanium detector, the energy spread of the X-ray beam can be extracted as $\Delta E_{beam} \approx$ 1.8 keV, equivalent to an energy bandwidth of $\Delta E/E \approx 4 \cdot 10^{-3}$.

The beam diameter at the target has been measured by the knife-edge collimator method to 1.03 mm, while the reduced photon flux after the monochromator has been estimated to 10^7 - 10^8 photons / (sec 0.1% BW), according to [178], a transmission of 10 % - 100 % of the monochromator was assumed. Unfortunately, it was not possible to obtain a more accurate number of the photon flux on target, because of an unknown absorber thickness in the beam of a simultaneously performed experiment.

7.2 The 478 keV nuclear transition of ^{7}Li

We performed a nuclear resonance fluorescence measurement of the 477.612 keV M1 transition of ^{7}Li. A photograph of the target and an excerpt of the nuclear level scheme of ^{7}Li can been seen in Fig. 7.4. The target was a plastic sample container filled with 1.08 g of Li_2O powder. The natural abundance of ^{7}Li is 94.5%, this results in a mass of 0.5 g of ^{7}Li in our target sample. The powder extended over 1.5 $\pm$ 0.1 cm of longitudinal space inside the container. Together with the diameter of 1.03 mm of the X-ray beam, the number of ^{7}Li target isotopes irradiated by the photon beam amounts to $4.3 \cdot 10^{20}$. The first excited state of ^{7}Li ($I^\Pi = 1/2^-$) decays after a half-life $t_{1/2}$ of 73 fs into the ground state ($I^\Pi = 3/2^-$) by emitting a γ ray of 477.612 keV [179].

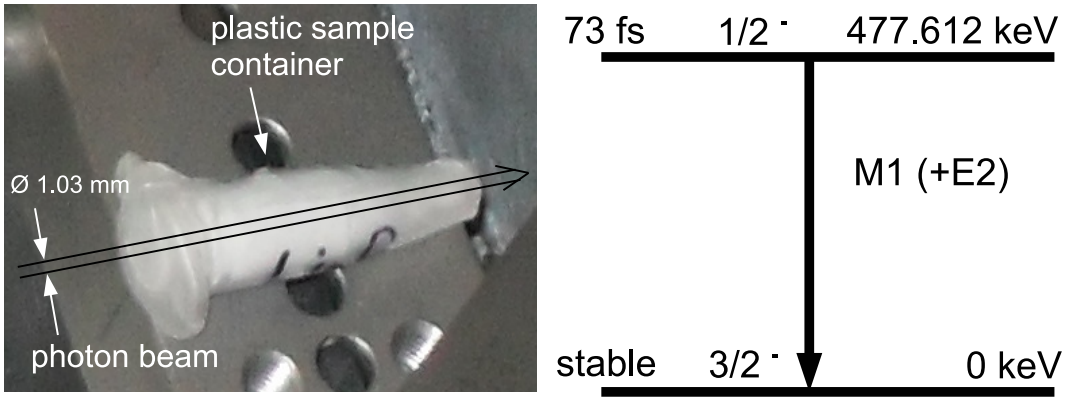

Figure 7.4: Left: Photograph of the target assembly. A plastic sample container was filled with 1.08 g of Li_2O powder, extended over 1.5 $\pm$ 0.1 cm along the longitudinal container axis. Right: Simplified excerpt of the nuclear level scheme of ^{7}Li. The first excited state has a spin and parity of $I^\Pi = \frac{1}{2}^-$. By emitting a γ ray of 477.612 keV with a half-life $t_{1/2}$ = 73 fs, it decays by an M1 (+E2) transition into the ground state with $I^\Pi = \frac{3}{2}^-$ [179].

The $LaBr_3$:Ce scintillator has been efficiently shielded with lead to suppress background radiation and was placed under a fixed backward angle of $\approx 45^\circ$ upstream from the target in a distance of 10.0 cm (see Fig. 7.5).
The same setup of the data acquisition and signal processing electronics was used, as described in Sect. 6.1.2. Three measured γ-ray energy spectra, recorded with the $LaBr_3$:Ce scintillator, are superimposed in Fig. 7.6 without further normalization. The runtime

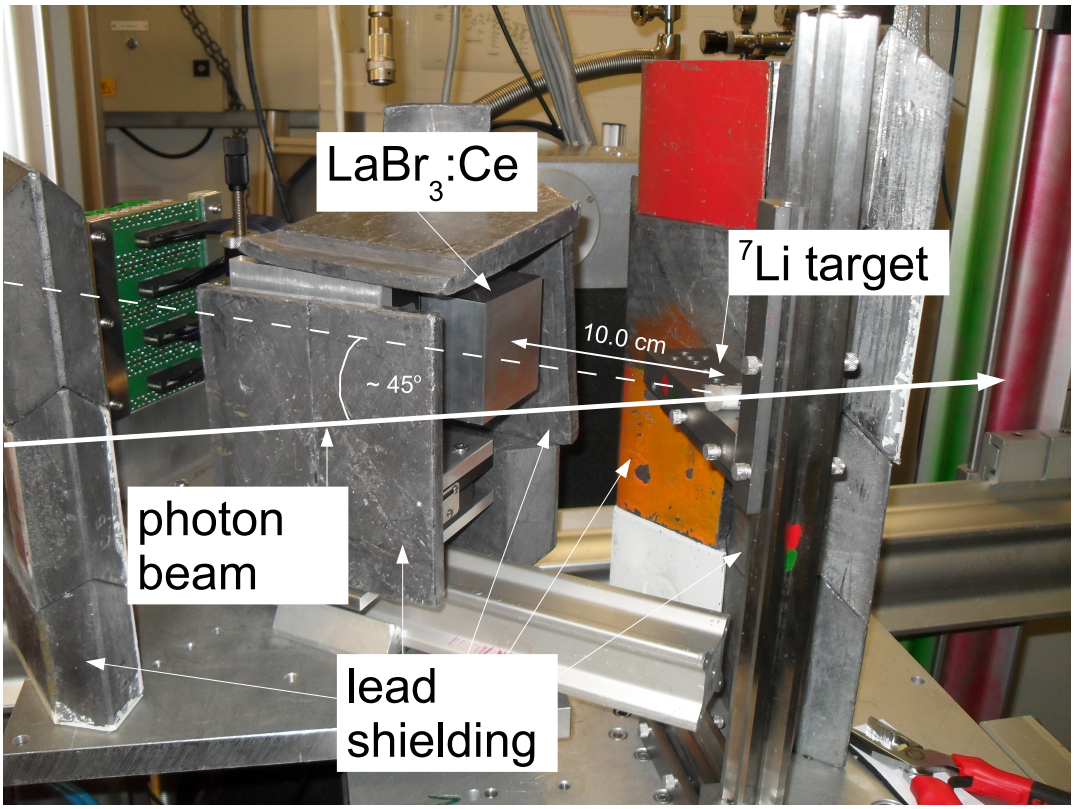

Figure 7.5: Setup of the nuclear resonance fluorescence measurement of the 478 keV nuclear transition of ^{7}Li. After the monochromator, the photon beam is irradiating the ^{7}Li target in a distance of several meters. In order to suppress background radiation, the $LaBr_3$:Ce scintillator (placed under a fixed backward angle of $\approx 45^\circ$ in a distance of 10.0 cm from the target) was efficiently shielded with lead bricks and plates.

of each measurement was 1800 s. The red curve shows the emitted energy spectrum in the case of a resonant adjustment of the X-ray beam energy of 477.5 keV (in the calibration measurement the X-ray beam energy was 477.1 keV) to the nuclear resonance of ^{7}Li (477.6 keV). The black curve represents a measurement with a monochromator adjustment of the X-ray beam energy off-resonant by 4 keV to 473.3 keV, while the blue curve displays the measured spectrum for an X-ray beam energy of 480.7 keV. The overall shapes of the recorded spectra look rather similar in the energy range beyond $\approx$ 200 keV, exhibiting different intensities in the low-energy Compton continuum below 200 keV. The major difference between the three measurements is a clear enhancement in the energy region between 450 - 500 keV for the case of the resonant adjustment of the photon beam energy to the nuclear transition of ^{7}Li (red curve). The resulting difference spectrum after subtracting the off-resonant measurement (X-ray beam energy at 473.3 keV) from the resonant measurement (477.5 keV) is displayed in Fig. 7.7 in logarithmic scale. It exhibits at low γ-ray energies ($<$ 200 keV) the difference of the Compton continuum of the two measurements, together with a prominent peak in the

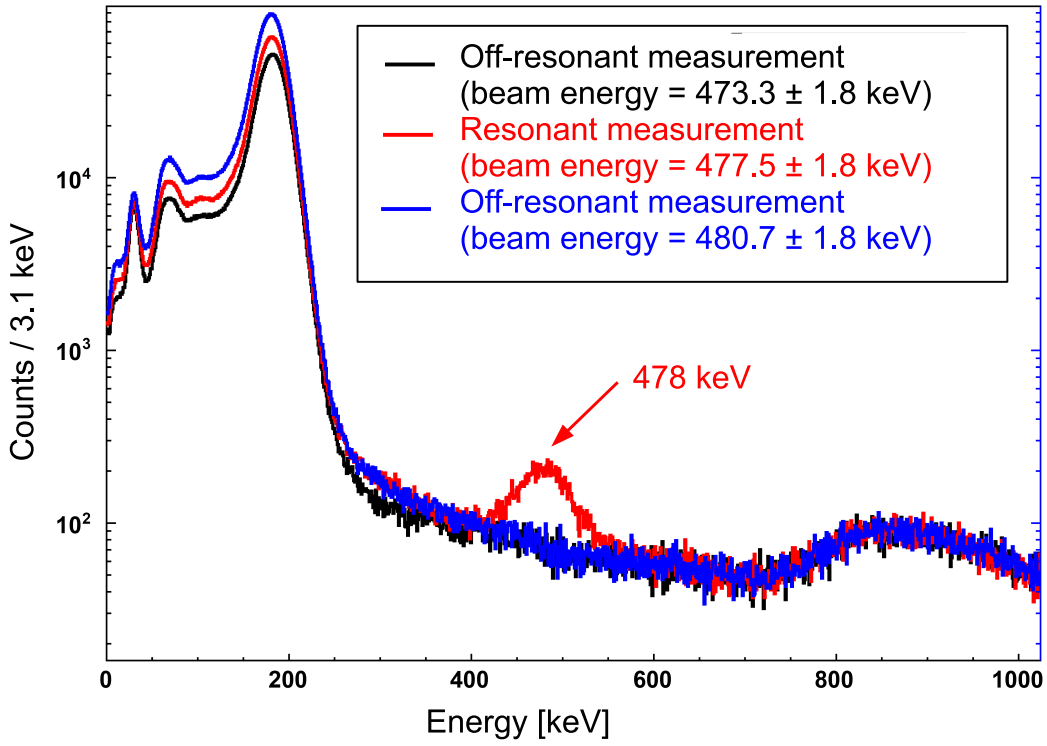

Figure 7.6: Unscaled superposition of three measurements (with 1800 s runtime each) obtained with different X-ray beam energies. The black and blue curves display off-resonant measurements with an X-ray beam energy of 473.3 keV and 480.7 keV, respectively. The red curve indicates a resonant adjustment to the nuclear transition of ^{7}Li (photon beam energy 477.5 keV). Only the resonant measurement shows the expected enhancement at $\approx$ 478 keV.

energy region of 450 - 500 keV. In Fig 7.8, this peak has been fitted by a Gaussian, resulting in a centroid energy of 480.7(8) keV, which is in reasonably good agreement with the ^{7}Li nuclear transition of 477.6 keV. The width of the peak is ΔE_γ = 61 keV (FWHM), corresponding to a relative energy resolution of $\Delta E/E$ = 12.7 %. This value is in agreement with the energy resolution determined for the identical $LaBr_3$:Ce scintillator in Sect. 6.1.3. As already discussed earlier, this much reduced energy resolution, compared to the typical value of 3 % - 4 % for $LaBr_3$ crystals, is due to the absorptive side-surface wrapping of our $LaBr_3$:Ce crystal at the time of the experiment. Thus the width of the detected fluorescence peak in Fig. 7.8, and consequently also the signal-to-background ratio, was only determined by the limited detector resolution. The (background corrected) content in the 480 keV peak, as determined by the Gaussian fit, amounts to $1.676 \cdot 10^4$, corresponding to a rate of $\approx$ 9.4 γ/s emitted from the 478 keV transition of ^{7}Li. The centroid of the fit is not exactly matching the resonance energy of 478 keV, probably caused by thermal shifts over time after the energy calibration of the detector. Thus the NRF cross section σ can be calculated according to [181]

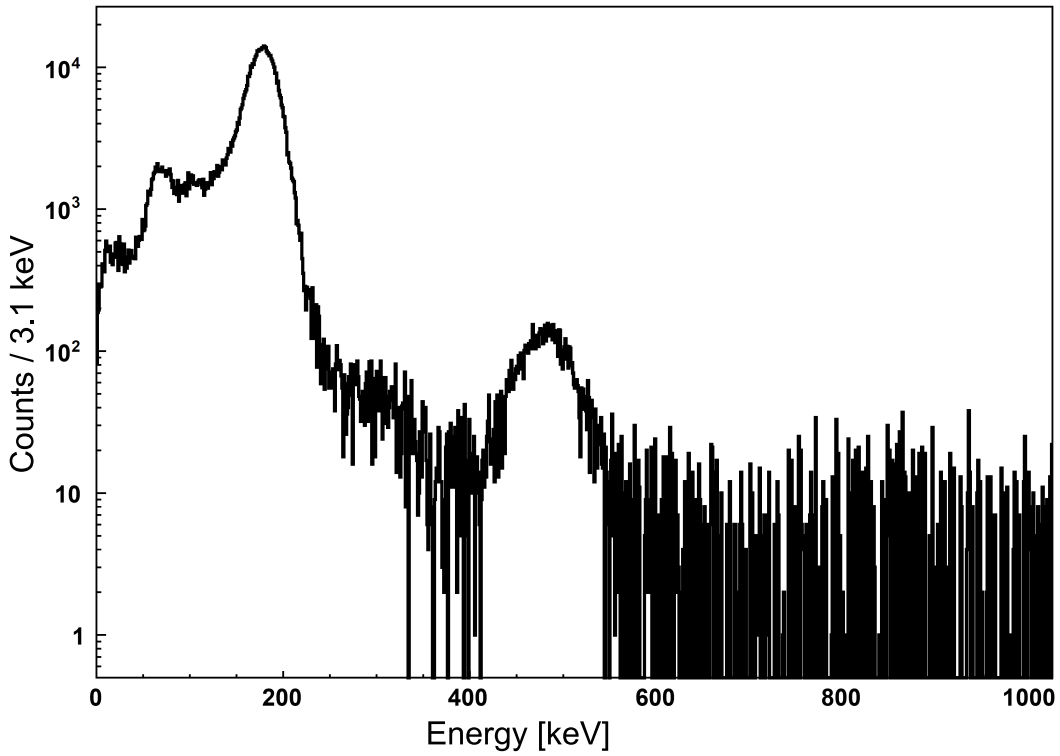

Figure 7.7: Resulting energy spectrum after subtracting the off-resonant energy spectrum measured at an X-ray beam energy of 473.3 keV from the resonant measurement (477.5 keV).

$$\sigma = \frac{\dot{N}_{Li}}{\Phi_{beam}\epsilon_{ph}d\Omega/4\pi N_t} \tag{7.2}$$

Here, $\dot{N}_{Li}$ denotes the extracted fluorescence rate of the 478 keV transition in ^{7}Li, Φ_{beam} represents the impinging photon flux, N_t is the number of target atoms within the beam area, ϵ_{ph} stands for the photopeak detection efficiency of the $LaBr_3$ scintillator and $d\Omega/4\pi$ is the solid angle coverage of the scintillator.

Table 7.1 lists the experimental parameters, which are necessary for calculating the cross section of the M1 nuclear transition of ^{7}Li. N corresponds to the number of entries in the Gaussian fit of the 480 keV peak as determined in Fig. 7.8, and t denotes the runtime of the measurement. N_t is the number of lithium target atoms inside the X-ray beam volume, Φ_{beam} the photon beam flux and BW represents the energy bandwidth of the photon beam on target. ϵ_{ph} indicates the photopeak detection efficiency of the $LaBr_3$:Ce scintillator at 475 keV, $d\Omega/4\pi$ the solid angle of the detector and Γ stands for the Doppler-broadened width of the nuclear transition of ^{7}Li [180]. These parameters allow to derive a measured cross section of σ = 0.61 $\pm$ 0.50 barn (with the lowest limit 0.11 barn corresponding to the estimated photon flux of 10^8 s^{-1}). To the best of our knowledge, this measurement repre-

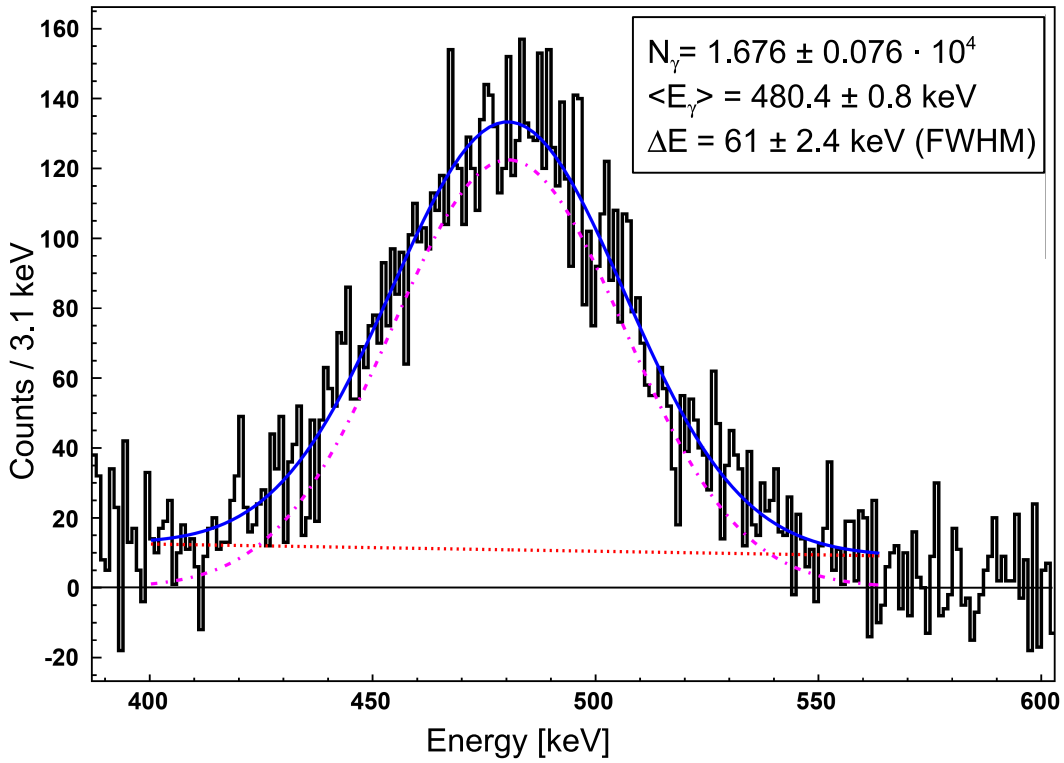

Figure 7.8: Gaussian fit of the (background-subtracted) NRF peak from ^{7}Li. The width of the peak at 480 keV is 61 keV (FWHM), corresponding to a relative energy resolution of ΔE/E = 12.7 %. The centroid of the fit is not exactly matching the resonance energy of 478 keV, most likely caused by thermal shifts over time after the energy calibration of the detector. The fit contains around $1.7 \cdot 10^4$ entries in the peak area.

sents the first direct resonant photonuclear excitation (via nuclear resonance fluorescence using a monoenergetic X-ray beam) of a low-lying M1 state in low-mass nuclei (here the first excited state in ^{7}Li). Due to the narrow γ-beam energy bandwidth of ΔE/E $\approx 4 \cdot 10^{-3}$, this measurement serves as an exploratory run with respect to planned experiments with even further improved experimental conditions at upcoming novel γ-beam facilities, that will provide unprecedented experimental opportunities, in particular for medical imaging of specific isotopes like the case of ^{7}Li studied here.

As an outlook to this kind of measurements, the upcoming highly brilliant and intense photon-beam facilities MEGa-Ray (Livermoore, USA) [182] and ELI-NP (Bucharest, Romania) [183] will allow for drastically improved NRF measurements. with about 10^4 - 10^5 higher photon flux, an improved energy bandwidth of ΔE/E $\approx 3 \cdot 10^{-3}$ and a resulting spectral density of $\approx 10^4$ γ/s eV. This will enable significantly improved experiments compared to the conditions at the ESRF (Grenoble, France) or to the presently worldwide leading γ-beam facility HIGS (Duke University, USA) with $\approx$ 10^2 γ/s eV and ΔE/E $\approx 3 \cdot 10^{-2}$. In view of the NRF in ^{7}Li, this will result in a fluorescence rate of ≈ 1 γ/s

N	t [s]	N_t	Φ_{beam} [s^{-1}]	BW [keV]	ϵ_{ph} [%]	$d\Omega/4\pi$ [%]	Γ [eV]
$1.7 \cdot 10^4$	1800	$4.3 \cdot 10^{20}$	10^7 - 10^8	1.8	25	2	0.77

Table 7.1: Experimental parameters of the nuclear resonance fluorescence measurement of the 478 keV transition of ^{7}Li. N denotes the number of entries in the Gaussian fit of the resonance peak in Fig. 7.8, t is the runtime, N_t the number of lithium target nuclei inside the X-ray beam volume, Φ_{beam} and BW are the photon beam flux and the energy bandwidth after the monochromator, respectively, ϵ_{ph} is the photopeak detection efficiency of the $LaBr_3$:Ce scintillator at 475 keV, $d\Omega/4\pi$ the solid angle of the detector and Γ represents the Doppler-broadened width of the nuclear transition of ^{7}Li [180].

per 10^{13} ^{7}Li centers. Additionally, due to the narrow bandwidth of MEGa-Ray and the ELI-NP facility, it will be possible to excite nuclear transitions very selectively, resulting in a drastic reduction of atomic background processes like Compton scattering and pair creation. This will open up a broad field of new applications based on the nuclear resonance fluorescence technique. For example, a high-resolution tomography of growing defects in Li batteries or the monitoring of the Li distribution in the brain during psychiatric medication of manic depressive patients will become possible [184].

Chapter 8

Conclusions and Perspectives

This final section presents the conclusions from the studies carried out in this thesis, furthermore, perspectives on the continuation of the Compton camera development, commissioning and optimization are outlined. The main objective of this thesis was the development of a detector system for online particle beam range monitoring of laser-accelerated proton or ion beams. Therefore, Monte-Carlo simulations for the design specifications and performance of a Compton camera with the capability of electron tracking, as well as the design specifications and performance of a "γ-PET" detector arrangement have been undertaken. Furthermore, the characteristics of the scatter- and the absorber detector components of the Compton camera have been investigated in the laboratory as well as at two synchrotron light sources. Additionally, the first steps of the commissioning of the full Compton camera setup have been completed.

8.1 Conclusion

Monte-Carlo simulations for the design specifications and performance of a Compton camera with the capability of electron tracking have been performed. The specific challenge here was to find an optimized camera geometry, designed primarily for a small-animal irradiation scenario in the environment of laser-accelerated particle beams, where the laser is uniquely providing a fast (sub-ps) trigger signal. This sharp trigger signal, together with the fast timing properties of a $LaBr_3$ scintillator, will help to suppress the (predominantly neutron) background radiation, and therefore enhance the signal-to-noise ratio of the prompt γ detection, mandatory for the online particle beam range monitoring. The achievable spatial resolution and the photon source image reconstruction efficiency of an optimized geometry for prompt γ detection have been determined in GEANT4-based Monte-Carlo simulations. The optimized geometry was found to consist of a fast timing $LaBr_3$ scintillator read out by position-sensitive photo sensor (here realized by a multi-anode photomultiplier tube), allowing to achieve a position resolution in the absorbing scintillator of 3 mm. This detector is combined with a stack of 6 DSSSD layers, enabling the electron tracking feature. Moreover, for an optimized detection of low-energy photons, an alternative absorber detector of the Compton camera has been investigated. Here, the scintillator was replaced by a 2D segmented planar germanium detector, resulting in

an improved spatial resolution for lower energies.

Subsequently, a hybrid system of PET and Compton camera, the "γ-PET" concept has been investigated. Most medical radioisotopes typically give rise to a lower spatial resolution for PET imaging, compared to the most widely used ^{18}F, due to their higher β^+ decay energies, resulting in a larger positron diffusion range. We investigated the γ-PET imaging technique, taking advantage of detecting the additionally emitted prompt γ ray in coincidence with the β^+ annihilation photons. The triple-coincidence measurement allows to reduce the image-blurring effect of the diffusion range of the positron prior to its annihilation, which increasingly gains importance when comparing radioisotopes with higher β^+ endpoint-energies compared to the 634 keV for ^{18}F. For the requirements of the γ-PET technique, the MEGAlib software toolkit has been modified to realize an event reconstruction from the Compton cone and the LOR. The simulations showed that it is possible to reach sub-millimeter spatial resolution in case of a small-animal imaging scenario, i.e. a small distance between the source and the detector, where the limiting influence of the acollinearity can be neglected. Even in case of high-energy positron emitting isotopes like ^{76}Br ($E_{e^+}^{max}$ = 3.38 MeV) or ^{10}C ($E_{e^+}^{max}$ = 2.93 MeV), the image reconstruction will again result in sub-millimeter spatial resolution. Moreover, being left only with the limiting effect of the acollinearity for whole-body PET scanning, most of the radioisotopes discussed in Sect. 4.4.1 still allow to reach sub-millimeter spatial resolution also for a clinical scenario. Particularly attractive is the highly sensitive image reconstruction capability provided by the γ-PET technique, found superior to conventional PET scanners. Presently the full potential of this advantage cannot be exploited, due to the much reduced reconstruction efficiency compared to conventional full-body or small-animal PET scanners. Thus research and development efforts should be directed towards optimizing the efficiency achievable with γ-PET. Moreover, the present study was limited to the performance involving a point source in a scattering medium, while further work will also address the characterization of the method with respect to extended photon sources. Finally, the Compton camera described here could also turn out to be beneficial in a therapeutic hadron beam irradiation, where $\beta^+\gamma$ emitters (^{10}C, ^{14}O) are generated via, e.g., the carbon beam. Especially the projectile (fragment) ^{10}C with its short half-life of 19.3 s and the quasi-simultaneous emission of a third photon from an excited state qualifies as an online marker isotope during hadron therapy. Its spatial distribution within the patient could be tomographically reconstructed, either from a (quasi-realtime) PET analysis (i.e. direct reconstruction using TOF-PET) or using the hybrid γ-PET technique, to achieve an improved spatial resolution together with an enhanced sensitivity, i.e. reduced requirements to the signal strength. The presented Compton camera (eventually upgraded by a thicker scatterer), could provide a versatile setup to assist with targeting one of the crucial issues of hadron therapy, which is ion beam range verification, either by detecting prompt γ radiation during the irradiation or (delayed) short-lived β^+-decaying reaction products (PET- or γ-PET operation) in between the irradiation cycles. Exploiting the perspectives of the γ-PET technique may thus allow to turn the present disadvantages of $\beta^+\gamma$-emitting PET isotopes into a benefit in resolution or sensitivity.

The design specifications and the performance of the Compton camera as well as of the γ-PET arrangement have been determined with MC simulations, subsequently the camera components have been characterized in the laboratory. The $LaBr_3$ crystal detector (for

this initial study equipped with absorptive surface wrapping), which is intended for use as an absorbing detector in the Compton camera, has been characterized, comprising the determination of the energy, time and spatial resolution, as well as the absolute photopeak detection efficiency. A relative energy resolution of 12.5 % at 662 keV has been found for the absorptively wrapped $LaBr_3$ detector, while reflectively coated crystals exhibit typically $\Delta E/E = 3.5$ %. The absorptively coated $LaBr_3$ crystal exhibits a clear correlation between the irradiation position and the energy resolution, i.e. best in the center and significantly degraded in the outer regions of the crystal, caused by light absorption in the edges and corners. The reflectively coated $LaBr_3$ detector shows a homogeneous (and much improved) energy resolution over the whole crystal surface. The time resolution has been determined to be 535 ps for the absorptively wrapped crystal. Considering the much improved time resolution of 275 ps for a detector with reflective side surface wrapping, advocates to favor the use of $LaBr_3$ scintillators in the environment of laser-accelerated therapeutic ion beams. The absolute photopeak detection efficiency of the $LaBr_3$ detector has been determined by the activity and the coincidence method, for an energy range of 120 keV - 1400 keV. Within minor deviations for both methods, the derived values range from $\approx$ 80 % for 121 keV to $\approx$ 10 % for 1408 keV. The significantly improved energy resolution and the faster timing of the reflectively wrapped crystal, compared to the scintillator with absorptive side surface coating, prefers its use as absorber detector. The application of the center-of-gravity method on the data recorded with the scintillator has revealed the limitations of this algorithm in case of a thick crystal. For ultimately reaching the required spatial resolution of the absorber detector, aiming at the projected properties of the Compton camera, the superior k-NN method developed in Delft has to be applied.

Moreover, for the realization of the scatter detector component of the Compton camera, double-sided silicon strip detectors have been designed and set up in a stacked array, designed for electron tracking. The substantial electronic effort of reading out all 6x 256 DSSSD channels made it necessary to implement an ASIC-based (GASSIPLEX) readout. For this purpose, the existing electronic circuit of the GASSIPLEX frontend board was adapted for the polarity requirements (handling both positive and negative input signals) and amplitude range ($<$ 500 keV) of the DSSSD signal. Operational experience has been gained in the laboratory, as well as first characterization measurements have been performed. However, due to the preliminary version of the available strip detectors with only one side fully functional at the time of the measurement, no quantitative measurements with position reconstruction could be done yet.

Additionally, as an alternative absorber of the Compton camera for optimized detection of low-energy photons, a 2D segmented high-purity planar germanium detector has been characterized. Besides the determination of the photopeak detection efficiency and the excellent energy resolution of about 2.5 keV (at 121 keV), an experiment with a polarized photon beam at the Deutsches Elektronen-Synchrotron (DESY) has been performed to experimentally characterize the polarization sensitivity of the planar germanium detector. With its segmentation of 1 mm step size per side, resulting in a pseudo-pixel size of 1 mm^2, a compromise has been found between the sharing of the charge cloud between the segments and the polarimeter sensitivity for polarized photons with energies above 100 keV. An operation under conditions with dominant background radiation has been proven

to be achievable.
Finally, an experiment at the European Synchrotron Radiation Facility (ESRF) in Grenoble was presented, where nuclear resonance fluorescence of the 478 keV nuclear transition of ^{7}Li, for the first time excited via synchrotron radiation, was studied using the above described $LaBr_3$ scintillation detector. A first estimate of the order of magnitude of the cross section of 0.61(50) barn of the nuclear transition of ^{7}Li has been derived, as well as a perspective on the prospering future of nuclear resonance fluorescence measurements, driven by upcoming highly brilliant and intense gamma-beam facilities. Drastically improved photon fluxes will open up a broad field of new applications based on the nuclear resonance fluorescence technique, e.g., monitoring of Li distributions in Li batteries or in the brain during psychiatric medication.

8.2 Perspectives

During the finalization of this thesis, the readout of the multi-anode PMT of the $LaBr_3$ scintillator has been upgraded to utilize its full segmentation of 256 PMT pixels, together with an upgrade of the corresponding individual spectroscopy electronics. Therefore, the averaging of the PMT non-uniformity matrix over 4 adjacent channels, as required in the 64-pixel readout version discussed in the framework of this thesis, is not required any more. This will allow for an improved precision of the analysis procedure and as such will contribute to an improved spatial resolution of the detector.
First preparatory steps have been completed for an application of the k-NN algorithms (in cooperation with the Delft University of Technology [152, 155]) to the data recorded with the $LaBr_3$ detector, aiming at the determination of the photon interaction point in the monolithic scintillator crystal. For this purpose, an existing automatic scanning system, installed at the Technische Universität Munich, has been adapted to enable to irradiate the whole crystal front face area with a collimated (initially $\varnothing$ 1 mm, $\varnothing$ 0.5 mm targeted) ^{137}Cs calibration source, in a 2-dimensional 0.5 mm pitch grid scan. Since the mechanically challenging manufacturing of the final 0.5 mm collimator, due to a re-design of the source holder, was not finalized within the scope of this thesis, the light amplitude reference library mandatory to exploit the full potential of the k-NN algorithm still has to be acquired, which is part of a parallel PhD thesis project. Moreover, while the k-NN method was applied with impressive results at TU Delft for the PET-relevant γ-ray energies up to 511 keV, transferring this algorithm to the realm of prompt-γ imaging requires the extension of the applicable photon energy range by more than an order of magnitude. The next step in the laboratory will be to repeat the 2D scan (presently performed with 662 keV from ^{137}Cs) with a ^{60}Co source, providing a photon energy of 1.3 MeV. This will require to significantly upgrade the source shielding and accordingly an extension of the length of the 0.5 mm collimator. Ultimately, this exercise would be desirable for the realistic prompt γ-ray energy range of 4 - 6 MeV. Such a high-energy detector scan can be performed at HIGS γ-beam facility (Duke University, USA), where energetic, monochromatic (ΔE/E $\approx 3 \cdot 10^{-2}$) photon beams can be collimated to a diameter of about 1-2 mm, sufficient for the descriped purpose.
Moreover, in the meanwhile the revised version of the high-purity double-sided silicon de-

tectors were provided by the manufacturer, which are expected to exhibit a significantly lower noise level on both detector sides compared to the preliminary version available during the here performed laboratory measurements. The so far missing energy calibration of the DSSSDs can soon be performed and compared to the information of the MC simulations discussed earlier, where a ΔE signal of $\approx$ 140 keV is expected in the spectrum for 4.4 MeV photon impinging to the tracking array by Compton-scattered electrons passing through the layers of 500 μm Si. In this context, special attention has to be paid to the electronic signal processing of the overall 1536 DSSSD signal channels, which presently is performed by an existing ASIC-based system built around the long-existing GASSIPLEX ASIC. While bringing the Compton camera project into good starting condition, as commissioning work moves on, more and more limitations of this readout system become apparent. Firstly, the GASSIPLEX chip has been designed for positive unipolar signals, whereas the DSSSD readout requires also handling negative signals from the n side. Presently this is achieved by a quick fix of shifting the baseline up to about 2 V, which, however, limits the dynamical ADC range due to otherwise saturation occuring in the amplifier stage. Optimized processing conditions would allow for arbitrary imput polarity, larger dynamic ADC range than the present 10 bit, more flexibilty in adjusting the amplifier shaping time, providing a trigger output signal from the discriminator stage and providing access to various monitoring output signals for controlling the signal processing on a (multiplexed) channel-by-channel basis. Therefore, a revision of the DSSSD readout by a new frontend board based on a modern ASIC is highly desirable.

Moreover, the requirement of low-noise performance of the DSSSD readout, allowing for the detection of low-energy Compton electron energy-loss signals, may also lead to the installation of an active cooling system inside the light-tight Faraday cage of the Compton camera. The presently used simple fan-based ventilation system could in a next step be replaced by an air cooling system. Thus the leakage current of the silicon detectors could be largely reduced in view of its quadratic dependence on the ambient temperature.

Within the completion of this thesis, the foundations for the Compton camera realization have been laid, a first prototype has been set up and characterization measurements of its detector components have been performed. In the next step of the project, the photon source reconstruction has to be targeted as the central and final stage of the goal to achieve a (ideally online) monitoring of the Bragg peak position in (first pre-clinical, later potentially also clinical) hadron therapy. Therefore, the list-mode data stream recorded with the Compton camera detectors has to be adapted to the format requirements of the Compton event analyzing module REVAN of the MEGAlib toolkit, where the ML-EM-based reconstruction will be performed. Moreover, modifications should be added to MEGAlib in order to facilitate the direct access to the GEANT4 level of the code package, thus enabling detailed performance studies specific to the medical physics applications. On the reconstruction level, this will require to include also the implementation of attenuation and scatter corrections, which, together with the simulation of an extended photon source (e.g. time-shaped in case of a proton tracked through tissue), would allow to predict the prompt-γ emission and detection properties as realistic as possible.

Altogether, prompt γ-ray imaging represents a highly promising diagnostics option for the indispensable range verification of therapeutic particle beams in tumor treatment. Hence the Compton camera concept, as specified and realized within the scope of this thesis,

bears the potential to translate these requirements into a practical diagnostical tool, even if still a long way has to be gone to achieve this final goal.

Appendix A

List of publications and conference contributions

Publication

2014

C. Lang, D. Habs, K. Parodi, P.G. Thirolf, *Submillimeter nuclear medical imaging with increased sensitivity in positron emission tomography using β-γ coincidences*, Jour. of Instrumentation 9, P01008 (2014).

P.G. Thirolf, C. Lang, S. Aldawood, H.G. v.d. Kolff, L. Maier, D.R. Schaart, K. Parodi, *Development of a Compton Camera for Online Range Monitoring of Laser-Accelerated Proton Beams via Prompt-Gamma Detection*, EPJ Web of Conferences 66, 11036 (2014).

Abstracts and conference proceedings

2015

S. Aldawood, S. Liprandi, T. Marinsek, J. Bortfeldt, L. Maier, C. Lang, H. van der Kolff, I. Castelhano, R. Lutter, G. Dedes, R. Gernhäuser, D.R. Schaart, K. Parodi and P. G. Thirolf, *Development of a Compton Camera for online ion beam range verification via prompt γ detection*, Verhandl. DPG (VI) 50, HK 12.4 (2015). S. Liprandi, S. Aldawood,

T. Marinsek, J. Bortfeldt, L. Maier, C. Lang, H. van der Kolff, I. Castelhano, R. Lutter, G. Dedes, R. Gernhäuser, D.R. Schaart, K. Parodi and P. G. Thirolf, *Commissioning of the scatter component of a Compton camera consisting of a stack of Si strip detectors*, Verhandl. DPG (VI) 50, HK 48.48 (2015). T. Marinsek, S. Aldawood, S. Liprandi, J.

Bortfeldt, L. Maier, C. Lang, H. van der Kolff, I. Castelhano, R. Lutter, G. Dedes, R. Gernhäuser, D.R. Schaart, K. Parodi and P. G. Thirolf, *Characterization of a Compton camera $LaBr_3$ absorber detector*, Verhandl. DPG (VI) 50, HK 48.50 (2015).

2014

P.G. Thirolf, S. Aldawood, M. Böhmer, J. Bortfeldt, I. Castelhano, R. Gernhäuser, H. v.d. Kolff, C. Lang, L. Maier, D.R. Schaart, K. Parodi, *Status of the Compton Camera prototype for online range verification of proton beams*, Joint Conference of the SSRMP, DGMP, OGMP, Zürich (Switzerland), September 7-10, 2014.

P.G. Thirolf, S. Aldawood, M. Böhmer, J. Bortfeldt, I. Castelhano, R. Gernhäuser, H. v.d. Kolff, C. Lang, L. Maier, D.R. Schaart and K. Parodi, *Development of a Compton Camera Prototype for Online Range Verification of Laser-Accelerated Proton Beams*, 56th Annual Meeting of AAPM, July 20-24, 2014, Austin (USA), Med. Phys. 41, 165 (2014).

S. Aldawood, C. Lang, H. v.d. Kolff, L. Maier, R. Lutter, J. Bortfeldt, K. Parodi, P.G. Thirolf, *Development of a Compton camera for online ion beam range verification via prompt γ detection*, Verhandl. DPG (VI) 49, HK 64.7 (2014).

B. Tegetmeyer, S. Aldawood, H. v.d. Kolff, C. Lang, K. Parodi, P. Thirolf, *Towards reaction cross section measurements of β^+ emitters produced in hadron therapy*, Verhandl. DPG (VI) 49, HK 46.38 (2014).

2013

P.G. Thirolf, S. Aldawood, C. Lang, K. Parodi, *Development of a Compton Camera for Online Range Monitoring of Laser-Accelerated Proton Beams*, Med. Phys. 40, 144 (2013).

P. Thirolf, C. Lang, S. Aldawood, H. v.d. Kolff, J. Bortfeldt, L. Maier, D.R. Schaart, K. Parodi, *Development of a Compton camera for online range monitoring of laser accelerated proton beams*, 44. Jahrestagung der Deutschen Gesellschaft für Medizinische Physik, Abstractband ISBN 978-3-9816002-1-6, p281-2 (2013).

P.G. Thirolf, C. Lang, S. Aldawood, D. Habs, L. Maier, K. Parodi, *Development of a Compton Camera for online monitoring and dosimetry of laser-accelerated proton beams*, Verhandl. DPG (VI) 48, HK 69.3 (2013).

S. Aldawood, C. Lang, D. Habs, L. Maier, K. Parodi, P.G. Thirolf, *Characterization of a $LaBr_3$ crystal with multi-anode PMT readout*, Verhandl. DPG (VI) 48, HK 52.7 (2013).

2012

C. Lang, D. Habs, P.G. Thirolf, A. Zoglauer, *Submillimeter nuclear medical imaging with a Compton Camera using triple coincidences of collinear β^+-annihilation photons and gamma rays*, Radiotherapy and Oncology 102, s1 (2012), S29; arXiv:1202.0397v1 [phys.ins-det] (2012).

C. Lang, D. Habs, P.G. Thirolf, A. Zoglauer, *Submillimeter medical imaging in emission tomography*, Verhandl. DPG (VI) 47, HK 17.9 (2012).

2011

D. Habs, S. Gasilov, C. Lang, P.G. Thirolf, M. Jentschel, R. Diehl, C. Schroer, C.P.J. Barty and N.V. Zamfir, *Intense, Brilliant Micro Gamma-Beams in Nuclear Physics and Applications*, Proceedings of SPIE 8075, 807507 (2011).

D. Habs, P.G. Thirolf, C. Lang, M. Jentschel, U. Köster, F. Negoita, V. Zamfir, *Medical Application Studies at ELI-NP*, Proc. SPIE 8079, 80791H (2011).

Appendix B

Simulated γ-ray energy spectra

The following energy spectra have been simulated as being recorded with the Compton camera during the investigations in Sect. 5.2.1. The geometry is displayed in Fig. 5.5, consisting of a $LaBr_3$ absorber and 6 DSSSD scatterer. Two different spatial resolution of the absorber (6 x 6 mm^2, 3 x 3 mm^2) and two different thicknesses of the scatterer (300 μm, 500 μm) are shown.

Figure B.1: Simulated γ-ray energy spectra recorded with the Compton Camera geometry (Fig. 5.5) consisting of a $LaBr_3$ absorber with 64 pixel and 6 DSSSD scatterer of 300 μm thickness. Spectra of 6 different γ point source energies E_γ are shown.

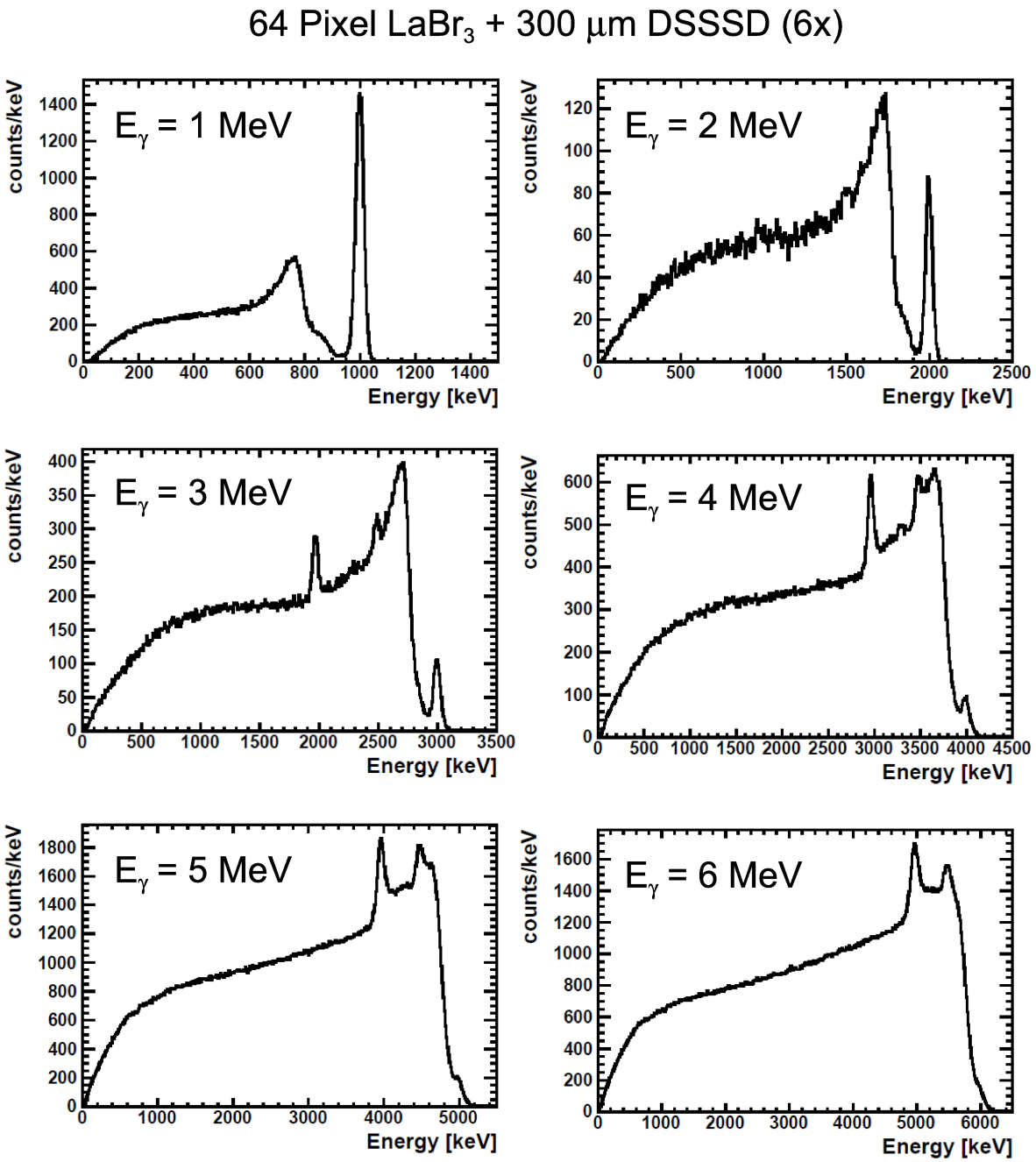

Figure B.2: Simulated γ-ray energy spectra recorded with the Compton Camera geometry (Fig. 5.5) consisting of a $LaBr_3$ absorber with 256 pixel and 6 DSSSD scatterer of 300 μm thickness. Spectra of 6 different γ point source energies E_γ are shown.

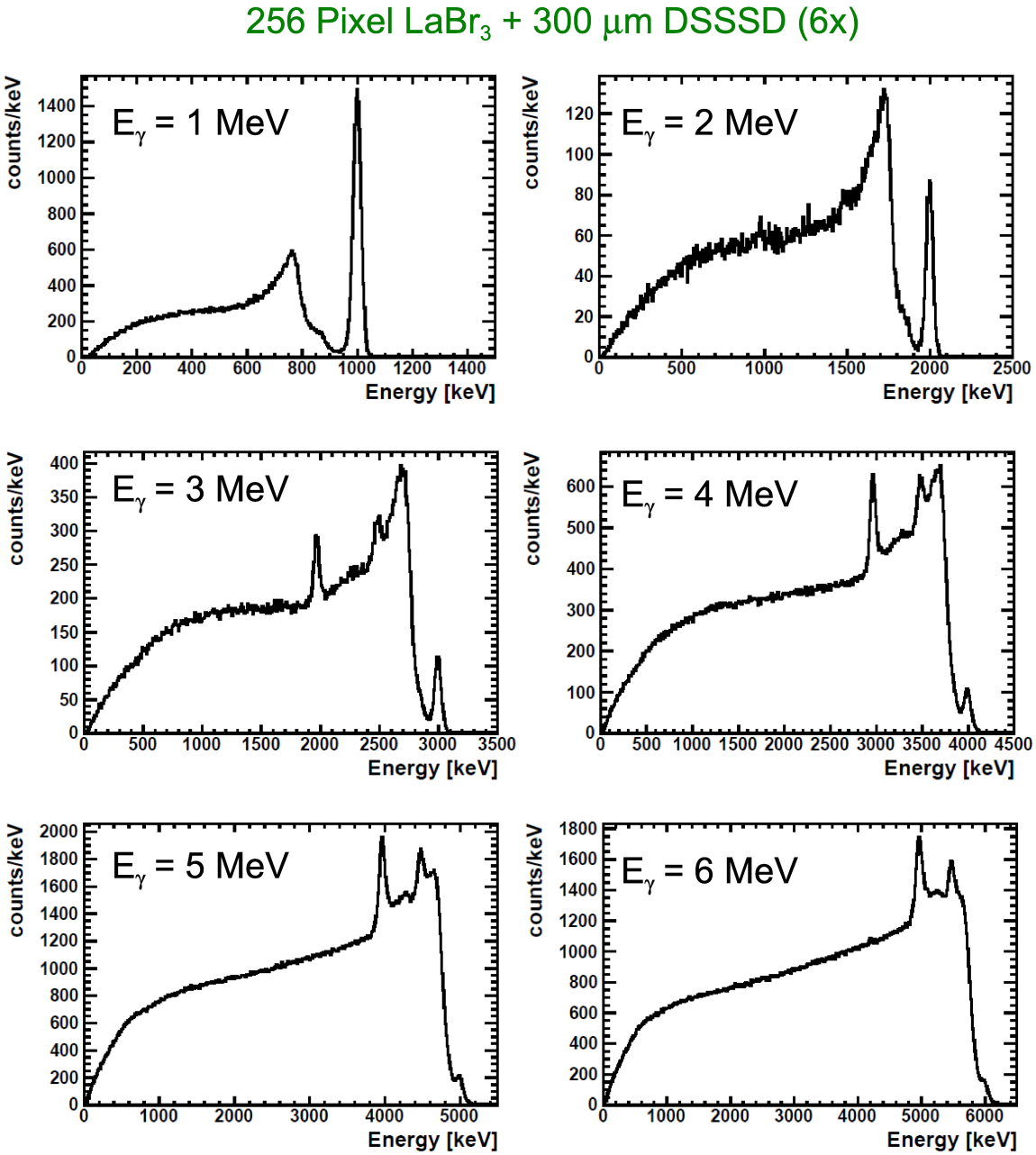

Figure B.3: Simulated γ-ray energy spectra recorded with the Compton Camera geometry (Fig. 5.5) consisting of a $LaBr_3$ absorber with 64 pixel and 6 DSSSD scatterer of 500 μm thickness. Spectra of 6 different γ point source energies E_γ are shown.

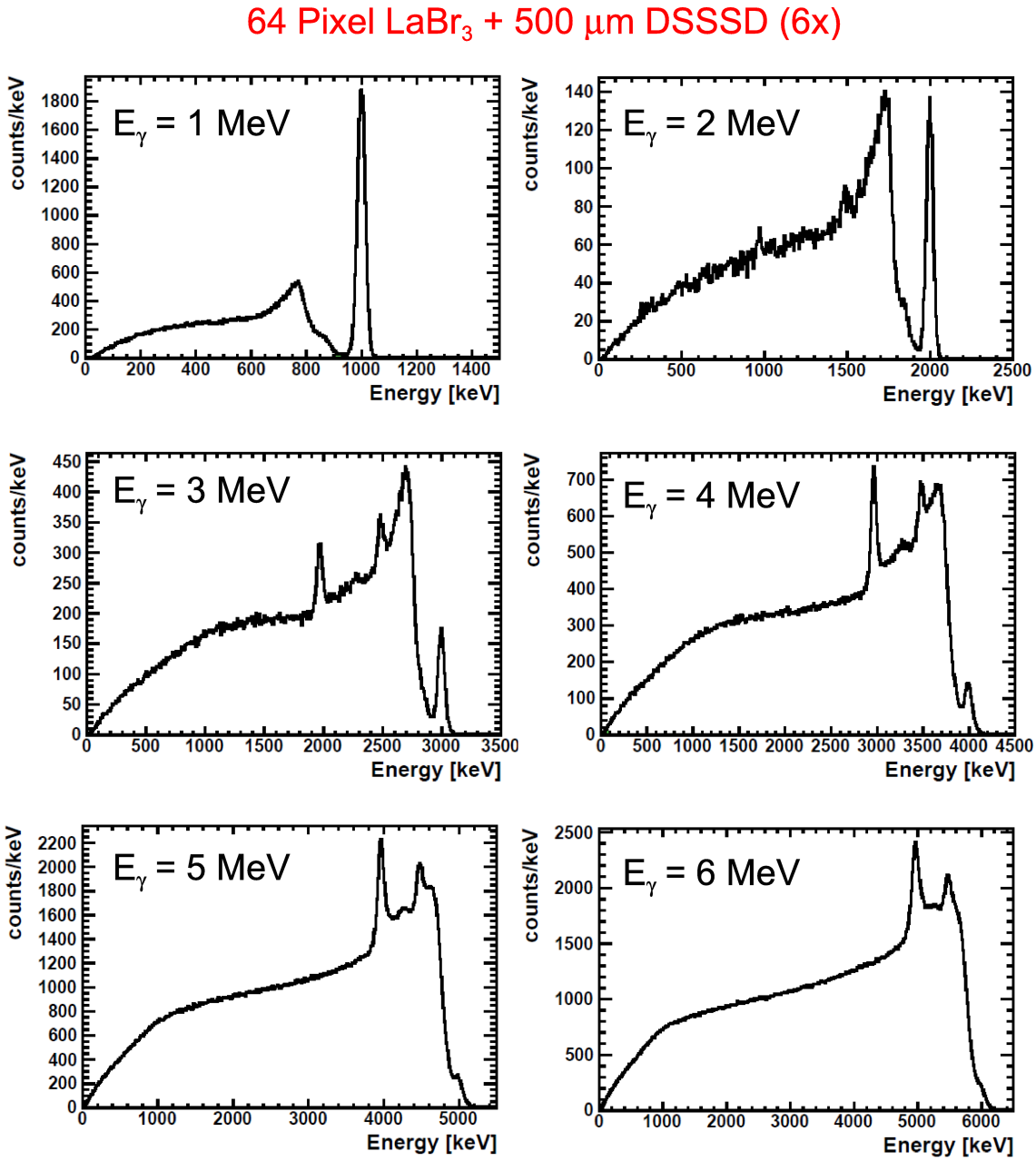

Figure B.4: Simulated γ-ray energy spectra recorded with the Compton Camera geometry (Fig. 5.5) consisting of a $LaBr_3$ absorber with 256 pixel and 6 DSSSD scatterer of 500 μm thickness. Spectra of 6 different γ point source energies E_γ are shown.

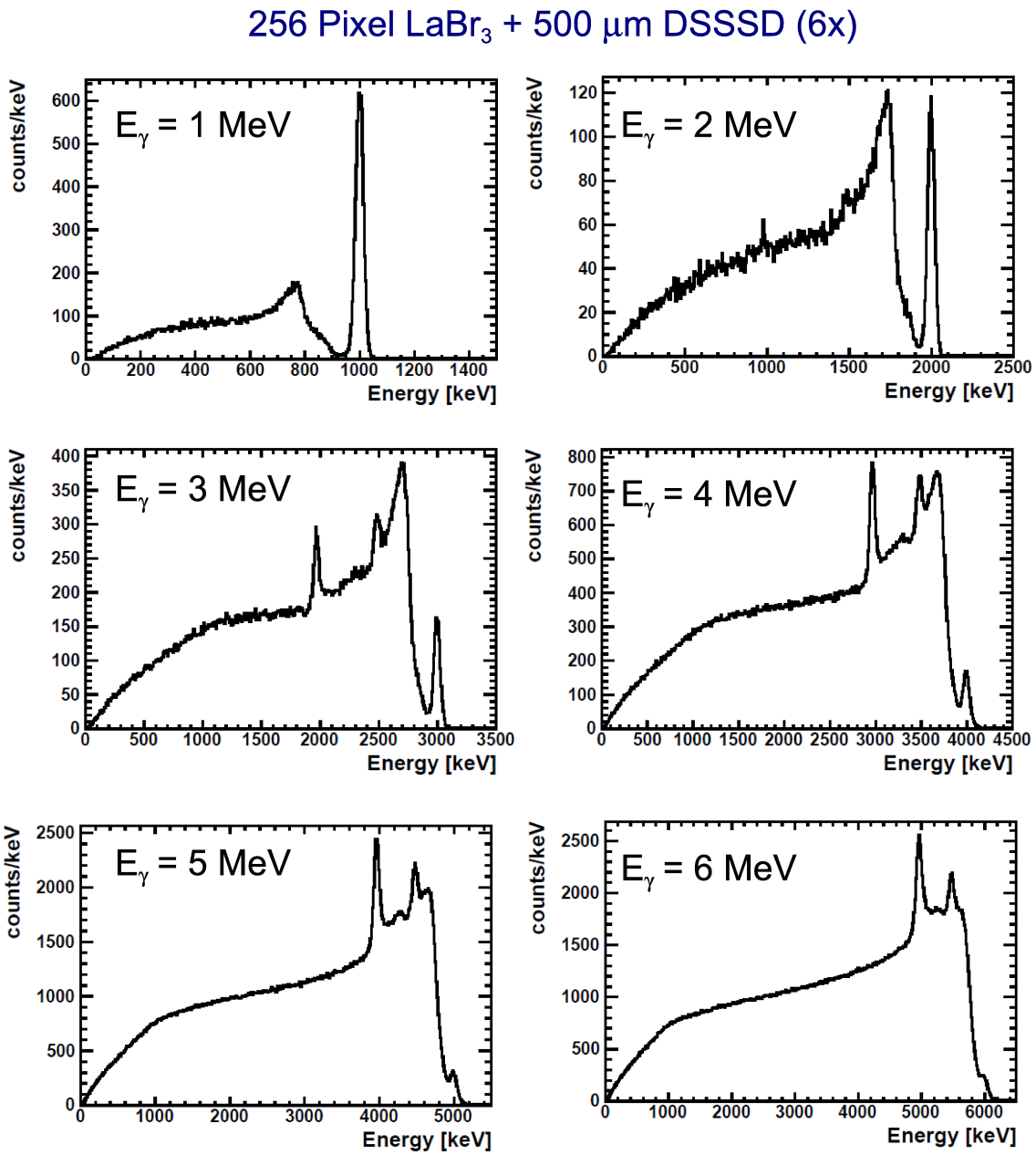

Appendix C

Correction values for the 2-dimensional light amplitude distribution of the $LaBr_3$ detector

All displayed correction values have been determined for the case of the absorptively coated $LaBr_3$ crystal. For all following tables, the numbering of the pixels is as follows:

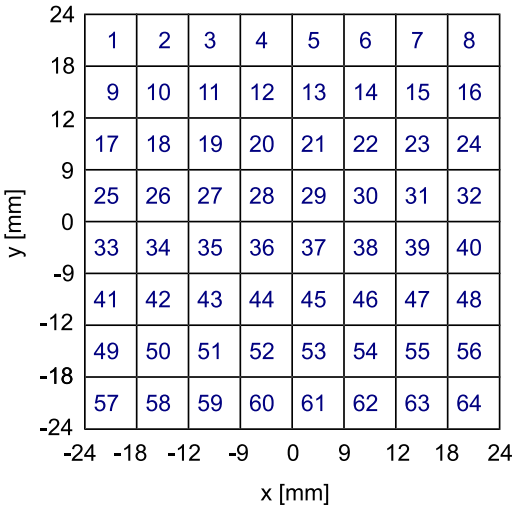

Figure C.1: Matrix of the PMT pixel number mapping, seen in front view.

Table C.1: Gain correction factors and offset values.

Pixel number	Gain correction factor	Offset	Pixel number	Gain correction factor	Offset
1	1.00	0.00	33	1.00	11.32
2	1.02	-13.34	34	1.01	10.97
3	1.02	-14.70	35	1.01	6.27
4	1.02	-3.12	36	1.01	-3.51
5	1.01	-13.20	37	1.00	-6.34
6	1.01	-6.20	38	1.01	-1.79
7	1.01	-4.47	39	1.01	-6.49
8	1.00	9.34	40	1.00	8.00
9	1.01	-21.08	41	0.99	17.73
10	1.01	-15.32	42	1.01	3.91
11	1.01	-14.96	43	1.00	4.73
12	1.01	-7.84	44	1.00	4.62
13	1.00	0.66	45	0.99	14.82
14	1.01	-3.49	46	1.01	1.58
15	1.00	1.98	47	1.00	0.96
16	1.01	4.59	48	1.01	3.58
17	1.01	-0.13	49	1.02	7.66
18	1.02	7.72	50	1.01	12.65
19	1.03	-7.16	51	1.01	11.66
20	1.02	-1.14	52	1.01	9.63
21	1.01	10.30	53	1.01	8.96
22	1.02	-0.45	54	1.00	9.37
23	1.00	17.00	55	1.00	-1.32
24	1.02	0.28	56	1.01	-0.45
25	1.01	-10.92	57	1.00	1.77
26	1.03	-43.50	58	1.01	-12.58
27	1.03	-30.41	59	1.00	-3.37
28	1.02	-19.13	60	1.01	-8.90
29	1.02	-7.90	61	1.00	31.31
30	1.01	-4.17	62	1.01	20.02
31	1.03	-18.44	63	1.00	14.99
32	1.02	-6.21	64	1.01	17.44

Table C.2: Pedestal subtraction values.

Pixel number	Pedestal subtraction value	Pixel number	Pedestal subtraction value
1	120	33	125
2	141	34	134
3	145	35	136
4	147	36	142
5	130	37	125
6	138	38	134
7	137	39	136
8	133	40	133
9	136	41	122
10	138	42	136
11	139	43	129
12	137	44	135
13	128	45	119
14	136	46	132
15	131	47	131
16	138	48	137
17	133	49	140
18	138	50	138
19	145	51	143
20	136	52	138
21	130	53	135
22	142	54	131
23	132	55	135
24	144	56	139
25	135	57	129
26	135	58	142
27	155	59	139
28	144	60	144
29	141	61	131
30	136	62	139
31	149	63	141
32	139	64	145

Table C.3: PMT non-uniformity correction values.

Pixel number	PMT non-uniformity correction factor	Pixel number	PMT non-uniformity correction factor
1	1.26	33	1.05
2	1.50	34	1.13
3	1.57	35	1.13
4	1.62	36	1.23
5	1.71	37	1.22
6	1.71	38	1.08
7	1.69	39	1.02
8	1.63	40	1.00
9	1.63	41	1.34
10	1.51	42	1.18
11	1.46	43	1.14
12	1.58	44	1.16
13	1.59	45	1.14
14	1.56	46	1.05
15	1.71	47	1.06
16	1.85	48	1.26
17	1.27	49	1.56
18	1.30	50	1.39
19	1.30	51	1.27
20	1.41	52	1.24
21	1.41	53	1.23
22	1.38	54	1.22
23	1.38	55	1.23
24	1.45	56	1.48
25	1.06	57	1.41
26	1.19	58	1.21
27	1.25	59	1.20
28	1.38	60	1.21
29	1.40	61	1.22
30	1.29	62	1.14
31	1.18	63	1.17
32	1.06	64	1.36

Table C.4: Light distribution correction values.

Pixel number	Light distribution correction factor	Pixel number	Light distribution correction factor
1	3.44	33	2.05
2	5.74	34	1.70
3	6.66	35	1.52
4	4.02	36	1.43
5	1.70	37	1.41
6	2.71	38	1.57
7	3.37	39	1.40
8	5.36	40	1.90
9	3.72	41	3.09
10	2.78	42	1.99
11	2.20	43	1.44
12	2.01	44	1.29
13	1.45	45	1.11
14	1.74	46	1.40
15	1.78	47	1.41
16	2.21	48	2.41
17	1.69	49	2.28
18	1.56	50	1.67
19	1.38	51	1.38
20	1.26	52	1.24
21	1.07	53	1.11
22	1.54	54	1.23
23	1.51	55	1.36
24	2.45	56	2.42
25	1.38	57	3.73
26	1.00	58	3.27
27	1.37	59	2.40
28	1.29	60	2.31
29	1.23	61	1.77
30	1.35	62	2.15
31	1.24	63	2.48
32	1.38	64	4.19

Appendix D

Technical drawings of the DSSSD board

The following technical drawings of the DSSSD printed circuit board indicate the pin assignment of the p side (oriented to be the front side) as well as of the n side (oriented to be the back side).

Figure D.1: Technical drawing of two corners of the DSSSD printed circuit board, showing the pin assignment of the front side (p side, part 1).

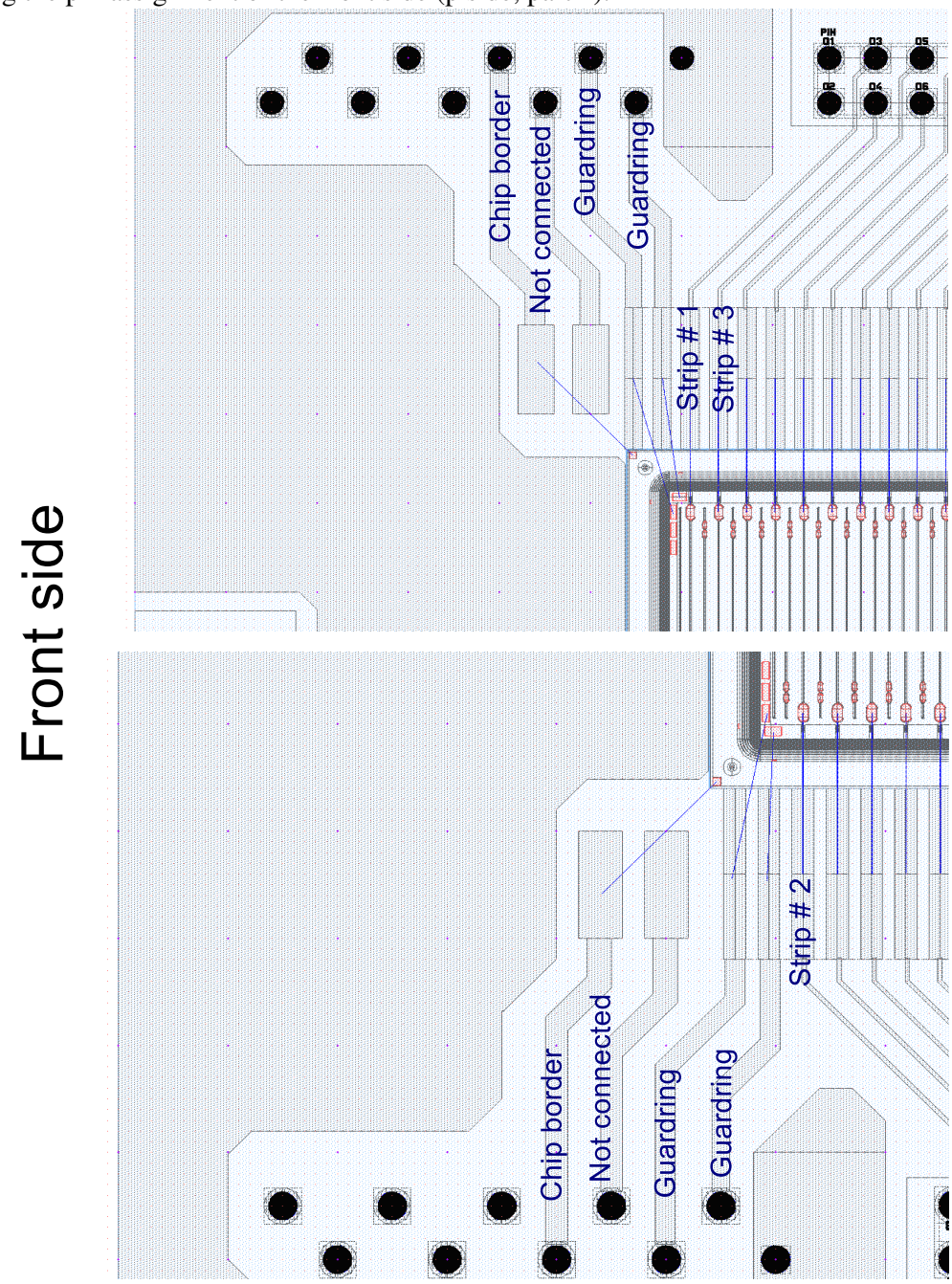

Figure D.2: Technical drawing of the complementary two corners of the DSSSD printed circuit board, showing the pin assignment of the front side (p side, part 2).

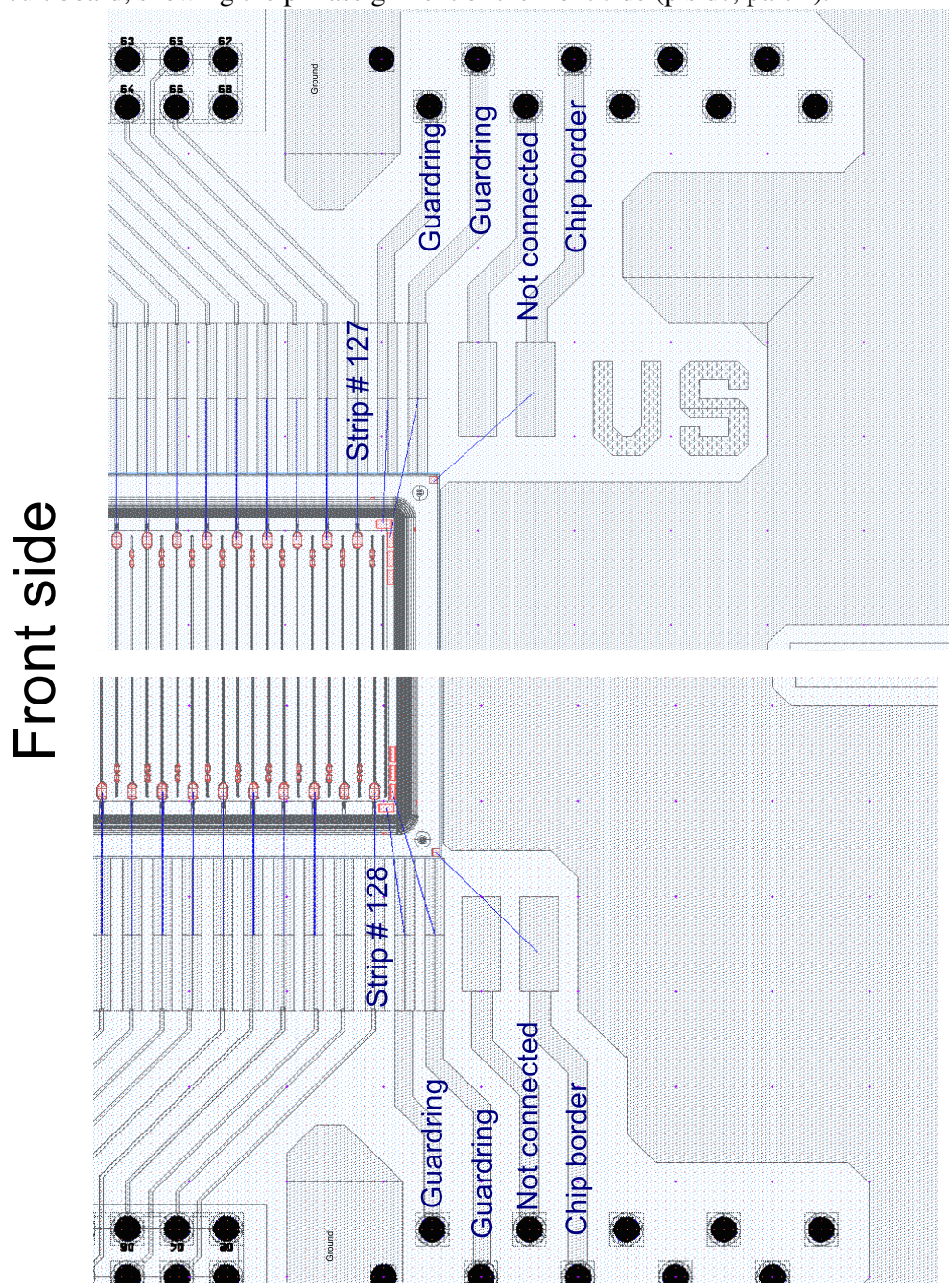

Figure D.3: Technical drawing of two corners of the DSSSD printed circuit board, showing the pin assignment of the back side (n side, part 1).

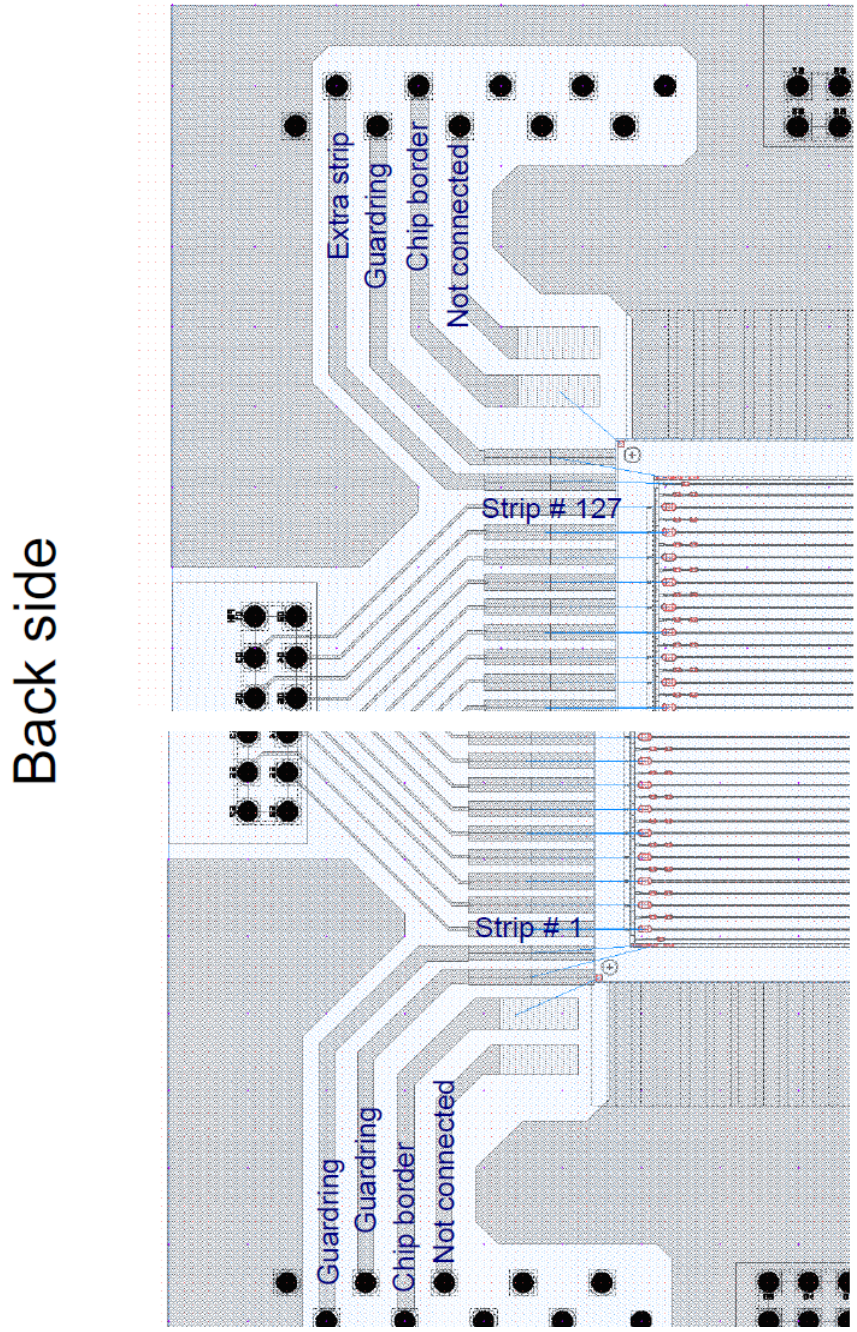

Figure D.4: Technical drawing of the complementary two corners of the DSSSD board printed circuit, showing the pin assignment of the back side (n side, part 2).

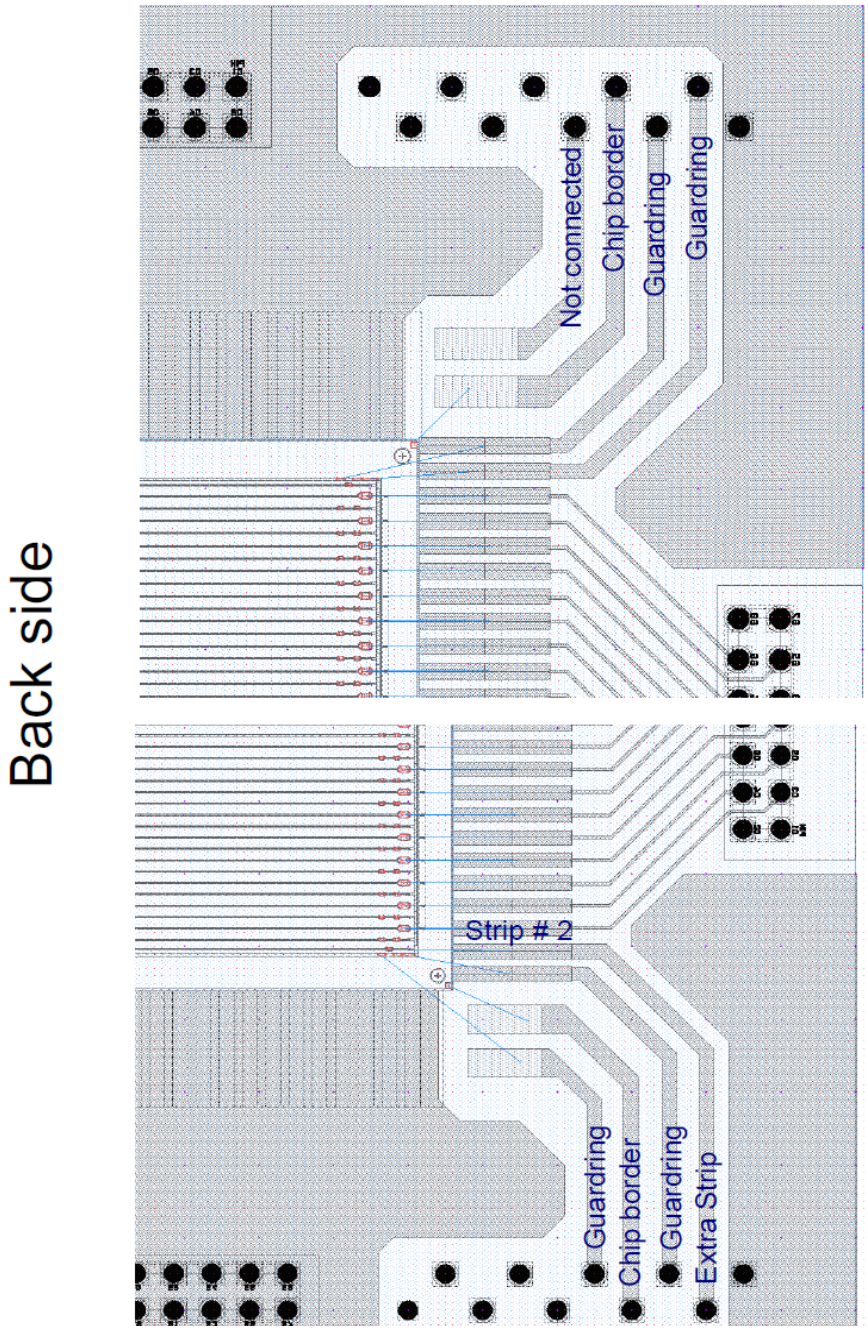

Appendix E

Modifications of MEGAlib

For the requirements of the γ-PET technique, MEGAlib has been modified to realize an event reconstruction from the intersection between the Compton cone of the third, prompt photon and the LOR from the positron annihilation. So far, the γ-PET additions have not yet been implemented in the official release of the MEGAlib software toolkit, therefore the following C++ code has to be added to the MEGAlib software libraries as described in the headlines.

```
//-------------------------------------------------------
// to be pasted in MImagerExternallyManaged.h
//-------------------------------------------------------

MBPData* CalculateResponseSliceLine(MPhysicalEvent* Event, double X1Position,
double Y1Position, double Z1Position, double X2Position, double Y2Position,
double Z2Position);

//-------------------------------------------------------
// to be pasted in MBackprojection.h
//-------------------------------------------------------

virtual bool Backproject(MPhysicalEvent* Event, double* Image, int* Bins,
int& NUsedBins, double& Maximum, double X1Position, double Y1Position,
double Z1Position, double X2Position, double Y2Position, double Z2Position) = 0;

//-------------------------------------------------------
// to be pasted in MBackprojectionSphere.h
//-------------------------------------------------------

virtual bool Backproject(MPhysicalEvent* Event, double* Image, int* Bins,
int& NUsedBins, double& Maximum, double X1Position, double Y1Position,
double Z1Position, double X2Position, double Y2Position, double Z2Position);

//-------------------------------------------------------
// to be pasted in MBackprojectionSphereArea.h
//-------------------------------------------------------

  bool Backproject(MPhysicalEvent* Event, double* Image, int* Bins,
  int& NUsedBins, double& Maximum, double X1Position, double Y1Position,
  double Z1Position, double X2Position, double Y2Position, double Z2Position);

//-------------------------------------------------------
// to be pasted in MBackprojectionSpherePoints.h
//-------------------------------------------------------

 bool Backproject(MPhysicalEvent* Event, double* Image, int* Bins,
 int& NUsedBins, double& Maximum, double X1Position, double Y1Position,
 double Z1Position, double X2Position, double Y2Position, double Z2Position);

//-------------------------------------------------------
// to be pasted in MBackprojectionCartesian.h
//-------------------------------------------------------

 virtual bool Backproject(MPhysicalEvent* Event, double* Image, int* Bins,
 int& NUsedBins, double& Maximum, double X1Position, double Y1Position,
  double Z1Position, double X2Position, double Y2Position, double Z2Position);
```

```
//-------------------------------------------------------------
// to be pasted in  MBackprojectionCartesian.cxx
//-------------------------------------------------------------

bool MBackprojectionCartesian::BackprojectionComptonLine(double* Image, int* Bins, int& NUsedBins, double& Maximum,
     double X1Position, double Y1Position, double Z1Position, double X2Position, double Y2Position, double Z2Position
     )
{
  // Compton-Backprojection-LOR-Intersection-algorithm:
  // The event expands to a double-gausshaped banana and gets intersected with a Line of Response
  //
  // Image            :  the produced binned image - must have the correct dimensions
  // Limit            :  the limit
  // NABoveLimit      :

  Maximum = 0.0;
  NUsedBins = 0;

  // Let the response get the event data:
  m_Response->AnalyzeEvent(m_C);  // <- not the correct place...

  int x, y, z;
  double AngleTrans, AngleLong;
  double InnerSum = 0;
  double ConeRadius = 0;

  double Content;

  // LOR axis vector
  double ContentLine, Distance;

  double ax = X2Position - X1Position;
  double ay = Y2Position - Y1Position;
  double az = Z2Position - Z1Position;

  double bx, by, bz;
  double Deno = ax*ax+ay*ay+az*az;


  // Cone axis vector (reverse direction of scattered gamma ray)
  double xCA = -m_C->Dg().X();
  double yCA = -m_C->Dg().Y();
  double zCA = -m_C->Dg().Z();
  Rotate(xCA, yCA, zCA);

  // Position of first interaction:
  double xCC = m_C->C1().X();
  double yCC = m_C->C1().Y();
  double zCC = m_C->C1().Z();
  Rotate(xCC, yCC, zCC);

  //cout<<"Cone center: "<<xCC<<":"<<yCC<<":"<<zCC<<endl;

  // The origin of the gamma ray:
  double xOrigin = -m_C->De().X();
  double yOrigin = -m_C->De().Y();
  double zOrigin = -m_C->De().Z();
  Rotate(xOrigin, yOrigin, zOrigin);

  double xBin, yBin, zBin;
  double xn1, yn1, zn1, xn2, yn2, zn2;


  // Important pre-computations
  double Phi = m_C->Phi();
  double tanPhi = tan(Phi);

  //double Threshold = 0.001;

  // Min and max Trans-angle above threshold:
  double Trans_max = m_Response->GetComptonTransversalMax();
  double Trans_min = m_Response->GetComptonTransversalMin();

  double PhiMin = Phi + Trans_min;
  double PhiMax = Phi + Trans_max;
  double cosPhiMin = cos(PhiMin);
  double cosPhiMax = cos(PhiMax);

  double L;


  bool HasTrack = m_C->HasTrack();


  // ---------> time critical --------->

  // Start the backprojections

  unsigned int i;
  unsigned int i_z;
  unsigned int i_yz;
  for (z = 0; z < m_x3NBins; z++) {
```

```
    i_z = z*m_x1NBins*m_x2NBins;
    for (y = 0; y < m_x2NBins; y++) {
      i_yz = y*m_x1NBins + i_z;
      for (x = 0; x < m_x1NBins; x++) {
        i = x + i_yz; // We fill each x-row


        Content = 0;
        ContentLine = 0;
        xBin = m_xBinCenter[x]-xCC;
        yBin = m_yBinCenter[y]-yCC;
        zBin = m_zBinCenter[z]-zCC;
        AngleTrans = Angle(xBin, yBin, zBin, xCA, yCA, zCA) - Phi;

// tmp: time coincidence only


 ////////////////////////////////////////////

        // Skip pixels below threshold:
        if (x < m_x1NBins - 1) { // We just do the optimization if there are bins left in x-direction:
          // We now calculate the intersection point between this axis and the cone
          // The cone is defined by (cone center is origin):
          // 0 = (X dot CA)^2 - (X dot X) * (CA dot CA) * sin phi  (CA: cone axis)
          // The axis is defined by:
          // X = P + l*(1, 0, 0) where P is the bin center relative to the cone center, i.e. xBin, yBin, zBin
          // Then we determine a, b, c of the Mitternachtsformel and calculate lambda1,2

          // Outside outer ring
          if (AngleTrans > Trans_max + 0.002 || AngleTrans < Trans_min - 0.002) {
            //cout<<m_xBinCenter[x]<<":"<<m_yBinCenter[y]<<endl;
            double CAdotCA = xCA*xCA + yCA*yCA + zCA*zCA; // Per definition "1"!
            double BCdotBC = xBin*xBin + yBin*yBin + zBin*zBin;
            double BCdotCA = xBin*xCA + yBin*yCA + zBin*zCA;

            double cos2PhiRelevant;
            if (AngleTrans > Trans_max) {
              //cout<<"Outside: "<<(AngleTrans - Trans_max)*c_Deg<<endl;
              cos2PhiRelevant = cosPhiMax;
            } else {
              //cout<<"Inside: "<<(AngleTrans - Trans_min)*c_Deg<<endl;
              cos2PhiRelevant = cosPhiMin;
            }
            cos2PhiRelevant *= cos2PhiRelevant;

            double a = xCA*xCA - CAdotCA*cos2PhiRelevant;
            double b = 2*(BCdotCA*xCA - xBin*CAdotCA*cos2PhiRelevant);
            double c = BCdotCA*BCdotCA - BCdotBC*CAdotCA*cos2PhiRelevant;

            double Diskriminante = b*b-4*a*c; // This has to be identical on one x-axis since the distance between
                 axis intersection stays the same
            //cout<<"Diskriminante: "<<Diskriminante<<":"<<a<<":"<<b<<":"<<c<<":"<<CAdotCA<<":"<<BCdotBC<<":"<<BCdotCA
                 <<":"<<cos2PhiRelevant<<endl;

            if (Diskriminante <= 0) { // We ignore the "academic" solution of a tangential point, it's simply not
                 relevant
                //cout<<"No intersection with cone"<<endl;
              break;
            }
            double Lambda1 = (-b-sqrt(Diskriminante))/(2*a);
            double Lambda2 = (-b+sqrt(Diskriminante))/(2*a);

            // Find the closest solution in x-direction (attention: we are in a coordiante system realtive to cone
                 center!):
            double xNext = 0.0;
            //cout<<"xBC: "<<m_xBinCenter[x]<<"  xBin: "<<xBin<<"  l1:"<<Lambda1<<"  l2:"<<Lambda2<<" dist: "<<Lambda1
                 -Lambda2<<endl;
            if (Lambda1 > 0 && Lambda2 > 0) {
              if (Lambda1 < Lambda2) {
                xNext = Lambda1;
              } else {
                xNext = Lambda2;
              }
            } else if (Lambda1 > 0) {
              xNext = Lambda1;
            } else if (Lambda2 > 0) {
              xNext = Lambda2;
            } else {
              //cout<<"Beyond intersection"<<endl;
             break;
            }
            //cout<<"Chosen lamda: "<<xNext<<endl;


            // Now skip ahead:
           // x+= (int) floor(xNext/m_x1IntervalLength);
            //if (x >= m_x1NBins) break; // Done

            //cout<<"New x: "<<m_xBinCenter[x]<<endl;
            continue;
          }
        }
```

```
        L = sqrt(xBin*xBin + yBin*yBin + zBin*zBin);
        ConeRadius = fabs(tanPhi*Acos(AngleTrans)*L);

        if (HasTrack == true) {
          // angle between two planes spanned by ...
          xn1 = yBin*zCA - zBin*yCA;
          yn1 = (zBin*xCA - xBin*zCA);
          zn1 = xBin*yCA - yBin*xCA;

          xn2 = (yOrigin*zCA - zOrigin*yCA);
          yn2 = (zOrigin*xCA - xOrigin*zCA);
          zn2 = (xOrigin*yCA - yOrigin*xCA);

          AngleLong = Acos((xn1*xn2+yn1*yn2+zn1*zn2)/sqrt((xn1*xn1+yn1*yn1+zn1*zn1)*(xn2*xn2+yn2*yn2+zn2*zn2)));

          //cout<<i<<": "<<ConeRadius<<"!"<<tanPhi<<"!"<<AngleTrans<<"!"<<L<<"-->"<<m_Response->GetResponse(AngleTrans
               , AngleLong)/ConeRadius<<endl;

          // Sample the 2d-Gauss-function: m_AreaBin[t] is missing ---> new geometry is missing!!!
          Content = m_Response->GetComptonResponse(AngleTrans, AngleLong)/ConeRadius;
        } else {
          Content = m_Response->GetComptonResponse(AngleTrans)/ConeRadius;
        }



// calculation of the Line of Response (LOR)
    bx = m_xBinCenter[x] - X1Position;
        by = m_yBinCenter[y] - Y1Position;
        bz = m_zBinCenter[z] - Z1Position;
        Distance = sqrt(  ((ay*bz-az*by)*(ay*bz-az*by)
                          +
                          (az*bx-ax*bz)*(az*bx-ax*bz)
                          +
                          (ax*by-ay*bx)*(ax*by-ay*bx))
                                / Deno );

// for simulation only!!  (gaussian distribution of a LOR with 0.5 mm FWHM)
        ContentLine = (1/( 0.02128*sqrt(2*c_Pi)) )*exp(-0.5*(Distance/ 0.02128)*(Distance/ 0.02128)); // LOR 0.5mm
              FWHM

        // Intersection of Compton Cone and LOR
        if (ContentLine > 0.0 && Content > 0.0) {
        //if (ContentLine > 0.0 ) {
          ContentLine = ContentLine * Content; // spatial conicidence
          // search the highest pixel...
          if (ContentLine > Maximum) {Maximum = ContentLine;}
          InnerSum += ContentLine;
          Image[NUsedBins] = ContentLine;
          Bins[NUsedBins] = i;
          ++NUsedBins;
        } else {
          // Due to acos-rounding error protection, we might get a few here.
          //cout<<"Event "<<m_Event->GetId()<<": I seem to still calculate image bins with no content: x="
          // <<m_xBinCenter[x]<<" y="<<m_yBinCenter[y]<<" z="<<m_yBinCenter[z]<<endl;
        }
      } // end x
    } // end y
  } // end z

  // <--------- time critical <---------

  // If one of the above computed numbers has been NaN
  // InnerSum is also NaN. Then we have to reject this event.
  if (InRange(InnerSum) == false) {
    cout<<"Event␣"<<m_Event->GetId()<<":␣Catched␣a␣NaN!"<<endl;
    cout<<m_C->ToString()<<endl;

    NUsedBins = 0;
    Maximum = 0;
    return false;
  }

  // If the image does not contain any content, return also false
  // This case should not really happen due to protections before, thus the error message
  if (InnerSum == 0 && NUsedBins != 0) {
    cout<<"Event␣"<<m_Event->GetId()<<":␣The␣image␣seems␣to␣be␣empty..."<<endl;
    NUsedBins = 0;
    Maximum = 0;
    return false;
  }


  return true;
}
```

```
//---------------------------------------------------------
// to be pasted in  MImagerExternallyManaged.cxx
//---------------------------------------------------------

MBPData* MImagerExternallyManaged::CalculateResponseSliceLine(MPhysicalEvent* Event, double X1Position, double
     Y1Position, double Z1Position, double X2Position, double Y2Position, double Z2Position)
{

  MBPData* Data = 0;

  // IsQualified is NOT reentrant --- but the only thing modified are its counters, which we do not use here...
  if (m_Selector.IsQualifiedEvent(Event) == true) {
    // Reinitialize the array keeping the events backprojection
    // Memcopy is only faster if the parallism of modern CPUs cannot be used. With gcc -O3 this is fastest:
    //for (int i = 0; i < m_NBins; ++i) BackprojectionImage[i] = 0.0;

    bool EnoughMemory = true;

    double* BackprojectionImage = new double[m_NBins];
    int* BackprojectionBins = new int[m_NBins];

    // Try to backproject the data and store the computed t_ij in BackprojectionImage
    int NUsedBins = 0;
    double Maximum = 0;

    if (m_BPs[0]->Backproject(Event, BackprojectionImage, BackprojectionBins, NUsedBins, Maximum, X1Position,
         Y1Position, Z1Position, X2Position, Y2Position, Z2Position) == true && NUsedBins > 0) {

      // It might happen that we go out of memory during imaging, catch it!
      // 1-byte-storage:
      if (m_ComputationAccuracy == 0) {
        // Test if we can store it as sparse matrix:
        if (NUsedBins < 0.33*m_NBins) {
          Data = new(nothrow) MBPDataSparseImageOneByte();
          if (Data != 0) {
            EnoughMemory = Data->Initialize(BackprojectionImage, BackprojectionBins, m_NBins, NUsedBins, Maximum);
          } else {
            EnoughMemory = false;
          }
        } else { // no sparse matrix
          Data = new(nothrow) MBPDataImageOneByte();
          if (Data != 0) {
            EnoughMemory = Data->Initialize(BackprojectionImage, BackprojectionBins, m_NBins, NUsedBins, Maximum);
          } else {
            EnoughMemory = false;
          }
        }
      }
      // 4-byte storage:
      else if (m_ComputationAccuracy == 1) {
        if (NUsedBins < 0.5*m_NBins) {
          Data = new(nothrow) MBPDataSparseImage();
          if (Data != 0) {
            EnoughMemory = Data->Initialize(BackprojectionImage, BackprojectionBins, m_NBins, NUsedBins, Maximum);
          } else {
            EnoughMemory = false;
          }
        }
        else { // no sparse matrix
          Data = new(nothrow) MBPDataImage();
          if (Data != 0) {
            EnoughMemory = Data->Initialize(BackprojectionImage, BackprojectionBins, m_NBins, NUsedBins, Maximum);
          } else {
            EnoughMemory = false;
          }
        }
      } else {
        merr<<"m_ComputationAccuracy must be 0 (1 byte storage) or 1 (4 byte storage): "<<m_ComputationAccuracy<<fatal
            ;
      }
    }

    delete [] BackprojectionImage;
    delete [] BackprojectionBins;

    if (EnoughMemory == false) {
      cout<<"Out of memory..."<<endl;
    }


//---------------------------------------------------------
// to be pasted in  MBackprojectionSphere.cxx
//---------------------------------------------------------

bool MBackprojectionSphere::Backproject(MPhysicalEvent* Event, double* Image, int* Bins, int& NUsedBins, double&
     Maximum, double X1Position, double Y1Position, double Z1Position, double X2Position, double Y2Position, double
     Z2Position)
{
  // Take over all the necessary event data and perform some elementary computations:
  // the compton angle, the cone axis, the most probable origin of the gamma ray
  // if possible, the center of the cone.
```

```
  if (Assimilate(Event) == false) return false;

  if (Event->GetType() == MPhysicalEvent::c_Compton) {
    return BackprojectionCompton(Image, Bins, NUsedBins, Maximum);
  } else if (Event->GetType() == MPhysicalEvent::c_Pair) {
    return BackprojectionPair(Image, Bins, NUsedBins, Maximum);
  } else if (Event->GetType() == MPhysicalEvent::c_Photo) {
    return BackprojectionPhoto(Image, Bins, NUsedBins, Maximum);
  } else {
    cout<<"Error: Unknown event type for imaging: "<<Event->GetType()<<". Skipping event."<<endl;
  }

  return false;
}
```

Appendix F

Analysis code for γ-PET

The following C++ analysis code reconstructs a photon source distribution via the γ-PET technique, from the intersection between the Compton cone of the third, prompt photon and the LOR from the positron annihilation.

```
/*
 * CHLGPETAnalysis.cxx
 *
 *              2011 by Christian Lang
 *
 *      based on ExternalAnalysisPipelineExample.cxx
 *    Copyright (C) 1998-2010 by Andreas Zoglauer.
 *
 * All rights reserved.
 *
 *
 * This code implementation is the intellectual property of
 * Andreas Zoglauer and Christian Lang.
 *
 * By copying, distributing or modifying the Program (or any work
 * based on the Program) you indicate your acceptance of this statement,
 * and all its terms.
 *
 */

// Standard
#include <iostream>
#include <string>
#include <sstream>
#include <vector>
#include <csignal>
#include <math.h>
#include <stdlib.h>

using namespace std;

// ROOT
#include <TROOT.h>
#include <TEnv.h>
#include <TSystem.h>
#include <TApplication.h>
#include <TStyle.h>
#include <TCanvas.h>
#include <TH1.h>
#include <TH2.h>
#include <TLine.h>

// MEGAlib
#include "MGlobal.h"
#include "MStreams.h"
#include "MDGeometryQuest.h"
#include "MDDetector.h"
#include "MFileEventsSim.h"
#include "MDVolumeSequence.h"
#include "MSimEvent.h"
#include "MSimHT.h"
#include "MGeometryRevan.h"
#include "MRERawEvent.h"
#include "MREHit.h"
#include "MRawEventAnalyzer.h"
#include "MERCSRChiSquare.h"
#include "MImagerExternallyManaged.h"
#include "MBPData.h"
#include "MImage.h"
#include "MVector.h"
```

```
 float  genergycutmin = 1200.0,
          genergycutmax = 1350.0;

/*****************************************************************************/

class ExternalAnalysisPipelineExample
{
public:
  /// Default constructor
  ExternalAnalysisPipelineExample();
  /// Default destructor
  ~ExternalAnalysisPipelineExample();

  /// Parse the command line
  bool ParseCommandLine(int argc, char** argv);
  /// Initialze the run
  bool Initialize();
  /// Analyze what eveer needs to be analyzed...
  bool Analyze();
  /// Interrupt the analysis
  void Interrupt() { m_Interrupt = true; }

private:
  ///
  MRERawEvent* Convert(MSimEvent*);

private:
  /// True, if the analysis needs to be interrupted
  bool m_Interrupt;
  /// The geometry file name
  MString m_GeometryFileName;
  /// The simulation file name
  MString m_SimulationFileName;

  /// A standard geometry
  MDGeometryQuest* m_Geometry;
  /// A special geometry for revan
  MGeometryRevan* m_RevanGeometry;

  /// The event reconstructor
  MRawEventAnalyzer* m_RawEventAnalyzer;
  MRawEventAnalyzer* m_RawEventAnalyzerOben;
  MRawEventAnalyzer* m_RawEventAnalyzerUnten;
  MRawEventAnalyzer* m_RawEventAnalyzerLinks;
  MRawEventAnalyzer* m_RawEventAnalyzerRechts;

  /// The image reconstructor
  MImagerExternallyManaged* m_Imager;

  MEventSelector S;


  TH1D* m_HistEnergyEmi;
  TH1D* m_HistEnergyObenDSSSD;
  TH1D* m_HistEnergySumCC;
  TH1D* m_HistEnergyObenCC;
  TH1D* m_HistEnergyISDSSSDOben;
  TH1D* m_HistEnergyISDSSSDRechts;
  TH1D* m_HistEnergyBeforeLinks;
  TH2D* m_HistAnglevsEnergy;

  TH2D* m_HistHits;
  TH1D* m_HistTime;
  TH1D* m_HistDiametral;
  TH2D* m_HistLines;

};

/*****************************************************************************/


/*****************************************************************************
 * Default constructor
 */
ExternalAnalysisPipelineExample::ExternalAnalysisPipelineExample() : m_Interrupt(false)
{
  gStyle->SetPalette(1, 0);
}


/*****************************************************************************
 * Default destructor
 */
ExternalAnalysisPipelineExample::~ExternalAnalysisPipelineExample()
{
  // Intentionally left blanck
}


/*****************************************************************************
 * Parse the command line
```

```
 */
bool ExternalAnalysisPipelineExample::ParseCommandLine(int argc, char** argv)
{
  ostringstream Usage;
  Usage<<endl;
  Usage<<"  Usage: ExternalAnalysisPipelineExample <options>"<<endl;
  Usage<<"    General options:"<<endl;
  Usage<<"          -g:   geometry file name"<<endl;
  Usage<<"          -s:   simulation file name"<<endl;
  Usage<<"          -h:   print this help"<<endl;
  Usage<<endl;

  string Option;

  // Check for help
  for (int i = 1; i < argc; i++) {
    Option = argv[i];
    if (Option == "-h" || Option == "--help" || Option == "?" || Option == "-?") {
      cout<<Usage.str()<<endl;
      return false;
    }
  }

  // Now parse the command line options:
  for (int i = 1; i < argc; i++) {
                Option = argv[i];

                // First check if each option has sufficient arguments:
                // Single argument
    if (Option == "-s" || Option == "-g") {
                        if (!((argc > i+1) &&
            (argv[i+1][0] != '-' || isalpha(argv[i+1][1]) == 0))){
                                cout<<"Error: Option "<<argv[i][1]<<" needs a second argument!"<<endl;
                                cout<<Usage.str()<<endl;
                                return false;
                        }
                }
                // Multiple arguments template
    /*
                else if (Option == "-??") {
                        if (!((argc > i+2) &&
            (argv[i+1][0] != '-' || isalpha(argv[i+1][1]) == 0) &&
            (argv[i+2][0] != '-' || isalpha(argv[i+2][1]) == 0))){
                                cout<<"Error: Option "<<argv[i][1]<<" needs two arguments!"<<endl;
                                cout<<Usage.str()<<endl;
                                return false;
                        }
                }
    */

                // Then fulfill the options:
    if (Option == "-s") {
      m_SimulationFileName = argv[++i];
      cout<<"Accepting simulation file name: "<<m_SimulationFileName<<endl;
    } else if (Option == "-g") {
      m_GeometryFileName = argv[++i];
      cout<<"Accepting geometry file name: "<<m_GeometryFileName<<endl;
                } else {
                        cout<<"Error: Unknown option \""<<Option<<"\"!"<<endl;
                        cout<<Usage.str()<<endl;
                        return false;
                }
  }

  return true;
}


/*****************************************************************************
 * Do whatever analysis is necessary
*
*                       I N I T I A L I Z E
*
 */
bool ExternalAnalysisPipelineExample::Initialize()
{
  // Load geometry:
  m_Geometry = new MDGeometryQuest();

  if (m_Geometry->ScanSetupFile(m_GeometryFileName) == true) {
    cout<<"Geometry "<<m_Geometry->GetName()<<" loaded!"<<endl;
    m_Geometry->ActivateNoising(true);
    m_Geometry->SetGlobalFailureRate(0.0);
  } else {
    cout<<"Loading of geometry "<<m_Geometry->GetName()<<" failed!!"<<endl;
    return false;
  }

  // Load geometry:
  m_RevanGeometry = new MGeometryRevan();

  if (m_RevanGeometry->ScanSetupFile(m_GeometryFileName) == true) {
```

```
  cout<<"Geometry␣"<<m_RevanGeometry->GetName()<<"␣loaded!"<<endl;
  m_RevanGeometry->ActivateNoising(true);
  m_RevanGeometry->SetGlobalFailureRate(0.0);
} else {
  cout<<"Loading␣of␣geometry␣"<<m_RevanGeometry->GetName()<<"␣failed!!"<<endl;
  return false;
}

// Initialize the raw event analyzer:

m_RawEventAnalyzer = new MRawEventAnalyzer();
m_RawEventAnalyzer->SetGeometry(m_RevanGeometry);
//m_RawEventAnalyzer->SetCoincidenceAlgorithm(MRawEventAnalyzer::c_CoincidenceAlgoWindow);
//m_RawEventAnalyzer->SetCoincidenceWindow(1E-9);
m_RawEventAnalyzer->SetClusteringAlgorithm(MRawEventAnalyzer::c_ClusteringAlgoDistance);
m_RawEventAnalyzer->SetStandardClusterizerMinDistanceD1(0.039);
m_RawEventAnalyzer->SetStandardClusterizerMinDistanceD2(0.625);
m_RawEventAnalyzer->SetStandardClusterizerMinDistanceD3(0.625);
m_RawEventAnalyzer->SetStandardClusterizerMinDistanceD4(0.625);
m_RawEventAnalyzer->SetStandardClusterizerMinDistanceD5(0.625);
m_RawEventAnalyzer->SetStandardClusterizerMinDistanceD6(0.625);
m_RawEventAnalyzer->SetStandardClusterizerCenterIsReference(true);

m_RawEventAnalyzer->SetTrackingAlgorithm(MRawEventAnalyzer::c_TrackingAlgoRank);
m_RawEventAnalyzer->SetDoTracking(false);
m_RawEventAnalyzer->SetRejectPurelyAmbiguousTrackSequences(true);
m_RawEventAnalyzer->SetMaxComptonJump(1);
m_RawEventAnalyzer->SetNTrackSequencesToKeep(1);
m_RawEventAnalyzer->SetSearchComptonTracks(true);
m_RawEventAnalyzer->SetSearchPairTracks(false);

//Chi-Square via angles
//m_RawEventAnalyzer->SetCSRAlgorithm(MRawEventAnalyzer::c_CSRAlgoFoM);
//Chi-Square via energies
m_RawEventAnalyzer->SetCSRAlgorithm(MRawEventAnalyzer::c_CSRAlgoFoME);
//m_RawEventAnalyzer->SetCSRAlgorithm(MRawEventAnalyzer::c_CSRAlgoFoMToF);
//Chi-Square via angles + time
//m_RawEventAnalyzer->SetCSRAlgorithm(MRawEventAnalyzer::c_CSRAlgoFoMToFAndE);
//Chi-Square via Bayesian
//m_RawEventAnalyzer->SetCSRAlgorithm(MRawEventAnalyzer::c_CSRAlgoBayesian);

//m_RawEventAnalyzer->SetClassicUndecidedHandling(MERCSRChiSquare::c_UndecidedLargerEnergyDeposit);
//m_RawEventAnalyzer->SetClassicUndecidedHandling(MERCSRChiSquare::c_UndecidedAssumestartD1);
//m_RawEventAnalyzer->SetClassicUndecidedHandling(MERCSRChiSquare::c_UndecidedLargerKleinNishina);
m_RawEventAnalyzer->SetClassicUndecidedHandling(MERCSRChiSquare::c_UndecidedIgnore);
m_RawEventAnalyzer->SetAssumeD1First(true);
m_RawEventAnalyzer->SetGuaranteeStartD1(true);
m_RawEventAnalyzer->SetUseComptelTypeEvents(true);
m_RawEventAnalyzer->SetRejectOneDetectorTypeOnlyEvents(true);
m_RawEventAnalyzer->SetCSRMaxNHits(6);

m_RawEventAnalyzer->SetDecayAlgorithm(MRawEventAnalyzer::c_DecayAlgoNone);
m_RawEventAnalyzer->SetRejectAllBadEvents(true);
//m_RawEventAnalyzer->SetCSRThresholdMin(0.5);
//m_RawEventAnalyzer->SetCSRThresholdMax(0.9);
m_RawEventAnalyzer->SetTotalEnergyMin(genergycutmin);
m_RawEventAnalyzer->SetTotalEnergyMax(genergycutmax);
if (m_RawEventAnalyzer->PreAnalysis() == false) return false;

// Some histograms....
m_HistEnergyEmi = new TH1D("HistEmi", "HistEmi", 500, 0, 2500);
m_HistEnergyObenDSSSD = new TH1D("HistObenDSSSD", "HistObenDSSSD", 500, 0, 2500);
m_HistEnergySumCC = new TH1D("HistSumCC", "HistSumCC", 500, 0, 2500);
m_HistEnergyObenCC = new TH1D("HistObenCC", "HistObenCC", 500, 0, 2500);
m_HistEnergyISDSSSDRechts = new TH1D("HistISDSSSDRechts", "HistISDSSSDRechts", 500, 0, 2500);
m_HistEnergyISDSSSDOben = new TH1D("HistISDSSSDOben", "HistISDSSSDOben", 500, 0, 2500);
m_HistEnergyBeforeLinks = new TH1D("HistBeforeLinks", "HistBeforeLinks", 200, 0, 2000);


m_Imager = new MImagerExternallyManaged(MProjection::c_Cartesian3D);
m_Imager->SetGeometry(m_Geometry);

m_Imager->SetViewport(
                      -0.51,
                       0.51,
                      100,
                       -0.51,
                       0.51,
                      100,
                       -0.51,
                       0.51,
                      100);


  // Set the draw modes
 m_Imager->SetPalette(0);
  // Palette: 0: Rainbow, 1: BW, 2: WB, 3: Blue, 4: Red/Blue, 5: Rainbow2, 6: Red, 7: Red/White, 8: Red2, 9:Red3,
       10:rainbow3

  //m_Imager->SetPalette(m_Data->GetImagePalette());
  //m_Imager->SetSourceCatalog(m_Data->GetImageSourceCatalog());
```

```
    //if (Animate == true) {
    //  m_Imager->SetAnimationMode(m_Data->GetAnimationMode());
    m_Imager->SetAnimationFrameTime(5);
    m_Imager->SetAnimationFileName("test.gif");
    //} else {
    m_Imager->SetAnimationMode(MImager::c_AnimateBackprojections);
    // }


  // Maths:
  m_Imager->SetApproximatedMaths(false);
  // Set the response type
  m_Imager->SetResponseGaussian(10, 30, 3, 2.5, false);
  m_Imager->SetMemoryManagment(60000, 60000, 2, 1);

  // A new event selector:
  //MEventSelector S;
  S.SetGeometry(m_Geometry);
  S.SetComptonAngle(0,180);
  S.UseComptons(true);
  S.UseTrackedComptons(false);
  S.UseNotTrackedComptons(true);
  S.UsePairs(false);
  S.UsePhotos(false);

  m_Imager->SetEventSelector(S);
  m_Imager->SetDeconvolutionAlgorithmClassicEM();
  //m_Imager->SetStopCriterionByIterations(90);
  m_Imager->SetStopCriterionByIterations(3);
  m_Imager->Initialize();

  return true;
}

/******************************************************************************
 * Do whatever analysis is necessary
 */
MRERawEvent* ExternalAnalysisPipelineExample::Convert(MSimEvent* SE)
{
  MRERawEvent* RE = new MRERawEvent();

  RE->SetEventTime(SE->GetTime());
  RE->SetEventId(SE->GetID());


  // Create raw event hit out of each SimHT and add it to the raw event (RE)
  for (unsigned int h = 0; h < SE->GetNHTs(); ++h) {
    MREHit* REHit = new MREHit();
    REHit->SetDetector(SE->GetHTAt(h)->GetDetectorType());
    REHit->SetPosition(SE->GetHTAt(h)->GetPosition());

    cout << "␣␣␣SE->GetHTAt(h)->GetNHTs():␣" <<  SE->GetNHTs() << endl;
    cout << "␣␣␣SE->GetHTAt(h)->GetPosition():␣" <<  SE->GetHTAt(h)->GetPosition() << endl;
    cout << "␣␣␣SE->GetHTAt(h)->GetPositionX():␣" << REHit->GetPositionX() << endl;
    cout << "␣␣␣SE->GetHTAt(h)->GetPositionY():␣" << REHit->GetPositionY() << endl;
    cout << "␣␣␣SE->GetHTAt(h)->GetPositionZ():␣" << REHit->GetPositionZ() << endl;
    cout << "␣␣␣SE->GetHTAt(h)->GetTime():␣" <<  SE->GetTime() << endl;
    cout << "␣␣␣SE->GetHTAt(h)->GetDetectorType():␣" <<  SE->GetHTAt(h)->GetDetectorType() << endl;

    REHit->SetEnergy(SE->GetHTAt(h)->GetEnergy());
    REHit->SetTime(SE->GetHTAt(h)->GetTime() + SE->GetTime());
    REHit->RetrieveResolutions(m_Geometry);
    REHit->Noise(m_Geometry);  // <- for sims only!!
    RE->AddRESE(REHit);
  }

  return RE;
}


/******************************************************************************
////////////////////////////////////////////////////////////////////////////////////////////////////////////////////
//
//                      A N A L Y Z E
////////////////////////////////////////////////////////////////////////////////////////////////////////////////////
 *////////////////////////////////////////////////////////////////////////////////////////////////////////////////

bool ExternalAnalysisPipelineExample::Analyze()
{
  if (m_Interrupt == true) return false;

  // Initialize:
  if (Initialize() == false) return false;

  MFileEventsSim* SimReader = new MFileEventsSim(m_Geometry);
  if (SimReader->Open(m_SimulationFileName) == false) {
    cout<<"Unable␣to␣open␣sim␣file!"<<endl;
    return false;
  }
  cout << "Opened␣file␣" << SimReader->GetFileName() << "␣created␣with␣MEGAlib␣version:␣" << SimReader->
       GetMEGAlibVersion()<<  endl;
  SimReader->ShowProgress();
```

```
  TCanvas* CanvasBackprojection = new TCanvas();
  TCanvas* CanvasIterated= new TCanvas();

  vector<MPhysicalEvent*> Events;
  vector<MBPData*> ResponseSlices;
  vector<MImage*> Images;


  int whileloopcounter = 0, RechtsLinksCounter = 0,  ObenUntenCounter = 0, FlagRechts = 0, FlagLinks = 0, FlagOben =
       0, FlagUnten = 0, RechtsCounter = 0, UntenCounter = 0, LinksCounter = 0, LinksCounterCalori = 0, ObenCounter =
        0, SimCounter = 0;

  int  LOR =0,
       Flag1275Rechts = 0, Flag1275Links = 0, Flag1275Oben = 0, Flag1275Unten = 0;

  double Time = 0.0, TimeTmp = 0.0, AnglePhi = 0.0,
              XPositionRechts = 0.0, YPositionRechts = 0.0, ZPositionRechts = 0.0,
              XPositionLinks = 0.0, YPositionLinks = 0.0, ZPositionLinks = 0.0,
              XPositionOben = 0.0, YPositionOben = 0.0, ZPositionOben = 0.0,
              XPositionUnten = 0.0, YPositionUnten = 0.0, ZPositionUnten = 0.0,
              XPositionRechts2 = 0.0, YPositionRechts2 = 0.0, ZPositionRechts2 = 0.0,
              XPositionLinks2 = 0.0, YPositionLinks2 = 0.0, ZPositionLinks2 = 0.0,
              XPositionOben2 = 0.0, YPositionOben2 = 0.0, ZPositionOben2 = 0.0,
              XPositionUnten2 = 0.0, YPositionUnten2 = 0.0, ZPositionUnten2 = 0.0,
              HitEnergyRechts = 0.0, HitEnergyRechts2 = 0.0,
              VMulti = 0.0, VNormL = 0.0, VNormR= 0.0 , Diametral = 0.0;

  double ScatterMin = 3.1,
              ScatterMax = 4.0,
              AbsorberMin = 6.0,
              AbsorberMax = 12.0;

 /*
  double ScatterMin = 4.5,
              ScatterMax = 8.0,
              AbsorberMin = 10.0,
              AbsorberMax = 16.0;

*/

  unsigned int ReturnCode;
  unsigned int ReturnCodeOben;
  unsigned int ReturnCodeUnten;
  unsigned int ReturnCodeRechts;
  unsigned int ReturnCodeLinks;


  MSimEvent* SimEvent = 0;

  MRERawEvent* RawEvent = 0;
  MRERawEvent* BestRawEvent = 0;

  MRawEventList* AllRawEvents = 0;


//*************************************************************************************************
// Loop over the events
//
//*************************************************************************************************


////////////////////////////////////////////////////////////////////////////////////////////////////
//                          While Loop
////////////////////////////////////////////////////////////////////////////////////////////////////

  while ((SimEvent = SimReader->GetNextEvent(false)) != 0) {

    FlagRechts = 0, FlagLinks = 0, FlagOben = 0, FlagUnten = 0,
    Flag1275Rechts = 0, Flag1275Links = 0, Flag1275Oben = 0, Flag1275Unten = 0,

    XPositionRechts = 0.0, YPositionRechts = 0.0, ZPositionRechts = 0.0,
    XPositionLinks = 0.0, YPositionLinks = 0.0, ZPositionLinks = 0.0,
    XPositionOben = 0.0, YPositionOben = 0.0, ZPositionOben = 0.0,
    XPositionUnten = 0.0, YPositionUnten = 0.0, ZPositionUnten = 0.0,
    XPositionRechts2 = 0.0, YPositionRechts2 = 0.0, ZPositionRechts2 = 0.0,
    XPositionLinks2 = 0.0, YPositionLinks2 = 0.0, ZPositionLinks2 = 0.0,
    XPositionOben2 = 0.0, YPositionOben2 = 0.0, ZPositionOben2 = 0.0,
    XPositionUnten2 = 0.0, YPositionUnten2 = 0.0, ZPositionUnten2 = 0.0,
    HitEnergyRechts = 0.0, HitEnergyRechts2 = 0.0,
    AnglePhi = 0.0,  VMulti = 0.0, VNormL = 0.0, VNormR= 0.0 , Diametral = 0.0;

    if (SimEvent->GetID() == 1) {
       Time = Time + TimeTmp;
    }
    TimeTmp = SimEvent->GetTime();
    whileloopcounter = whileloopcounter + 1;

    // Convert to MRERawEvent
   // RawEvent = Convert(SimEvent);
```

```
//
     ////////////////////////////////////////////////////////////////////////////////////////////////////////////////////

//*************************************************************************************
//
//                    Event Sorter
//
//                    Assign events from cubic Compton camera setup (4 modules)
//                    to their respective camera module
//
//                    by Christian Lang 2011
//
//*************************************************************************************
//
     ////////////////////////////////////////////////////////////////////////////////////////////////////////////////////


  MBPData* Data = 0;

  MRERawEvent* RE = new MRERawEvent();
  MRERawEvent* RELinks = new MRERawEvent();
  MRERawEvent* RERechts = new MRERawEvent();
  MRERawEvent* REOben = new MRERawEvent();
  MRERawEvent* REUnten = new MRERawEvent();

  RE->SetEventTime(SimEvent->GetTime());
  RE->SetEventId(SimEvent->GetID());
  REOben->SetEventTime(SimEvent->GetTime());
  REOben->SetEventId(SimEvent->GetID());
  REUnten->SetEventTime(SimEvent->GetTime());
  REUnten->SetEventId(SimEvent->GetID());
  RELinks->SetEventTime(SimEvent->GetTime());
  RELinks->SetEventId(SimEvent->GetID());
  RERechts->SetEventTime(SimEvent->GetTime());
  RERechts->SetEventId(SimEvent->GetID());

  //m_HistTime->Fill(SimEvent->GetTime());


////////////////////////
// Create raw event hit out of each SimHT and add it to the raw event (RE)
////////////////////////
  for (unsigned int h = 0; h < SimEvent->GetNHTs(); ++h) {

    MREHit* REHit = new MREHit();
    REHit->SetDetector(SimEvent->GetHTAt(h)->GetDetectorType());
    REHit->SetPosition(SimEvent->GetHTAt(h)->GetPosition());
    REHit->SetEnergy(SimEvent->GetHTAt(h)->GetEnergy());
    REHit->SetTime(SimEvent->GetHTAt(h)->GetTime() + SimEvent->GetTime());
    REHit->RetrieveResolutions(m_Geometry);
    REHit->Noise(m_Geometry);  // <- for sims only

    m_HistEnergyEmi->Fill(REHit->GetEnergy());

//////////  flag selection of hits due to Compton camera arrangement and threshold

   // if (REHit->GetEnergy < 10) continue;
   if (REHit->GetPositionZ() > ScatterMin && REHit->GetPositionZ() < ScatterMax && FlagRechts == 1 && REHit->GetEnergy
       () > 0.0) {
     //cout << " Treffer RECHTS " << endl;
     FlagRechts = 2;
     XPositionRechts2 = REHit->GetPositionX();
     YPositionRechts2 = REHit->GetPositionY();
     ZPositionRechts2 = REHit->GetPositionZ();
     HitEnergyRechts2 = SimEvent->GetHTAt(h)->GetEnergy();
   }
   if (REHit->GetPositionZ() > ScatterMin && REHit->GetPositionZ() < ScatterMax && FlagRechts == 0 && REHit->
       GetEnergy() > 0.0) {
     //cout << " Treffer RECHTS " << endl;
     FlagRechts = 1;
     XPositionRechts = REHit->GetPositionX();
     YPositionRechts = REHit->GetPositionY();
     ZPositionRechts = REHit->GetPositionZ();
     HitEnergyRechts = SimEvent->GetHTAt(h)->GetEnergy();
   }
   if (REHit->GetPositionZ() < (ScatterMin * -1) && REHit->GetPositionZ() > (ScatterMax * -1) && FlagLinks == 1 &&
       REHit->GetEnergy() > 0.0) {
     //cout << " Treffer LINKS " << endl;
     FlagLinks = 2;
     XPositionLinks2 = REHit->GetPositionX();
     YPositionLinks2 = REHit->GetPositionY();
     ZPositionLinks2 = REHit->GetPositionZ();
   }
   if (REHit->GetPositionZ() < (ScatterMin * -1)  && REHit->GetPositionZ() > (ScatterMax  * -1) && FlagLinks == 0 &&
       REHit->GetEnergy() > 0.0) {
    // cout << " Treffer LINKS " << endl;
     FlagLinks = 1;
     XPositionLinks = REHit->GetPositionX();
     YPositionLinks = REHit->GetPositionY();
     ZPositionLinks = REHit->GetPositionZ();
   }
```

```
   if (REHit->GetPositionX() > ScatterMin && REHit->GetPositionX() < ScatterMax && FlagOben == 1 && REHit->GetEnergy()
        > 0.0) {
      //cout << " Treffer OBEN " << endl;
      FlagOben = 2;
      XPositionOben2 = REHit->GetPositionX();
      YPositionOben2 = REHit->GetPositionY();
      ZPositionOben2 = REHit->GetPositionZ();
    }
    if (REHit->GetPositionX() > ScatterMin && REHit->GetPositionX() < ScatterMax && FlagOben == 0 && REHit->GetEnergy
        () > 0.0) {
      //cout << " Treffer OBEN " << endl;
      FlagOben = 1;
      XPositionOben = REHit->GetPositionX();
      YPositionOben = REHit->GetPositionY();
      ZPositionOben = REHit->GetPositionZ();
    }
    if (REHit->GetPositionX() < (ScatterMin * -1) && REHit->GetPositionX() > (ScatterMax * -1) && FlagUnten == 1 &&
        REHit->GetEnergy() > 0.0) {
      //cout << " Treffer UNTEN " << endl;
      FlagUnten = 2;
      XPositionUnten2 = REHit->GetPositionX();
      YPositionUnten2 = REHit->GetPositionY();
      ZPositionUnten2 = REHit->GetPositionZ();
    }
    if (REHit->GetPositionX() < (ScatterMin * -1) && REHit->GetPositionX() > (ScatterMax * -1) && FlagUnten == 0 &&
        REHit->GetEnergy() > 0.0) {
      //cout << " Treffer UNTEN " << endl;
      FlagUnten = 1;
      XPositionUnten = REHit->GetPositionX();
      YPositionUnten = REHit->GetPositionY();
      ZPositionUnten = REHit->GetPositionZ();
    }

//////////  geometrical selection of hits due to Compton camera arrangement and threshold

    if (REHit->GetPositionZ() < (ScatterMin * -1) && REHit->GetEnergy() > 0.0) {
       RELinks->AddRESE(REHit);
       LinksCounter = LinksCounter + 1;
    }
    if (REHit->GetPositionZ() > ScatterMin && REHit->GetEnergy() > 0.0) {
       RERechts->AddRESE(REHit);
       RechtsCounter = RechtsCounter + 1;
    }
    if (REHit->GetPositionX() < (ScatterMin * -1) && REHit->GetEnergy() > 0.0) {
       REUnten->AddRESE(REHit);
       UntenCounter = UntenCounter + 1;
    }
    if (REHit->GetPositionX() > ScatterMin && REHit->GetEnergy() > 0.0) {
       REOben->AddRESE(REHit);
       ObenCounter = ObenCounter + 1;
    }
    if (REHit->GetPositionZ() < -AbsorberMin) {
       LinksCounterCalori = LinksCounterCalori + 1;
    }

    if (REHit->GetPositionX() > ScatterMin && REHit->GetPositionX() < ScatterMax) {
       m_HistEnergyObenDSSSD->Fill(REHit->GetEnergy());
    }



   // cout << " SE->GetHTAt(h)->GetNHTs(): " <<  SimEvent->GetNHTs() << endl;
    //cout << " SE->GetHTAt(h)->GetPosition(): " <<  SimEvent->GetHTAt(h)->GetPosition() << endl;

    RE->AddRESE(REHit);
  }
//
     ////////////////////////////////////////////////////////////////////////////////////////////////////////////////////////////////////////////////

//*(b)*********************************************************************
// E N D E      Event Selector
//*(e)*********************************************************************
//
     ////////////////////////////////////////////////////////////////////////////////////////////////////////////////////////////////////////////////


    RawEvent = 0;
    //RawEvent = RE;

// Histogram of all 4 Compton camera modules
    m_HistEnergySumCC->Fill(REOben->GetEnergy() + REUnten->GetEnergy() + RERechts->GetEnergy() + RELinks->GetEnergy())
        ;

// Histogram of one Compton camera modules (Oben)
    if (REOben->GetEnergy() > 0.0) m_HistEnergyObenCC->Fill(REOben->GetEnergy());

    Flag1275Rechts = 0;
    Flag1275Links = 0;
    Flag1275Oben = 0;
    Flag1275Unten = 0;

 // 511 keV Rechts AND Links
```

```
    if (RELinks->GetEnergy() > 480.0 && RELinks->GetEnergy() < 540.0 && RERechts->GetEnergy() > 480.0 && RERechts->
        GetEnergy() < 540.0)
      LOR = LOR + 1;
    if (REUnten->GetEnergy() > 480.0 && REUnten->GetEnergy() < 540.0 && REOben->GetEnergy() > 480.0 && REOben->
        GetEnergy() < 540.0)
      LOR = LOR + 1;


    if (RELinks != 0 && LinksCounter > 1 && FlagOben  > 0 && FlagUnten > 0 && RELinks->GetEnergy() > genergycutmin &&
        RELinks->GetEnergy() < genergycutmax) {
      RawEvent = RELinks;
      Flag1275Links = 1;
      //cout << "                                                    Treffer OBEN<->UNTEN " << endl;
    }
    if (REUnten != 0 && UntenCounter > 1 && FlagRechts  > 0 && FlagLinks > 0 && REUnten->GetEnergy() > genergycutmin
        && REUnten->GetEnergy() <  genergycutmax) {
      RawEvent = REUnten;
      Flag1275Unten = 1;
      //cout << "                                                    Treffer RECHTS<->LINKS " << endl;
    }
    if (RERechts != 0 && RechtsCounter > 1 && FlagOben  > 0 && FlagUnten > 0 && RERechts->GetEnergy() > genergycutmin
        && RERechts->GetEnergy() <  genergycutmax) {
      RawEvent = RERechts;
      Flag1275Rechts = 1;
      //cout << "                                                    Treffer OBEN<->UNTEN " << endl;
    }
    if (REOben != 0 && ObenCounter > 1  && FlagRechts  > 0 && FlagLinks > 0 && REOben->GetEnergy() > genergycutmin &&
        REOben->GetEnergy() <  genergycutmax) {
      RawEvent = REOben;
      Flag1275Oben = 1;
      //cout << "                                                    Treffer RECHTS<->LINKS " << endl;
    }

   delete SimEvent;


   if (RawEvent == 0) continue;
   //if (whileloopcounter > 1500) break;
   //if (RE->GetEnergy() < 2200.0) continue;

////////////////////////////////////////////////
// Reconstruct
////////////////////////////////////////////////
   m_RawEventAnalyzer->AddRawEvent(RawEvent);
   ReturnCode = m_RawEventAnalyzer->AnalyzeEvent();
   if (ReturnCode == MRawEventAnalyzer::c_AnalysisSucess) {
     BestRawEvent = 0;
     if (m_RawEventAnalyzer->GetOptimumEvent() != 0) {
       BestRawEvent = m_RawEventAnalyzer->GetOptimumEvent();
       //cout << " GetOptimumEvent:  "  << BestRawEvent << endl;
       //cout << " Event type: " << BestRawEvent->GetEventTypeAsString() <<endl;
       //cout << "ToString: " << BestRawEvent->ToString()<<endl;
     } else if (m_RawEventAnalyzer->GetBestTryEvent() != 0) {
       BestRawEvent = m_RawEventAnalyzer->GetBestTryEvent();
       //cout << " GetBestTryEvent:  "  << BestRawEvent << endl;
     }
     if (BestRawEvent != 0 ) {
       MPhysicalEvent* Phys = BestRawEvent->GetPhysicalEvent();
       //cout << "Physical event type: " << Phys->GetType() <<endl;
       /*
       cout << "GetPosition: " << Phys->GetPosition() <<endl;
       if (dynamic_cast<MComptonEvent*>(Phys) != 0) {
           MComptonEvent* C = dynamic_cast<MComptonEvent*>(Phys);
           cout << "           First Compton interactions point :" << C->C1() << endl;
       }
       */
       Events.push_back(Phys);
  ////////////////////////////////////
  // Image
  ////////////////////////////////////

       if (FlagRechts > 0 && FlagLinks > 0 && (Flag1275Oben == 1 || Flag1275Unten == 1 )) {
         Data = m_Imager->CalculateResponseSliceLine(Phys, XPositionRechts,YPositionRechts, ZPositionRechts,
              XPositionLinks,YPositionLinks, ZPositionLinks);
         RechtsLinksCounter = RechtsLinksCounter + 1;

         if (Data != 0 && RERechts->GetEnergy() > 480 && RERechts->GetEnergy() < 540 && RELinks->GetEnergy() > 480 &&
              RELinks->GetEnergy() < 540) m_HistEnergyISDSSSDRechts->Fill(RERechts->GetEnergy());

       }
       if (FlagOben > 0 && FlagUnten > 0  && (Flag1275Rechts == 1 || Flag1275Links == 1 ))  {
         Data = m_Imager->CalculateResponseSliceLine(Phys, XPositionOben,YPositionOben, ZPositionOben, XPositionUnten,
              YPositionUnten, ZPositionUnten);
         ObenUntenCounter = ObenUntenCounter + 1;

         if (Data != 0) m_HistEnergyISDSSSDOben->Fill(REOben->GetEnergy());
       }

       //MBPData* Data = m_Imager->CalculateResponseSlice(Phys);  // normal Compton camera cone calculation
       if (Data != 0) {
         ResponseSlices.push_back(Data);
         //cout<< " Data->BPDataType(): " << Data->BPDataType() << endl;
```

```
        if ((ResponseSlices.size() % 5) == 0 && ResponseSlices.size() > 1  && ResponseSlices.size() < 40000 ) {
        for (unsigned int i = 0; i < Images.size(); ++i) delete Images[i];
           m_Imager->ResetStopCriterion();
           cout<<"Content: "<<ResponseSlices.size()<<endl;
           Images = m_Imager->Deconvolve(ResponseSlices);
           Images.front()->Display(CanvasBackprojection);
           Images.back()->Display(CanvasIterated);
        }
      }
      if ((ResponseSlices.size() % 10) == 0 && ResponseSlices.size() > 0  && ResponseSlices.size() < 4000 ) {

        cout << "IS#_: " << ResponseSlices.size() << endl;
        cout << "Eff(LOR): (only true if T11): " << LOR / (Time * 120000 * 10) << endl;
        cout << "Eff(IS): " << ResponseSlices.size() / (Time * 120000 * 10) << endl;
      }

      } else {
         //cout << "No good event found..." << endl;
      }
    }

////////////////////////////////////////
//  E N D E    While Loop
////////////////////////////////////////
  //if (ResponseSlices.size() > 1000) break;

  }
  Time = Time + TimeTmp;
  SimReader->ShowProgress(true);

//////////////////////////
// Finalize:
//////////////////////////

  cout << "                                    Events.size(): " << Events.size() << endl;
  cout << "                                    IS#: " << ResponseSlices.size() << endl;
  cout << "                                    LOR# " << LOR << endl;
  cout << "                                    WhileLoop counter: " << whileloopcounter << endl;
  cout << "                                    Links counter: " << LinksCounter << endl;
  cout << "                                    Rechts counter: " << RechtsCounter << endl;
  cout << "                                    Oben counter: " << ObenCounter << endl;
  cout << "                                    Unten counter: " << UntenCounter << endl;
  cout << "                                    RechtsLinks counter: " << RechtsLinksCounter << endl;
  cout << "                                    ObenUnten counter: " << ObenUntenCounter << endl;
  cout << "                                    Observation time: " << Time << endl;
  cout << "                                    Eff(IS): " << ResponseSlices.size() / (Time * 120000 * 10) << endl;
  cout << "                                    Eff(LOR): (only true if T11): " << LOR / (Time * 120000 * 10) << endl;

  TCanvas* CanvasEnergyEmi = new TCanvas();
  CanvasEnergyEmi->cd();
  m_HistEnergyEmi->Draw();
  CanvasEnergyEmi->Update();

  TCanvas* CanvasEnergyObenDSSSD = new TCanvas();
  CanvasEnergyObenDSSSD->cd();
  m_HistEnergyObenDSSSD->Draw();
  CanvasEnergyObenDSSSD->Update();

  TCanvas* CanvasEnergySumCC = new TCanvas();
  CanvasEnergySumCC->cd();
  m_HistEnergySumCC->Draw();
  CanvasEnergySumCC->Update();

  TCanvas* CanvasEnergyObenCC = new TCanvas();
  CanvasEnergyObenCC->cd();
  m_HistEnergyObenCC->Draw();
  CanvasEnergyObenCC->Update();

  TCanvas* CanvasEnergyISDSSSDRechts = new TCanvas();
  CanvasEnergyISDSSSDRechts->cd();
  m_HistEnergyISDSSSDRechts->Draw();
  CanvasEnergyISDSSSDRechts->Update();

  TCanvas* CanvasEnergyISDSSSDOben = new TCanvas();
  CanvasEnergyISDSSSDOben->cd();
  m_HistEnergyISDSSSDOben->Draw();
  CanvasEnergyISDSSSDOben->Update();

  TCanvas* CanvasEnergyBeforeLinks = new TCanvas();
  CanvasEnergyBeforeLinks->cd();
  m_HistEnergyBeforeLinks->Draw();
  CanvasEnergyBeforeLinks->Update();


  for (unsigned int i = 0; i < Images.size(); ++i) delete Images[i];
   m_Imager->ResetStopCriterion();
   Images = m_Imager->Deconvolve(ResponseSlices);
   Images.front()->Display(CanvasBackprojection);
   Images.back()->Display(CanvasIterated);
```

```
  return true;
}


/*****************************************************************************/

ExternalAnalysisPipelineExample* g_Prg = 0;
int g_NInterruptCatches = 1;

/*****************************************************************************/


/*****************************************************************************
 * Called when an interrupt signal is flagged
 * All catched signals lead to a well defined exit of the program
 */
void CatchSignal(int a)
{
  if (g_Prg != 0 && g_NInterruptCatches-- > 0) {
    cout<<"Catched signal Ctrl-C (ID="<<a<<"):"<<endl;
    g_Prg->Interrupt();
  } else {
    abort();
  }
}


/*****************************************************************************
 * Main program
 */
int main(int argc, char** argv)
{
  //void (*handler)(int);
        //handler = CatchSignal;
  //(void) signal(SIGINT, CatchSignal);

  // Initialize global MEGALIB variables, especially mgui, etc.
  MGlobal::Initialize();

  TApplication ExternalAnalysisPipelineExampleApp("ExternalAnalysisPipelineExampleApp", 0, 0);

  g_Prg = new ExternalAnalysisPipelineExample();

  if (g_Prg->ParseCommandLine(argc, argv) == false) {
    cerr<<"Error during parsing of command line!"<<endl;
    return -1;
  }
  if (g_Prg->Analyze() == false) {
    cerr<<"Error during analysis!"<<endl;
    return -2;
  }


  ExternalAnalysisPipelineExampleApp.Run();

  cout<<"Program exited normally!"<<endl;

  return 0;
}
```

Bibliography

[1] International Agency for Research on Cancer, *World Health Organization, World cancer factsheet*, http://publications.cancerresearchuk.org/downloads/product/CS_REPORT_WORLD.pdf (last access Mar. 2015).

[2] NuPECC, *Nuclear Physics for Medicine*, Report, 2014, http://www.nupecc.org/pub/npmed2014.pdf (last access Mar. 2015).

[3] R.R. Wilson, *Radiological use of fast protons*, Radiology **47**, 487 (1946).

[4] E. Fokas et al., *Ion beam radiobiology and cancer: Time to update ourselves*, Biochim. Biophys. Acta. **1796(2)**, 216 (2009).

[5] C.H. Min et al., *Prompt gamma measurements for locating the dose falloff region in the proton therapy*, Appl. Phys. Lett. **89**, 183517 (2006).

[6] M. Engelsman et al., *Physics controversies in proton therapy*, Semin. Radiat. Oncol. **23**, 88 (2013).

[7] J.F. Sutcliffe, *A review of in vivo experimental methods to determine the composition of the human body*, Phys. Med. Biol. **41**, 791 (1996).

[8] K. Parodi et al., *Patient study on in-vivo verification of beam delivery and range using PET/CT imaging after proton therapy*, Int. J. Radiat. Oncol. Biol. Phys. **68**, 920 (2007).

[9] P.G. Thirolf, *On the role of nuclear fragmentation for the advancement of in-vivo medical imaging*, 4th Int. Conf. on Nuclear Fragmentation (Kemer (Antalya), Turkey), (2013).

[10] K. Parodi, W. Enghardt and T. Haberer, *In-Beam PET measurements of β^+ radioactivity induced by proton beams*, Phys. Med. Biol. **47**, 21 (2002).

[11] X. Zhu and G. El Fakhri, *Proton Therapy Verification with PET Imaging*, Theranostics **3**, 731 (2013).

[12] J. Pawelke et al., *In-beam PET imaging of the control of heavy-ion tumour therapy*, IEEE Trans. Nucl. Sci. **44**, 1492 (1997).

[13] W. Enghardt et al., *Charged hadron tumour therapy monitoring by means of PET*, Nucl. Instr. Meth. **A 525**, 284 (2004).

[14] Y. Iseki et al., *Positron camera for range verification of heavy-ion radiotherapy*, Nucl. Instr. Meth. **A 515**, 840 (2003).

[15] S. Vecchio et al., *A PET prototype for in-beam monitoring of proton therapy*, IEEE Nucl. Sci. Symp. Honolulu, 24-362 (2007).

[16] W. Enghardt at al., *The application of PET to quality assurance of heavy-ion tumor therapy*, Strahlenther. Onkol. **175** Suppl 2, 33 (1999).

[17] D.R. Schaart, *Private communication* (Jan 13).

[18] P. Lecoq et al., *Factors influencing time resolution of scintillators and ways to improve them*, IEEE. Trans. Nucl. Sci. **57**, 2411 (2010).

[19] D. R. Schaart et al., *$LaBr_3$:Ce and SiPMs for time-to-flight PET: achieving 100 ps conicidence resolving time*, Phys. Med. Biol. **55**, N179 (2010).

[20] G. Landry, G. Dedes at al., presented at DGMP 2014.

[21] G. Battistoni et al., *The FLUKA code: Description and benchmarking*, AIP Conf. Proc. **896**, 31 (2007).

[22] A. Ferrari et al., *FLUKA: a multi-particle transport code*, CERN-2005-10, INFN/TC_05/11, SLAC-R-773 (2005).

[23] M. Moteabbed, S. Espana, and H. Paganetti *Monte carlo patient study on the comparison of prompt gamma and PET imaging for range verification in proton therapy*, Phys. Med. Biol. **56**, 1063 (2011).

[24] G.W. Phillips, *Gamma-ray imaging with Compton cameras*, Nucl. Instr. Meth. **B 99**, 674 (1995).

[25] G. Kanbach et al., *Development and calibration of the tracking Compton/Pair telescope MEGA*, Nucl. Instr. Meth. **A 545**, 310 (2005).

[26] A.C. Zoglauer, *First Light for the Next Generation of Compton and Pair Telescopes*, PhD thesis, Technical University Munich, 2005.

[27] T. Kormoll et al., *A prototype Compton camera for in-vivo dosimetry of ion beam cancer irradiation*, IEEE Nuclear Science Symposium and Medical Imaging Conference (NSS/MIC), 3484 (2011).

[28] M. Frandes, *Gamma-ray detection and Compton camera image reconstruction with application to hadron therapy*, PhD thesis, University Lyon, 2010.

[29] L.J. Harkness et al., *Optimization of a dual head semiconductor Compton camera using GEANT4*, Nucl. Instr. Meth. **A 604**, 351 (2009).

[30] M.-H. Richard, *Design study of a Compton Camera for prompt-gamma imaging during ion-beam therapy*, PhD thesis, Univ. Lyon (2012).

[31] C. Lang, D. Habs, K. Parodi, and P.G. Thirolf, *Sub-millimeter nuclear medical imaging with high sensitivity in positron emission tomography using $\beta^+\gamma$ coincidences*, Journ. Instr. **9**, P01008 (2014).

[32] Munich-Centre for Advanced Photonics (MAP), http://www.munich-photonics.de (last access Mar. 2015).

[33] J. Schreiber et al., *Analytical model for ion acceleration by high-intensity laser pulses*, Phys. Rev. Lett. **97**, 045005 (2006).

[34] http://www.lex-photonics.de (last access Mar. 2015).

[35] W.C. Röntgen, *On a new Kind of Rays*, Nature **53**, 275 (1896).

[36] H. Becquerel, *Sur les Radiations émises par Phosphorescence*, C. R. Acad. Sci. **CXXII**, 420 (1896).

[37] M. Laue, W. Friedrich and P. Knipping, *Interferenz-Erscheinungen bei Röntgenstrahlen*, Kgl. Bay. Akad. der Wiss., Munich, June 1912.

[38] E. Rutherford and E.N. da Andrade, *The Reflection of Gamma Rays from Crystals*, Nature **92**, 267 (1913).

[39] G.F. Knoll, *Radiation Detection and Measurements*, Wiley, 4th ed., 2010.

[40] R.D. Evans, *The Atomic Nucleus*, Krieger, New York, 1982.

[41] U. Spillmann, *Charakterisierung und erster experimenteller Einsatz von ortsauflösenden, energiedispersiven Germanium-Detektoren zur Präzisionsspektroskopie an schweren Ionen*, PhD thesis, Johann Wolfgang Goethe-University Frankfurt, 2008.

[42] S. Tashenov, *Hard X-Ray polarimetry with position sensitive germanium detectors - studies of the recombination transitions into highly charged ions*, PhD thesis, Johann Wolfgang Goethe-University Frankfurt, 2005.

[43] A.H. Compton, *A quantum theory of the scattering of X-rays by light elements*, Phys. Rev. **21**, 483 (1923).

[44] A.H. Compton and A.W. Simon, *Relation between the direction of a recoil electron and that of the scattered X-Ray quantum*, Phys. Rev. **26**, 289 (1925).

[45] G. Weber, Compton scattering calculator, http://www.physi.uni-heidelberg.de/~apixuser/compton/index.php (last access Mar. 2015).

[46] O. Klein and Y. Nishina, *Über die Streuung von Strahlung durch freie Elektronen nach der neuen relativistischen Quantenmechanik von Dirac*, Z. f. Phys. **52**, 853 (1929).

[47] NIST XCOM, Photon Cross Section Database, http://www.nist.gov/pml/data/xcom/index.cfm (last access Mar. 2015).

[48] T. Kormoll, *A Compton Camera For In-Vivo Dosimetry in Ion-Beam Radiotherapy*, PhD thesis, Technical University Dresden, 2012.

[49] PSTAR, Stopping power and range tables for protons, http://physics.nist.gov/PhysRefData/Star/Text/PSTAR.html (last access Mar. 2015).

[50] M. Kramer et al., *Treatment planning for heavy-ion radiotherapy: physical beam model and dose optimization*, Phys. Med. Biol. **45**, 11 (2000).

[51] F. Sommerer et al., *In-beam PET monitoring of mono-energetic ^{16}O and ^{12}C beams: experiments and FLUKA simulations for homogeneous targets*, Phys. Med. Biol. **54**, 3979 (2009).

[52] K. Parodi et al., *Clinical CT-based calculations of dose and positron emitter distributions in proton therapy using the FLUKA Monte Carlo code*, Phys. Med. Biol. **52**, 3369 (2007).

[53] E. Urakabe et al., *Spot scanning using radioactive ^{11}C beams for heavy-ion radiotherapy*, Jpn. J. Appl. Phys. **40**, 2540 (2001).

[54] M. Kanazawa et al., *Application of an RI-beam for cancer therapy: in-vivo verification of the ion-beam range by means of positron imaging*, Nucl. Phys. **A 701**, 244c (2002).

[55] T. Tomitani et al., *Washout studies of ^{11}C in rabbit thigh muscle implanted by secondary beams of HIMAC*, Phys. Med. Biol. **48**, 875 (2003).

[56] H. Mizuno et al., *Washout measurement of radioisotope implanted by radioactive beams in the rabbit*, Phys. Med. Biol. **48**, 2269 (2003).

[57] T. Inaniwa et al., *Quantitative comparison of suitability of various beams for range monitoring with induced β^+ activity in hadron therapy*, Phys. Med. Biol. **50**, 1131 (2005).

[58] S.E. Combs et al., *Heidelberg Ion-Therapy Center (HIT): initial clinical experience in the first 80 patients*, Acta. Oncol. **49**, 1132 (2010).

[59] http://www.klinikum.uni-heidelberg.de/fileadmin/pressestelle/PM_neu/10_2012/121029HIT_Grafik.pdf (last access Mar. 2015).

[60] http://www.rptc.de/en/proton-therapy/proton-radiation-technology.html (last access Mar. 2015).

[61] S. Verdú-Andrés et al., *CABOTO, a high-gradient linac for hadron therapy*, J. Radiat. Res. **54** (Suppl 1), i155 (2013).

[62] K. Zeil et al., *Dose-controlled irradiation of cancer cells with laser-accelerated proton pulses*, Appl. Phys. B **110**, 437 (2013).

[63] J. Bin et al., *A laser-driven nanosecond proton source for radiobiological studies*, Appl. Phys. Lett. **101**, 243701 (2012).

[64] http://www.oncoray.de (last access Mar. 2015).

[65] R.A. Snavely et al., *Monoenergetic ion beams from ultrathin foils irradiated by ultrahigh-contrast circularly polarized laser pulses*, Phys. Rev. ST Accel. Beams **11**, 031301 (2008).

[66] A. Macchi et al., *Laser acceleration of ion bunches at the front surface of over-dense plasmas*, Phys. Rev. Lett. **94**, 165003 (2005).

[67] S.C. Wilks et al., *Energetic proton generation in ultra-intense laser-solid interactions*, Phys. Plasmas **8**, 542 (2001).

[68] S.P. Hatchett et al., *Electron, photon and ion beams from the relativistic interaction of petawatt laser pulses with solid targets*, Phys. Plasmas **7**, 2076 (2000).

[69] R.A. Snavely et al., *Intense high-energy proton beams from petawatt-laser irradiation of solids*, Phys. Rev. Lett. **85**, 2945 (2000).

[70] Rad-icon Imaging Corp, RadEye1 Large Area Image Sensor, http://www.rad-icon.de/pdf/RadEye1.pdf (last access Mar. 2015).

[71] X. Llopart and M. Campbell, *First test measurements of a 64k pixel readout chip working in single photon counting mode*, Nucl. Instr. Meth. **A 509**, 157 (2003).

[72] X. Llopart et al., *Timepix, a 65k programmable pixel readout chip for arrival time, energy and/or photon counting measurements*, Nucl. Instr. Meth. **A 581**, 485 (2007).

[73] S. Reinhardt, *Detection of laser-accelerated protons*, PhD thesis, Ludwig-Maximilians-University München, 2012.

[74] M. Durante et al., *Charged particles in radiation oncology*, Nat. Rev. Clin. Oncol. **7**, 37 (2010).

[75] B.L.T. Ramaekers et al., *Systematic review and meta-analysis of radiotherapy in various head and neck cancers: Comparing photons, carbon-ions and protons*, Canc. Treat. Rev. **37**, 185 (2011).

[76] M. Nikl, *Scintillation detectors for x-rays*, Meas. Sci. Technol. **17**, R37 (2006).

[77] T. Kato, *High resolution phoswich gamma-ray imager utilizing monolithic MPPC arrays with submillimeter pixelized crystals*, Journ. Instr. **8**, P05022 (2013).

[78] C. van Eijk, in: S. Tavernier et al. (ed.), *Radiation detectors for medical imaging*, Springer, 2006.

[79] H.T. van Dam et al., *Improved nearest neighbor methods for gamma photon interaction position determination in monolithic scintillator PET detectors*, IEEE Trans. **58**, 2139 (2011).

[80] http://www.crystals.saint-gobain.com (last access Mar. 2015).

[81] http://www.eljentechnology.com (last access Mar. 2015).

[82] V. Schoenfelder et al., *A telescope for soft gamma ray imaging*, Nucl. Instr. Meth. **107**, 113 (1973).

[83] M. Singh and D. Doria, *Single photon imaging with electronic collimation*, IEEE. Trans. Nucl. Sci. **32**, 843 (1985).

[84] S.W. Peterson et al., *Optimizing a three-stage Compton Camera for measuring prompt gamma rays emitted during proton radiotherapy*, Phys. Med. Biol. **55**, 6841 (2010).

[85] D. Robertson et al., *Material efficiency studies for a Compton Camera Designed to Measure Characteristic Prompt Gamma Rays emitted During Proton Beam Radiotherapy*, Phys. Med. Biol. **56**, 047 (2011).

[86] F. Roellinghoff et al., *Design of a Compton Camera for 3D Prompt-gamma Imaging During Ion Beam Therapy*, Nucl. Instr. Meth. A **648**, Suppl. 1, s20 (2011).

[87] M.-H. Richard et al., *Design Study of The Absorber Detector of a Compton Camera for On-line in Ion Beam Therapy*, IEEE. Trans. Nucl. Sci. **59**, 1850 (2012).

[88] G. Llosa et al., *First Compton telescope prototype based on continuous $LaBr_3$ - SiPM detectors*, Nucl. Instr. Meth. **A 718**, 130 (2013).

[89] A. Zoglauer et al., *MEGAlib The Medium Energy Gamma-ray Astronomy Library*, New Astron. Rev. **50**, 629 (2006).

[90] R. Andritschke, *Calibration of the MEGA prototype*, PhD thesis, Technical University Munich, 2006.

[91] J. Donnard et al., *Compton imaging with liquid xenon and ^{44}Sc: recent progress toward 3 gamma imaging*, Nucl. Med. Rev. **15**, Suppl. C, C64 (2012).

[92] H. A. Bethe, *Molière's theory of multiple scattering*, Phys. Rev. **89**, 1256 (1953).

[93] Particle Data Group, *Review of Particle Physics*, Phys. Lett. B **592**, (2004).

[94] M.M. Ter-Pogossian et al., *A Positron-Emission Transaxial Tomograph for Nuclear Imaging (PETT)*, Radiology **114**, 89 (1975).

[95] M.E. Phelps et al., *Application of annihilation coincidence detection to transaxial reconstruction tomography*, J. Nucl. Med. **16**, 210 (1975).

[96] N. Watanabe et al., *Potential Requirement of Positron Emission Tomography Apparatuses in Asia and Latin America Including Mexico*, World J. Nucl. Med. **12**, 33 (2013).

[97] P. Suetens, *Fundamentals of Medical Imaging*, Cambridge Univ. Press 2002.

[98] K. Shibuya et al., *Annihilation photon acollinearity in PET: volunteer and phantom FDG studies*, Phys. Med. Biol. **52**, 5249 (2007).

[99] D.C. Oxley et al., *Quantifying the limitations of small animal positron emission tomography*, Nucl. Instr. Meth. **A 604**, 343 (2009).

[100] L. Torrisi, C. La Mela and G. Foti, *Doppler-broadening of positron annihilation in a biological environment*, Q. Jour. Nucl. Med. **41**, 18 (1997).

[101] K. Iwata, R.G. Greaves and C.M. Surko, *γ-ray spectra from positron annihilation on atoms and molecules*, Phys. Rev. **A 55**, 3586 (1997).

[102] D.R. Schaart et al., *SiPM-array based PET detectors with depth-of-interaction correction*, Nucl. Sci. Symp. Conf. Rec. **NSS 08**, 3581 (2008).

[103] http://www.healthcare.philips.com/main/products/nuclearmedicine/products/geminitfbigbore (last access Mar. 2015).

[104] http://www3.gehealthcare.co.uk/en-GB/Products/Categories/Molecular_Imaging/PET-CT/Discovery_PET-CT_710 (last access Mar. 2015).

[105] M.-J. Martinez et al., *Recent Results in Cancer Research* **170**, Springer Verlag 2008.

[106] http://www.healthcare.siemens.com/molecular-imaging/pet-ct/biograph-mct (last access Mar. 2015).

[107] S. Seifert et al., *First characterization of a digital SiPM based time-of-flight PET detector with 1 mm spatial resolution*, Phys. Med. Biol. **58**, 3061 (2013).

[108] A. Sitek, *Data analysis in emission tomography using emission-count posteriors*, Phys. Med. Biol. **57**, 6779 (2012).

[109] S.-J. Park et al., *A Prototype of a Very High-Resolution Small Animal PET Scanner using Silicon Pad Detectors*, Nucl. Instr. Meth. **A 570**, 543 (2007).

[110] Y. Yang, Y.C. Tai, S. Siegel et al., *Optimization and performance evaluation of the microPET II scanner for in vivo small-animal imaging*, Phys. Med. Biol. **49**, 2527 (2004).

[111] G. Llosa et al., *Towards a Sub-Millimeter PET Prototype with Continuous LYSO Crystals and SiPM Matrices*, Contrib. to IEEE NSS-MIC2012, Anaheim/USA M05-5 (2012).

[112] C. Grignon et al., *Nuclear medical imaging using $\beta^+\gamma$ coincidence from ^{44}Sc radio-nuclide with liquid xenon as detection medium*, Nucl. Instr. Meth. **A 571**, 142 (2007).

[113] G.D. Hutchins et al., *Small animal PET imaging*, ILAR Jour. **49**, 54 (2008).

[114] M.R. Bhat, *Evaluated Nuclear Structure Data File (ENSDF)*, Nuclear Data for Science and Technology **B 103**, Springer-Verlag, Berlin, Germany (1992).

[115] J.L. Humm, A. Rosenfeld and A. Del Guerra, *From PET detectors to PET scanners*, Eur. Jour. Nucl. Med. Mol. Imaging **30**, 1574 (2003).

[116] S. Agostinelli et al., *Geant4 - a simulation toolkit*, Nucl. Instr. Meth. **A 506**, 250 (2003).

[117] D. Habs and U. Köster, *Production of medical radioisotopes with high specific activity in photonuclear reactions with high intensity and large brilliance*, Appl. Phys. **B 103**, 501 (2011).

[118] F. Rösch and R.P. Baum, *Generator-based PET radiopharmaceuticals for molecular imaging of tumours: on the way to THERANOSTICS*, Dalton Trans. **40**, 6104 (2011).

[119] M. Pruszynski, N.S. Loktionova, D.V. Filosofov, F. Rösch, *Post-elution processing of ^{44}Ti/^{44}Sc generator-derived ^{44}Sc for clinical application*, Appl. Radiat. Isot. **68**, 1636 (2010).

[120] F. Poenisch et al., *Attenuation and scatter correction for in-beam positron emission tomography monitoring of tumour irradiations with heavy ions*, Phys. Med. Biol. **48**, 2419 (2003).

[121] J.M. Ollinger, *Model-based scatter correction for fully 3D PET*, Phys. Med. Biol. **41**, 153 (1996).

[122] A. Zoglauer, *Methoden der Bildrekonstruktion für das Comptonteleskop MEGA*, Diploma thesis, Technical University Munich, 2000.

[123] K. Lange and R. Carson, *EM reconstruction algorithms for emission and transmission tomography*, J. Comput. Assist. Tomogr. **8**(2), 306 (1984).

[124] S. Wilderman et al., *List-mode Maximum Likelihood Reconstruction of Compton Scatter Camera Images in Nuclear Medicine*, IEEE Trans. Nucl. Sci. **45**, 957 (1998).

[125] A. Zoglauer, *Private communication* (Jun 2013).

[126] S.E. Derenzo et al., *Imaging properties of a positron tomograph with 280 BGO crystals*, IEEE Trans. Nucl. Sci. **28**, 81 (1981).

[127] H.M. Hudson et al., *Accelerated image reconstruction using ordered subsets of projection data*, IEEE Trans. Med. Imag. **13**, 601 (1994).

[128] E.P. Visser et al., *Spatial Resolution and Sensitivity of the Inveon Small-Animal PET Scanner*, Jour. Nucl. Med. **50**, 139 (2009).

[129] L. Eriksson et al., *An investigation of sensitivity limits in PET scanners*, Nucl. Instr. Meth. **A 580**, 836 (2007).

[130] H. Mizuno et al., *Washout measurement of radioisotope implanted by radioactive beams in the rabbit*, Phys. Med. Biol. **48**, 2269 (2003).

[131] M. Sajjad et al., *Production and dosimetry of [^{14}O]water for PET activation studies*, Appl. Rad. Iso. **57**, 607 (2002).

[132] C.-L. Lee et al., *Radiation dose estimation using preclinical imaging with ^{124}I-metaiodobenzylguanidine (MBIG) PET*, Med. Phys. **37** , 4861 (2010).

[133] S. Senthamizhchelvan et al., *Radiation Dosimetry of ^{82}Rb in Humans under Pharmacologic Stress*, J. Nucl. Med. **52**, 485 (2011).

[134] A. Lövqvist et al., *Kinetics of ^{76}Br-labeled anti-CEA antibodies in pigs; Aspects of dosimetry and PET imaging properties*, Med. Phys. **26**, 249 (1999).

[135] S. Aldawood, *PhD thesis (in preparation)*, Ludwig-Maximilians-Universität München.

[136] http://www.crystals.saint-gobain.com/BrilLanCe_380_Scintillator.aspx (last access Mar. 2015).

[137] http://www.hamamatsu.com/us/en/product/category/3100/3002/H9500/index.html (last access Mar. 2015).

[138] http://www.mesytec.com/datasheets/MCFD-16.pdf (last access Mar. 2015).

[139] http://www.mesytec.com/datasheets/MQDC-32.pdf (last access Mar. 2015).

[140] ROOT - An Object Oriented Data Analysis Framework http://root.cern.ch (last access Mar. 2015).

[141] R. Lutter et al., *MARaBOU- An MBS and ROOT Based Online/Offline Utility*, IEEE Trans. Nucl. Sci. **47(2)**, 363 (1999).

[142] http://www.crystals.saint-gobain.com/Cast_Plastic_Scintillator.aspx (last access Mar. 2015).

[143] http://www.caen.it/csite/CaenProd.jsp?idmod=35&parent=11 (last access Mar. 2015).

[144] F. Quarati et al., *Study of ^{138}La radioactive decays using $LaBr_3$ scintillators*, Nucl. Instr. Meth. **A 683**, 46 (2012).

[145] R. Milbrath et al., *Characterization of alpha contamination in lanthanum trichloride scintillators using coincidence measurements*, Nucl. Instr. Meth. **A 547**, 504 (2005).

[146] F. Quarati et al., *X-ray and gamma-ray response of a 2" x 2" $LaBr_3$:Ce scintillation detector*, Nucl. Instr. Meth. **A 574**, 115 (2007).

[147] Lawrence Berkeley National Laboratory X-ray Data Booklet, 3rd ed., 2009. Available from http://xdb.lbl.gov (last access Mar. 2015).

[148] W.W. Moses and K.S. Shah, *Potential for $RbGd_2Br_7$:Ce, $LaBr_3$:Ce and LuI_3:Ce in nuclear medical imaging*, Nucl. Instr. Meth. **A 537**, 317 (2005).

[149] A. Fabbri et al., *A new iterative algorithm for pixilated and continuous scintillating crystals*, Nucl. Instr. Meth. **A 648**, S17 (2011).

[150] R. Pani et al., *Lanthanum scintillation crystals for gamma ray imaging*, Nucl. Instr. Meth. **A 567**, 294 (2006).

[151] I. Deloncle et al., *Fast timing: Lifetime measurements with $LaBr_3$ scintillators*, Jour. Phys. Conf. Ser. **205**, 012044 (2010).

[152] H. v.d. Kolff, *Characterization of the absorbing detector component of a Compton camera designed for beam range verification in hadron therapy*, Master thesis, TU Delft/LMU Munich, 2014.

[153] R. Pani et al., *Ce doped lanthanum tri-bromide SPET scanner for molecular imaging*, Nucl. Instr. Meth. **A 567**, 187 (2007).

[154] J.W. Scrimger and R.G. Baker, *Investigation of Light Distribution from Scintillations in a Gamma Camera Crystal*, Phys. Med. Biol. **12**, 101 (1967).

[155] I. Castelhano, *Development of a Compton Camera for Prompt-Gamma Detection in Hadron therapy*, Master thesis, Univ. Lisbon/LMU Munich, 2014.

[156] http://www.cismst.de (last access Mar. 2015).

[157] http://www.fischerelektronik.de/web_fischer/en_GB/connectors/G02/Female%20headers/VA/BLR4100Z100/index.xhtml;jsessionid=4C5B0C46F8556C880D65B21E1F4E9A06 (last access Mar. 2015).

[158] W. Beusch et al, *GASSIPLEX: a low analog signal processor for readout of gaseous detectors*, Internal note, CERN-ECP/94-17, (1994).

[159] K. Zeitelhack et al., *The HADES RICH Detector*, Nucl. Instr. Meth. **A 433**, 201 (1999).

[160] M. Böhmer, *Das Auslesesystem für den Ringabbildenden Cerenkovdetektor im HADES Spektrometer*, Diploma thesis, Technical University Munich, 1999.

[161] A. Kastenmüller. 64-channel Preprocessing Frontend Module http://www.e12.ph.tum.de/~gernhaus/projects/pfm/pfm.pdf (last access Mar. 2015), Technical University Munich, 2001.

[162] J. Bortfeldt, *Development of Micro -Pattern Gaseous Detectors - Micromegas*, Diploma thesis, Ludwig-Maximilians-University Munich, 2010.

[163] Elantec. EL4441C data sheet. http://www.e12.ph.tum.de/~mboehmer (last access Mar. 2015).

[164] Burr-Brown Corporation. 10-bit, 20 MHz Sampling Analog-to-Digital Converter. http://www.ti.com (last access Mar. 2015).

[165] M. Hoek et al., *Performance and response of scintillating fiber modules to protons and pions*, Nucl. Instr. Meth. **A 572**, 808 (2007).

[166] http://www.semikon-detector.de/ (last access Mar. 2015).

[167] D. Protić and T. Krings *Microstructures on Ge detectors with amorphous Ge contacts*, IEEE. Trans. Nucl. Sci. **50**, 998 (2003).

[168] http://www.mesytec.com/datasheets/MCFD-16.pdf (last access Mar. 2015).

[169] http://www.caen.it/csite/CaenProd.jsp?parent=11&idmod=37 (last access Mar. 2015).

[170] http://photon-science.desy.de/facilities/doris_iii_archive/facility_information/index_eng.html (last access Mar. 2015).

[171] http://doris.desy.de (last access Mar. 2015).

[172] R.J. Baldessarini et al., *Decreased risk of suicides and attempts during long-term lithium treatment: a meta-analytic review*, Bipolar Disorders **8**, 625 (2006).

[173] O. Beckman and R. Sandström, *X-ray photoexcitation of ^7Li*, Nucl. Phys. **5**, 595 (1958).

[174] E.C. Booth, *Nuclear resonance scattering of bremsstrahlung*, Nucl. Phys. **19**, 426 (1960).

[175] J.J. Carroll et al., *Photoexcitation of nuclear isomers by (γ, γ') reactions*, Phys. Rev. C **43**, 1238 (1991).

[176] http://www.esrf.eu (last access Mar. 2015).

[177] http://www.esrf.eu/UsersAndScience/Experiments/StructMaterials/ID15 (last access Mar. 2015).

[178] T. Buslaps, *Private communication* (Aug 2014).

[179] R.B. Firestone et al., *Table of Isotopes*, John Wiley & Sons, 8th ed., 1996.

[180] E.C. Booth et al., *Nuclear resonance fluorescence from light to medium weight nuclei*, Nucl. Phys. **57**, 403 (1964).

[181] W. Demtröder, *Experimentalphysik Band 4, Kern-, Teilchen- und Astrophysik*, Springer, 2nd ed., 2005.

[182] C.P.J. Barty, ELI-NP-meeting, http://www.eli-np.ro/documents/ELI-NP-WhiteBook.pdf (last access Mar. 2015).

[183] http://www.eli-np.ro (last access Mar. 2015).

[184] D. Habs et al., *Refractive index of Silicon at γ Ray Energies*, Phys. Rev. Lett. **108**, 184802 (2012).

Acknowledgements

Many people have supported me throughout my thesis. I want to mention some of them and express my gratitude to ...

... Prof. Dr. Dieter Habs for giving me the topic of this thesis.

... PD Dr. Peter G. Thirolf for his supervision of this thesis, his patience with uncountable problems I was confronted with, and especially for the freedom I had in the research, which emancipated me.

... Prof. Dr. Katia Parodi for her interest and support.

... Dr. Andreas Zoglauer for providing the MEGAlib Monte-Carlo simulation software.

... Dr. Ludwig Maier, Dr. Michael Böhmer and Dr. Jonathan Bortfeldt for providing the Gassiplex readout of the DSSSD and for their generous support and help.

... Rudi Lutter for providing the MARABOU analyzing software.

... Saad Aldawood, who joined the project during the end of this thesis, for participating in settting up the camera.

... Johann Karg, Johann Krapfl and Rolf Oehm representative for the whole team of the LMU electronics and hardware workshop, for providing me with the electronics and hardware needed.

... and the colleagues in Garching, whose help was relevant for completion of this thesis: Christine Weber, Peter Hilz, Lorant Csige, Sergie Gasilov and Stefan Gärtner.